The Hofstadter Model and Other Fractional Chern Insulators

Fenner Thomas Pearson Harper
St Hugh's College
University of Oxford

A thesis submitted for the degree of
Doctor of Philosophy in Theoretical Physics

Trinity Term 2015

The Hofstadter Model and Other Fractional Chern Insulators

Fenner Thomas Pearson Harper

St Hugh's College, University of Oxford

A thesis submitted for the degree of *Doctor of Philosophy in Theoretical Physics*

Trinity Term 2015

Abstract

Fractional Chern insulators (FCIs) are strongly correlated, topological phases of matter that may exist on a lattice in the presence of broken time-reversal symmetry. This thesis explores the link between FCI states and the quantum Hall effect of the continuum in the context of the Hofstadter model, using a combination of non-perturbative, perturbative and numerical methods. We draw links to experimental realisations of topological phases, and go on to consider a novel way of generating general FCI states using strong interactions on a lattice.

We begin by considering the Hofstadter model at weak field, where we use a semi-classical analysis to obtain nonperturbative expressions for the band structure and Berry curvature of the single-particle eigenstates. We use this calculation to justify a perturbative approximation, an approach that we extend to the case when the amount of flux per plaquette is close to a rational fraction with a small denominator. We find that eigenstates of the system are single- or multicomponent wavefunctions that connect smoothly to the Landau levels of the continuum. The perturbative corrections to these are higher Landau level contributions that break rotational invariance and allow the perturbed states to adopt the symmetry of the lattice. In the presence of interactions, this approach allows for the calculation of generalised Haldane pseudopotentials, and in turn, the many-body properties of the system. The method is sufficiently general that it can apply to a wide variety of lattices, interactions, and magnetic field strengths.

We present numerical simulations of the Hofstadter model relevant to its recent experimental realisation using optical lattices, noting the additional complications that arise in the presence of an external trap.

Finally, we show that even if a noninteracting system is topologically trivial, it is possible to stabilise an FCI state by introducing strong interactions that break time-reversal symmetry. We show that this method may also be used to create a (time-reversal symmetric) fractional topological insulator, and provide numerical evidence to support our argument.

Acknowledgements

First and foremost, I am extremely grateful to my supervisor, Steve Simon, for opening my eyes to new areas of physics, teaching me how to do research, and for passing on his infectious enthusiasm for the subject. I have benefited greatly from his knowledge, guidance, time and wit, and I thank him wholeheartedly.

The Rudolf Peierls Centre has provided a stimulating and rich environment in which to work, and I am grateful for the many useful interactions I have had over the past four years with Fiona Burnell, John Cardy, Fabian Essler, Paul Fendley, Eliot Kapit, Zohar Ringel, Jesper Romers, Robin Stinchcombe, and Stefanie Thiem. I thank John Chalker in particular, for providing sage advice on so many occasions, for granting me a college teaching opportunity—and of course, for examining this thesis. I also thank my external examiner, Ryan Barnett, in this regard.

In addition, I acknowledge the use of computer time on the *Hydra* cluster, and am very grateful to Jonathan Patterson for his efficient technical support. I also thank Michelle Bosher, Sarah Loving, Stephanie Shen and Sara Williams, who have been extremely helpful during the course of my DPhil.

I have shared my time at Oxford with many talented DPhil students. Particular thanks go to Bruno Bertini and Thomas Veness for blackboard discussions and office camaraderie; Neil Robinson for teaching me a great deal and for providing a year of regular squash matches; and to Thomas Scaffidi for many enlightening discussions and comments. I also thank Simon Davenport, Richard Fern, Gábor Halász, Curt von Keyserlingk, Dillon Liu, Lisa Moevius, Adam Nahum, Mathias Rufino, Pablo Serna, and Darren Tan for stimulating conversations, both in the department and in the pub. Outside the department, I am extremely grateful to my friends from St Hugh's College and elsewhere, too numerous to list, for their encouragement over the years.

Many aspects of this thesis were a direct result of fruitful collaborations. I gratefully acknowledge the many productive discussions I have had with Rahul Roy and Nick Read, and I look forward to many more such discussions in the future. I have also benefited from speaking with other researchers from outside of the department, and particularly thank Nigel Cooper, Philipp Dumitrescu, Mark Goerbig, Adolfo Grushin, Chris Hooley, Layla Hormozi, Gunnar Möller, Roderich Moessner, and Frank Pollman. In addition, I am very grateful to the organisers and participants of the 2014 École de Physique des Houches for an inspiring month in the French Alps.

Finally, and most importantly, I thank Katharina, my parents, and my sister, for their patience and unending support.

Chapters 2–3 in this thesis are based upon a published paper [1] and Chapter 5 is based upon a submitted preprint [2]. This research was made possible by the generous financial support of the EPSRC through the grants EP/I032487/1 and EP/I031014/1.

Contents

List of Figures

List of Tables

List of Abbreviations

CDW—charge density wave

CI—Chern insulator

COM—centre of mass

ED—exact diagonalisation

FCI—fractional Chern insulator

FD—Fock-Darwin

FQHE—fractional quantum Hall effect

FTI—fractional topological insulator

HFD—Hofstadter-Fock-Darwin

HH—Haldane honeycomb

IQHE—integer quantum Hall effect

LG—Landau gauge

LL—Landau level

LLL—lowest Landau level

LRE—long-range entangled

NN—nearest neighbour

NNN—next-nearest neighbour

PBC—periodic boundary condition

PES—particle entanglement spectrum

QHE—quantum Hall effect

SG—symmetric gauge

SPT—symmetry-protected topological phase

SRE—short-range entangled

TKNN—Thouless, Kohmoto, Nightingale, den Nijs

TQFT—topological quantum field theory

TR—time reversal

2DEG—two-dimensional electron gas

1. Introduction

1.1 Overview

In recent decades, condensed matter physics has undergone a small revolution. Triggered by a series of unexpected experimental results in the early 1980s, the ensuing years have seen the inception and evolution of an entirely new subfield: *topological phases of matter*. This new class of matter has been found to demonstrate an abundance of exotic physical phenomena, and offers many potentially transformative technological applications. Its discovery was accompanied by a flurry of activity and excitement, a trend which looks set to continue well into the twenty-first century.

The pioneering experimental results in question were the twin discoveries of the integer and fractional quantum Hall effects (IQHE and FQHE) [3, 4]. Comprising a two-dimensional electron gas (2DEG) permeated by a strong magnetic field, these remarkable systems were found to demonstrate a precisely quantised transverse ('Hall') conductivity and almost dissipationless transport in the longitudinal direction. Most notably, these macroscopic properties were shown to persist even in the presence of moderate perturbations, and were independent of the size and shape of the experimental system. This stability strongly suggested a dependence on the global properties of the system, rather than on the small-scale geometry, and heralded the introduction of concepts from topology into the study of condensed matter.

The quantum hall effects (QHE) are now reasonably well understood [5], and the term 'topological phase' has grown to encompass a wide variety of physical models, from spin systems [6] to string-net systems [7], and from band structures [8, 9] to heterostructures [3, 4]. Many of these models remain purely theoretical, while others occur naturally or can be readily realised in a laboratory. Some of the latter offer the potential for ground-breaking advances in technology, with a long-term ambition being the development of a topological quantum computer [10]: a system of qubits which uses the inherent stability and novel statistics present in a topological phase to carry out data processing operations.

Although many classification schemes have been developed to characterise topological phases, there still lacks a widely agreed upon set of definitions. Most descriptions, however, draw a distinction between long-range entangled (LRE) and short-range entangled (SRE) systems [11]. LRE phases exhibit intrinsic topological order that is typically manifested through exotic

quasiparticle excitations [12], a wavefunction degeneracy that depends on the genus of the underlying surface, and topological contributions to the entanglement entropy [13]. In addition, LRE topological phases are robust against local perturbations, and may be described in terms of topological field theories [14]. As well as the quantum Hall effects, LRE topological phases include lattice models known as (integer and fractional) Chern insulators [8, 9], the main focus of this thesis.[1]

Conversely, SRE phases do not display topological order. However, in the presence of symmetries, they may share certain similar features with conventional topological phases, including protected edge excitations and a description in terms of topological invariants [16]. These symmetry-protected topological states (SPT phases [17]) are robust against local perturbations that preserve the symmetry of the system, and (according to most definitions) include the time-reversal protected band systems known simply as topological insulators [16, 18].

In this thesis, we are primarily concerned with Chern insulators (CIs), a type of tight-binding model that breaks time reversal symmetry through its hopping phases, and exhibits long-range entanglement. Although related to the QHE [19, 20], CIs boast additional features and complications that stem from the underlying lattice. Notably, the discrete translational symmetry permits a description in terms of topological band theory [8, 9].

We will be particularly interested in the connections between the QHE and the CI. What effect does the breaking of translational and rotational symmetry have on a continuum quantum Hall state? Are there topological states which can *only* be realised in the presence of a lattice? Questions such as these can be answered, at least in part, by a specific model: the Hofstadter model [21, 22]. Describing electrons hopping on a lattice in the presence of an external magnetic field, the Hofstadter model can be thought of as a lattice realisation of the QHE. By adjusting the strength of the magnetic field, the natural length scale of the resulting wavefunctions can be varied relative to the lattice spacing, tuning its effects. In this way, the Hofstadter model interpolates between the continuum QHE and the lattice CI.

In this section, we will introduce topological band models and Chern insulators in detail. The main body of the thesis will then set out to answer the questions given above. However, in common with many other topological phases, much insight into the behaviour of a Chern insulator can be garnered from the study of the continuum QHEs. We therefore begin our introduction with a discussion of the IQHE and FQHE, the original topological phases.

[1] We note that some definitions do not class *integer* quantum Hall and Chern insulator phases as LRE, owing to their lack of a ground state degeneracy on a torus and their nonfractional quasiparticle excitations [15].

1.2 The Classical Hall Effect

The behaviour of charged particles moving in a magnetic field has been of interest to physicists for many decades. In 1879, E. H. Hall [23] carried out the first measurements of the current flowing through a thin metallic strip in the presence of a perpendicular magnetic field, using the set-up shown in Fig. 1.1a. Remarkably, he detected a current that flows in a *perpendicular* direction to the applied voltage, and whose strength is proportional to the applied magnetic field and the longitudinal current.

This behaviour was attributed to the Lorentz force, $F = q\left[\mathbf{E} + \mathbf{v} \times \mathbf{B}\right]$, which acts on a particle with charge q travelling with velocity $\mathbf{v}$ in the presence of an electric field, $\mathbf{E}$, and magnetic field, $\mathbf{B}$. In free (two-dimensional) space, the presence of a perpendicular magnetic field causes moving charged particles to form circular cyclotron orbits, oscillating at the cyclotron frequency, $\omega_c = |q|B/m$. In a classical two-dimensional slab of metal, however, deflected electrons near the edge cannot complete circular orbits, and so charge starts to build up at the side of the sample. In turn, this creates a transverse voltage and electric field, which eventually opposes the Lorentz force. When these forces are balanced, the equilibrium potential difference is known as the Hall voltage (V_H), and leads to a current in a four-terminal measurement.

The classical Hall effect may be explained using the hydrodynamic Drude model of an electron fluid [24], which describes the coarse-grained electron momentum distribution in terms of the Lorentz force and elastic scattering events. Solving for the steady-state momentum distribution [24], one finds that the classical Hall effect is characterised by the Hall coefficient,

$$R_H = \frac{E_y}{J_x B} = -\frac{1}{\rho e}, \tag{1.1}$$

where coordinate definitions are as shown in Fig. 1.1a, e is the magnitude of the carrier charge and ρ is the carrier density. In general, the carrier density may depend on factors including temperature and the magnetic field itself, and the Hall coefficient may even be positive if the relevant charge carriers are holes. Nonetheless, this classical expression provides good quantitative agreement with experimental values in the classical regime [24].

1.3 The Two-Dimensional Electron Gas

In both the classical and quantum Hall effects, it is essential to have a system that can be treated as two dimensional. There are many reasons why two dimensions is important, but its

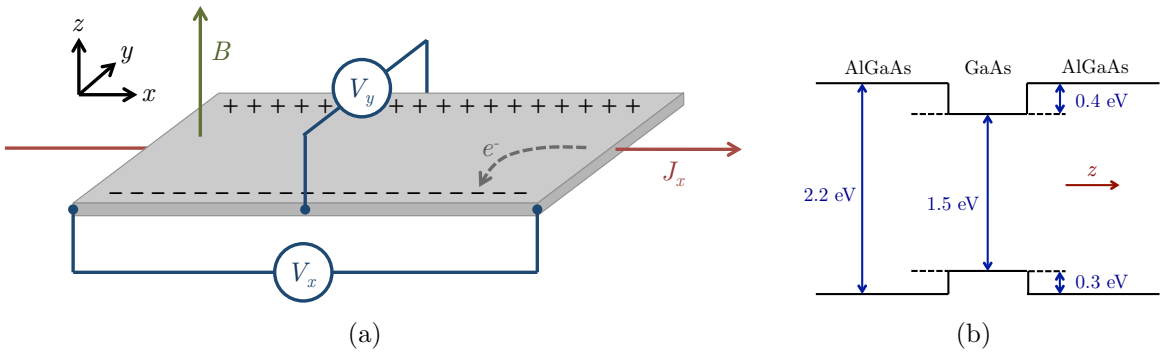

(a) (b)

Figure 1.1: (a) Schematic diagram of the experimental set-up used to measure the Hall effect (known as the Hall bar geometry). Dark grey dashed line indicates the deflection of an electron in the classical Hall effect, and lines of charge indicate the build up and depletion of electrons at the edge of the sample. (b) Band diagram of an (undoped) AlGaAs-GaAs-AlGaAs interface. If the AlGaAs regions are doped with, for example, silicon impurities, excess electrons fall into the GaAs quantum well region and form subbands.

uniqueness can be seen most clearly from scaling theory [25]. In a d-dimensional hypercube with dimension L, the resistance (R) and resistivity (ρ) are related through

$$R = \rho L^{2-d}.$$

When $d = 2$, therefore, the resistance is scale invariant and may be cast in a dimensionless form just by multiplying with the universal number e^2/h. In the QHE this scale invariance manifests itself through the universality of the resistance measurements, which are independent of the size and shape of the sample, as well as the precise locations of the contacts.

In the original experiments, Hall achieved a quasi-two-dimensional system by using very thin sheets of gold leaf. In modern experiments, something similar is achieved using a narrow quantum well that confines the motion in the third direction [26]. One of the most commonly used such wells is an AlGaAs-GaAs-AlGaAs interface, shown schematically in Fig. 1.1b. Although AlGaAs and GaAs have similar lattice structures, their bandwidths are rather different. If the AlGaAs regions are doped with n-type donor atoms (such as silicon atoms), some of these extra electrons fall into the GaAs region where they are confined by the regions of AlGaAs.

If the well is narrow, and if the temperature is low enough, the electrons are essentially trapped in the lowest energy z-mode, leaving an effective 2DEG in the remaining xy-directions. Other 2DEG systems may be made with a single AlGaAs-GaAs heterojunction or by using a MOSFET as in the original IQHE experiment [3] (see Ref. [26] for a review of these). In addition, there are also systems that are truly single-layer, such as graphene, which exhibit the QHE [27, 28, 29].

The systems considered above have a clear lattice structure, while the 2DEG is usually assumed to have continuous translational symmetry. As a specific example, GaAs has a zincblende lattice with a unit cell size of 5.65 Å [30], and we might wonder whether this should be included in the discussion. We will return to this question in more detail later on, but for now we note that this lattice constant is much smaller than the characteristic length of the wavefunction at the parameter values typically achieved in an experiment. In this situation, the 2DEG can be approximated as continuous.

1.4 Landau Levels

Much of the physics of the QHE builds upon the concept of Landau levels (LLs) [31]: quantised cyclotron orbits that arise when a charged particle moves under the influence of a magnetic field, according to quantum mechanics. We will be making substantial use of LLs in this thesis, and so spend this section revisiting the single-particle LL problem.

We seek solutions to the time-independent Schrödinger equation, $\hat{H}\psi = E\psi$, where $\hat{H}$ is the Landau Hamiltonian,

$$\hat{H} = \frac{1}{2m}\left(\mathbf{p} + e\mathbf{A}\right)^2, \tag{1.2}$$

with e the magnitude of the electron charge and $\mathbf{p} = -i\hbar\nabla$. The magnetic field strength is given by $\mathbf{B} = \nabla \times \mathbf{A} = -B\hat{\mathbf{z}}$.[2] With this Hamiltonian, the Schrödinger equation has a gauge symmetry: it is invariant under the simultaneous transformations

$$\mathbf{A}(\mathbf{r}) \to \mathbf{A}(\mathbf{r}) + \nabla\chi(\mathbf{r}), \qquad \psi(\mathbf{r}) \to \exp\left[-\frac{ie}{\hbar}\chi(\mathbf{r})\right]\psi(\mathbf{r}), \tag{1.3}$$

where $\chi(\mathbf{r})$ is any well-behaved scalar function of position. We are therefore free to solve the problem using whichever gauge is most convenient, or indeed to solve the system in an entirely gauge-independent manner. We will mostly be interested in the solution for two specific gauges, and so leave a gauge-independent discussion of Landau levels to one of the many substantial references on the QHE (see, for example, Sec. 3.8 of Ref. [32]).

1.4.1 The Landau Gauge

The first, and simplest, gauge we will choose is the Landau gauge in the y-direction, $\mathbf{A}_L = B(0, -x, 0)$. With this choice, Eq. (1.2) is independent of the coordinate y, and the momentum

[2] We choose a magnetic field in the negative z-direction in order to simplify the wavefunction expressions below.

in the y-direction, $\hbar k_y$, is a good quantum number (since $[\hat{p}_y, \hat{H}] = 0$). Wavefunction solutions therefore factorise into a plane wave in the y-direction multiplied by a factor that depends on the x-coordinate, $\psi(x)$, which satisfies the one-dimensional Schrödinger equation

$$\frac{1}{2m}\left[-\hbar^2\partial_x^2 + e^2B^2\left(x - \frac{\hbar k_y}{eB}\right)^2\right]\psi(x) \;=\; E\psi(x). \tag{1.4}$$

Since this is just the Hamiltonian for a (translated) one-dimensional quantum harmonic oscillator, we may solve it using standard methods to find the energy levels and wavefunctions,

$$\begin{aligned} E_n &= \left(n + \frac{1}{2}\right)\hbar\omega_c \\ \psi_{n,k_y}(\mathbf{r}) &= \frac{e^{ik_y y}}{\sqrt{2\pi}}\frac{1}{\sqrt[4]{\pi}}\frac{1}{\sqrt{2^n n! l_B}}e^{-\frac{1}{2}\left(\frac{x}{l_B} - l_B k_y\right)^2} H_n\left(\frac{x}{l_B} - l_B k_y\right). \end{aligned} \tag{1.5}$$

In these expressions, H_n is the nth Hermite polynomial, the magnetic length $l_B = \sqrt{\hbar/(eB)}$ is the characteristic length of the wavefunctions, and we have recalled the cyclotron frequency $\omega_c = eB/m$. We have also normalised the wavefunctions according to

$$\int \mathrm{d}^2\mathbf{r}\,\left[\psi_{n'k'_y}(\mathbf{r})\right]^*\psi_{n,k_y}(\mathbf{r}) \;=\; \delta_{nn'}\delta(k_y - k'_y). \tag{1.6}$$

We can obtain the same solutions by identifying the dimensionless ladder operators,

$$a = \frac{1}{\sqrt{2}l_B}\hat{x} + \frac{il_B}{\sqrt{2}}\hat{p}_x, \qquad a^\dagger = \frac{1}{\sqrt{2}l_B}\hat{x} - \frac{il_B}{\sqrt{2}}\hat{p}_x, \tag{1.7}$$

which are written in terms of $\hat{x}$, the position operator in the x-direction, and $\hat{p}_x = -i\hbar\partial_x$, the momentum operator in the x-direction. These operators satisfy the bosonic commutation relations $\left[a, a^\dagger\right] = 1$ and $[a, a] = \left[a^\dagger, a^\dagger\right] = 0$, and for simplicity, we have set $k_y = 0$ in the above expressions, since it merely applies a translation. In terms of these operators, we may rewrite Hamiltonian (1.4) as $\hbar\omega_c\left(a^\dagger a + \frac{1}{2}\right)|n\rangle = E_n|n\rangle$, where $|n\rangle = (a^\dagger)^n/\sqrt{n!}\,|0\rangle$ and $|0\rangle$ satisfies $a|0\rangle = 0$.

Each of the energy levels above corresponds to a Landau level, with the $n = 0$ energy level known as the lowest Landau level (LLL). Within each LL, there are many states with equal energy, each distinguished by a single parameter, k_y, which is the momentum in the y-direction and which also translates the wavefunction in the x-direction. In the LLL, the x-dependent part of the wavefunction is a Gaussian centred on $x = l_B k_y$, with a width that scales with l_B, plotted in Fig. 1.2a.

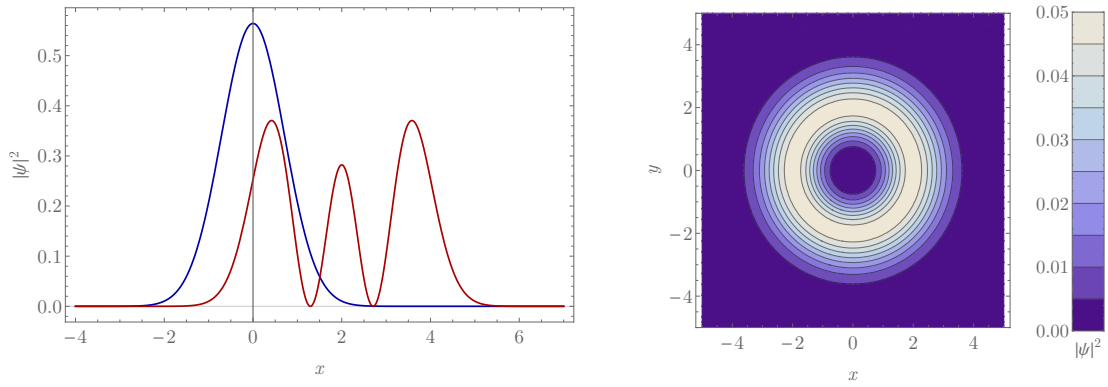

(a) Landau gauge

(b) Symmetric gauge

Figure 1.2: Wavefunction density plots for some Landau level wavefunctions (axes are in units of the magnetic length, l_B). (a) x-dependent part of two Landau gauge wavefunctions, showing $|\psi_{n=0,k=0}(x)|^2$ (blue) and $|\psi_{n=2,k=2l_B}|^2$ (red). (b) Two-dimensional density plot of $|\psi_{n=0,m=2}(x,y)|^2$.

Landau gauge solutions are useful in the rectangular (i.e. Hall bar) geometry and in the cylindrical geometry—where the y-direction is taken to be periodic. In these situations the wavefunctions share the same symmetry as the underlying system, and the k_y-dependent translation may be interpreted as a charge pumping as magnetic flux is threaded through the system (see Sec. 1.7). It should be noted that although these wavefunctions are localised in the x-direction, they are completely delocalised in the y-direction. Indeed, in systems with a Hall conductance, one cannot define a set of completely localised and completely orthogonal (Wannier) wavefunctions [33].

1.4.2 The Symmetric Gauge

Our second gauge choice is the symmetric gauge, $\mathbf{A}_S = -(\mathbf{B}\times\mathbf{r})/2 = B/2(y,-x,0)$. In this case, neither k_x nor k_y is a good quantum number, and we must solve the two-dimensional system in full. The system can be simplified greatly by introducing the complex coordinates, $z = x+iy$, $\partial_z = (\partial_x - i\partial_y)/2$ etc., in terms of which, the Schrödinger equation becomes

$$\frac{\hbar\omega_c}{2}\left[-4l_B^2\partial_z\partial_{\bar{z}} + \frac{1}{4l_B^2}z\bar{z} + \bar{z}\partial_{\bar{z}} - z\partial_z\right]\psi(z,\bar{z}) \quad = \quad E\psi(z,\bar{z}). \tag{1.8}$$

We can either solve this equation directly or, more easily, identify a set of ladder operators that simplify the expression. In this case, there are two useful pairs of ladder operators,

$$\begin{aligned} a &= \frac{1}{\sqrt{2}}\left(\frac{1}{2l_B}z + 2l_B\partial_{\bar{z}}\right), & a^\dagger &= \frac{1}{\sqrt{2}}\left(\frac{1}{2l_B}\bar{z} - 2l_B\partial_z\right), \\ b &= \frac{1}{\sqrt{2}}\left(\frac{1}{2l_B}\bar{z} + 2l_B\partial_z\right), & b^\dagger &= \frac{1}{\sqrt{2}}\left(\frac{1}{2l_B}z - 2l_B\partial_{\bar{z}}\right), \end{aligned} \tag{1.9}$$

which satisfy $\left[a, a^\dagger\right] = \left[b, b^\dagger\right] = 1$ and which otherwise commute.[3] In terms of these, the Hamiltonian again takes the simple operator form, $\hat{H} = \hbar\omega_c \left(a^\dagger a + \frac{1}{2}\right)$, with lowest-energy states satisfying the condition $a\left|0\right\rangle = 0$ and higher energy states obtained from $\left|n\right\rangle = \left(a^\dagger\right)^n / \sqrt{n!}\left|0\right\rangle$. If we have a state from a given LL, we can generate other states within the same LL by acting with b and $b^\dagger$, since these commute with a and $a^\dagger$: the operators $(a, a^\dagger)$ move between states in different LLs, while the operators $(b, b^\dagger)$ move between states within the same LL.

Before we write down the explicit wavefunctions, we can understand what the b-operators represent by considering the angular momentum about the z-axis. This may be written in operator form (with θ the azimuthal angle about the z-axis) as

$$\hat{L}_z = -i\hbar\frac{\partial}{\partial\theta} = \hbar\left(z\partial_z - \bar{z}\partial_{\bar{z}}\right) = \hbar\left(b^\dagger b - a^\dagger a\right). \tag{1.10}$$

Since $\hat{L}_z$ commutes with the Hamiltonian, the angular momentum about the z-axis is a good quantum number and, for Landau level n, takes the possible values $L_z = -n, -n+1, \ldots, 0, 1, \ldots$ in units of $\hbar$. We note that acting with $a^\dagger$ decreases the angular momentum by one unit and acting with $b^\dagger$ increases the angular momentum by one unit.

Overall, we may label a state with a Landau level index n and angular momentum index m through

$$\left|n, m\right\rangle = \frac{\left(a^\dagger\right)^n}{\sqrt{n!}}\frac{\left(b^\dagger\right)^m}{\sqrt{m!}}\left|0, 0\right\rangle,$$

where the state has total angular momentum $L_z = \hbar(m-n)$,[4] and where $\left|0,0\right\rangle$ satisfies $a\left|0,0\right\rangle = b\left|0,0\right\rangle = 0$. The energy depends only on the LL index as before, with $E_n = (n + 1/2)\hbar\omega_c$, and the real-space wavefunctions may be written explicitly as

$$\psi_{n,m}(z,\bar{z}) \;=\; (-1)^n\sqrt{\frac{n!}{2\pi l_B^2 m!}}\left(\frac{z}{\sqrt{2}l_B}\right)^{m-n} L_n^{m-n}\left[\frac{z\bar{z}}{2l_B^2}\right] e^{-\frac{z\bar{z}}{4l_B^2}}, \tag{1.11}$$

where L_n^{m-n} is a generalised Laguerre polynomial. In the LLL, these states take a particularly simple form,

$$\psi_{0,m}(z,\bar{z}) = \sqrt{\frac{1}{2\pi l_B^2 m!}}\left(\frac{z}{\sqrt{2}l_B}\right)^m e^{-\frac{z\bar{z}}{4l_B^2}}, \tag{1.12}$$

which, apart from the Gaussian factor, are just monomials in z. The most general LLL wave-

[3] We note from the operator expressions that $(\partial_z)^\dagger = -\partial_{\bar{z}}$. This change of sign can be seen to arise from integration by parts through $\left[\int \mathrm{d}z\mathrm{d}\bar{z}\, u^*\left(\partial_z v\right)\right]^\dagger = \int \mathrm{d}z\mathrm{d}\bar{z}\,\left(\partial_{\bar{z}} v^*\right) u = \int \mathrm{d}z\mathrm{d}\bar{z}\, v^*\left(-\partial_{\bar{z}} u\right)$, for arbitrary functions u and v with a vanishing boundary contribution.

[4] Note that many references label the symmetric gauge wavefunctions by the Landau level index, n, and the total angular momentum, $L_z = m - n$. We choose instead to label the states by m and n, the number of $a^\dagger$ and $b^\dagger$ operators required to generate the state from the vacuum: this significantly simplifies notation in later sections.

function in the symmetric gauge is then $\psi_{\mathrm{LLL}}(z,\bar{z}) = f(z)e^{-\frac{z\bar{z}}{4l_B^2}}$, where $f(z)$ is *any* analytic function.

The angular momentum eigenstates in the LLL form concentric rings about the origin. The state with angular momentum m has a mean radius of $\sqrt{2m}l_B$ and a width which scales with l_B, as shown in Fig. 1.2b. Although states with low values of m are localised in both directions near the origin, as we take m larger and larger, the wavefunctions become more and more delocalised—as in the Landau gauge, it is impossible to define a full set of states which are completely localised.

The symmetric gauge is the natural choice for situations with rotational symmetry, such as in a system of atoms confined by a harmonic trap or in a 'droplet' of particles with conserved total angular momentum. Moreover, many properties of the FQHE can be understood most easily in the symmetric gauge, owing to the analytic structure of the LLL. For this reason, we will mostly consider the symmetric gauge in the following sections.

1.4.3 Relation Between Landau and Symmetric Gauges

The Landau gauge and symmetric gauge wavefunctions given above are just different ways of describing a degenerate Landau level. Since each basis of wavefunctions is complete, a wavefunction written in the symmetric gauge can always be expressed as a linear combination of Landau gauge wavefunctions, multiplied by a gauge transformation phase factor, $e^{i\chi(x,y)}$. As we ultimately wish to switch between these gauges freely, we now give the explicit transformation required to do this. Using the definitions in Eqs. (1.5) and (1.11), and introducing the labels LG (SG) to indicate Landau (symmetric) gauge, the transformations may be written

$$\psi^{\mathrm{SG}}_{n,m} = e^{-\frac{ixy}{2l_B^2}} \int \mathrm{d}k\, B_m(k)\psi^{\mathrm{LG}}_{n,k}(x,y), \qquad \psi^{\mathrm{LG}}_{n,k} = e^{\frac{ixy}{2l_B^2}} \sum_m B^*_m(k)\psi^{\mathrm{SG}}_{n,m}(x,y),$$

with

$$B_m(k) = \frac{\sqrt{l_B}}{\sqrt[4]{\pi}} \frac{1}{\sqrt{2^m m!}} H_m\left(l_B k\right) e^{-\frac{k^2 l_B^2}{2}}. \tag{1.13}$$

In this expression, H_m is again the mth Hermite polynomial and we have relabelled $k_y \to k$ for convenience. We give the derivation of this expression in Appendix 1.A.

1.4.4 Landau Level Degeneracy

The number of LL states per unit area is the same in any gauge. We consider Landau gauge wavefunctions on an infinite cylinder, taking the circumference (in the y-direction) to be L_y,

and consider only the range $0 \leq x \leq L_x$ in the infinite direction. Periodic boundary conditions in the y-direction force the momentum to take the quantised values $k_y = \frac{2\pi p}{L_y}$, where p is an integer, and so the wavefunctions may be written, following Eq. (1.5),

$$\psi_{n,p}^{\text{cylinder}}(\mathbf{r}) = \frac{e^{i2\pi py/L_y}}{\sqrt{L_y}} \frac{1}{\sqrt[4]{\pi}} \frac{1}{\sqrt{2^n n! l_B}} e^{-\frac{1}{2}\left(\frac{x}{l_B} - \frac{2\pi l_B}{L_y} p\right)^2} H_n\left(\frac{x}{l_B} - \frac{2\pi l_B}{L_y} p\right). \tag{1.14}$$

In the x-direction, we observe that only states with $0 \leq p \leq L_x L_y/(2\pi l_B^2)$ lie within our chosen horizontal range. The total number of states within this region of area $L_x L_y$ is therefore $N_\phi = L_x L_y/(2\pi l_B^2)$, and the number of states per unit area is $g = N_\phi/(L_x L_y) = 1/(2\pi l_B^2)$.

Each LL state therefore occupies an area of approximately $2\pi l_B^2$, and the total number of states in a given area A is

$$N_\phi = \frac{A}{2\pi l_B^2} = \frac{BA}{\phi_0}, \tag{1.15}$$

where $\phi_0 = h/e$ is the magnetic flux quantum. In this way, we see that the number of available LL states in a given area is equal to the number of flux quanta passing through it, which justifies the notation N_ϕ.

Finally, we note that in general we will only occupy some of the available LL states. We define the filling factor, ν, to be the fraction of the available single-particle LL states that are occupied. For N_P particles in an area with N_ϕ available LL states,

$$\nu = \frac{N_P}{N_\phi} = \frac{\rho}{g} = \frac{\rho\phi_0}{B}, \tag{1.16}$$

where we have also expressed this in terms of the LL degeneracy, g, and the particle number density, ρ.[5] If ν is an integer, then there are enough particles to completely fill an integer number of LLs; if ν is a fraction, then some LLs are necessarily only partially filled. Since ν is inversely proportional to B, we can modify the fraction of occupied LL states by tuning the external magnetic field. Of course, this discussion is only clear at the single-particle level: in general, particle-particle interactions will cause mixing between states from many different Landau levels.

1.4.5 Periodic Landau Level Wavefunctions

In this subsection, we briefly discuss the LL wavefunctions that may be found in a system with periodic boundary conditions (PBCs) [35]. This will be of use later in the thesis when

[5] On some surfaces, such as the sphere, this relation must be generalised to $\nu^{-1} N_P = N_\phi + \mathcal{S}$, where $\mathcal{S}$ is known as the shift [34].

we compare quantum Hall wavefunctions to their lattice analogues, which are typically studied on a torus. For simplicity we will consider only the rectangular torus: we refer the reader to Refs. [36, 37, 38] for the general case.

We start from the Landau gauge wavefunctions on an infinite cylinder, which were given previously in Eq. (1.14). We now impose additional PBCs in the x-direction, setting the x-dimension to be L_x. In order for the PBCs to be consistent, the closed torus must contain an integer number of flux quanta, which, from Eq. (1.15), may be calculated through $N_\phi = L_x L_y/(2\pi l_B^2)$. We therefore need to form N_ϕ wavefunctions that are periodic in x and which are combinations of the cylinder wavefunctions given in Eq. (1.14). We achieve this by summing over the redundant values of the k_y-momentum to give

$$\begin{aligned}\psi_{n,p}^{\text{torus}}(\mathbf{r}) &= \sum_{j=-\infty}^{\infty} \psi_{n,p+jN_\phi}^{\text{cylinder}}(\mathbf{r}) \qquad (1.17)\\ &= \sum_{j=-\infty}^{\infty} \frac{e^{i2\pi(p+jN_\phi)y/L_y}}{\sqrt{L_y}} \frac{1}{\sqrt[4]{\pi}} \frac{1}{\sqrt{2^n n! l_B}} e^{-\frac{1}{2}\left(\frac{x}{l_B}-\frac{2\pi l_B}{L_y}(p+jN_\phi)\right)^2} H_n\left(\frac{x}{l_B}-\frac{2\pi l_B}{L_y}(p+jN_\phi)\right),\end{aligned}$$

an expression that may also be written in terms of Jacobi theta functions [36, 39].

1.5 The Integer Quantum Hall Effect

The *quantum* Hall effect, as distinct from the *classical* Hall effect, is the remarkable observation of well-defined plateaux in the Hall conductivity, σ_{xy}, which arises when quantum effects become important. Experimentally, the quantum regime is typically achieved in semiconductor quantum wells (Sec. 1.3), using very low temperatures and samples with very high mobility. A quantised Hall conductance has now been observed in many different semiconductor heterostructures [40, 41, 3, 4], as well as in more exotic materials such as suspended graphene [27, 29] and on the surfaces of 3D topological insulators [42].

The QHE is a large and well-established field of study, and there is a vast body of literature on the subject. In the introductory part of this thesis, we will only be able to scratch the surface of this body of knowledge, focusing on those aspects which are most relevant to later sections. For a full review, we refer the reader to one of the many excellent books on the subject, such as Ref. [5].

We begin by discussing the integer effect, which arises when an integer number of Landau levels are very close to being completely full. This was originally observed in 1980 [3], and can be explained using the theory of LLs developed in the previous section. Throughout this discussion we will ignore the spin degree of freedom and treat the particles as spinless fermions,

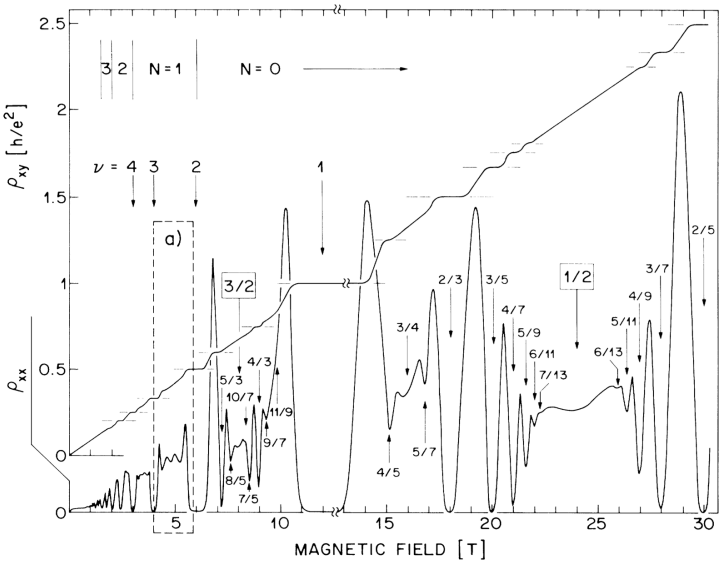

Figure 1.3: The quantum Hall 'skyline', showing a variety of plateaux with filling fractions between $\nu = 2/5$ and $\nu = 5$. Vertical axis shows transverse resistivity (ρ_{xy}) and longitudinal resistivity (ρ_{xx}), with the high field ($\gtrsim 12T$) longitudinal trace reduced by a factor of 2.5 for clarity. Note that not all values of ν given correspond to a QHE effect (notably $\nu = 1/2$). Reprinted figure with permission from R. Willett et al., Phys. Rev. Lett. 59, 1776 (1987). Ref. [43]. Copyright (1987) by the American Physical Society.

which does not change the qualitative argument. In a real system, Zeeman splitting will lead to a set of LLs for each spin species, which may be ignored if only a single, spin-polarised LL is energetically relevant. We will also ignore electron-electron interactions, since the important features of the IQHE can be understood at the single-particle level.

In an IQHE experiment, the filling factor, ν, is tuned by sweeping the magnetic field as in Eq. 1.16. Near to integer values of ν, the Hall conductivity takes the precisely quantised value

$$\sigma_{xy} = \frac{e^2}{h} \times \text{Integer}, \tag{1.18}$$

which persists even as ν is tuned away from the nearby integer. In addition, for this range of ν, the longitudinal resistance simultaneously becomes very small. Experimental results highlighting these integer plateaux are shown in Fig. 1.3 (along with many plateaux corresponding to FQHE states).

Assuming zero longitudinal resistivity, the classical description of the Hall effect from Sec. 1.2 gives a transverse conductance of

$$\sigma_{xy} = \frac{1}{B\,|R_H|} = \frac{\nu e^2}{h}, \tag{1.19}$$

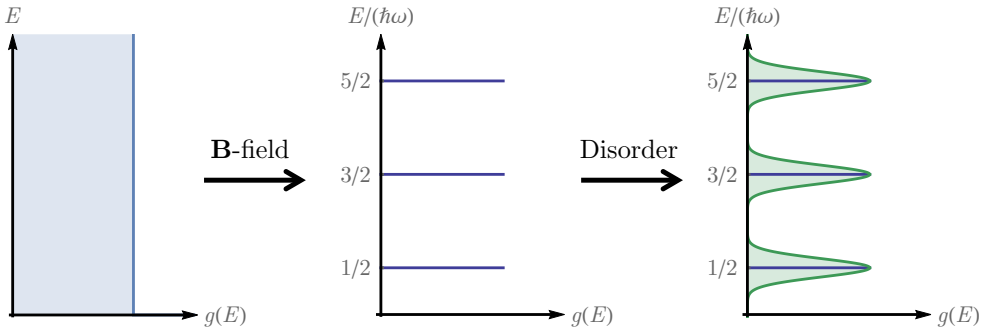

Figure 1.4: Changes in the energy spectrum of a 2DEG that occur as a magnetic field is switched on and weak disorder is added. The density of states is initially constant, but forms Landau levels when the magnetic field is switched on. These then form broad Landau bands in the presence of disorder. In the disordered energy spectrum, extended states are shown in blue and localised states are shown in green.

where we have inserted the charge density $\rho = \nu/(2\pi l_B^2)$ from Eq. (1.16) into Eq. (1.1).[6] If ν is an integer, so that the Fermi energy lies between LLs, then this expression predicts the Hall conductance to be an integer multiple of the conductance quantum. Unfortunately, the expression does not suggest the formation of plateaux: instead, Eq. (1.19) predicts the Hall conductance to vary linearly with ν.

The crucial missing ingredient is the presence of disorder [44]. If there is a small number of weakly interacting impurities in the system, then the local potential energy experienced by an electron will be slightly perturbed. In this way, each degenerate LL becomes an energy landscape in real space, with peaks and troughs in energy near impurities and extended, percolating contours of constant energy in between. Electrons move throughout this energy landscape by travelling along contour lines, with some electrons percolating through the sample and others forming Anderson localised orbits around the troughs and peaks in energy. In the spectrum, the presence of disorder deforms the highly degenerate LLs into broad Landau bands, with conducting orbits at the centre and localised orbits away from the centre, as shown in Fig. 1.4.

The localised states form an electron 'reservoir', onto which we can pin the Fermi energy: filling a localised state has no effect on the overall transport properties of the system. Instead, the conductance can only change when we fill or empty the extended states at the centre of a Landau band.[7] As we alter ν by changing the magnetic field strength, the Hall conductance remains constant except when we empty or fill these conducting states, leading to the observed plateaux in σ_{xy}.

However, this is still not the complete story. Although disorder explains the existence of the

[6] This classical expression can be derived rigorously for a disorder-free system using Galilean invariance [32].

[7] It can be shown that there always remains at least one delocalised state at the centre of the Landau band, provided the disorder is not too strong [45, 46].

plateaux, it does not fully explain the value of the conductance. Since many of the electrons are in Anderson-localised states, we would naively expect the total Hall conductance to be *less* than the value for a filled Landau level. It nevertheless turns out that the conducting states carry additional current to compensate for the localised states, restoring the Hall conductance to its integer-quantised value.

There are a number of arguments to show that the Hall conductance is quantised as expected. The first is a Landauer-Büttiker approach [47, 48], which treats the transport as a one-dimensional scattering problem at the edge of the quantum Hall bar. This is discussed in Refs. [48, 49, 50]. A second approach is to use a thought experiment originally introduced by Laughlin [51] and then refined by Halperin [46]. This considers bending the Hall bar into an annulus (a 'Corbino disk'), and then adiabatically threading magnetic flux through the centre. Using the fact that the spectrum of the system is unchanged if exactly one flux quantum is inserted, it can be shown that the transverse conductivity must be an integer multiple of e/h. This can be shown to hold whether or not disorder is present [46].

Unfortunately, these arguments appear to hold even if the Fermi level lies in an energy gap *within* a Landau level. For this reason, if we fractionally fill a Landau level and open a gap (by, for example, turning on a periodic potential [52, 53]), we would still expect an integer Hall conductance. The fact that this is not observed in experiments tells us that the FQHE cannot be explained using the single-particle theory developed so far.

1.6 The Fractional Quantum Hall Effect

The additional element we need to include in order to understand the FQHE is the electron-electron interaction. Without interactions, a fractionally filled LL has a huge degeneracy, corresponding to the large number of ways of choosing to partially fill the available LL states. Switching on interactions dramatically breaks this degeneracy, and at certain fractional filling factors leads to fractional Hall conductance plateaux [4, 43] (see Fig. 1.3).

Interactions in a partially-filled LL are highly nonperturbative: since the kinetic energy is quenched, there is no weakly interacting limit, and no 'normal' state to which we can add perturbative corrections. Instead, we must solve the many-body FQHE Hamiltonian in its entirety, which makes the problem significantly more complex than the IQHE. In contrast to that case, it is simplest to ignore the effects of disorder altogether, and to instead focus on the complicated, correlated wavefunctions that describe the fractional states.[8]

[8]Note, however, that weak disorder is once again necessary in order to observe a well-defined plateaux. It can

The full FQHE Hamiltonian, assuming once again that the particles are spinless, may be written

$$\hat{H}_{\mathrm{FQHE}} = \sum_{i}^{N_P} \frac{1}{2m} \left(\mathbf{p}_i + e\mathbf{A}_i\right)^2 + \sum_{i<j}^{N_P} V_{\mathrm{int}} \left(|\mathbf{r}_i - \mathbf{r}_j|\right), \tag{1.20}$$

where the subscripts i and j label the N_P particles, $\mathbf{p}_i = -i\hbar\nabla_i$, and $\mathbf{A}_i = \mathbf{A}(\mathbf{r}_i)$. We have assumed that the interaction depends only on the magnitude of the distance between particles, and is therefore translationally and rotationally symmetric. In an electronic system, the interaction is usually the Coulomb interaction,

$$V_{\mathrm{Coulomb}} \left(|\mathbf{r}_i - \mathbf{r}_j|\right) = \frac{e^2}{4\pi\epsilon \left|\mathbf{r}_i - \mathbf{r}_j\right|}, \tag{1.21}$$

although more general interactions will be discussed in Sec. 1.6.2.

If the interaction strength is weak compared to $\hbar\omega_c$, then it mostly acts within the partially filled LL. In this case, we can ignore the kinetic energy term in Eq. (1.20) altogether and consider only wavefunctions from the LLL. This *band projection* procedure simplifies the problem considerably while retaining the essential physical features. Corrections to this picture, known as LL mixing effects, can then be treated perturbatively [55, 56, 57, 58].

After projecting, the Hamiltonian (1.20) may be rewritten

$$\hat{H}_{\mathrm{FQHE}} = \sum_{i<j}^{N_P} \mathcal{P}_{\mathrm{LLL}} V_{\mathrm{int}} \left(|\mathbf{r}_i - \mathbf{r}_j|\right) \mathcal{P}_{\mathrm{LLL}}, \tag{1.22}$$

with $\mathcal{P}_{\mathrm{LLL}}$ a projection operator onto the LLL.[9] In this way, the interaction provides the only relevant energy scale of the system, and solution of the FQHE problem reduces to finding solutions to the Schrödinger equation with the Hamiltonian given in Eq. (1.22).

Since the interaction is rotationally symmetric, we will consider wavefunctions in the symmetric gauge and use conservation of angular momentum (implicitly using the infinite plane geometry). The basis of our many-body Hilbert space then, from Eq. (1.12), consists of monomials of the form

$$\psi_{\{m_i\}} \left(\{z_i\}\right) \sim \mathcal{A} \left(\prod_{i}^{N_P} z_i^{m_i}\right) \exp\left[-\sum_{i}^{N_P} \frac{|z_i|^2}{4l_B^2}\right], \tag{1.23}$$

where m_i is the angular momentum of the ith particle and $\mathcal{A}$ is the antisymmetrisation operator appropriate for fermions (for bosonic systems, the symmetrisation operator should be used

be shown that if there is a cusp in the total energy at a particular filling factor ν_0, i.e. a discontinuity in $\partial E/\partial\nu$, then weak disorder will stabilise a plateaux around ν_0 [54].

[9] There exists an analytical prescription for writing a general interaction in projected form [59].

intead). In second quantisation we can label these states in the occupation number basis as $|\psi_{n_m}\rangle = |n_{m=0}, n_{m=1}, \ldots\rangle$, where $n_{m=k}$ is the number of particles with angular momentum k. This takes into account the antisymmetrisation (or symmetrisation) required implicitly. Since angular momentum is conserved, each sector with total angular momentum $M_{tot} = \sum_i n_{m_i}$ can be considered independently. In principle, we could diagonalise the projected Hamiltonian (1.22) exactly within this basis in each angular momentum sector—and indeed, this is often the simplest way to generate numerical wavefunctions when the interaction is complicated. We will return to this subject in Chapter 4 when we carry out some exact diagonalisation of our own.

In general, however, most progress is made by motivating trial wavefunctions that are the exact ground states of certain idealised interactions. These trial states often show remarkably high overlap with the true numerical wavefunctions, and capture all of the essential physical features.

1.6.1 The Laughlin Wavefunction

The first successful trial wavefunction was the Laughlin state [60], which aimed to explain the FQHE plateaux observed at $\nu = 1/p$ (with p an odd integer). It may be written

$$\Psi_{\nu=1/p}\left(\{z_i\}\right) = \mathcal{N} \prod_{i<j}^{N_P} (z_i - z_j)^p \exp\left[-\frac{1}{4}\sum_i^{N_P} |z_i|^2\right], \tag{1.24}$$

where $\mathcal{N}$ is a normalisation factor and we have set $l_B = 1$. This satisfies the requirements that (a) apart from the Gaussian factors, the wavefunction is an analytic function of the coordinates; and (b) the wavefunction is antisymmetric under particle exchange, since p is odd. Additionally, the wavefunction vanishes rapidly when two particles approach each other, which should reduce the energy of the Coulomb interaction. We recover the filled LLL if we set $p = 1$, but for other values of p, Eq. (1.24) is highly correlated and cannot be expressed as a single Slater determinant. Detailed numerical studies have confirmed that Laughlin's wavefunction is a valid and accurate representation of the true (numerical) ground states at $\nu = 1/3$ and $\nu = 1/5$ [36]. When m is an even integer, Eq. (1.24) also gives a good description of *bosonic* FQHE ground states, which might be achieved in systems of cold atoms [61, 62, 63].

It can be seen from power counting that the Laughlin wavefunction has total angular momentum

$$M_0 = \frac{1}{2} p N_P \left(N_P - 1\right), \tag{1.25}$$

as every term in the expansion of Eq. (1.24) has this many powers of $\{z_i\}$ in total. By counting

the powers of a single coordinate, we can calculate the droplet size and verify that the Laughlin state occurs at a filling fraction of $\nu = 1/p$ (in the thermodynamic limit). For later reference, we also note that each pair of particles has a relative angular momentum of at least p.

Further insight into the Laughlin state can be obtained from the plasma analogy, which interprets the square magnitude of the wavefunction as a classical Boltzmann factor (see Ref. [60] and Chapter 7 in Ref. [5]). Notably, this approach allows one to infer that the Laughlin state exhibits quasihole excitations with fractional charge $q = 1/p$. This is an example of *fractionalisation*, a remarkable phenomenon that occurs in certain correlated systems, where collective excitations have quantum numbers that are fractions of the quantum numbers of the constituent particles. Even more remarkably, the quasihole and quasiparticle excitations of the Laughlin state obey *fractional statistics* [64]: when two such particles, known as anyons [65], are exchanged in a clockwise manner, the wavefunction picks up a phase of $\theta = \pi/p$.

Although a good approximation, the Laughlin state $\Psi_{\nu=1/p}$ is not the exact ground state of the Coulomb interaction. It is, however, the unique, highest-density, zero-energy state of the much simpler interaction [66], $V_p(\mathbf{r}) = \sum_{m=0}^{p-1} v_m(\mathbf{r})$, with

$$v_m(\mathbf{r}) = U L_m \left[-\nabla^2\right] \delta^{(2)}(\mathbf{r}), \tag{1.26}$$

where U is an interaction strength, L_m is the mth Laguerre polynomial, and $\mathbf{r} = \mathbf{r}_i - \mathbf{r}_j$. This interaction is short-range, has translational and rotational symmetry, and is the *parent Hamiltonian* for the Laughlin state. We will discuss how this interaction differs from the true Coulomb interaction in Sec. 1.6.2.

1.6.1.1 Alternative Formulations of the Laughlin Wavefunction

In this thesis, we will mostly be interested in the current formulation of the Laughlin wavefunction, which uses a first-quantised language in the symmetric gauge. For completeness, we briefly mention some of the other formulations of the Laughlin wavefunction that can be used.

The spherical geometry [67, 68] places the system on a sphere and inserts a magnetic monopole at the centre to provide a radial magnetic field. This geometry was used for much of the early numerical work, and is useful because it has no boundary and because the spherical LLs contain a finite number of states.

The Laughlin wavefunction also has a simple expression in the cylinder geometry [69], which is described most easily using the Landau gauge wavefunctions given in Eq. (1.14). The cylinder

geometry allows one to consider edge excitations more readily, and if the radius of the cylinder is taken to be very small (the thin-cylinder or Tao-Thouless limit [70]), the Laughlin wavefunction adiabatically deforms into a simple charge-density wave state [71, 72].

In the torus geometry, the Laughlin state can be expressed in terms of periodic theta functions [35, 39]. This geometry is significant because it has genus one, and as a consequence, the ground state wavefunction has a degeneracy in the thermodynamic limit (specifically, the torus Laughlin state $\Psi^{\text{torus}}_{\nu=1/p}$ has degeneracy p). Furthermore, the torus is the natural way to understand lattice systems, since it is flat, periodic and has finite extent. This formulation is therefore often used to make connections to Chern insulators [73] (see Sec. 1.7.4).

Finally, we note that there have been several attempts to understand the Laughlin state in a second-quantised language. These have notably included occupation-number descriptions in terms of Jack polynomials [74], and lattice-based studies of the zero modes of Laughlin-like Hamiltonians [75]. Work in this direction is ongoing.

1.6.2 General Interactions and Haldane Pseudopotentials

We now turn to consider more general interactions, and introduce the formalism of Haldane pseudopotentials that will provide an important tool in this thesis. First, we note from Hamiltonian 1.22 that the interactions we are interested in only act on two particles at a time. To understand the effects of such an interaction, we need therefore only to consider how it acts on a complete set of two-particle wavefunctions: any general wavefunction can always be decomposed into a sum of terms which each contain one two-body factor and one factor which contains everything else [67, 76],

$$\Psi\left(\{\mathbf{r}_i\}\right) = \sum_a \Psi_a\left(\mathbf{r}_1, \mathbf{r}_2\right) \tilde{\Psi}_a\left(\mathbf{r}_3, \ldots \mathbf{r}_{N_P}\right). \tag{1.27}$$

We can further decompose the two-body factor into a centre-of-mass (COM) coordinate part and a relative coordinate part,

$$\begin{aligned} \Psi_a\left(\mathbf{r}_i, \mathbf{r}_j\right) &= \sum_{b,c} A_{bc} \Psi_b^{\text{COM}}\left(\frac{\mathbf{r}_i + \mathbf{r}_j}{2}\right) \Psi_c^{\text{rel}}\left(\mathbf{r}_i - \mathbf{r}_j\right) \\ &= \sum_{L,M} A_{LM} \frac{1}{2\pi l_B^2} \frac{1}{\left(2l_B\right)^{L+M} \sqrt{L!M!}} \left(z_i - z_j\right)^L \left(z_i + z_j\right)^M e^{-\frac{1}{8l_B^2}\left(|z_i - z_j|^2 + |z_i + z_j|^2\right)}, \end{aligned} \tag{1.28}$$

where in the second line we have explicitly written out a two-body wavefunction expansion in the symmetric gauge, with L the relative angular momentum and M the COM angular

momentum.

Now, since the interaction couples only to the relative displacement between two particles, its action will only affect the part of the wavefunction that depends on the relative coordinate, $\Psi_c^{\text{rel}}(\mathbf{r}_i - \mathbf{r}_j)$. Since angular momentum is a good quantum number, we will label these two-body wavefunctions by L, writing $\Psi_c^{\text{rel}}(\mathbf{r}_i - \mathbf{r}_j) \to \Psi_L^{\text{rel}}(\mathbf{r})$, where we have also defined the relative coordinate $\mathbf{r} = \mathbf{r}_i - \mathbf{r}_j$. Finally, since the interaction is rotationally invariant, the interaction matrix elements will be diagonal in L, and are known as Haldane pseudopotentials [67, 76],

$$V_L = \int \mathrm{d}^2\mathbf{r} \left[\psi_L^{\text{rel}}(\mathbf{r})\right]^* V_{\text{int}}(\mathbf{r})\psi_L^{\text{rel}}(\mathbf{r}). \tag{1.29}$$

Every rotationally invariant interaction can be characterised by its unique set of pseudopotentials, V_L, with $L \geq 0$. These may be calculated using Eq. (1.29), or equivalently, using the Fourier transformed interaction [5],

$$V_L = \langle L| V(\mathbf{r}_1 - \mathbf{r}_2) |L\rangle = \int \frac{\mathrm{d}^2\mathbf{q}}{(2\pi)^2} V(\mathbf{q}) e^{-l_B^2 q^2} L_L(l_B^2 q^2) \tag{1.30}$$

with $V(\mathbf{q}) = \int \mathrm{d}^2\mathbf{r}\, e^{-i\mathbf{q}\cdot\mathbf{r}} V(\mathbf{r})$ and where $L_L(l_B^2 q^2)$ is the Lth Laguerre polynomial. Conversely, given a set of pseudopotentials, one can always construct the corresponding interaction through $V(q) = 4\pi l_B^2 \sum_L V_L L_L(l_B^2 q^2)$.

We can use the Haldane pseudopotentials to simplify the interaction Hamiltonian (1.22) as follows. A complete basis for the relative angular momentum part of the wavefunction may be written $|L; i, j\rangle = C_L (z_i - z_j)^L$, where C_L is a normalisation constant. Inserting this complete basis into Eq. (1.22), we find

$$\hat{H}_{\text{FQHE}} = \sum_{i<j} \sum_{L,L'} |L; i, j\rangle \langle L; i, j| V_{\text{int}}(\mathbf{r}_i - \mathbf{r}_j) \left|L'; i, j\right\rangle \left\langle L'; i, j\right| = \sum_{i<j} \sum_L V_L P_{ij}^L, \tag{1.31}$$

where we have identified the pseudopotentials from Eq. (1.29) and defined projection operators $P_{ij}^L = |L; i, j\rangle \langle L; i, j|$. This has reduced a complicated two-body interaction to a sum over projection operators.

We can now justify why the Laughlin wavefunction is an exact zero energy ground state of the interaction given in Eq. (1.26). Inserting the interaction $v_m(\mathbf{r})$ into Eq. 1.30, we find that it corresponds to the single nonzero pseudopotential, $V_L = (U/4\pi)\delta_{mL}$. In this way, the full

interaction, $V_p(\mathbf{r}) = \sum_{m=0}^{p-1} v_m(\mathbf{r})$, has pseudopotentials

$$V_L = \begin{cases} U/(4\pi) & \text{if } L < p \\ 0 & \text{if } L \geq p \end{cases}.$$

A pair of particles will therefore only have zero interaction energy if their relative angular momentum is at least p. The Laughlin wavefunction satisfies this condition for every pair of particles, and can additionally be shown to be the unique, highest-density wavefunction to do so [66].

A general interaction will have a much more complicated pseudopotential character. For example, the pure Coulomb interaction given in Eq. 1.21 corresponds to the pseudopotential values

$$V_L = \frac{e^2\sqrt{\pi}}{8\pi\epsilon l_B}\frac{(2L-1)!!}{2^L L!}. \tag{1.32}$$

We cannot neatly write down an exact ground state for this interaction as we could for the Laughlin parent interaction. However, since these pseudopotentials decay with increasing L (roughly $V_L \sim 1/\sqrt{L}$), smaller values of L are suppressed more strongly than larger ones. In this way, we would expect the Laughlin state to be a good starting point to describe the many-body ground state even for the Coulomb interaction. The differences between the Coulomb and ideal pseudopotentials can then be treated perturbatively (see Chapter 8 of [5]).

For a general interaction, studying the pseudopotentials directly may allow one to motivate a possible trial wavefunction. We will follow this approach in Chapter 3. Ultimately, however, except in certain idealised cases, only numerical and experimental data can decide whether the trial wavefunction is a good approximation to the true wavefunction.

1.6.3 Edge Excitations of the Laughlin State

The Laughlin state exhibits several different modes of excitation, in addition to the elementary quasiparticle excitations mentioned briefly above (see Ref. [60] for a full discussion of these). Also in the bulk, there exists a neutral collective mode, corresponding to phonon-like density fluctuations. These were investigated by Girvin, Macdonald and Platzman [77, 78], who found a gapped branch of excitations with a minimum energy at finite momentum (the 'magneto-roton' minimum). See Chapter 9 in Ref. [5] for an overview of these.

In this thesis, we will be most interested in the neutral, gapless excitations of the Laughlin state that occur at a boundary. These can be interpreted as area-preserving distortions of the

ΔM	0	1	2	3	4	5
$\{p_n\}$	–	p_1	p_2	p_3	p_4	p_5
			$(p_1)^2$	p_2p_1	p_3p_1	p_4p_1
				$(p_1)^3$	$(p_2)^2$	p_3p_2
					$p_2(p_1)^2$	$p_3(p_1)^2$
					$(p_1)^4$	$(p_2)^2p_1$
						$p_2(p_1)^3$
						$(p_1)^5$
degeneracy	1	1	2	3	5	7

Table 1.1: Basis states and degeneracies for FQHE edge states with small ΔM.

droplet edge. Consider the wavefunction

$$\Psi'(\{z_i\}) = f(\{z_i\})\,\Psi_{\nu=1/p}(\{z_i\}),$$

where $f(\{z_i\})$ is a totally symmetric polynomial in the coordinates $\{z_i\}$. Since $f(\{z_i\})$ is symmetric, the new wavefunction $\Psi'(\{z_i\})$ will inherit the (bose or fermi) particle statistics from the Laughlin state. Furthermore, since each pair of particles in $\Psi_{\nu=1/p}$ has relative angular momentum of at least p, so too does each pair of particles in $\Psi'(\{z_i\})$, since the polynomial $f(\{z_i\})$ can only increase angular momentum. The Laughlin state is therefore just the first zero-energy state in a sequence of zero-energy states with successively higher values of total angular momentum.

A basis for the functions $f(\{z_i\})$ is generated by the polynomials, $p_n = \sum_i z_i^n$. Since the Laughlin state has total angular momentum M_0 (from Eq. (1.25)), the edge excitations will have angular momentum $M = M_0 + \Delta M$, and may be obtained at each ΔM from the set of polynomials p_n with total degree ΔM. The appropriate p_n and corresponding degeneracies for $\Delta M \leq 5$ are given in Table. 1.1.

For the ideal parent interaction, Eq. (1.26), the edge states in each angular momentum sector will be exactly degenerate, although each ΔM set may be raised in energy by adding a harmonic trap (see Chapter 4 for a discussion of this). For a physical interaction, such as Coulomb repulsion, each multiplet will be split in energy. Good approximations to the lowest energy Coulomb edge state in each sector were obtained in terms of the p_n in Refs. [79, 80].

On a macroscopic level, FQHE edge excitations may equivalently be described using a hydrodynamic approach introduced by Wen [81]. This uses bosonisation to express the physics of the edge as a chiral Luttinger liquid [82, 83], and allows one to simply calculate correlation

functions and transport properties. These are found to agree well with experiments [84].

1.6.4 Other FQHE States

The discussion so far has focused mostly on the Laughlin state, which will play a leading role in this thesis. However, it is clear from Fig. 1.3 that most FQHE states are *not* at filling fractions $\nu = 1/p$. In this final subsection we will briefly outline some of the more exotic FQHE states that have been predicted theoretically (and in many cases, discovered experimentally).

A simple generalisation of the Laughlin state uses particle-hole symmetry. By filling a complete LL and considering a condensation of holes rather than electrons, Laughlin-like states with filling factors $\nu = 1 - 1/m$ can be obtained. These FQHE states were first proposed in Refs. [85, 86], and plateaux at these fractions have been observed experimentally (see Fig. 1.3).

Most other fractions with odd denominators can be derived using either of two alternative approaches. The first approach, known as the hierarchical construction, was put forward by Haldane and others [67, 85, 87]. The idea is to take quasiparticles or quasiholes of a Laughlin state, and condense them into their own Laughlin-like state. This can be repeated iteratively to generate successive levels of the hierarchy, each time generating a filling fraction with a larger denominator. This approach is discussed in Chapter 8 of Ref. [5].

The alternative theory, proposed by Jain [32, 88], is the *composite fermion* approach. This imagines binding an even number of magnetic flux quanta to each electron to form a quasiparticle, known as a composite fermion. These quasiparticles then undergo an IQHE in the residual magnetic field, with the resulting filling fractions forming another hierarchy (although the fractions occur at different hierarchical levels as compared to the Haldane hierarchy [89]). While Jain argues [32] that the composite fermion approach is fundamentally distinct from the hierarchical approach, others, including Read [90] and Blok and Wen [91], have proposed that they are alternative formulations of the same physics.

A simple generalisation of the Laughlin and hierarchy states arises in multicomponent systems, such as systems of spin-1/2 fermions or a quantum Hall bilayer. In these cases, there are several distinguishable particle species, and fermi or bose statistics only holds within each species. Halperin [54] generalised the Laughlin state to the multicomponent states,

$$\Psi_{mmn}\left(\{z_i\}\right) \;=\; \mathcal{N}\prod_{i<j}\left(z_i - z_j\right)^m \prod_{k<l}\left(w_k - w_l\right)^m \prod_{i,k}\left(z_i - w_k\right)^n e^{-\frac{1}{4l_B^2}\left[\sum_i |z_i|^2 + \sum_k |w_k|^2\right]}, \quad (1.33)$$

where $\{z_i\}$ and $\{w_k\}$ are the coordinates of particles from each species. These states have become known as Halperin-mmn states, where the parity of m is determined by particle statistics

but n may be any integer, and is determined by the interaction between species. Using a similar argument to Sec. 1.6.1, we observe that for $N_P/2$ particles of each species, the Halperin-mmn wavefunction occurs at filling factor $\nu_{mmn} = 2/(m+n)$ and with total angular momentum $M_0 = N_P^2 (m+n)/4 - N_P m/2$. We will describe lattice states analogous to these in the Hofstadter model in Chapter 3.

The most exotic FQHE states are, however, those which might enable topological quantum computing. In particular, the observed state at $\nu = 5/2$ [43] is believed to host nonabelian quasiparticles: particles whose exchange statistics are described by a set of noncommuting matrices [10, 12]. Experimental investigation of this phase is ongoing (see Ref. [92] for a review), but there is reasonable evidence that this state is described by a Moore-Read anti-Pfaffian wavefunction [93]. Beyond this, Read and Rezayi [94] formulated a hierarchy of nonabelian $\mathbb{Z}_k$ parafermion states at many other filling fractions. These could potentially realise a *universal* quantum computer, and a possible candidate state at $\nu = 12/5$ has been observed in experiments [95]. We refer the reader to Ref. [12] for a review of these nonabelian FQHE phases.

Finally, although we have described the Laughlin state from a wavefunction perspective, FQHE phases can also be effectively described using topological quantum field theories (TQFTs). In particular, most can be described using abelian and nonabelian Chern-Simons theories, and the associated K-matrix formalism. We will not follow this approach in this thesis, but we refer the reader to Refs. [12, 81, 14] for reviews.

1.7 Chern Insulators

In this section, we consider topologically nontrivial *lattice* models, which we will find bear a certain resemblance to quantum Hall systems. The differences between these two types of topological phase will form an important theme of this thesis.

In experimental quantum Hall systems, lattice effects can usually be neglected, since the electron density is low and the lattice spacing is much smaller than the characteristic (magnetic) length scale of the wavefunctions. For example, typical magnetic field values [4] of 10–15 T correspond to a magnetic length on the order of 10 nm, which is far greater than the unit cell size in GaAs of 5.65 Å [30]. The question naturally arises whether quantum Hall physics persists when this is no longer the case—when there is a large amount of magnetic flux per lattice plaquette. There have been many numerical and analytical studies of lattice quantum Hall systems over the past decades which have answered this question positively, at least in

certain cases [21, 96, 97, 98, 99, 52, 100, 101, 102, 63, 103].

In addition to these, many other tight-binding models—such as the Haldane model [104]—have been developed that exhibit a quantised Hall conductivity even in the absence of a net external field. There is little physical difference between models with an external field and models without an external field, since magnetic flux per plaquette is only defined modulo 2π and may be removed through a gauge transformation. Indeed, in some cases, both types of system have been shown to be adiabatically connected [19, 20]. In this thesis, we will treat both types of lattice system on an equal footing. We begin by introducing some of the band theory that is required to understand these models—for further details, we refer the reader to the reviews in Refs. [8, 9, 105].

1.7.1 Topological Band Theory

A general, noninteracting tight-binding model is described by a kinetic energy Hamiltonian,

$$\hat{H} = \sum_{\mathbf{r}\mathbf{r}',ab} t^{ab}_{\mathbf{r}\mathbf{r}'} c^\dagger_{\mathbf{r}a} c_{\mathbf{r}'b}, \tag{1.34}$$

where $c^\dagger_{\mathbf{r}a}$ creates a particle on a lattice site at $\mathbf{r}$ with quantum numbers described by the index a (which may include spin, sublattice index, etc.). The $t^{ab}_{\mathbf{r}\mathbf{r}'}$ encode on-site energies and lattice hopping amplitudes, which will usually be short-range.

We typically consider the system to have periodic boundary conditions, which allows us to define the Fourier transformed operators,

$$c^\dagger_{\mathbf{k}a} = \frac{1}{\sqrt{N_s}} \sum_{\mathbf{r}} c^\dagger_{\mathbf{r}a} e^{-i\mathbf{k}\cdot\mathbf{r}}, \qquad c^\dagger_{\mathbf{r}a} = \frac{1}{\sqrt{N_s}} \sum_{\mathbf{k}} c^\dagger_{\mathbf{k}a} e^{i\mathbf{k}\cdot\mathbf{r}}, \tag{1.35}$$

where N_s is the total number of lattice sites and $\mathbf{k}$ takes momentum values within the Brillouin zone. After taking the Fourier transform, Hamiltonian (1.34) may be recast in terms of momentum as

$$\hat{H} = \sum_{\mathbf{k},ab} H^{ab}(\mathbf{k}) c^\dagger_{\mathbf{k}a} c_{\mathbf{k}b}. \tag{1.36}$$

We can then diagonalise $H^{ab}(\mathbf{k})$ to obtain the band solutions,

$$\hat{H} = \sum_{\mathbf{k},\alpha} E_\alpha(\mathbf{k}) c^\dagger_{\mathbf{k}\alpha} c_{\mathbf{k}\alpha}. \tag{1.37}$$

In this expression, α is the band index, $E_\alpha(\mathbf{k})$ gives the band energies, and the band creation op-

erators are related to the original operators through a unitary transformation, $c^\dagger_{\mathbf{k}\alpha} = \sum_a U^a_{\mathbf{k}\alpha} c^\dagger_{\mathbf{k}a}$. The total number of bands is equal to the total number of states contained in the index a, and the explicit wavefunctions are given by $|\psi^\alpha_{\mathbf{k}}\rangle = \sum_a U^a_{\mathbf{k}\alpha} c^\dagger_{\mathbf{k}a} |0\rangle$, with $\psi^\alpha_{\mathbf{k}}(\mathbf{r}) = \langle \mathbf{r} | \psi^\alpha_{\mathbf{k}} \rangle$. These satisfy the Bloch periodicity condition, $\psi^\alpha_{\mathbf{k}}(\mathbf{r} + \mathbf{a}_i) = e^{i\mathbf{k}\cdot\mathbf{a}_i} \psi^\alpha_{\mathbf{k}}(\mathbf{r})$, where $\mathbf{a}_i$ is a lattice vector. We will be particularly interested in the periodic part of the Bloch wavefunction, which may be obtained through

$$u^\alpha_{\mathbf{k}}(\mathbf{r}) = e^{-i\mathbf{k}\cdot\mathbf{r}} \psi^\alpha_{\mathbf{k}}(\mathbf{r}) = \langle \mathbf{r} | \sum_a e^{-i\mathbf{k}\cdot\delta\mathbf{r}_a} U^a_{\mathbf{k}\alpha} c^\dagger_{\mathbf{k}a} |0\rangle , \tag{1.38}$$

where $\delta\mathbf{r}_a$ is the relative position of the particle described by the index a within the unit cell. For later reference, we note that the overall phase of the wavefunctions $\psi^\alpha_{\mathbf{k}}(\mathbf{r})$ and $u^\alpha_{\mathbf{k}}(\mathbf{r})$ is not defined by the diagonalisation: we can perform a (generically $\mathbf{k}$-dependent) $U(1)$ gauge transformation on each band independently without changing the physics,

$$\psi^\alpha_{\mathbf{k}}(\mathbf{r}) \to e^{i\chi^\alpha_{\mathbf{k}}} \psi^\alpha_{\mathbf{k}}(\mathbf{r}), \qquad u^\alpha_{\mathbf{k}}(\mathbf{r}) \to e^{i\chi^\alpha_{\mathbf{k}}} u^\alpha_{\mathbf{k}}(\mathbf{r}). \tag{1.39}$$

Up to this point, we have simply followed conventional band theory: we have diagonalised a periodic tight-binding model to obtain band solutions. If an integer number of these bands are completely filled, then the system has zero longitudinal conductance, and is hence a (band) insulator. However, in cases such as the Haldane or Hofstadter models, even systems with filled bands can have nonzero quantised Hall conductance. These systems are known as Chern insulators, and the bands carrying the Hall current are correspondingly known as Chern bands [8, 9]. In order to have nonzero Hall conductance, a tight-binding model must have broken time-reversal (TR) symmetry. Following Ref. [105], we introduce the TR operator $\hat{\Theta}$, which acts on a particle with spin S through $\hat{\Theta} = e^{-i\pi S_y} \hat{K}$, where S_y is the y-component of the spin vector in the standard representation and $\hat{K}$ is the complex conjugation operator. The TR operator therefore flips the sign of any imaginary numbers and reverses the spin direction.

For the majority of this thesis we will be considering bosons and spinless fermions, and so we will break TR symmetry by including complex hopping phases in the tight-binding Hamiltonian (1.34).[10] This arises automatically in the presence of a background field, but may also occur in physical systems through a spatially inhomogeneous magnetic field with zero average or through spin-orbit coupling.

[10] We note that there also exist topologically nontrivial tight binding models that *preserve* TR symmetry—notably, the band models known as topological insulators [16, 18].

The Hall conductivity of a filled band is determined by its Chern number (C), which is analogous to the integer in the IQHE. In a seminal paper in 1982, Thouless, Kohmoto, Nightingale and Den Nijs (TKNN) showed that this can be calculated directly from the wavefunction [52], via a geometrical property known as the Berry curvature [106, 107]. We describe how to calculate this below.

We start by finding the Berry connection [106] from the periodic part of the Bloch wavefunction, $\mathbf{A}^\alpha = -i \langle u^\alpha_{\mathbf{k}} | \nabla_{\mathbf{k}} | u^\alpha_{\mathbf{k}} \rangle$, where the overlap involves an implicit sum over the index a through the definition in Eq. (1.38). This expression is gauge dependent, transforming as a $U(1)$ potential under the gauge transformation described in Eq. (1.39),

$$\mathbf{A}^\alpha \to \mathbf{A}^\alpha + \nabla_{\mathbf{k}} \chi^\alpha_{\mathbf{k}}. \tag{1.40}$$

For this reason, only gauge-invariant quantities derived from the Berry connection may have physical effects. In particular, the closed line integral of $\mathbf{A}^\alpha$ in momentum space defines a Berry phase, which may have subtle effects on the transport properties of a material [108].

The Berry curvature may then be obtained from the derivatives of the Berry connection. Assuming a two-dimensional system in the xy-plane, the Berry curvature is defined through

$$F^\alpha(\mathbf{k}) = (\nabla_{\mathbf{k}} \times \mathbf{A}^\alpha)_z = i \left[\left\langle \frac{\partial u_{\mathbf{k}}}{\partial k_x} \middle| \frac{\partial u_{\mathbf{k}}}{\partial k_y} \right\rangle - \left\langle \frac{\partial u_{\mathbf{k}}}{\partial k_y} \middle| \frac{\partial u_{\mathbf{k}}}{\partial k_x} \right\rangle \right]. \tag{1.41}$$

This quantity is gauge-invariant (although it depends on the spatial embedding of the orbitals defined through the index a), and behaves similarly to a magnetic field in momentum space [109, 108]. Moreover, integrating the Berry curvature over the Brillouin zone (BZ) recovers the Chern number of the αth band [52], $C^\alpha = \frac{1}{2\pi} \int_{BZ} \mathrm{d}^2\mathbf{k}\, F^\alpha(\mathbf{k})$. In this way, a nonzero Hall conductivity is associated with a nontrivial winding of the Bloch periodic wavefunctions around the BZ torus. Notably, in a band system, we now have the possibility of a *single* band having a Chern number $C > 1$, marking a qualitative difference from LLs, which each have $C = 1$.

For the case of N_b degenerate (or close to degenerate) bands, the situation is more complicated. Since we can take arbitrary linear combinations of the bands in the multiplet and remain within the degenerate subspace, the multiplet as a whole is invariant under a $U(N_b)$ gauge transformation [108]. The relevant quantities are then the nonabelian Berry connections,

$\mathbf{A}^{\alpha\beta} = -i\langle u_{\mathbf{k}}^{\alpha}|\nabla_{\mathbf{k}}|u_{\mathbf{k}}^{\beta}\rangle$, and the nonabelian Berry matrix

$$F^{\alpha\beta}(\mathbf{k}) = \left(\nabla_{\mathbf{k}} \times \mathbf{A}^{\alpha\beta}\right)_z - i\sum_{\gamma}\left(\mathbf{A}^{\alpha\gamma} \times \mathbf{A}^{\gamma\beta}\right)_z, \tag{1.42}$$

where the indices α, β, γ label the bands within the degenerate multiplet. However, the Berry matrix is now gauge dependent: physical observables may be obtained only from gauge-independent quantities such as the trace (whose BZ integral yields the total Chern number of the multiplet). It may be shown from above, by inserting a resolution of identity, that the sum of the Chern numbers of *all* the bands in a system is zero, and in particular, a single-band system must always have Chern number zero. To be topologically nontrivial, a tight-binding model requires a sublattice or spin structure.

Just as with LLs, we can consider what happens when a Chern band is fractionally filled and an interaction term is switched on,

$$\hat{V}_{\text{int}} = \sum_{ijkl}\sum_{abcd} V_{ijkl}^{abcd} c_{\mathbf{r}_i a}^{\dagger} c_{\mathbf{r}_j b}^{\dagger} c_{\mathbf{r}_k c} c_{\mathbf{r}_l d}. \tag{1.43}$$

If the resulting system has a quantised fractional Hall conductance, it is known as a fractional Chern insulator (FCI) in analogy to the FQHE [110, 111, 112, 113, 9, 8]. In contrast to the FQHE, however, there are several features of lattice systems that may act to destabilise a fractional state. We will return to this topic in Sec. 1.7.2.

In an FCI state, the noninteracting band picture breaks down and we can no longer calculate the Chern number from the single-particle properties. Instead, the many-body Berry curvature may be calculated by threading flux through the handles of the underlying torus [114]. If the many-body ground state is written as $|\Psi\rangle$, and we thread flux ϕ_1 and ϕ_2 through each handle, then the many-body Berry curvature is defined through

$$F(\phi_1, \phi_2) = i\left[\left\langle \frac{\partial\Psi}{\partial\phi_1}\middle|\frac{\partial\Psi}{\partial\phi_2}\right\rangle - \left\langle \frac{\partial\Psi}{\partial\phi_2}\middle|\frac{\partial\Psi}{\partial\phi_1}\right\rangle\right]. \tag{1.44}$$

The many-body Chern number can then be calculated by integrating the above quantity over ϕ_1 and ϕ_2.

1.7.2 FCI Models

There is now a wide range of tight-binding models that are believed to host fractional topological states. In this subsection, we briefly describe some of the general features that such models must

possess in order to generate stable FCIs. We will introduce specific topological tight-binding models later in this thesis as and when we need them.

Although it is reasonably simple to write down a model with a Chern band, it is somewhat harder to write down a model that is amenable to a fractional state. The conventional approach is to use Chern bands that have a flat energy dispersion and a flat Berry curvature—so that they resemble LLs as closely as possible. With a flat dispersion, the interaction strength becomes the dominant energy scale and only the interaction term (1.43) in the Hamiltonian need be considered. In addition, the bandgap should be large enough that the interaction does not mix in contributions from higher bands, which then allows the use of band projection methods. Overall, we require

$$W \ll V_{\text{int}} \ll E_G, \tag{1.45}$$

with W, V_{int} and E_G the bandwidth, interaction strength and bandgap respectively. The relative arrangement of energy scales may be captured by the flatness ratio, $F = E_G/W$, which should typically be made very large.

In practice, however, neither of these inequalities are particularly stringent: FCI states often persist even when the interaction strength far exceeds the bandgap [115]. In addition, the bandwidth inequality can usually be circumvented if the model parameters are tuneable. This is because it is always possible to make an energy dispersion arbitrarily flat without affecting the single-particle wavefunctions and associated topological properties [111]. Given the band solution in Eq. (1.37), we define the flattened model by replacing each original dispersive band with a constant energy level, $E_\alpha(\mathbf{k}) \to E_\alpha^{\text{flat}}$. Formally, this can be achieved by dividing through by the original band energies, a process which can be carried out without mixing the order of the bands (shifting the energies away from zero if necessary). Since we have not changed the definition of the operators $c^\dagger_{\mathbf{k}\alpha}$, the band wavefunctions of the flattened model are exactly the same as the band wavefunctions of the original model.

We can transform this flattened band solution back to real space through the unitary matrix $U^a_{\mathbf{k}\alpha}$ and an inverse Fourier transform to find

$$\sum_{\mathbf{k},\alpha} E_\alpha^{\text{flat}} c^\dagger_{\mathbf{k}\alpha} c_{\mathbf{k}\alpha} \to \sum_{\mathbf{k},ab} H^{ab,\text{flat}}(\mathbf{k}) c^\dagger_{\mathbf{k}a} c_{\mathbf{k}b} \to \sum_{\mathbf{r}\mathbf{r}',ab} t^{ab,\text{flat}}_{\mathbf{r}\mathbf{r}'} c^\dagger_{\mathbf{r}a} c_{\mathbf{r}'b}$$

with $H^{ab,\text{flat}}(\mathbf{k})$ and $t^{ab,\text{flat}}_{\mathbf{r}\mathbf{r}'}$ 'flattened' Hamiltonian and hopping parameters respectively. The final real space model has exactly the same band solutions as the original, unflattened model,

but its energy bands are completely flat. The new hopping parameters, $t^{ab,\mathrm{flat}}_{\mathbf{r}\mathbf{r}'}$, are formally very long-range, and indeed it has been proved that one cannot simultaneously have (1) exactly flat bands, (2) a nonzero Chern number, and (3) strictly local hopping [116].[11] However, the flattened hopping amplitudes decay exponentially with distance [111], and in practice, extremely flat bands can be achieved by adding hopping that extends over only a few nearby neighbours.

A less well-understood problem arises due to deviations in the Berry curvature from uniformity—a property that cannot be 'flattened' by tuning the hopping. Since LLs have exactly flat Berry curvature, it is believed that FCI states will be most stable in models with reasonably flat Berry curvature. Indeed, it has been shown that the algebra of density operators projected to a Chern band approaches the FQHE case (the so-called 'Girvin-Macdonald-Platzman' algebra [78]) in the limit of constant Berry curvature [118, 119]. Numerical evidence also shows an inverse correlation between the Berry curvature deviation and the stability of an FCI ground state (quantified using the energy gap to excitations) [120].[12] However, this criterion may occasionally be misleading: the Kapit-Mueller model [110] has large deviations in its Berry curvature but nonetheless exhibits an FCI state as its exact many-body ground state.

We now briefly mention some of the tight-binding models that are believed to host Chern bands and FCI states. The system of most relevance to this thesis is the Hofstadter model [22, 21], which describes a charged particle hopping on a square lattice in the presence of a perpendicular magnetic field. Owing to the background field, this model closely resembles LL physics in the weak-field limit, where it supports many-body states that are adiabatically connected to the FQHE. However, this model also has a strong-field regime, whose many-body states are distinct from the states of the continuum FQHE. We will introduce the Hofstadter model in full in Chapter. 2.

Many other tight-binding models have been developed that demonstrate a Chern number in the absence of an external field. The first of these was the Haldane honeycomb model [104], which considers spinless fermions hopping on a honeycomb with a spatially inhomogeneous magnetic field that is zero on average. This model will be discussed in Chapter 5.

Since these discoveries, many other Chern insulator models have been forthcoming. Qi et al [121] considered a generic two-band model, and interpreted the Chern number as a wrapping of the BZ torus onto a sphere, while Kapit and Mueller [110] modified the Hofstadter model to produce a flat lowest band whose exact single-particle eigenstates were discretised LLL states.

[11] This holds only in the thermodynamic limit: in finite systems, it is possible to satisfy all three conditions [117].

[12] Ref. [120] also considers another quantity, the momentum-space Fubini-Study metric, whose deviations also disfavour the formation of FCI states.

In addition, topological bands have been generated on the kagome [122], checkerboard [112], dice [123] and ruby [124] lattices, and a scheme has been developed to generate a topological band with *arbitrary* Chern number out of stacked layers of the pyrochlore lattice [125]. We refer the reader to the reviews in [8, 9] for further details on these models.

1.7.3 Numerical Signatures of FCI States

Much of the literature in the field of FCIs has been devoted to numerical studies, which is often the only way to identify models that support topological states. Bosonic and fermionic Laughlin-like FCI states have been observed numerically in the Haldane model and others [126, 127], along with several states analogous to the hierarchy/composite fermion FQHE states [128, 129]. Nonabelian states (analogues of the Moore-Read and Read-Rezayi states) have been stabilised numerically using many-body interactions [73, 127, 130] and more recently using more physically realistic two-body interactions [131, 37, 132].

The process of verifying that an FCI state has been stabilised numerically is rather involved, since topologically trivial charge density wave (CDW) states often occur at the same momentum and can be difficult to distinguish from FCIs. Typically, numerical procedures involve exactly diagonalising the interaction Hamiltonian (1.43) on a torus, usually projecting to the lowest single-particle band and making use of the translational symmetries. For examples of the numerical signatures outlined below, we refer the reader to the references in the previous paragraph; we also give some of our own numerical results in Chapter 5.

The first numerical signature that should be observed is a topological ground state degeneracy in the energy spectrum, occurring at momentum values that may be predicted from a generalised Pauli principle [133]. The gap between the ground state manifold and the excited states should persist in the thermodynamic limit, which may be verified by comparing numerics for different system sizes. In finite systems, the ground states will not be exactly degenerate, but will instead have a splitting that vanishes in the thermodynamic limit.

Furthermore, if the boundary conditions are twisted (by inserting magnetic flux through the handles of the torus), then the quasidegenerate ground state energies should cyclically rearrange themselves without mixing with the energy levels of the excitations, a phenomenon known as spectral flow [111, 133] (see Fig. 5.2 in this thesis).[13] The total number of magnetic flux quanta required for the spectrum to return to its original form indicates the denominator

[13] If the degenerate ground states all occur in the same momentum sector, then there will instead be an avoided level crossing as flux is inserted.

of the fractional Chern number.

Unfortunately, CDW states may also exhibit spectral flow [127]. A second numerical feature that may be calculated to confirm the presence of an FCI is the quasihole spectrum [133]. This is obtained by reducing the filling factor ν (by reducing the number of particles or increasing the lattice size) and diagonalising the interaction Hamiltonian in the new system size. In this way, the system effectively undergoes a flux insertion, and the resulting energy spectrum displays the energy levels of the quasihole excitations. The expected degeneracy in each momentum sector may be calculated by analogy to the FQHE [73], and these values can be compared to the numerics. It should be noted, however, that if ν is made too small then a different FCI state may be stabilised instead, and the resulting spectrum may be unreliable.

Finally, strong evidence of an FCI state may be obtained from the entanglement spectrum [134], which is calculated using the ground state wavefunction itself. An entanglement spectrum is generated by performing a cut on the system (which may be in real space, orbital space, or in particle space, for example) and tracing out the degrees of freedom on one side of the cut. Formally, one partitions the underlying Fock space into two parts, $\mathcal{H} = \mathcal{H}_A \otimes \mathcal{H}_B$, and expands the ground state wavefunction as a Schmidt decomposition in this new partitioned basis,

$$|\Psi\rangle \quad = \quad \sum_i e^{-\xi_i/2} \, |\Psi_i\rangle_A \otimes |\Psi_i\rangle_B \, , \tag{1.46}$$

where $e^{-\xi_i/2}$ are positive coefficients and $|\Psi_i\rangle_{A,B}$ are basis states from subsystem (A, B). Next, one forms the density matrix through $\rho = |\Psi\rangle \langle\Psi|$ and traces out the degrees of freedom for one subspace, leaving the reduced density matrix,

$$\rho_A = \mathrm{Tr}_B \rho = \sum_i e^{-\xi_i} \, |\Psi_i\rangle_A \langle\Psi_i|_A \, . \tag{1.47}$$

The entanglement spectrum is then described by the ξ_i, and has been shown to encode many of the edge and quasihole excitations of the ground state [134, 39, 135]. The entanglement spectrum can also be compared to the entanglement spectra of ideal states (such as the Laughlin state), which take simple, characteristic forms [134]. Of most use when studying FCIs is the particle entanglement spectrum (PES) [39], which is obtained by integrating out the degrees of freedom corresponding to one or more particles. The resulting spectrum exhibits a distinct entanglement gap (analogous to the many-body gap in the energy spectrum), and the counting of states below the gap precisely matches the expected degeneracy of quasihole states in each

sector. The entanglement spectrum often provides a more stable measure of the quasihole spectrum than the exact diagonalisation of a system with a reduced number of particles [127]. We give an example of a PES in Fig. 5.3.

1.7.4 FQHE Approaches to FCI States

A number of approaches have been developed to apply the theory of the FQHE to the study of Chern insulators. Notably, Qi [136] introduced a set of semi-localised Wannier orbitals that mimic the Landau gauge wavefunctions of the continuum (Eq. (1.5)). These are defined by taking the partial Fourier transform of the single-particle Bloch wavefunctions through

$$|W_\alpha(k_y,x)\rangle \;=\; \frac{1}{\sqrt{L_x}}\sum_{k_x} e^{-i\int_0^{k_x} A_x^\alpha(p_x,k_y)\mathrm{d}p_x - ik_x[x-\theta^\alpha(k_y)/(2\pi)]}\,|\psi_{\mathbf{k}}^\alpha\rangle\,, \tag{1.48}$$

where L_x is the torus size in the x-direction, A_x^α is the k_x-component of the Berry connection of the αth band and $\theta^\alpha(k_y)=\int_0^{2\pi}A_x^\alpha(p_x,k_y)\mathrm{d}p_x$. The centre of mass of these Wannier orbitals is found to be

$$\langle W_\alpha(k_y,x)|\,\hat{x}\,|W_\alpha(k_y,x)\rangle = x - \frac{\theta^\alpha(k_y)}{2\pi}, \tag{1.49}$$

where $\theta^\alpha(k_y)/(2\pi)$ acts like a charge polarisation. By considering the movement of the Wannier function as k_y is changed by 2π, we identify the Chern number as $C=-\left[\theta^\alpha(2\pi)-\theta^\alpha(0)\right]/(2\pi)$, and note that $|W_\alpha(k_y,x)\rangle$ is a function of the single parameter $K_y=2\pi x+Ck_y$. The centre of mass moves continuously as a function of K_y in a characteristic staircase manner (see Fig. 1 of Ref. [136]). By mapping K_y directly onto the p-degree of freedom of the LL states on a torus (Eq. 1.17), the two sets of single-particle states, $|W_\alpha(K_y)\rangle \leftrightarrow \left|\psi_{\alpha,p}^{\mathrm{torus}}\right\rangle$, may be identified.

Although this Wannier state mapping is satisfying, the phase of the Bloch wavefunctions is undefined and must be chosen carefully to ensure good overlaps with numerical states [137]. However, if this is carried out correctly, it provides a recipe for writing down FCI states based on a chosen FQHE state. This was used to show the adiabatic continuation between FQHE and FCI states in Ref. [19] and may also be used to study the bulk-edge correspondence of a cylindrical system [132]. We will find in Chapter 3 that our perturbative wavefunctions correspond to Qi's Wannier wavefunctions in a particular limit.

An alternative to the Wannier mapping is to keep the FCI states in the Bloch basis but to map the FQHE wavefunctions onto Bloch LL states on a torus. This approach was carried out in Ref. [38], in a which a mapping was developed between a Chern band with Chern number C and C 'colour-entangled' copies of a LL. With this mapping, a chosen FQHE state can once

again be mapped directly onto an FCI. The perturbative wavefunctions we consider in this thesis bear a certain resemblance to colour-entangled LLs, a feature which we discuss in Chapter 3.

Finally, we note that it is possible to numerically calculate lattice analogues of the Haldane pseudopotentials, which were outlined in Sec 1.6.2. Although FQHE pseudopotentials are usually calculated in the disk geometry, two-body interaction energies may be calculated in any system. On a torus in the continuum (using the LL basis given in Eq. (1.17)), the two-body interaction energies form degenerate groups with energies equal to the pseudopotential values, V_L [129] (up to weak finite-size effects). These groups each contain $2N_\phi$ states, corresponding to the different values the centre of mass momentum may take.

This energy level structure can be directly compared to the numerical two-body interaction energies calculated for a given FCI lattice model on a torus. In general, these lattice pseudopotentials are not degenerate and may overlap due to the broken translational symmetry. However, the most stable FCI states are found in models whose two-particle interaction energies closely resemble the flat pseudopotential levels expected from the continuum [8, 129]. We discuss two-particle interaction energies in the Hofstadter model in Chapter 3.

1.7.5 Experimental Realisations of FCI States

Recent advances in cold atom experiments and in the solid state have led to the possibility of realising model Hamiltonians in the laboratory, with an ultimate goal being to produce a topological state that does not require strong fields and which is stable at room temperature.

In the solid state, several proposals to realise topological flat bands in transition metal oxides have been suggested, notably in perovskites [138] and pyrochlore oxides [125, 139], although experimental evidence of such bands remains to be seen. The first quantum Hall effect to be realised in the absence of an external field (described as the 'quantum anomalous Hall effect' in the literature) was in ferromagnetic layers of $(Bi,Sb)_2Te_3$ [140], a result which has since been confirmed by other groups [141].

Most relevant to this thesis are realisations of the Hofstadter model. In electronic systems, implementations typically use an external magnetic field, where a key difficulty lies in obtaining field strengths that are large enough for lattice effects to become important (in contrast to the original QHE experiments). The most promising results in this direction are the recent observations of the Hofstadter energy spectrum in graphene superlattices [142, 143, 144], where the large superlattice spacing means that the magnetic flux per plaquette can be large even in weak external fields.

A large number of encouraging experimental proposals come from the realm of cold atoms, where it has recently become possible to simulate complex tight-binding Hamiltonians using optical lattices and artificial magnetic fields [145, 146, 147, 148, 102, 149, 150, 151]. Of particular interest are the realisations of the Hofstadter model [152, 153] and the Haldane honeycomb model [154] using this setup, where work is ongoing. Finally, we note that several novel methods of generating effective flat Chern bands using 'optical flux lattices' [131] and spin degrees of freedom [155] have also been proposed.

1.8 This Thesis

The observation of FQHE-like states in bands that look little like Landau levels is quite surprising. While most of the literature in the field has been devoted to numerical studies, a number of theoretical pictures have also been proposed to explain the physics of these FCI states, as outlined in the previous section. However, we are still far from having as complete an understanding of FCI states as we do for the usual FQHE. As a step in the direction of understanding FCI states better, in the first part of this thesis, we study FCI states in the Hofstadter model, where we are able to make analytical progress by building on the large literature of analysis of the single particle Hofstadter problem and the well-studied QHEs.

In Chapter 2, we introduce the Hofstadter model in detail and study the single-particle wavefunctions from a semiclassical perspective in the weak field limit. We interpret our results in light of the band theory and FCI stability criteria described above, and use them to justify the approximations we employ later on. We introduce a perturbative approach that takes the magnetic flux per plaquette as its small parameter. In Chapter 3 we extend this approach to general magnetic field strengths, valid when the magnetic flux per plaquette is close to certain 'simple' values. We consider corrections to both the single-body and many-body physics of the system, and generalise the results to other lattices and interactions. The main results of this chapter are a set of Haldane pseudopotential matrices, which generalise the conventional pseudopotential approach outlined in Sec. 1.6.2. In Chapter 4 we use the machinery developed in the preceding Chapters to generate some numerical energy spectra and wavefunctions which may be relevant to experimental realisations of the Hofstadter model, and consider the additional complications that arise due to an external trapping potential.

The final part of this thesis considers FCI models more generally. In Chapter 5, we describe a class of FCI states that may be stabilised solely through interactions, rendering the underlying

band structure essentially irrelevant. This method for generating fractional topological states is fundamentally different from the conventional approach outlined in this introduction, and crucially requires the presence of a lattice. We support our argument with numerical evidence, observing many of the signatures outlined in Sec. 1.7.3.

Appendices for Chapter 1

1.A Conversion Between Landau Gauge and Symmetric Gauge Wavefunctions

In this Appendix we derive the transformation required to convert between Landau gauge and symmetric gauge wavefunctions, which we will use throughout this thesis. We first recall the definitions of the wavefunctions in each gauge, given originally in Sec. 1.4, now writing them explicitly in terms of x and y,

$$\begin{aligned}\psi^{\mathrm{LG}}_{n,k}(x,y) &= \frac{e^{iky}}{\sqrt{2\pi}}\frac{1}{\sqrt[4]{\pi}}\frac{1}{\sqrt{2^n n! l_B}}e^{-\frac{1}{2}\left(\frac{x}{l_B}-l_B k\right)^2}H_n\left(\frac{x}{l_B}-l_B k\right),\\ \psi^{\mathrm{SG}}_{n,m}(x,y) &= (-1)^n\sqrt{\frac{n!}{2\pi l_B^2 m!}}\left(\frac{x+iy}{\sqrt{2}l_B}\right)^{m-n}L_n^{m-n}\left[\frac{x^2+y^2}{2l_B^2}\right]e^{-\frac{1}{4l_B^2}(x^2+y^2)}.\end{aligned}$$

We have relabelled $k_y \to k$ for notational convenience. We can convert from the Landau gauge to the symmetric gauge by imposing a gauge transformation phase and taking a linear combination of k-states, according to

$$e^{ie\chi(x,y)/\hbar}\psi^{\mathrm{SG}}_{n,m} = \int \mathrm{d}k\, B_m(k)\psi^{\mathrm{LG}}_{n,k}(x,y). \tag{1.50}$$

The phase, $\chi(x,y)$, can be obtained from the gauge transformation, $\mathbf{A}_{\mathrm{SG}} = \mathbf{A}_{\mathrm{LG}} + \nabla(Bxy/2)$, where from Eq. (1.3), we see that $\chi(x,y) = Bxy/2$. All that remains is to find the function $B_m(k)$. This is simply an overlap integral, which we see by expanding

$$e^{\frac{ixy}{l_B^2}}\psi^{\mathrm{SG}}_{n,m}(x,y) = e^{\frac{ixy}{l_B^2}}\langle x,y|n,m\rangle = \int \mathrm{d}k\,\langle x,y|n,k\rangle\langle n,k|n,m\rangle \equiv \int \mathrm{d}k\, B_m(k)\psi^{\mathrm{LG}}_{n,k}(x,y),$$

and identifying $B_m(k)$ as $\langle n,k|n,m\rangle = \int \mathrm{d}x\mathrm{d}y\,\left[\psi^{\mathrm{LG}}(x,y)\right]^*\psi^{\mathrm{SG}}(x,y)$. Rather than explicitly calculating this integral, it is much simpler to work with Eq. (1.50) directly. Considering first the LLL ($n=0$), we substitute for $\chi(x,y)$ and the wavefunctions to find

$$e^{\frac{ixy}{l_B^2}}\sqrt{\frac{1}{2\pi l_B^2 m!}}\left(\frac{x+iy}{\sqrt{2}l_B}\right)^m e^{-\frac{1}{4l_B^2}(x^2+y^2)} = \int \mathrm{d}k\, B_m(k)\frac{e^{iky}}{\sqrt{2\pi}}\frac{1}{\sqrt[4]{\pi}}\frac{1}{\sqrt{l_B}}e^{-\frac{1}{2}\left(\frac{x}{l_B}-l_B k\right)^2}.$$

We now multiply by $e^{-ik'y}$ and integrate with respect to y,

$$\int_{-\infty}^{\infty} \mathrm{d}y \sqrt{\frac{1}{2\pi l_B^2 m!}} \left(\frac{x+iy}{\sqrt{2}l_B}\right)^m e^{-\frac{1}{4l_B^2}(x^2+y^2)+\frac{ixy}{l_B^2}-ik'y} = \int_{-\infty}^{\infty} \mathrm{d}y \int_{-\infty}^{\infty} \mathrm{d}k\, B_m(k) \frac{e^{iky}}{\sqrt{2\pi}\sqrt[4]{\pi}\sqrt{l_B}} e^{-\frac{1}{2}\left(\frac{x}{l_B}-l_B k\right)^2 - ik'y}.$$

On the right-hand side, the integration over y generates a Dirac delta function in $(k-k')$, which then allows us to simply evaluate the integration over k. On the left-hand side, we identify the integral representation of the Hermite polynomials [156], $H_n(x) = \frac{2^n}{\sqrt{\pi}} \int_{-\infty}^{\infty} \mathrm{d}t\ (x+it)^n\, e^{-t^2}$. After carrying out these steps, we obtain

$$\frac{\sqrt{2}}{\sqrt{2^m m!}} H_m\left(l_B k'\right) e^{-\frac{1}{2l_B^2}\left(x-l_B^2 k'\right)^2} e^{-\frac{l_B^2 k'}{2}} \quad = \quad B_m(k') \sqrt{\frac{2\sqrt{\pi}}{l_B}} e^{-\frac{1}{2l_B^2}\left(x-l_B^2 k'\right)^2},$$

from which we can read off

$$B_m(k) = \frac{\sqrt{l_B}}{\sqrt[4]{\pi}} \frac{1}{\sqrt{2^m m!}} H_m\left(l_B k\right) e^{-\frac{k^2 l_B^2}{2}}. \tag{1.51}$$

The inverse transformation, $\psi_{n,k}^{\mathrm{LG}} = e^{ie\chi(x,y)/\hbar} \sum_m B_m^*(k) \psi_{n,m}^{\mathrm{SG}}(x,y)$, can be verified using the completeness relation of Hermite polynomials [157],

$$e^{-x^2} \sum_{n=0}^{\infty} \frac{1}{2^n n! \sqrt{\pi}} H_n(x) H_n(y) \quad = \quad \delta\left(x-y\right).$$

For higher Landau level states, it is simplest to assume that this expression for $B_m(k)$ holds for $n \geq 0$ and then to verify that this is true directly. We again begin from Eq. (1.50) and substitute for the symmetric gauge and Landau gauge wavefunctions. Using the dimensionless quantities, $\tilde{x} = x/l_B$, $\tilde{y} = y/l_B$ and $\tilde{k} = l_B k$, the right-hands side (RHS) of this equation becomes

$$\mathrm{RHS} \quad = \quad e^{\frac{i\tilde{x}\tilde{y}}{2}} e^{-\frac{\tilde{x}^2+\tilde{y}^2}{4}} \frac{1}{\sqrt{2}\pi l_B} \frac{1}{\sqrt{2^{m+n} m! n!}} \int \mathrm{d}k\, H_n\left[\tilde{x}-\tilde{k}\right] H_m\left[\tilde{k}\right] e^{-\left(\tilde{k}-\frac{(\tilde{x}+i\tilde{y})}{2}\right)^2},$$

where we have completed the square. Comparing to the left hand side of Eq. (1.50),

$$\mathrm{LHS} = e^{\frac{i\tilde{x}\tilde{y}}{2}} e^{-\frac{\tilde{x}^2+\tilde{y}^2}{4}} (-1)^n \sqrt{\frac{n!}{m!}} \frac{1}{\sqrt{2\pi} l_B} \left(\frac{\tilde{x}+i\tilde{y}}{\sqrt{2}}\right)^{m-n} L_n^{m-n}\left[\frac{\tilde{x}^2+\tilde{y}^2}{2}\right], \tag{1.52}$$

we see that for equality, we would require

$$\int \mathrm{d}k\, H_n\left[\tilde{x}-\tilde{k}\right] H_m\left[\tilde{k}\right] e^{-\left(\tilde{k}-\frac{(\tilde{x}+i\tilde{y})}{2}\right)^2} \quad = \quad (-2)^n \sqrt{\pi} n! \left(\tilde{x}+i\tilde{y}\right)^{m-n} L_n^{m-n}\left[\frac{\tilde{x}^2+\tilde{y}^2}{2}\right].$$

We set $z = \tilde{x} + i\tilde{y}$ and $k = \tilde{k} - z/2$ to rewrite the above condition as

$$\int \mathrm{d}k\,(-1)^n H_n\left[k - \frac{\bar{z}}{2}\right] H_m\left[k + \frac{z}{2}\right] e^{-k^2} = \sqrt{\pi}(-2)^n n! z^{m-n} L_n^{m-n}\left[\frac{|z|^2}{2}\right]. \tag{1.53}$$

We use the contour integral representation of the Hermite polynomials [156],

$$H_n(x) \;=\; \frac{n!}{2\pi i}\oint \frac{e^{2tx-t^2}}{t^{n+1}}\mathrm{d}t,$$

where the closed contour encircles the origin, to rewrite the LHS of Eq. (1.53) as

$$\text{LHS} = (-1)^n \frac{n!m!}{(2\pi i)^2}\int \mathrm{d}k \oint \mathrm{d}t \oint \mathrm{d}s \frac{e^{2tk-t\bar{z}-t^2} e^{2sk+sz-s^2} e^{-k^2}}{t^{n+1}s^{m+1}} = \sqrt{\pi}(-1)^n \frac{n!m!}{4\pi^2 i^2}\oint \mathrm{d}t \oint \mathrm{d}s \frac{e^{-t\bar{z}} e^{sz} e^{2st}}{t^{n+1}s^{m+1}}.$$

In the second expression we have completed the square in k and carried out the Gaussian integral. We now carry out the s-integration in a contour around the origin, where there is an order $m+1$ pole. Ignoring the prefactors, the residue at this point is

$$\text{Res} = \frac{1}{m!}\lim_{s\to 0}\frac{d^m}{ds^m}\left(\frac{e^{-t\bar{z}}e^{s(z+2t)}}{t^{n+1}}\right) = \frac{1}{m!}\frac{(z+2t)^m e^{-t\bar{z}}}{t^{n+1}},$$

which gives the integral as

$$\int \mathrm{d}k\,(-1)^n H_n\left[k - \frac{\bar{z}}{2}\right] H_m\left[k + \frac{z}{2}\right] e^{-k^2} \;=\; \sqrt{\pi}(-1)^n \frac{n!}{2\pi i}\oint \mathrm{d}t \frac{(z+2t)^m e^{-t\bar{z}}}{t^{n+1}}.$$

Next, we substitute $2t = zu/(1-u)$ to rewrite this as

$$\int \mathrm{d}k\,(-1)^n H_n\left[k - \frac{\bar{z}}{2}\right] H_m\left[k + \frac{z}{2}\right] e^{-k^2} \;=\; \sqrt{\pi}(-2)^n \frac{n!}{2\pi i} z^{m-n}\oint \mathrm{d}u \frac{e^{-\frac{|z|^2}{2}\left(\frac{u}{1-u}\right)}}{u^{n+1}(1-u)^{m-n+1}}.$$

Finally, using the contour integral representation of the generalised Laguerre polynomials [156],

$$L_n^\alpha(x) \;=\; \frac{1}{2\pi i}\oint \frac{e^{-\frac{xt}{1-t}}}{(1-t)^{\alpha+1}t^{n+1}},$$

where the contour again encircles the origin, we recover Eq. (1.53). Hence, the function $B_m(k)$ described in Eq. (1.51) gives the correct linear combination of single-particle states required to convert between the Landau and symmetric gauge, and is independent of the Landau level index, n.

2. Perturbative Approach to the Hofstadter Model at Small Flux

In this chapter, we begin our discussion of the Hofstadter model in earnest. We start by introducing the model in Sec. 2.1, giving a historical overview and some details of the single-particle problem. In Sec. 2.2, we consider the exact band structure and Berry curvature of the model in some simple cases, using numerical and analytical methods. In Sec. 2.3 we use a semiclassical approximation to derive nonperturbative properties of the wavefunctions and band structure at weak fields, building on the work in Ref. [158]. We then use these results to motivate a perturbative approach to the Hofstadter model at weak fields in Sec. 2.4. Finally, we discuss our results in the context of FCI models, and consider the many-body Hofstadter states that may arise at weak fields in Sec. 2.5.

2.1 Introduction to The Hofstadter Model

The Hofstadter model describes a charged, tight-binding particle hopping on a square lattice in the presence of an external magnetic field. The tuneable parameters of the system are the hopping amplitude, t (assumed, for most of this thesis, to have fixed magnitude in all lattice directions), and the amount of magnetic flux per plaquette, ϕ, which we measure in units of the flux quantum, $\phi_0 = h/e$. In the limit of weak flux per plaquette, the model reproduces the LLs of the continuum, while at larger ϕ, the spectrum takes on the remarkable fractal structure known as Hofstadter's Butterfly (see Fig. 2.1a) [21].

2.1.1 History

As a plentiful source of interesting physical phenomena, the Hofstadter model has received a great deal of attention since it was first written down in the mid-20th Century. In this subsection, we will outline some of the lines of investigation from the past decades which have directly influenced the present work. This is not intended to be an exhaustive review, however: we refer the reader to the historical overview in Ref. [1] for additional details.

Motivated by the Peierls substitution for charged particles in a magnetic field [159], Harper first considered the broadening effect of a uniform background field on a tight-binding conduction band of electrons [22]. The resulting discrete hopping equation has become known as the

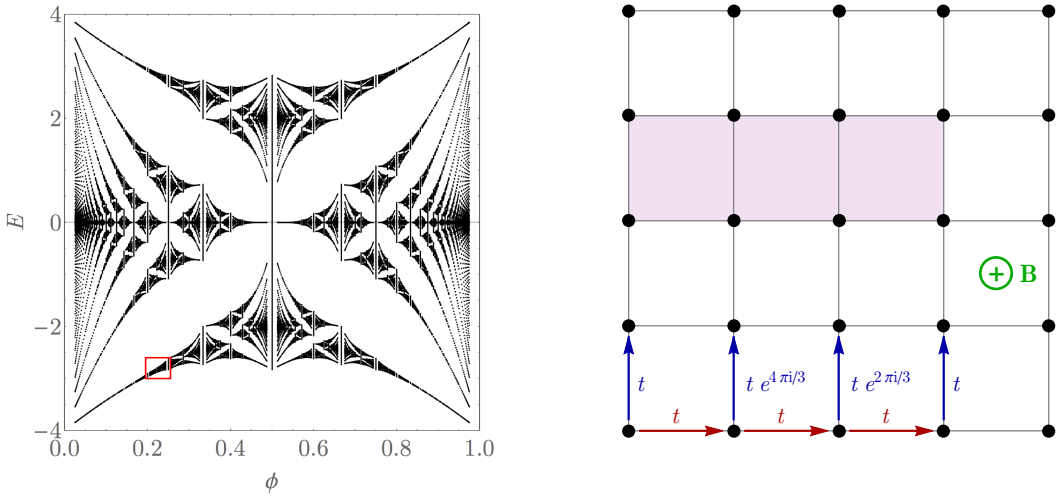

(a) (b)

Figure 2.1: (a) Hofstadter's Butterfly shows the fractal spectrum of the Hofstadter model (with energy E) as a function of magnetic flux per plaquette, ϕ. The entire pattern repeats for flux filling outside of the range 0 to 1. Landau level-like lines can be observed near to the points $(0, -4)$ and $(1/2, -2\sqrt{2})$, for example. Area in red box is shown in detail in Fig. 2.2a. (b) Hofstadter lattice model for the case $\phi = 1/3$, showing complex hopping phases in red and blue and with a magnetic unit cell shaded in purple.

Harper Equation, which we introduce in the next section (Eq. (2.2)). This idea was developed further by Azbel [160] and Hofstadter [21], who studied the detailed band structure of the model. These three authors are responsible for the model being variously called the Hofstadter model, Harper-Hofstadter model, or Azbel-Harper-Hofstadter model: in this thesis we will refer to the Hofstadter model, although we note the important contributions made in its development by the other authors.

Shortly after its discovery, studies of the Hofstadter model were carried out in the context of the magnetic translation group [161, 162, 163], while other authors considered the differences between rational and irrational magnetic flux values [164, 165]. The density of states was calculated in [166], which may be compared with our Figure 3.1. Aubry and André [167] studied the duality properties of the Harper equation (outlined in Appendix 2.A) and showed the existence of a localisation transition.

A key development in the understanding of the Hofstadter model arose when Thouless, Kohmoto, Nightingale and den Nijs (TKNN) calculated the Hall conductivity using the Kubo formula and found it to be related to an invariant integer [52]. This invariant integer was shown to be topological in origin and equal to the first Chern number of the Bloch band wavefunction [168, 169, 107]—or the integral of the Berry curvature over the Brillouin zone (see Sec. 1.7.1 for details). A decade later, it was shown [170] that the invariant Chern number was also related to the winding number of the edge states [46] in a finite system.

In their seminal paper, TKNN also perturbatively derived a Diophantine equation, from which one can directly obtain the Chern number (see Ref. [105] for an expanded discussion of this derivation). The existence of such a Diophantine equation for *any* system with magnetic translational symmetry was later proved by Dana et al. [171], although it should be noted that the equation only yields an unambiguous value for the Chern number in certain lattice systems [172]. We introduce the TKNN equation in Subsection 2.1.2 (Eq. (2.3)) and apply it to several cases of interest later in this thesis.

A semiclassical analysis of the Hofstadter model is an approach that has been in use for many decades. Early work in the weak-field limit is reviewed in Ref. [173], while the case of finite flux was considered by Wilkinson in Refs. [174, 175]. Most relevant to this thesis is the weak-field approach carried out by Watson [158], which we build on in Sec. 2.3. Complementary operator algebra approaches were also developed in Refs. [176, 177], whose general conclusions are in agreement with our single-particle results in Sec. 3.2.

In the mathematics literature, the Harper equation has been studied in the more general context of the *almost Mathieu operator*, where the major line of enquiry has been towards understanding the spectral properties of the system for different values of the coupling strength and irrational magnetic flux. Reviews of this approach may be found in [178, 179, 180]. However, in this this thesis we are most interested in the case of rational flux, since any irrational number can be approximated to arbitrary accuracy by a nearby rational number. In this situation, Bloch solutions are shown to exist within a finite magnetic unit cell.

Most recently, studies have focussed on the relation between the Hofstadter model and other Chern insulators. There have also been significant advances in the development of experimental realisations of the model—in graphene multilayers and optical lattices, for example. A discussion of these areas, and accompanying references, may be found above in Sec. 1.7.

2.1.2 Details of the Model

The Hofstadter Hamiltonian [21, 22] is

$$\hat{H} = -t \sum_{\langle \mathbf{r}\mathbf{r}' \rangle} \left[c_{\mathbf{r}}^{\dagger} c_{\mathbf{r}'} \exp\left[i \int_{\mathbf{r}'}^{\mathbf{r}} \mathbf{A} \cdot \mathrm{d}\mathbf{l} \right] + \mathrm{h.c.} \right], \tag{2.1}$$

where $\mathbf{r}$ and $\mathbf{r}'$ are site coordinates, t is the (real) hopping amplitude, $c_{\mathbf{r}}^{\dagger}$ is an electron creation operator, and we have set $e = \hbar = 1$. The sum is over neighbouring sites of a square lattice with periodic boundary conditions and a (uniform) magnetic field described by the vector potential

A. If the Landau gauge is chosen ($\mathbf{A} = B(0, -x, 0)$), the wavefunctions separate into pure Bloch waves in the y-direction so that $\psi_{\mathbf{r}} = e^{ik_y y}\psi_x$, where $\mathbf{r} = (x, y)$ and we have also set the lattice spacing to one. The states in the x-direction are given by solutions to the discrete Harper equation [22],

$$-\psi_{x-1} - \psi_{x+1} - 2\cos(2\pi\phi x - k_y)\,\psi_x = E\psi_x, \tag{2.2}$$

where we have introduced $\phi = B/(2\pi)$ as the magnetic flux quanta per plaquette. We measure ϕ in units of the flux quantum using the units $e = \hbar = 1$, so that $\phi_0 = e/h = 1/(2\pi)$. We have also divided through by t (so that $E \to E/t$) and used x as the discrete site index in the x-direction. We note the similarity between this discussion and the derivation of LL wavefunctions in the Landau gauge given in Sec. 1.4.1.

Let us choose a rational $\phi = p/q$ with p and q coprime (we refer to the mathematical literature cited in Section 2.1.1 for a discussion of irrational flux). In this case, Eq. (2.2) is periodic under the substitution $x \to x + q$, and the magnetic unit cell is elongated in the x-direction to become $q \times 1$ plaquettes in size (see Fig. 2.1b). The wavefunctions are then Bloch solutions ($\psi_{\mathbf{k}}(\mathbf{r}) = e^{i\mathbf{k}\cdot\mathbf{r}}u_{\mathbf{k}}(\mathbf{r})$), which form q bands in $\mathbf{k}$-space. The q bands for a given $\phi = p/q$ are easily identified in the butterfly spectrum in Fig. 2.1a, and are gapped in all cases except for the two central bands when the denominator q is even [21].

As described in Sec. 1.7.1, the Hall conductivity of a filled band is determined by its Chern number (C), which can be calculated directly from the Bloch wavefunction. It can also be obtained simply from the TKNN Diophantine equation for the rth band [52],

$$t_r p + s_r q = r, \tag{2.3}$$

which, under the constraint $|t_r| < q/2$, has a unique integer solution (s_r, t_r). The Chern number of the rth band is then given by $C_r = t_r - t_{r-1}$.

2.2 Band Structure Considerations for $\phi = M/N$

2.2.1 Band Dispersion

We observe, from the butterfly spectrum in Fig. 2.1a, that at small ϕ, the bands of the Hofstadter model resemble LLs. These can be seen as linear structures emanating from the point $(0, -4)$ and following the approximate relation $E \sim \phi$. At some flux fractions, when $\phi = 1/N$ with N

large, each 'LL' is made up of a single Hofstadter band. At other flux fractions, when $\phi = M/N$ with N large, the M lowest Hofstadter bands *together* form part of the LL-like structure, as shown in Fig. 2.2a.

For most of this thesis, we will group each set of M Hofstadter bands together and study the behaviour of the LL-like band as a whole. We justify this approximation by noting from numerics (and also our semiclassical approach in Sec. 2.6) that the energy gaps between the M bands are exponentially small in q, while the energy gaps between the LL-like structures are much larger (and are in fact algebraic in ϕ). In an experiment, finite temperature and interaction effects would, at some energy scale, render the exponentially small energy splittings in the band structure unresolvable. We refer to the M constituent Hofstadter bands as 'mini-bands' and the LL-like structures as 'bands'.

We can verify that the LL-like bands have the correct Chern number from the TKNN equation. Setting $\phi = p/q = M/N \ll 1$, Eq. (2.3) becomes

$$t_r M + s_r N = r, \tag{2.4}$$

which we must solve for $\lfloor t_r \rfloor < N/2$. To find the Chern number of the lowest band, we set $r = M$, which fills the lowest M mini-bands. This is solved by $(t_M, s_M) = (1, 0)$, and so the lowest band has total Chern number $C = 1$. Similarly, we can find the total Chern number of the lowest l bands by setting $r = lM$, which yields $(t_M, s_M) = (l, 0)$ (provided we remain in the lower half of the energy spectrum so that $\lfloor t_r \rfloor < N/2$). Each LL-like band therefore carries Chern number one.

We now consider the dispersion of the energy bands. It is clear from Fig. 2.1a that the bandwidth decreases as ϕ gets smaller, and we expect that in the limit $\phi \to 0$, the bands tend towards the LL limit and become completely flat. For simple flux fractions, we can calculate the band dispersion exactly by diagonalising Eq. (2.2). For $\phi = 1/3$ and $\phi = 1/4$, we find

$$\begin{aligned} E_{\phi=1/3}(\mathbf{k}) &= 2\sqrt{2}\cos\left[\theta_{\mathbf{k}} + \frac{2\pi}{3}\right] \\ E_{\phi=1/4}(\mathbf{k}) &= -\sqrt{4 + \sqrt{12 + 2\cos(4k_x) + 2\cos(4k_y)}}, \end{aligned} \tag{2.5}$$

where in the first expression we have defined

$$\theta_{\mathbf{k}} = \frac{1}{3}\arccos\left[-\frac{1}{2\sqrt{2}}\left(\cos(3k_x) + \cos(3k_y)\right)\right]. \tag{2.6}$$

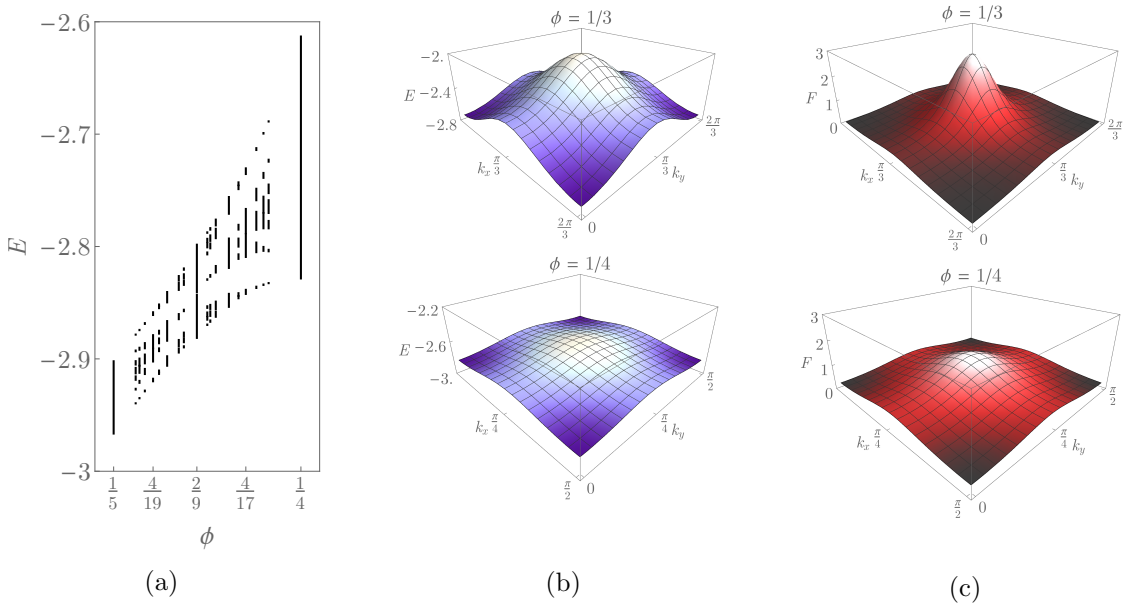

(a) (b) (c)

Figure 2.2: (a) Close up of butterfly region indicated in red in Fig. 2.1a. Lowest M mini-bands shown for $\phi = M/N$ between $\phi = 1/4$ and $\phi = 1/5$, for $M \leq 7$ (see text). (b) Analytic energy dispersion for $\phi = 1/3, 1/4$ (vertical scale has same range in each case). (c) Analytic Berry curvature for $\phi = 1/3, 1/4$ (vertical scale has same range in each case).

In both cases, the dependence on $\mathbf{k}$ occurs only through the combination $\cos(Nk_x) + \cos(Nk_y)$, a feature that holds for *any* band with *any* $\phi = M/N$. This property may be derived by considering the self-dualilty of the Harper equation under a Fourier transform [167, 175, 181], an approach that is outlined in Appendix 2.A.

By expanding Eqs. (2.5) as a power series in $\cos(Nk_x) + \cos(Nk_y)$, we see that the leading band dispersion takes the form $E(\mathbf{k}) \approx A + B\,(\cos(Nk_x) + \cos(Nk_y))$, where A and B are constants that depend on ϕ. This functional form is easily verified numerically, and in Sec. 2.3 we use a semiclassical method to derive this leading dependence explicitly. We will also show that B, the coefficient of the dispersive term, is exponentially small in N—and indeed, even for the cases considered above, the lowest band is already very flat (see Fig. 2.2b). For the case where there are M mini-bands, we are interested in the total bandwidth of the group, which is also found to be exponentially small in N (see discussion in Sec. 2.6).

2.2.2 Berry Curvature

We now consider the Berry curvature of the lowest Hofstadter band, which we recall should become flat in the LL limit, $\phi \to 0$. As with the band dispersion, we are able to calculate the Berry curvature of the lowest band analytically for certain simple values of ϕ. The standard approach would be to take the periodic part of the Bloch wavefunctions (obtained by diagonalising Eq. (2.2)) and substitute these into the equation for Berry curvature (1.41). However,

we find that analytic results are obtained most easily using the method given in Ref. [182], which is outlined briefly in Appendix 2.B. In the cited paper, the Hofstadter Berry curvature for $\phi = 1/3$ is shown to be

$$F_{\phi=1/3}(\mathbf{k}) = \frac{3 - 2\cos\left(4\theta_{\mathbf{k}} + \frac{2\pi}{3}\right)}{\sqrt{3}\left[1 + 2\cos\left(2\theta_{\mathbf{k}} - \frac{2\pi}{3}\right)\right]^3}. \tag{2.7}$$

with $\theta_{\mathbf{k}}$ as in Eq. (2.6). From our own calculations we find the Hofstadter Berry curvature for the lowest band with $\phi = 1/4$ to be

$$F_{\phi=1/4}(\mathbf{k}) = \frac{\sqrt{2}\left(6 - \cos(4k_x) - \cos(4k_y)\right)}{\left(6 + \cos(4k_x) + \cos(4k_y)\right)^{3/2}}, \tag{2.8}$$

and in principle this could be carried out for higher values of N. Notably, we again find that the $\mathbf{k}$-dependence of the Berry curvature only enters through the combination $(\cos(Nk_x) + \cos(Nk_y))$, a functional form that is easily verified numerically. There is no simple duality argument that can prove that this dependence holds for all values of N, but it may be argued through symmetry instead (see discussion in Sec. 2.3).

Moreover, we again find that the dispersion in the Berry curvature is exponentially small in N and has leading $\mathbf{k}$-dependence $F(\mathbf{k}) \approx A + B\left(\cos(Nk_x) + \cos(Nk_y)\right)$. This will be shown from a semiclassical argument in Sec. 2.3. However, we note that the decay in the spread of the Berry curvature is not as rapid as the decay in the energy band dispersion, as may be seen in Fig. 2.2c. For the case where $M \neq 1$, we are interested in the combined topological properties of the multiplet, which are characterised by the trace of the Berry matrix (see Sec. 1.7.1). We find numerically that the dispersion in this quantity is exponentially small in N as required, and in Appendix 3.D we discuss the properties of the Berry matrix in the context of our perturbation theory.

2.3 Semiclassical Approach for $\phi = 1/N$

We now use a semiclassical approach to explain the band flattening exhibited by the Hofstadter model when $\phi = 1/N$ and N is large. The Harper equation has been studied many times before using the WKB approximation, as outlined in Section 2.1.1; we are most interested in applying the approach of Ref. [158] to the lowest band of the Hofstadter model for small flux. We extend Watson's original calculation to consider the second order turning points in the lowest band, and use the resulting wavefunction to calculate the Berry curvature. We note that the flattening

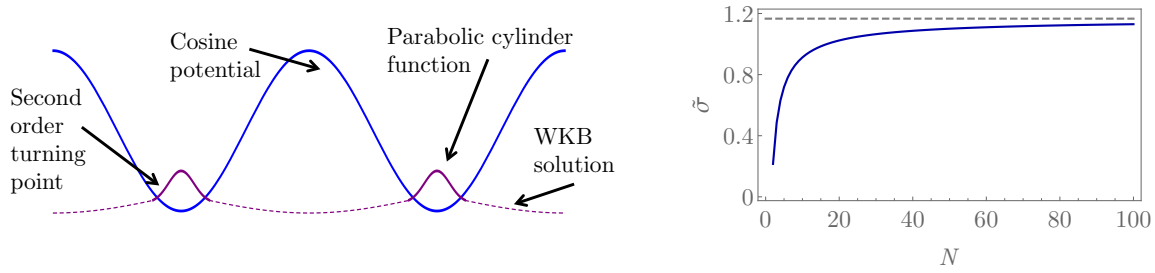

(a) (b)

Figure 2.3: (a) Harper's equation may be thought of as describing a particle moving in a cosine potential. Semiclassically, we envisage a ground state wavefunction that consists of localised Gaussians in the troughs of the potential, coupled together by tunnelling. For the lowest energy states, the turning point is a quadratic turning point, since the first derivative of the potential is vanishingly small. (b) The function $\tilde{\sigma}(N)$ (continuous line) and its limiting value (dashed line).

we consider here is different from the *exactly* flat bands and Berry curvature that arise in the Hofstadter model at certain special system sizes [117].

Beginning with the Harper equation (2.2), we note that if N is very large we may expand the discrete derivative to find

$$-\frac{1}{2}\psi''(x) - \cos\left(\frac{2\pi x}{N} - k_y\right)\psi(x) = \frac{(2+E)}{2}\psi(x),$$

where we have substituted $\psi_x \to \psi(x)$ as if it were a continuum function. This equation now looks similar to the Schrödinger equation for a particle moving in a cosine potential with period N. Intuitively, we would expect the ground state of this Hamiltonian to consist of localised wavefunctions at each trough of the potential, coupled weakly together by tunnelling through the barrier, as shown in Figure 2.3a.

We formalise this idea using the WKB approximation. Following Watson [158], we define $x' = x/N$ to obtain

$$\psi(x' + 1/N) + \psi(x' - 1/N) = 2\cos\left[p(x')\right]\psi(x') \tag{2.9}$$

with

$$p(x) = \cos^{-1}\left[-E/2 - \cos(2\pi x)\right]. \tag{2.10}$$

We have set $k_y = 0$ here as in the continuum approximation it merely applies a translation in the x-direction: this will be reinstated later. We we also drop the prime on x from now on.[1]

[1] According to the discussions in Refs. [22, 183], we do not need to use a discrete WKB approach in this case.

Assuming a semiclassical solution

$$\psi(x) = e^{NS_0(x)+S_1(x)},$$

we solve for S_0 and S_1 using Harper's equation to find the (oscillating and exponential) WKB solutions

$$\begin{aligned} \psi^{\pm}_{\rm osc}(x) &= \tfrac{1}{\sqrt{\sin p(x)}} \exp\left[\pm iN \textstyle\int^x p(t)\,\mathrm{d}t\right] \\ \psi^{\pm}_{\rm exp}(x) &= \tfrac{1}{\sqrt{\sinh \tilde{p}(x)}} \exp\left[\pm N \textstyle\int^x \tilde{p}(t)\,\mathrm{d}t\right], \end{aligned} \tag{2.11}$$

with

$$\tilde{p}(x) = \cosh^{-1}\left[-E/2 - \cos(2\pi x)\right]. \tag{2.12}$$

Turning points occur whenever $p(x) = 0$, or when $x = \pm\beta, 1 \pm \beta, 2 \pm \beta \ldots$ with

$$\beta = \frac{1}{2\pi}\cos^{-1}\left(-\frac{E}{2} - 1\right). \tag{2.13}$$

For the lowest band, the potential is so flat that two of these turning points coalesce to form a single, second order turning point. The exact solution in this region is a parabolic cylinder function [156], which sews together parts of the wavefunction from either side of the crossing. We expand this parabolic cylinder function to large values of its argument to arrive at the formulae that connect exponential WKB solutions from the left- and right-hand side of the trough—these connection formulae are given and derived in Appendix 2.C.

From this, we propagate the WKB solution from the right-hand side of the trough across the classically forbidden region of the unit cell until we reach the next trough in the cosine potential (see Fig. 2.3a). We can then impose Bloch periodicity on the entire wavefunction to obtain the band energy,

$$E = -4 + \frac{2\pi}{N} - \frac{4}{N}\sqrt{\frac{\pi}{e}}e^{-\sigma}\cos(k_x N), \tag{2.14}$$

and periodic piecewise wavefunction

$$u(x,k_x,k_y) = \begin{cases} (i) & e^{-ik_x n}A\left(\frac{N}{\pi}\right)^{\frac{1}{4}}\Big[(2e)^{\frac{1}{4}}\left(1-\frac{\ln 2}{2}\left(\frac{1}{2}+a\right)\right)U\left[\xi(x-Nk_y/(2\pi)),a\right] \\ & \quad +e^{-ik_x N}e^{-\sigma}(2e)^{-\frac{1}{4}}\left(1+\frac{\ln 2}{2}\left(\frac{1}{2}+a\right)\right)\sqrt{\frac{\pi}{2}}V\left[\xi(x-Nk_y/(2\pi)),a\right]\Big] \\ (ii) & e^{-ik_x n}A\left[\psi^{-}_{\rm exp}(x-Nk_y/(2\pi)) + e^{-ik_x N}e^{-\sigma}\psi^{+}_{\rm exp}(x-Nk_y/(2\pi))\right] \\ (iii) & e^{ik_x(N-n)}A\left(\frac{N}{\pi}\right)^{\frac{1}{4}}\Big[(2e)^{\frac{1}{4}}\left(1-\frac{\ln 2}{2}\left(\frac{1}{2}+a\right)\right)U\left[\xi(x-Nk_y/(2\pi))-\xi_1,a\right] \\ & \quad +e^{-ik_x N}e^{-\sigma}(2e)^{-\frac{1}{4}}\left(1+\frac{\ln 2}{2}\left(\frac{1}{2}+a\right)\right)\sqrt{\frac{\pi}{2}}V\left[\xi(x-Nk_y/(2\pi))-\xi_1,a\right]\Big]. \end{cases} \tag{2.15}$$

The three wavefunction pieces correspond to the regions

$$(i) : 0 \leq x \leq \alpha\beta \qquad (ii) : \alpha\beta \leq x \leq (1-\alpha\beta) \qquad (iii) : (1-\alpha\beta) \leq x \leq 1,$$

where α quantifies the extent of the parabolic cylinder functions in a manner described below.

The derivation of the expressions above is given in more detail in Appendix. 2.C, but we note here that $\xi \equiv \xi(x)$ is an appropriately scaled version of x, $\xi_1 \equiv \xi(1)$ and a is very close to $-1/2$. In addition, A is an overall normalisation constant and the quantity σ describes the exponential decay of the bandwidth and Berry curvature through the implicit definition

$$\sigma = N \int_{\beta}^{1-\beta} \cosh^{-1}\left(-\frac{E}{2} - \cos(2\pi t)\right) \mathrm{d}t \equiv \tilde{\sigma} N \approx 1.166N.$$

The last equality gives the value of σ in the large N limit, and we show $\tilde{\sigma}(N)$ in general in Figure 2.3b.

In the expressions above, we have taken only the leading order algebraic and leading order exponential corrections (at $O(1/N)$ and $O(e^{-\tilde{\sigma}N})$ respectively). The wavefunction is split into three parts: a parabolic cylinder solution near the troughs on the left and on the right of the magnetic unit cell, and a WKB solution in the classically forbidden region in the middle.

There is some choice over where we choose to switch from the parabolic cylinder solution to the WKB solution, which we parameterise with α. As the WKB solution is inaccurate close to the turning point, we allow the parabolic cylinder function to permeate a distance proportional to βN beyond the crossing, until $x = \alpha\beta N$. This remains an unconstrained parameter in our wavefunction, but we shall see that it has a very limited effect on the results. Normally we choose $\alpha = 2.3$.

If we try to read off the bandwidth from Equation (2.14), we notice that only the k_x-dependence has been captured: by assuming a continuous translational dependence on k_y we have lost information. However, due to the duality of Harper's equation (Ref. [167] and Appendix. 2.A), we know that the bandwidth must be a function of $\cos(k_x N) + \cos(k_y N)$. The complete dispersion relation must therefore be

$$E = -4 + \frac{2\pi}{N} - \frac{4}{N}\sqrt{\frac{\pi}{e}} e^{-\sigma} \left[\cos(k_x N) + \cos(k_y N)\right], \tag{2.16}$$

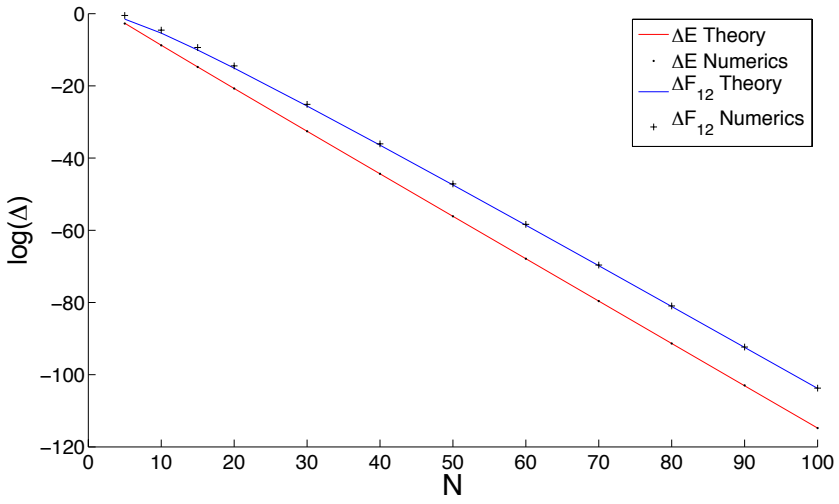

Figure 2.4: Comparison of analytic bandwidth and Berry curvature with numerics ($\alpha = 2.3$ here).

giving a bandwidth ($\Delta E = E_{\max} - E_{\min}$) of

$$\Delta E = \frac{16}{N}\sqrt{\frac{\pi}{e}}e^{-\tilde{\sigma}N}, \tag{2.17}$$

where we make the N dependence in the exponent explicit. This shows excellent agreement with the bandwidth obtained from exact diagonalisation, as demonstrated in Figure 2.4.[2]

Similarly, we can calculate the Berry curvature from the semiclassical wavefunction by inserting the wavefunction (Eq. (2.15)) into the definition of the Berry curvature in Eq. (1.41). The full calculation (given in Appendix. 2.C) yields

$$F(\mathbf{k}) \quad = \quad \frac{N}{2\pi} + \left(\frac{\tilde{\sigma}P^2}{\sqrt{\pi e}\mathrm{Erf}(\alpha)}\right) N^2 e^{-\tilde{\sigma}N}\cos(k_x N),$$

where the factor in brackets is of order unity and varies only very weakly with N (see Appendix 2.C for definitions). Even though the Berry curvature depends on the free parameter α, for any sensible value ($\alpha \gtrsim 2$), $\mathrm{Erf}(\alpha)$ and P are very close to unity and vary by less than one percent.

We see that only the k_x-dependence of the Berry curvature has been captured because we have again assumed a continuous translational dependence on k_y. However, as argued in Appendix B of Ref. [1], the Berry curvature must be unchanged under the exchanges $k_x \to -k_y, k_y \to k_x$, and so can depend only on the expressions $\cos(k_x N) + \cos(k_y N)$ and $\cos(k_x N)\cos(k_y N)$. We argue that it must only be a function of the former as follows.

[2]We note that Ref. [158] considers a more general $\phi = M/N$ with first order turning points, where the bandwidth is also found to vary with N according to $e^{-\tilde{\sigma}N}$.

First, if there were any dependence on the product $\cos(k_x N)\cos(k_y N)$, we would expect the coefficient of $\cos(k_x N)$ to depend on which value of k_y we choose when we carry out the WKB analysis. We would also expect this coefficient to have certain symmetries if the hopping is made anisotropic, which are found not to hold [1].

Secondly, in Sec. 2.2.2 we derived some analytical expressions for the Berry curvature at $\phi = 1/3, 1/4$ which were found to be only a function of $\cos(Nk_x) + \cos(Nk_y)$. In order for our WKB Berry curvature to connect to these analytic low-N expressions, we would expect it also to be a function of $\cos(Nk_x) + \cos(Nk_y)$ only.

Finally, extensive numerical studies have verified that the leading Berry curvature deviation is exponentially small in N and proportional to $\cos(Nk_x) + \cos(Nk_y)$. Subleading curvature deviations are suppressed by a further exponentially small factor and are proportional to $(\cos(Nk_x) + \cos(Nk_y))^2$.

In this way, we replace $\cos(Nk_x) \to \cos(Nk_x) + \cos(Nk_y)$ in our WKB expression for the Berry curvature and obtain the leading Berry curvature deviation

$$\Delta F = \frac{4\tilde{\sigma}N^2P^2e^{-\tilde{\sigma}N}}{\sqrt{\pi e}\mathrm{Erf}(\alpha)}. \tag{2.18}$$

This is plotted alongside the Berry curvature deviation obtained from exact diagonalisation in Figure 2.4, and again shows very good agreement.

2.4 Perturbation Theory for $\phi = 1/N$

In the previous section, we showed from a semiclassical argument that the discreteness of the lattice and the tunnelling between troughs each have only exponentially small effects on the energies and wavefunctions.[3] We now make the main assumption of this part of the thesis: we ignore anything exponentially small in N. In the language of WKB, this amounts to ignoring tunnelling between neighbouring magnetic unit cells (where the sewing together of wavefunctions would introduce a **k**-dependence) and treating the wavefunctions as continuous instead of discrete. In this way, the bands are assumed to be completely flat (and also completely Berry flat). We will find a localised wavefunction, perturbative in ϕ, in each unit cell, and combine these into a Bloch solution by hand.

To begin, we return to the Harper equation and make the continuum substitution $\psi_x \to$

[3] In fact, the discreteness and tunnelling corrections are related through a Fourier transform. The Harper equation is self-dual under such a transformation [167], and the potential barrier and discrete derivative terms exchange places (see also Appendix 2.A).

$\psi(x)$. We rewrite the discrete differences in terms of derivatives using translation operators,

$$\hat{T}_+ = e^{\partial_x}, \qquad \hat{T}_- = e^{-\partial_x},$$

so that Harper's equation becomes

$$-\left[\hat{T}_+ + \hat{T}_- + 2\cos(2\pi\phi x - k_y)\right]\psi(x) = E\psi(x).$$

Up to this point, the transformed Harper equation is still exact. We now make an approximation by expanding the $\hat{T}$ operators and the cosine potential in powers of $1/N$. The left side of Harper's equation separates consistently into terms at successive orders in $1/N$, and to first order we find

$$\left[-\frac{1}{2}\partial_x^2 + \frac{1}{2}\left(\frac{2\pi}{N}\right)^2 x^2\right]\psi(x) = \frac{(4+E)}{2}\psi(x), \tag{2.19}$$

where for consistency we note that $x \sim \sqrt{N}$ scales with the magnetic length. In the continuum, changing k_y merely translates the wavefunction in the x-direction (as can be seen by considering the substitution $x' = x - Nk_y/2\pi$) so we have set $k_y = 0$ without loss of generality.

The first order equation just describes a Landau gauge LL wavefunction (Sec. 1.4.1), and so we can make the standard ladder operator substitutions,

$$a = \frac{1}{\sqrt{2}l_B}\hat{x} + \frac{il_B}{\sqrt{2}}\hat{p}_x, \qquad a^\dagger = \frac{1}{\sqrt{2}l_B}\hat{x} - \frac{il_B}{\sqrt{2}}\hat{p}_x. \tag{2.20}$$

We set the universal constants $e = \hbar = m = 1$, so that $B = 2\pi/N$ and $l_B^2 = N/(2\pi) = 1/\omega_c$.

The spectrum forms the usual harmonic ladder, with energies (E_n) and wavefunctions ($|n\rangle$) as given in Eq. 1.5. In this way, at first order the Hofstadter model recovers the LL states of the continuum. The differences are that k_y is now strictly only defined modulo 2π, the wavefunctions really exist only at discrete lattice points, and in the x-direction the wavefunctions are Bloch periodic with period N. The magnetic length gets larger as the magnetic field gets weaker, but is much less than the period N of the potential. In the limit of large N, the magnetic length is so large that the underlying lattice is not 'seen' by the wavefunction, and the wavefunction is close to an ideal continuum state.

To go beyond the LL states we must consider higher order terms in the Harper equation.

In general, the kth order term on the left hand side of (2.19) will be of the form

$$\begin{aligned}\hat{H}_k &= -\frac{1}{(2k)!}\left[\partial_x^{2k} + (-1)^k \left(\frac{2\pi}{N}\right)^{2k} x^{2k}\right] \\ &= -\frac{1}{(2k)!}\left(\frac{\pi}{N}\right)^k \left[\left(a - a^\dagger\right)^{2k} + (-1)^k \left(a + a^\dagger\right)^{2k}\right].\end{aligned} \tag{2.21}$$

The Harper equation thus includes contributions at all orders in $1/N$, each of which will perturb the energy levels and wavefunctions at all orders of perturbation theory. While the first few corrections can be calculated easily using elementary perturbation theory, the process is made more efficient by defining a (canonical) unitary operator that acts on an unperturbed state, $|n\rangle$, to give the corresponding perturbed state, $|\tilde{n}\rangle$, at a given order,

$$|\tilde{n}\rangle = U^\dagger\left(a^\dagger, a\right)|l\rangle \equiv e^{-f(a^\dagger,a)}|n\rangle\,, \tag{2.22}$$

where f is anti-Hermitian in the bosonic ladder operators. By choosing an appropriate ansatz for f and using the Baker-Campbell-Hausdorff formula, finding the corrections amounts to ensuring that the canonical transformation

$$\langle m|\, e^{-f^\dagger(a^\dagger,a)}\hat{H}e^{-f(a^\dagger,a)}|n\rangle \equiv E\delta_{mn} \tag{2.23}$$

is diagonal, a process which can be easily automated. In most cases we do not need to calculate to high order as N is presumed large (and necessarily greater than one).

Since the perturbing Hamiltonians may be written entirely in terms of ladder operators, the wavefunction corrections will mix in higher and lower LLs, and will preserve the (assumed) degeneracy of the different k_y-states. Including contributions up to third order, we find the energy levels are

$$E_n = -4 + \frac{4\pi}{N}\left(n + \frac{1}{2}\right) - \frac{1}{2}\left(\frac{\pi}{N}\right)^2\left(2n^2 + 2n + 1\right) + \frac{1}{24}\left(1 + 3n + 3n^2 + 2n^3\right)\left(\frac{\pi}{N}\right)^3, \tag{2.24}$$

and the unitary operator, which generates the wavefunctions from the unperturbed states is,

$$\begin{aligned}U^\dagger &= \exp\left[\left(\frac{1}{96}\left(\frac{\pi}{N}\right) + \frac{1}{128}\left(\frac{\pi}{N}\right)^2 + \frac{37}{6912}\left(\frac{\pi}{N}\right)^3\right)\left(\left(a^\dagger\right)^4 - (a)^4\right)\right. \\ &\quad + \left(\frac{1}{320}\left(\frac{\pi}{N}\right)^2 + \frac{7}{1152}\left(\frac{\pi}{N}\right)^3\right)\left(\left(a^\dagger\right)^5 a - a^\dagger\,(a)^5\right) \\ &\quad \left. + \frac{7}{6912}\left(\frac{\pi}{N}\right)^3\left((a^\dagger)^6 a^2 - (a^\dagger)^2 a^6\right) - \frac{11}{215040}\left(\frac{\pi}{N}\right)^3\left((a^\dagger)^8 - a^8\right)\right].\end{aligned} \tag{2.25}$$

These perturbative corrections mix in components from LLs whose indices differ by multiples of four. In this way, the perturbed wavefunctions adopt the fourfold rotational symmetry of the underlying lattice.

Finally, if we write the nth perturbed x-direction wavefunction as $\tilde{\psi}_n(x - k_y N/(2\pi))$, then we can form Bloch solutions through

$$\Psi_{n\mathbf{k}}(\mathbf{r}) = \frac{1}{2\pi} \sum_m e^{ik_x mN} e^{ik_y y} \tilde{\psi}_n \left(x - \frac{k_y N}{2\pi} - mN \right). \tag{2.26}$$

We have normalised these wavefunctions for the infinite system so that

$$\int \mathrm{d}x\, \mathrm{d}y \, \left[\Psi_{n',\mathbf{k}'}(\mathbf{r})\right]^* \Psi_{n,\mathbf{k}}(\mathbf{r}) \quad = \quad \delta_{n'n}\delta(\mathbf{k}' - \mathbf{k}).$$

2.5 Two-body Interactions

2.5.1 Band Flatness

We argued in Sec. 1.7.2 that to favour the formation of FCI states, a 'good' Chern band should have a reasonably small bandwidth (W). There should also be a large enough gap to excitations (E_G), that we can switch on an interaction that satisfies the inequality $W \ll V_{\mathrm{int}} \ll E_G$, where V_{int} is the interaction strength.

In this chapter so far, we have shown that for the lowest band in the Hofstadter model at weak fields, the bandwidth is exponentially small in N, varying as $W \sim Ae^{-\tilde{\sigma}N}$ for some (only weakly varying) A and $\tilde{\sigma}$. On the other hand, we have found that the bandgap is only algebraically small, varying as $E_G \sim 1/N$. For large enough N, the bandwidth must therefore be negligible compared to the bandgap. For the lowest band, we find a flatness ratio $F = E_G/W > 10$ for $N > 3$: if we choose V_{int} to lie between W and E_G, then the required energy inequality is satisfied.[4]

2.5.2 Perturbed Interaction Matrix Elements

We now include interactions and study the effects of the lattice on the many-body wavefunctions, continuing to ignore any corrections that are exponentially small in N. For now we consider

[4]We note, however, that the flatness ratio generally becomes smaller if we consider higher bands at fixed N.

only the simple two-body delta-function interaction,

$$\hat{V} = \sum_{i<j} V(\mathbf{r}_i, \mathbf{r}_j) = V_{\text{int}} \sum_{i<j} \delta(\mathbf{r}_i - \mathbf{r}_j),$$

which acts between each pair of particles (i, j) in turn and is relevant for bosonic systems.

For simplicity we will focus on the lowest Hofstadter band ($n = 0$), which is adiabatically connected to the lowest Landau level. We project to this lowest single-particle band and form noninteracting many-body states from the perturbed wavefunctions found previously. Then, using these states as a basis, we calculate the overlap integrals between an initial two-body state, the interaction potential, and a final two-body state. Using the Bloch states defined in (2.26), the two-body interaction matrix elements for the lowest band are

$$\begin{aligned} V_{\mathbf{k}_1\mathbf{k}_2\mathbf{k}_3\mathbf{k}_4} &= \langle \Psi_{0,\mathbf{k}_1}(\mathbf{r}_1)\Psi_{0,\mathbf{k}_2}(\mathbf{r}_2)| \, V_{\text{int}}\delta\left(\mathbf{r}_1 - \mathbf{r}_2\right) |\Psi_{0,\mathbf{k}_3}(\mathbf{r}_1)\Psi_{0,\mathbf{k}_4}(\mathbf{r}_2)\rangle \\ &\equiv \frac{V_{\text{int}}}{(2\pi)^2}\delta\left(\Sigma k_x\right)\delta\left(\Sigma k_y\right) T_{k_{1y}k_{2y}k_{3y}k_{4y}}, \end{aligned} \tag{2.27}$$

where we have defined the useful notation

$$\sum k_x = k_{1x} + k_{2x} - k_{3x} - k_{4x} \tag{2.28}$$

and similarly for $\sum k_y$. The matrix element $T_{k_{1y}k_{2y}k_{3y}k_{4y}}$ is given by

$$T_{k_{1y}k_{2y}k_{3y}k_{4y}} = \int \mathrm{d}x \left[\tilde{\psi}_0\left(x - \kappa_1\right)\right]^* \left[\tilde{\psi}_0\left(x - \kappa_2\right)\right]^* \tilde{\psi}_0\left(x - \kappa_3\right)\tilde{\psi}_0\left(x - \kappa_4\right), \tag{2.29}$$

where we have also defined $\kappa_i = k_{iy}N/(2\pi)$. The δ functions in $V_{\mathbf{k}_1\mathbf{k}_2\mathbf{k}_3\mathbf{k}_4}$ ensure that crystal momentum is conserved, while the matrix element magnitudes are contained within the quantities $T_{k_{1y}k_{2y}k_{3y}k_{4y}}$. Explicitly, these are made up of Gaussian and polynomial factors that depend on the set of $\{k_{iy}\}$.[5] From the two-body matrix elements we can in principle write down the matrix elements between states with any number of particles. If this larger matrix is then diagonalised, we can obtain the low-lying many-body wavefunctions and energies for a given system size.

Although it is possible to work in the Landau gauge, in order to interpret our results in terms of the usual continuum theories, we will switch to the symmetric gauge (and associated disk geometry). We will therefore calculate the symmetric gauge matrix elements, the Haldane

[5] We observe that umklapp scattering is suppressed, in contrast to the general case considered later in Chapter. 3.

pseudopotentials, which were outlined in Sec. 1.6.2. However, in the Hofstadter model, the lattice breaks rotational symmetry and we no longer expect the angular momentum to be conserved. Instead of the sequence of pseudopotentials V_L that we find in the continuum, the Hofstadter pseudopotentials will instead form a matrix in L with elements $V_{LL'}$.

We postpone a discussion of the gauge transformation required to convert Landau gauge Hofstadter wavefunctions into symmetric gauge wavefunctions until Section 3.3.2. For now, we merely observe that the operator $U^\dagger$ defined earlier is gauge independent and has the same expression (in terms of inter-Landau level operators) in any gauge we choose. The pseudopotential matrix elements for the delta-function interaction are then given by

$$V_{LL'} \quad = \quad V_{\text{int}} \left\langle L \right| U_i U_j \delta\left(z_i - z_j\right) U_i^\dagger U_j^\dagger \left| L' \right\rangle .$$

Here we have dropped the labels i and j from the two-particle states $|L\rangle$ but added them to the $U^\dagger$ operators to show that each of the two particles is individually perturbed by the unitary operator defined in Eq. (2.25).

The pseudopotential matrix to second order is then (showing only rows and columns corresponding to $L, L' \in \{0, 2, 4, 6, 8\}$, and with $\delta = 1/N$)

$$V_{LL'} = \frac{V_{\text{int}}}{4\pi l_B^2} \begin{pmatrix} 1 - \frac{7}{1536}\left(\pi\delta\right)^2 & 0 & \frac{\sqrt{6}}{96}\left(\pi\delta\right) + \frac{\sqrt{6}}{128}\left(\pi\delta\right)^2 & 0 & \frac{\sqrt{70}}{3072}\left(\pi\delta\right)^2 \\ 0 & \frac{1}{256}\left(\pi\delta\right)^2 & 0 & 0 & 0 \\ \frac{\sqrt{6}}{96}\left(\pi\delta\right) + \frac{\sqrt{6}}{128}\left(\pi\delta\right)^2 & 0 & \frac{1}{1536}\left(\pi\delta\right)^2 & 0 & 0 \\ 0 & 0 & 0 & 0 & 0 \\ \frac{\sqrt{70}}{3072}\left(\pi\delta\right)^2 & 0 & 0 & 0 & 0 \end{pmatrix} . \tag{2.30}$$

We note that the rotational symmetry-breaking (off-diagonal) terms arise at a lower order than the diagonal corrections and that all of the coefficients are small (< 0.03). Angular momentum is only conserved modulo four, and so we expect any many-body spectrum to split into four sectors—this is to be expected from the form of the lattice, which has a discrete, fourfold rotational symmetry.

We emphasise that we are able to describe the interaction in terms of pseudopotentials only when the lattice can be treated as a small perturbation to the continuum. As δ is increased, the exponentially small terms that we previously neglected become important and the pseudopotential description would break down. We need to consider the full pseudopotential matrix because the two-body interaction now depends on $(z_i - z_j)$ rather than $|z_i - z_j|$. In general, for larger δ, the interaction will depend also on $(z_i + z_j)$, which would make the pseudopotentials

one step more complicated.

2.6 Perturbation Theory for $\phi = M/N$

The analysis carried out above assumed that $\phi = 1/N$ with N large. However, we noted in Sec. 2.2 that for $\phi = M/N$ with N large, the lowest M mini-bands *together* formed part of the lowest LL-like band. In this section, we briefly discuss how our results may be extended to this general case.

First, we note from numerics that, although the mini-bands each have a bandwidth that scales as $e^{-\tilde{\sigma}N}$ [158], the *total* bandwidth of the M mini-bands scales as $e^{-\tilde{\sigma}N/M}$. This flattening can be observed in Fig. 2.2a, for example, and we expect that the dependence may be derived analytically using a similar approach to that in Sec. 2.3. We can therefore ignore this exponentially small bandwidth under the same approximations as above, and consider the M mini-bands as a degenerate flat band. We also observe numerically that the trace of the Berry matrix of the M mini-bands follows the dependence in Eq. (2.18) under the replacement $1/N \to M/N$—this is discussed further in Appendix 3.D.

We can explain the origin of the mini-bands by returning to the Harper equation and looking at the cosine potential for $\phi = M/N$,

$$V(x) \quad = \quad -2\cos\left(\frac{2\pi M x}{N} - k_y\right).$$

Since M/N is small, we can again expand perturbatively about the trough at $x = 0$, and the discussion follows as in Sec. 2.4 under the replacement $1/N \to M/N$. However, we can also make the replacement $x = x' + N/M$, which leaves the cosine potential unchanged. There is now a trough located at $x' = 0$, and if we expand perturbatively about this, we obtain exactly the same energy levels and wavefunctions as before—except that the wavefunctions are now centred on $x = N/M$.

In total, we find M perturbed wavefunctions centred at the positions $x = rN/M$, where $r = 0, 1, \ldots, M-1$. The true (numerical) wavefunctions will be linear combinations of these states, and will have exponentially small corrections due to the discreteness of the lattice and tunnelling between the M troughs. This leads to the formation of the M mini-bands observed in the numerical energy spectrum.

In our perturbative approach we ignore this splitting, since it would easily be overcome by thermal excitations or the many-body interaction between particles. Instead, we group the set

of M mini-bands together and interpret them as collectively representing a single LL on the lattice. The energy levels are exactly as in Eq. (2.24) with the replacement $1/N \to M/N$. The M perturbed wavefunctions are also described by the same unitary operator (given in Eq. (2.25)) under the replacement $1/N \to M/N$, but there is now one state localised in each of the M troughs.

As described in Sec. 2.2, the total Chern number of the M degenerate bands is one, as expected for a Landau level, although the individual Chern numbers of the mini-bands vary significantly. We justify this value for the total Chern number from our perturbative wavefunctions in Appendix 3.D (where we extend it to other field filling fractions).

In terms of our perturbation theory, the energies, the wavefunctions, and hence the pseudopotentials, depend on $\delta \equiv M/N$ as if it were a continuous parameter. The precise values of M and N only affect the periodicity properties of the wavefunctions, which we will find in Chapter 3 do not significantly change the many-body physics. Therefore, provided we neglect the tunnelling between troughs, we can treat δ generally and extrapolate even to irrational values.

Appendices for Chapter 2

2.A Duality in the Hofstadter Model

In this appendix we describe the self-duality of the Harper equation originally studied in Ref. [167]. We recall that Harper's equation may be written

$$-\psi_{x-1} - \psi_{x+1} - 2\cos\left(\frac{2\pi p}{q}x - k_y\right)\psi_x = E\psi_x,$$

where we have explicitly written $\phi = p/q$ for the flux fraction. This is a discrete Schrödinger equation that may be written in determinant form as

$$\begin{vmatrix} -2\cos(-k_y) - E & -1 & 0 & -e^{-ik_x q} \\ -1 & -2\cos\left(\frac{2\pi p}{q} - k_y\right) - E & -1 & 0 \\ 0 & \ddots & \ddots & \ddots \\ -e^{ik_x q} & 0 & -1 & -2\cos\left(\frac{(q-1)\pi p}{q} - k_y\right) - E \end{vmatrix} = 0,$$

where we have imposed Bloch periodicity on the unit cell of length q, and all elements not on the tridiagonal or in the corners are zero. Looking at the structure of this matrix, we see that the only terms of the determinant which depend on k_x are those which involve a single corner element (the dependence cancels out in the term involving both corners). There is only one nonzero term which includes just one corner,

$$\begin{vmatrix} * & * & & & & \times \\ \times & * & * & & & \\ & \times & * & * & & \\ & & \times & * & * & \\ & & & \times & * & * \\ * & & & & \times & * \end{vmatrix},$$

where $\times$ indicates elements which are multiplied together in this term of the determinant and $*$ indicates other nonzero matrix elements. There is a similar term which includes the other corner. The determinant therefore takes the form $f(E, k_y) - 2\cos(qk_x) = 0$, where $f(E, k_y)$ is a polynomial in E that also depends on k_y.

By taking the Fourier transform [167],

$$\psi_x = e^{ik_x x}\sum_j e^{\frac{2\pi i p}{q}mx}e^{-ik_y m}\tilde{\psi}_m,$$

the Harper equation may be transformed into

$$-\tilde{\psi}_{m-1}-\tilde{\psi}_{m+1}-2\cos\left(\frac{2\pi p}{q}m-k_x\right)\tilde{\psi}_m=E\tilde{\psi}_m,$$

where the roles of k_x and k_y have been interchanged. Using the same argument as above, we now see that $f(E,k_x)-2\cos(qk_y)=0$. Combining both of these, we see that $f(E)-2\left[\cos(qk_x)+\cos(qk_y)\right]=0$, and so the $\mathbf{k}$-dependence of the band dispersion only occurs through the combination $\cos(qk_x)+\cos(qk_y)$.

2.B Algebraic Method to Calculate Berry Curvature

In this appendix we outline the algebraic approach used in Ref. [182] to calculate the Berry curvature of the Hofstadter model for $\phi=1/3$, and apply it to our own case of $\phi=1/4$. The method makes use of the projector expression for the Berry curvature [169], which may be written

$$F^{\alpha}(\mathbf{k}) = i\mathrm{Tr}\left[\hat{P}_{\mathbf{k}\alpha}\left(\frac{\partial\hat{P}_{\mathbf{k}\alpha}}{\partial k_x}\frac{\partial\hat{P}_{\mathbf{k}\alpha}}{\partial k_y}-\frac{\partial\hat{P}_{\mathbf{k}\alpha}}{\partial k_y}\frac{\partial\hat{P}_{\mathbf{k}\alpha}}{\partial k_x}\right)\right], \tag{2.31}$$

where $\hat{P}_{\mathbf{k}\alpha}=|u^{\alpha}_{\mathbf{k}}\rangle\langle u^{\alpha}_{\mathbf{k}}|$ is the single-particle projector onto the periodic part of the Bloch wavefunction, $|u^{\alpha}_{\mathbf{k}}\rangle$. We will calculate the projector explicitly using the SU(N) structure of the Hamiltonian.

It is useful to work with the periodic part of the Bloch wavefunction directly, so we rewrite the Harper equation as

$$-e^{-ik_x}u_{x-1}-e^{ik_x}u_{x+1}-2\cos\left(\frac{2\pi p}{q}x-k_y\right)u_x = Eu_x$$

with $u_{x+q}=u_x$. This equation may be written in matrix form as $\tilde{H}(\mathbf{k})\mathbf{u}_{\mathbf{k}}=E\mathbf{u}_{\mathbf{k}}$, where $\tilde{H}(\mathbf{k})$ is an Hermitian matrix with dimension $N\times N$ for $\phi=1/N$. Since $\tilde{H}(\mathbf{k})$ is Hermitian, it may expanded as $\tilde{H}(\mathbf{k})=a(\mathbf{k})\hat{I}+\mathbf{b}(\mathbf{k})\cdot\hat{\boldsymbol{\lambda}}$, where $\hat{I}$ is the identity matrix, $\hat{\boldsymbol{\lambda}}$ is a vector of SU(N) generator matrices, $a(\mathbf{k})$ is a $\mathbf{k}$-dependent scalar, and $\mathbf{b}(\mathbf{k})$ is a $\mathbf{k}$-dependent vector of length

$N^2 - 1$. For example, the Bloch Hamiltonian corresponding to $\phi = 1/3$ is

$$\tilde{H}_{\phi=1/3}(\mathbf{k}) = \begin{pmatrix} -2\cos(-k_y) & -e^{ik_x} & -e^{-ik_x} \\ -e^{-ik_x} & -2\cos(2\pi/3 - k_y) & -e^{ik_x} \\ -e^{ik_x} & -e^{-ik_x} & -2\cos(4\pi/3 - k_y) \end{pmatrix}.$$

This may be expanded as in terms of SU(3) generators by setting $a(\mathbf{k}) = 0$,

$$b_1 = b_4 = b_6 = -\cos(k_x) \qquad b_2 = -b_5 = b_7 = \sin(k_x)$$
$$b_3 = -\frac{3}{2}\cos(k_y) + \frac{\sqrt{3}}{2}\sin(k_y) \qquad b_8 = -\frac{\sqrt{3}}{2}\cos(k_y) - \frac{\sqrt{3}}{2}\sin(k_y)$$

and identifying $\hat{\boldsymbol{\lambda}}$ as the vector of standard Gell-Mann matrices, which are given, for example, in Ref. [184]. For later use, we recall that the Gell-Mann matrices satisfy the property

$$\lambda_a \lambda_b = \frac{2}{3}\delta_{ab} + d_{abc}\lambda_c + i f_{abc}\lambda_c, \tag{2.32}$$

where d_{abc} and f_{abc} are (respectively) the totally symmetric and totally antisymmetric structure constants, which may also be found in Ref. [184]. These structure constants define three bilinears for two general eight-component vectors $\mathbf{u}$ and $\mathbf{v}$,

$$\mathbf{u}\cdot\mathbf{v} = u_i v_i, \qquad (\mathbf{u}\times\mathbf{v})_i = f_{ijk}u_j v_k, \qquad (\mathbf{u}*\mathbf{v})_i = \sqrt{3}d_{ijk}u_j v_k,$$

where the last of these is known as the star product [184].

We can use these algebraic relations to deduce an expression for the projector. By definition, the projector is Hermitian and has unit trace, so we can express it in terms of the (traceless) Gell-Mann matrices as

$$\hat{P}_{\mathbf{k}\alpha} = \frac{1}{3}\left[\hat{I} + \sqrt{3}\mathbf{n}_{\mathbf{k}\alpha}\cdot\hat{\boldsymbol{\lambda}}\right], \tag{2.33}$$

where the $\sqrt{3}$ is a normalisation constant. The symmetry of the set-up tells us that $\mathbf{n}_{\mathbf{k}\alpha}$ must depend somehow on $\mathbf{b}$. We now impose the projector property $\hat{P}^2_{\mathbf{k}\alpha} = \hat{P}_{\mathbf{k}\alpha}$ and find, using the identity in Eq. (2.32) and the symmetry of the structure constants,

$$\hat{P}^2_{\mathbf{k}\alpha} = \frac{1}{3}\left[\frac{1 + 2\mathbf{n}_{\mathbf{k}\alpha}\cdot\mathbf{n}_{\mathbf{k}\alpha}}{3}\hat{I} + \frac{2}{\sqrt{3}}\mathbf{n}_{\mathbf{k}\alpha}\cdot\hat{\boldsymbol{\lambda}} + \frac{1}{\sqrt{3}}(\mathbf{n}_{\mathbf{k}\alpha}*\mathbf{n}_{\mathbf{k}\alpha})\cdot\hat{\boldsymbol{\lambda}}\right],$$

which, for consistency, requires $\mathbf{n}_{\mathbf{k}\alpha}\cdot\mathbf{n}_{\mathbf{k}\alpha} = 1$ and $\mathbf{n}_{\mathbf{k}\alpha}*\mathbf{n}_{\mathbf{k}\alpha} = \mathbf{n}_{\mathbf{k}\alpha}$. We also require the projector

to commute with the Bloch Hamiltonian,

$$0 = \left[\hat{P}_{\mathbf{k}\alpha}, \tilde{H}(\mathbf{k})\right] = \frac{i}{\sqrt{3}} \left(\mathbf{n}_{\mathbf{k}\alpha} \times \mathbf{b}\right) \cdot \hat{\boldsymbol{\lambda}},$$

which enforces $\mathbf{n}_{\mathbf{k}\alpha} \times \mathbf{b} = 0$. This final condition tells us that $\mathbf{n}_{\mathbf{k}\alpha}$ must be a symmetric function of $\mathbf{b}$. The only symmetric vectors we can form from $\mathbf{b}$ are $\mathbf{b}$ itself and $\mathbf{b} * \mathbf{b}$, since $\mathbf{b} * \mathbf{b} * \mathbf{b}$ is proportional to $\mathbf{b}$. We therefore try

$$\mathbf{n}_{\mathbf{k}\alpha} \quad = \quad A_{\mathbf{k}\alpha}\mathbf{b} + B_{\mathbf{k}\alpha}\mathbf{b} * \mathbf{b}$$

and fix the coefficients $A_{\mathbf{k}\alpha}$ and $B_{\mathbf{k}\alpha}$ using the conditions $\mathbf{n}_{\mathbf{k}\alpha} \cdot \mathbf{n}_{\mathbf{k}\alpha} = 1$ and $\mathbf{n}_{\mathbf{k}\alpha} * \mathbf{n}_{\mathbf{k}\alpha} = \mathbf{n}_{\mathbf{k}\alpha}$. This yields [182] the three solutions

$$A_{\mathbf{k}\alpha} = \frac{2\cos\left(\theta_{\mathbf{k}} + \frac{2\pi}{3}\alpha\right)}{|\mathbf{b}(\mathbf{k})|\left[4\cos^2\left(\theta_{\mathbf{k}} + \frac{2\pi}{3}\alpha\right) - 1\right]}, \qquad B_{\mathbf{k}\alpha} = \frac{1}{|\mathbf{b}(\mathbf{k})|^2\left[4\cos^2\left(\theta_{\mathbf{k}} + \frac{2\pi}{3}\alpha\right) - 1\right]}$$

with

$$\theta_{\mathbf{k}} \quad = \quad \frac{1}{3}\arccos\left[\frac{\mathbf{b}(\mathbf{k}) \cdot \mathbf{b}(\mathbf{k}) * \mathbf{b}(\mathbf{k})}{|\mathbf{b}(\mathbf{k})|^3}\right],$$

in agreement with Eq. 2.6, and where the band index $\alpha = 0, 1, 2$. We can insert these projector expressions into Eq. 2.31 to obtain the Berry curvature, given previously in Eq. 2.7.

For $\phi = 1/4$ we extend the dimension of the Gell-Mann matrices to 4×4 and add the additional seven SU(4) generators, which are given, for example, in Ref. [185]. In terms of these, we can again write the Bloch Hamiltonian as $\tilde{H}(\mathbf{k}) = a(\mathbf{k})\hat{I} + \mathbf{b}(\mathbf{k}) \cdot \hat{\boldsymbol{\lambda}}$.

The SU(4) generators satisfy the relation

$$\lambda_i\lambda_j \quad = \quad \frac{1}{2}\delta_{ij} + d_{ijk}\lambda_k + if_{ijk}\lambda_k,$$

where the structure constants f_{ijk} and d_{ijk} are now augmented to include indices up to 15. The

new f_{ijk} may be found in Chapter 5 of Ref. [185], while we find the new d_{ijk} to be

$$d_{1,1,15} = d_{2,2,15} = d_{3,3,15} = d_{4,4,15} = d_{5,5,15} = d_{6,6,15} = d_{7,7,15} = d_{8,8,15} = \frac{1}{\sqrt{6}},$$
$$d_{9,9,15} = d_{10,10,15} = d_{11,11,15} = d_{12,12,15} = d_{13,13,15} = d_{14,14,15} = -\frac{1}{\sqrt{6}},$$
$$d_{1,1,8} = d_{2,2,8} = d_{3,3,8} = \frac{1}{\sqrt{3}}, \qquad d_{8,8,8} = d_{8,13,13} = d_{8,14,14} = -\frac{1}{\sqrt{3}}, \qquad d_{15,15,15} = -\frac{2}{\sqrt{6}},$$
$$d_{8,9,9} = d_{8,10,10} = d_{8,11,11} = d_{8,12,12} = \frac{1}{2\sqrt{3}}, \qquad d_{4,4,8} = d_{5,5,8} = d_{6,6,8} = d_{7,7,8} = -\frac{1}{2\sqrt{3}},$$
$$d_{1,4,6} = d_{1,5,7} = d_{1,9,11} = d_{1,10,12} = d_{2,5,6} = d_{2,10,11} = d_{3,4,4} = d_{3,5,5} = d_{3,9,9} = d_{3,10,10} = ...$$
$$... = d_{4,9,13} = d_{4,10,14} = d_{5,10,13} = d_{6,11,13} = d_{6,12,14} = d_{7,12,13} = \frac{1}{2},$$
$$d_{2,4,7} = d_{2,9,12} = d_{3,6,6} = d_{3,7,7} = d_{3,11,11} = d_{3,12,12} = d_{5,9,14} = d_{7,11,14} = -\frac{1}{2}.$$

We define the same three bilinears as before, but rescale the star product to read $(\mathbf{u} * \mathbf{v})_i = \sqrt{3/2} d_{ijk} u_j v_k$. The new SU(4) projectors are of the form

$$\hat{P}_{\mathbf{k}\alpha} = \frac{1}{4}\left[\hat{I} + \sqrt{6}\mathbf{n}_{\mathbf{k}\alpha} \cdot \hat{\boldsymbol{\lambda}}\right],$$

and must satisfy the conditions

$$\mathbf{n}_{\mathbf{k}\alpha} \cdot \mathbf{n}_{\mathbf{k}\alpha} = 1, \qquad \mathbf{n}_{\mathbf{k}\alpha} * \mathbf{n}_{\mathbf{k}\alpha} = \mathbf{n}_{\mathbf{k}\alpha}, \qquad \mathbf{n}_{\mathbf{k}\alpha} \times \mathbf{b} = 0,$$

as before. This time the three vectors $\{\mathbf{b}, \mathbf{b}*\mathbf{b}, \mathbf{b}*\mathbf{b}*\mathbf{b}\}$ are linearly independent, but $\mathbf{b}*\mathbf{b}*\mathbf{b}*\mathbf{b}$ lies within the subspace, so we try

$$\mathbf{n}_{\mathbf{k}\alpha} = A_{\mathbf{k}\alpha}\mathbf{b} + B_{\mathbf{k}\alpha}\mathbf{b} * \mathbf{b} + C_{\mathbf{k}\alpha}\mathbf{b} * \mathbf{b} * \mathbf{b}.$$

There are two pairs of solutions that satisfy the conditions $\mathbf{n}_{\mathbf{k}\alpha} \cdot \mathbf{n}_{\mathbf{k}\alpha} = 1$ and $\mathbf{n}_{\mathbf{k}\alpha} * \mathbf{n}_{\mathbf{k}\alpha} = \mathbf{n}_{\mathbf{k}\alpha}$, which are

$$A_{\mathbf{k}\alpha} = \pm\tfrac{1}{\sqrt{6}\sqrt{4+\sqrt{2\phi_{\mathbf{k}}}}}, \qquad B_{\mathbf{k}\alpha} = \tfrac{1}{3\sqrt{2\phi_{\mathbf{k}}}}, \qquad C = \pm\tfrac{1}{3\sqrt{3\phi_{\mathbf{k}}}\sqrt{4+\sqrt{2\phi_{\mathbf{k}}}}}$$
$$A_{\mathbf{k}\alpha} = \pm\tfrac{1}{\sqrt{6}\sqrt{4-\sqrt{2\phi_{\mathbf{k}}}}}, \qquad B_{\mathbf{k}\alpha} = -\tfrac{1}{3\sqrt{2\phi_{\mathbf{k}}}}, \qquad C = \mp\tfrac{1}{3\sqrt{3\phi_{\mathbf{k}}}\sqrt{4-\sqrt{2\phi_{\mathbf{k}}}}},$$

with $\phi_{\mathbf{k}} = 6+\cos(4k_x)+\cos(4k_y) = \mathbf{b}\cdot(\mathbf{b}*\mathbf{b}*\mathbf{b})/6$. After inserting these projector expressions into Eq. 2.31 we obtain the Berry curvature given in Eq. 2.8.

2.C Further Details on the WKB Approach

2.C.1 Derivation of WKB Connection Formulae and Bandwidth

In this appendix we fill in some of the details of the WKB approach outlined in Sec. 2.3. We write the WKB solution in the classically forbidden region as

$$\psi_{l,r}^{\pm} = (\sinh\tilde{p})^{-1/2} \exp\left[\pm\phi^{-1}\int_{\beta_{l,r}}^{x}\tilde{p}(t)\mathrm{d}t\right], \tag{2.34}$$

with $\beta_r = \beta$, $\beta_l = -\beta$ as in Eq. (2.13) and $\tilde{p}(x)$ as in Eq. (2.12). We wish to connect this WKB solution to the exact solution near the second order turning point. To this end, we define

$$\begin{aligned} E &= -4 + \tilde{E} \qquad & b &= 4\pi^2 \\ \xi \equiv \xi(x) &= \left(4\phi^{-2}b\right)^{1/4} x \qquad & a &= -(4b)^{-1/2}\phi^{-1}\tilde{E} \approx -\frac{1}{2} \end{aligned}$$

and expand Harper's equation for small x to find

$$\frac{\mathrm{d}^2\psi}{\mathrm{d}\xi^2} - \left(\frac{1}{4}\xi^2 + a\right)\psi(\xi) \;=\; 0.$$

This is the parabolic cylinder function equation, with solutions $U(a,\xi)$ and $V(a,\xi)$ (in the notation of [156]), which have the following asymptotic forms as $\xi \to \infty$

$$U(a,\xi) \sim e^{-\frac{1}{4}\xi^2}\xi^{-a-\frac{1}{2}}, \qquad V(a,\xi) \sim \sqrt{\frac{2}{\pi}}e^{\frac{1}{4}\xi^2}\xi^{a-\frac{1}{2}}. \tag{2.35}$$

The expressions for $\xi \to -\infty$ are found using the parabolic cylinder function connection formulae [156], which may be written as

$$\begin{pmatrix} U(a,-\xi) \\ V(a,-\xi) \end{pmatrix} = \begin{pmatrix} -\sin(\pi a) & \frac{\pi}{\Gamma\left(\frac{1}{2}+a\right)} \\ \frac{\cos(\pi a)}{\Gamma\left(\frac{1}{2}-a\right)} & \sin(\pi a) \end{pmatrix} \begin{pmatrix} U(a,\xi) \\ V(a,\xi) \end{pmatrix}.$$

This transformation matrix is its own inverse (which can be shown using Euler's reflection formula for Gamma functions).

To connect these parabolic cylinder functions to the WKB solution in Eq. (2.34), we expand the WKB integral for small x to find

$$\phi^{-1}\int_{\beta_r}^{x}\tilde{p}(t)\mathrm{d}t = \phi^{-1}\int_{\beta_r}^{x}\sqrt{bt^2-\tilde{E}}\mathrm{d}t = \frac{\xi^2}{4} + \frac{a}{2} + a\ln\xi - \frac{a}{2}\ln(-a).$$

This leads to the following asymptotic forms for the WKB wavefunctions

$$\psi_{l,r}^{\pm} = \left(\frac{4|a|}{\tilde{E}}\right)^{\frac{1}{4}} \left|\frac{a}{e}\right|^{\mp\frac{a}{2}} e^{\pm\frac{1}{4}\xi^2} |\xi|^{-\frac{1}{2}\pm a}.$$

Comparing these asymptotic expressions to the asymptotic forms of the parabolic cylinder functions in Eq. (2.35), we arrive at the connection formulae between wavefunctions to the left and to the right of the turning point,

$$\begin{pmatrix} \psi_r^- \\ \psi_r^+ \end{pmatrix} = \left(\frac{4|a|}{\tilde{E}}\right)^{\frac{1}{4}} \begin{pmatrix} |a/e|^{\frac{a}{2}} U(a,\xi) \\ |a/e|^{-\frac{a}{2}} \sqrt{\tfrac{\pi}{2}} V(a,\xi) \end{pmatrix}$$

$$\to \left(\frac{4|a|}{\tilde{E}}\right)^{\frac{1}{4}} \begin{pmatrix} |a/e|^{\frac{a}{2}} U(a,-\xi) \\ |a/e|^{-\frac{a}{2}} \sqrt{\tfrac{\pi}{2}} V(a,-\xi) \end{pmatrix} = \begin{pmatrix} -\sin(\pi a) & \frac{|a/e|^a \sqrt{2\pi}}{\Gamma\left(\frac{1}{2}+a\right)} \\ \frac{|a/e|^{-a}\cos(\pi a)}{\Gamma\left(\frac{1}{2}-a\right)} \sqrt{\frac{\pi}{2}} & \sin(\pi a) \end{pmatrix} \begin{pmatrix} \psi_l^- \\ \psi_l^+ \end{pmatrix}$$

The transformation matrix is again self-inverse.

Now we propagate the WKB wavefunction immediately to the right of the first turning point ($\psi_r^{\pm}$) until we are immediately to the left of the next turning point ($\psi_{2l}^{\pm}$), defining the $\pm$ sign in the wavefunction labels to indicate a solution which either grows or decays away from the nearest turning point. We find that

$$\begin{pmatrix} \psi_{2l}^- \\ \psi_{2l}^+ \end{pmatrix} = \begin{pmatrix} e^{-\sigma} \left|\frac{a}{e}\right|^{-a} \cos^2(\pi a) \frac{\Gamma\left(\frac{1}{2}+a\right)}{\sqrt{2\pi}} & e^{-\sigma}\sin(\pi a) \\ -e^{\sigma}\sin(\pi a) & e^{\sigma}\left|\frac{a}{e}\right|^{a} \frac{\sqrt{2\pi}}{\Gamma\left(\frac{1}{2}+a\right)} \end{pmatrix} \begin{pmatrix} \psi_l^- \\ \psi_l^+ \end{pmatrix}.$$

This is our final transformation matrix between the WKB wavefunction to the left of the turning point near $x = 0$ and the same wavefunction to the left of the turning point near $x = N$.

We are now interested in finding a Bloch periodic solution to the problem. Writing the wavefunction in each of the two regions as

$$\Psi(x) = A\psi_l^-(x) + B\psi_l^+(x), \qquad \Psi(x) = C\psi_{2l}^-(x) + Dg\psi_{2l}^-(x),$$

we see that the coefficients are related by,

$$\begin{pmatrix} C \\ D \end{pmatrix} = \begin{pmatrix} e^{\sigma}\left|\frac{a}{e}\right|^{a} \frac{\sqrt{2\pi}}{\Gamma\left(\frac{1}{2}+a\right)} & e^{\sigma}\sin(\pi a) \\ -e^{-\sigma}\sin(\pi a) & e^{-\sigma}\left|\frac{a}{e}\right|^{-a}\cos^2(\pi a)\frac{\Gamma\left(\frac{1}{2}+a\right)}{\sqrt{2\pi}} \end{pmatrix} \begin{pmatrix} A \\ B \end{pmatrix} \stackrel{!}{=} e^{ik_x N} \begin{pmatrix} A \\ B \end{pmatrix}.$$

This leads to the determinant equation

$$\left[e^{\sigma}\left|\frac{a}{e}\right|^{a}\frac{\sqrt{2\pi}}{\Gamma\left(\frac{1}{2}+a\right)}+e^{-\sigma}\left|\frac{a}{e}\right|^{-a}\cos^{2}(\pi a)\frac{\Gamma\left(\frac{1}{2}+a\right)}{\sqrt{2\pi}}\right] \;=\; 2\cos(k_{x}N).$$

which in the limit that N is large (and $a \approx \frac{1}{2}$) can be rearranged to give

$$E \;=\; \frac{2\pi}{N}-\frac{4}{N}\sqrt{\frac{\pi}{e}}e^{-\sigma}\cos(k_{x}N).$$

We can also read off the relationship between the coefficients, $B = e^{-\sigma}e^{-ik_{x}N}A$, from which all other coefficients follow (up to normalisation).

2.C.2 Derivation of WKB Berry Curvature

The Berry curvature calculation is much more involved than the bandwidth calculation. Beginning with the wavefunction as written in Equation 2.15, we must first find the normalisation constant A. The leading contribution to this comes from the parabolic cylinder part of the wavefunction (the first and third sections of the wavefunction).

Noting that the third part of the piecewise wavefunction may be mapped onto the first through the substitution $x' = x - N$, we see that the integral of the square modulus of the parabolic cylinder parts of the wavefunction may be written

$$\int_{-x_{c}}^{x_{c}}|u_{1}|^{2}\mathrm{d}x=\int_{-x_{c}}^{x_{c}}\mathrm{d}x|A|^{2}\left(\frac{N}{\pi}\right)^{\frac{1}{2}}\left[(2e)^{\frac{1}{2}}\left(1-\ln 2\left(\frac{1}{2}+a\right)\right)U^{2}+\sqrt{2\pi}e^{-\sigma}UV\cos(k_{x}N)+O(e^{-2\sigma})\right],$$

where we have set $k_y = 0$ and $x_c = \alpha\beta N$. We may ignore the $|V|^2$ term as its prefactor is $O(e^{-2\sigma})$ and the integral is not exponentially large in sigma. We have also used the fact that U and V are real. We carry out the integral order by order in U and V using

$$U\left(a,\xi\right) \;=\; U\left(-\frac{1}{2},\xi\right)+\left(a+\frac{1}{2}\right)\left.\frac{\partial U\left(a,\xi\right)}{\partial a}\right|_{a=-\frac{1}{2}}+\ldots$$

and a similar expression for $V(a, \xi)$, where the $a = -\frac{1}{2}$ wavefunctions are given by

$$U\left(-\frac{1}{2},\xi\right)=e^{-\frac{\xi^{2}}{4}},\qquad V\left(-\frac{1}{2},\xi\right)=\left(\frac{2}{\sqrt{\pi}}\right)e^{\frac{\xi^{2}}{4}}F\left(\frac{\xi}{\sqrt{2}}\right)$$

with $F(x)$ Dawson's integral [156]. To zeroth order, the cross term in the normalisation integral vanishes due to the respective even and odd symmetry of U and V. In terms of ξ, the limits of

integration for the one remaining integral are

$$-\sqrt{2}\alpha\left(1-\frac{1}{\sqrt{\pi e}}e^{-\sigma}\cos(k_xN)\right)\leq\quad\xi\quad\leq\sqrt{2}\alpha\left(1-\frac{1}{\sqrt{\pi e}}e^{-\sigma}\cos(k_xN)\right),$$

where we have used the large N expression for β. The integral we are interested in is then

$$\int_{-\alpha\beta N}^{\alpha\beta N}|U|^2\mathrm{d}x\quad=\quad\sqrt{\frac{N}{2}}\mathrm{Erf}(\alpha)-\frac{\alpha e^{-\alpha^2}}{\pi}\sqrt{\frac{2N}{e}}e^{-\sigma}\cos(qN).$$

In fact, only the first term above is relevant, and all successive terms (from the Taylor expansion in U and V) are also negligible in the large N limit. The leading expression to the normalisation integral is then

$$1=N|A|^2\sqrt{\frac{e}{\pi}}\mathrm{Erf}(\alpha)+O\left(\frac{1}{\sqrt{N}}\right)+O\left(e^{-\sigma}\right). \tag{2.36}$$

The Berry curvature itself consists of a constant part (which fixes the Chern number at one) with an overlaid sinusoidal **k**-dependent contribution. The constant contribution comes from the parabolic cylinder part of the wavefunction. Defining this part of the wavefunction as u_{PC}, we find the leading contribution gives the same integral as above, but with additional prefactors,

$$\partial_{k_y}A_{k_x,\mathrm{PC}}=\partial_{k_y}\left\langle u_{\mathrm{PC}}\right|\partial_{k_x}\left|u_{\mathrm{PC}}\right\rangle=\frac{iN^2|A|^2}{2\pi}\sqrt{\frac{e}{\pi}}\mathrm{Erf}(\alpha)=\frac{iN}{2\pi}, \tag{2.37}$$

where in the final expression we have substituted for $|A|$. For this part of the calculation, we have reinstated the k_y dependence from Eq. (2.15) in order to differentiate.

The leading **k**-dependent term comes from the WKB part of the wavefunction, $\partial_{k_x}A_{k_y,\mathrm{WKB}}$. We approximate the WKB wavefunctions using a Fourier cosine series (defining $y=x/N$),

$$\psi^{\pm}_{\mathrm{WKB}}(y)=\frac{1}{\sqrt{\sinh\tilde{p}(y)}}\exp\left[\pm N\int_{\beta}^{y}\tilde{p}(t)\,\mathrm{d}t\right]\approx P\exp\left[\pm\frac{\sigma}{2}\mp\sum_{j\,\mathrm{odd}}\frac{\rho_j}{2}\cos\left(\frac{\pi(y-\beta)}{1-2\beta}j\right)\right],$$

where the coefficients ρ_j are given by

$$\rho_j\quad=\quad\frac{2}{1-2\beta}\int_{\beta}^{1-\beta}\cos\left(\frac{\pi\,(y-\beta)\,j}{1-2\beta}\right)\mathrm{d}y\,2N\int_{y}^{1/2}\cosh^{-1}\left[-\frac{E}{2}-\cos(2\pi t)\right]\mathrm{d}t,$$

although their exact values are not relevant as the Fourier series will be resummed in our final answer. The prefactor P is an average of the sinh term in the WKB wavefunction,

$$P=\left\langle\frac{1}{\sqrt{\sinh\tilde{p}}}\right\rangle_{\mathrm{WKB}}=\left\langle\frac{1}{\sqrt{\left(-\frac{E}{2}-\cos(2\pi x)\right)^2-1}}\right\rangle_{\mathrm{WKB}},$$

where the average is taken over the range $\alpha\beta N \leq x \leq 1-\alpha\beta N$. Restoring the k_y dependence, and using the full wavefunction expression from Eq. 2.15, we find that the relevant term in the Berry curvature expression is

$$\begin{aligned}\langle u_{\mathrm{WKB}}|\partial_{k_y}|u_{\mathrm{WKB}}\rangle &= \frac{N|A|^2P^2e^{-\sigma}}{4\pi}\int_{\frac{\pi(\alpha-1)\beta}{1-2\beta}}^{\frac{\pi(1-(\alpha+1)\beta)}{1-2\beta}}\left[\sum_{j\ \mathrm{odd}} j\rho_j\sin\left(jy'\right)\right] \\ &\quad \left[-2\sinh\left(\sum_{j\ \mathrm{odd}}\rho_j\cos\left(jy'\right)\right)+2i\sin(k_xN)\right]\mathrm{d}y',\end{aligned}$$

where we have defined $y' = \pi(y-\beta-k_y/(2\pi))/(1-2\beta)$. We only require the k_x-dependent term, given by

$$A_{k_y} \approx \frac{iN|A|^2P^2e^{-\sigma}}{\pi}\sin(k_xN)\left[\rho_1+\rho_3+\rho_5+\ldots\right] \approx \frac{iP^2e^{-\sigma}\sigma}{\sqrt{\pi e}\mathrm{Erf}(\alpha)}\sin(k_xN),$$

where we have dropped all subleading terms and noted that $\sigma = \sum_{j\ \mathrm{odd}}\rho_j$. Finally, we can differentiate to find the nonzero Berry curvature contribution

$$\partial_{k_x}A_{k_y} = \frac{NP^2e^{-\sigma}\sigma}{\sqrt{\pi e}\mathrm{Erf}(\alpha)}\cos(k_xN),$$

which gives the total Berry curvature

$$F = \frac{N}{2\pi}+\frac{NP^2e^{-\sigma}\sigma}{\sqrt{\pi e}\mathrm{Erf}(\alpha)}\cos(k_xN).$$

Changing the cutoff α has very little effect on the second term, provided $\alpha \gtrsim 2$, and we find that contributions from other parts of the wavefunction are smaller than those given above. Since k_y only acts as a translation, the k_y-dependence of the Berry curvature is not captured by this WKB approach. Instead, this must be reinstated by hand as discussed in the main text.

3. Perturbative Approach to the Hofstadter Model at General Flux

In this chapter, we extend the perturbation theory of the previous section to general magnetic flux fractions. This will allow us to explore the LL-like lines that exist throughout the Hofstadter butterfly spectrum. We begin by discussing the band structure that arises at a general $\phi = p/q$ in Sec. 3.1, noting the important qualitative differences compared to the case of weak field. We generalise our perturbative approach to the single-particle states in Sec. 3.2, before considering the many-particle problem in Sec. 3.3. We give the main results of this chapter, a set of multicomponent pseudopotential matrices, in Sec. 3.4, before discussing some extensions and applications in Secs. 3.5–3.6.

3.1 Band Structure for $\phi = P/Q \pm M/N$

The band structure is significantly more complicated when we are not in the small-flux regime. In general, we wish to consider a value of $\phi = p/q$ that is close (in magnitude) to a fraction with a small denominator. To this end, we write the simple fraction as P/Q with P and Q coprime, and perturb around this point by adding or subtracting a small amount of flux, δ. For the most part we will choose $\delta = 1/N$ for simplicity, but this can be extended to $\delta = M/N$ without loss of generality. To relate this general discussion to the small flux case considered in the previous chapter, it is simplest to choose $P = 0$, $Q = 1$ in all that follows.

The first complication arises when we try to identify the size of the magnetic unit cell. At $\phi = M/N$ this was fixed at $N \times 1$ plaquettes, but in general the cell length is given by the denominator of ϕ, which may be affected by cancellation between P, Q and N. With Q prime, there are three possible cancelled forms for ϕ,

$$\phi \equiv \frac{p}{q} = \frac{P}{Q} + \frac{1}{N} = \begin{cases} \frac{PN+Q}{QN} & (a) \\ \frac{PN/Q+1}{N} & (b) \\ \frac{(PN+Q)/Q^2}{N/Q} & (c) \end{cases} \tag{3.1}$$

which arise when

$$\begin{array}{lllllllll} (a) & N & \mathrm{mod}\ Q & \neq & 0 & & & & \\ (b) & N & \mathrm{mod}\ Q & = & 0 & \text{and} & (PN+Q) & \mathrm{mod}\ Q^2 & \neq & 0 \\ (c) & N & \mathrm{mod}\ Q & = & 0 & \text{and} & (PN+Q) & \mathrm{mod}\ Q^2 & = & 0. \end{array}$$

Although our approach does not require Q to be prime, this choice is varied enough to discuss the main complications in the band structure, so we will assume it to be the case from now on. We prove that the cancelled fractions given above are the only possibilities for Q prime, and consider the additional cancellation possibilities with Q not prime and $M \neq 1$ in Appendix C of Ref. [1].

From Eq. (3.1), we see that the unit cell in this case may be QN, N or N/Q sites in length. This integer also gives the number of sites within each unit cell and the number of bands we should observe in total. Although this number can take three different forms, we will argue that the physics remains essentially the same in each case. To motivate this, we will first describe the band structure we find from exact diagonalisation, and then explain it according to our perturbation theory.

In Figure 3.1, we show the band structure and integrated density of states for $\phi = 1/3$ and two nearby fractions, $\phi = 11/30$ (corresponding to $\delta = 1/30$) and $\phi = 4/11$ (corresponding to $\delta = 1/33$). We notice that the three-band structure from the 'pure' $\phi = 1/3$ case is still apparent when $\phi \approx 1/3$: even though there are now q bands in total, these group themselves into three energy regions. In general, near to a flux fraction P/Q, the q band solutions arrange themselves into Q energy regions that correspond to the Q original bands of the pure fraction. This reproduction becomes more accurate as p/q gets closer to P/Q. Since the q band solutions are generally close together in energy, we will refer to them as 'mini-bands' as we did in the previous chapter. We refer to the Q large groups of mini-bands as 'bands' to emphasise that these are the energy structures that derive from the pure P/Q case. We remark that the lowest band is formed of p mini-bands if $p < q/2$ and is formed of $(q-p)$ mini-bands if $p > q/2$.

There is an additional, hidden structure to the energy levels for general $\phi \approx P/Q$: some of the mini-bands are separated by exponentially small energy gaps ($\Delta E \sim e^{-\alpha N}$ for some α) and others are separated by algebraically small energy gaps ($\Delta E \sim 1/N$). For $\phi = 11/30$ shown in Figure 3.1, the three lowest mini-bands are exponentially close in energy but are separated algebraically from the fourth lowest mini-band. For the case with $\phi = 4/11$ all of the gaps are algebraically small.

We group together all of the mini-bands that are exponentially close in energy to form a

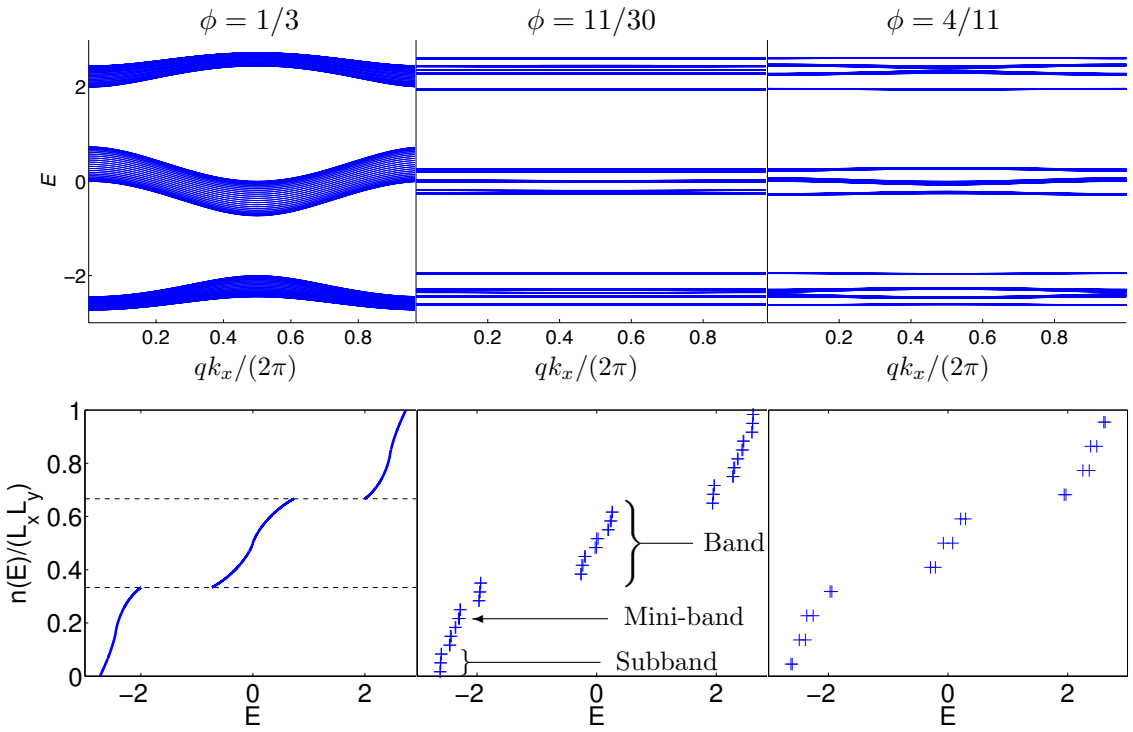

Figure 3.1: Energy bands (top) and integrated density of states per unit area (bottom) for $\phi = 1/3$, $\phi = 1/3 + 1/30 \equiv 11/30$, and $\phi = 1/3 + 1/33 \equiv 4/11$. *Top*: The energy spectra are plotted against k_x for fifty equally-spaced values of k_y for each band. The spectra for the latter two field values show a clear energy gap above the lowest subband. *Bottom*: The integrated density of states for the three complete bands is shown for $\phi = 1/3$, while the individual mini-bands are plotted for $\phi \approx 1/3$ with bandwidth given by the x-error bars. The band structure of the 'pure' $\phi = 1/3$ case carries over to the $\phi \approx 1/3$ cases: the mini-bands arrange themselves into three bands and several subbands.

subband. We will find that these subbands are similar to the set of M mini-bands we grouped together in the previous chapter, and are closely related to the LLs of the continuum. In this way, it is these subbands that form harmonic oscillator energy levels, and it is these that are responsible for the LL-like lines that emanate from the various points of the butterfly spectrum (see, for example, the lines emanating from $(0.5, -2\sqrt{2})$ in Fig. 2.1a). As N is increased, more and more subbands become apparent in the band structure.

The number of mini-bands in each subband depends on the cancellation of the fraction p/q and is given in general by $n_s = qQM/N$. If Q is prime and $M = 1$, n_s takes the values $\{Q^2, Q, 1\}$ for cases (a), (b) and (c) in Eq. (3.1) respectively. In general, n_s must lie between $1 \leq n_s \leq Q^2$ [1]. For the two cases shown in Figure 3.1, we see that $n_s = 3$ for $\phi = 11/30$ and $n_s = 1$ for $\phi = 4/11$. Crucially, we find that the total Chern number of all of the mini-bands in a subband is equal to Q, irrespective of the number of mini-bands that comprise it. This can be verified from the TKNN equation: inserting p and q from Eq. (3.1) into Eq. (2.3) and considering the lowest n_s mini-bands, one obtains the solution $(t, s) = (Q, -P)$ in each case. In this way, the subbands near a flux fraction $\phi = P/Q$ act like Q copies of a Landau level.

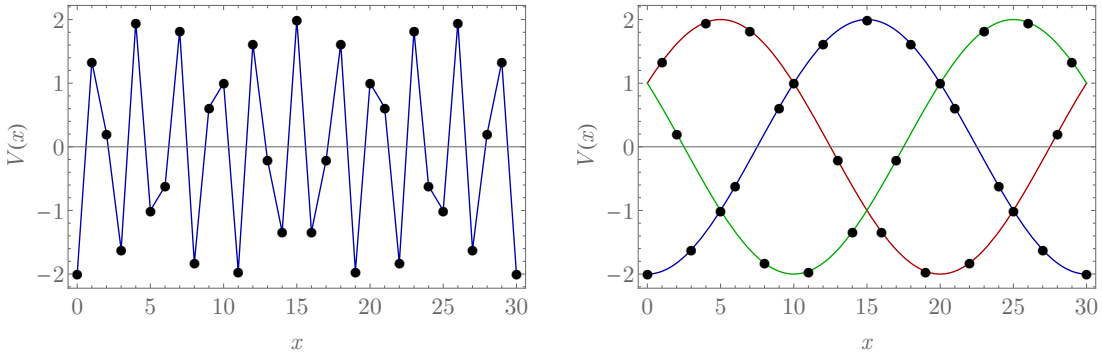

(a) (b)

Figure 3.2: (a) Rapidly oscillating cosine potential for $\phi = 1/3 + 1/30 = 11/30$. The eleven lattice sites in the troughs form the eleven mini-bands of the lowest band. (b) Three effective potentials for $\phi = 1/3 + 1/30 = 11/30$. The three troughs of the effective potentials give rise to the three mini-bands which form the lowest subband. (See band structure in Fig. 3.1).

We will now explain these observations using our perturbative method, and in doing so justify why the subbands are the useful structures to consider in a real system. We recall that we can interpret Harper's equation as the Schrödinger equation with a cosine potential,

$$-\psi_{x-1} - \psi_{x+1} - 2\cos\left(\frac{2\pi px}{q} - k_y\right)\psi_x = E\psi_x.$$

This potential has p periods fitted between $x = 0$ and $x = q$, which are evaluated at lattice points (integer values of x). The lattice effectively 'samples' the cosine potential, and if $p < q/2$ we can resolve all p periods, while if $p > q/2$ we can only resolve $q - p$ effective periods. The lattice sites at the p or $(q - p)$ resolved troughs of the cosine potential form the p or $(q - p)$ mini-bands that comprise the lowest band (see Figure 3.2).

If we substitute $\phi = P/Q + M/N$, the cosine potential becomes

$$V(x) = -2\cos\left[\left(\frac{2\pi xM}{N} + \frac{2\pi Px}{Q}\right) - k_y\right]. \tag{3.2}$$

Written like this, the potential looks like a single cosine curve with period N/M but with an additional offset $2\pi Px/Q$. This offset takes Q different values modulo 2π (depending on $(x \mod Q)$), and so in total there will be Q offset cosine potentials which we call *effective potentials*, each lying on a different sublattice. These are entirely consistent with the single rapidly oscillating potential that comes from considering $\phi = p/q$, as shown in Figure 3.2.

The subbands are formed from the states that lie in the troughs of the effective potentials. As the troughs are separated by $N/(MQ)$, but the length of the unit cell is given by q, the number of troughs per unit cell varies and is given by $n_s = qQM/N$, as stated above.

When we carry out perturbation theory, we will expand about the troughs of the effective potentials and, as in the previous chapter, we will obtain a ladder of harmonic oscillator states with leading energy separation $O(1/N)$. However, we may now choose to expand about a trough from any of the Q effective potentials: we will find that the different effective potentials lead to the same energy perturbation series but different wavefunction perturbation series.

This is in contrast to the small flux case with $\phi = M/N$, where we found that expanding about the M troughs led to the *same* wavefunction perturbation series. Indeed, this is a general feature: replacing $\delta = 1/N \to M/N$ leads to more troughs per unit cell corresponding to the same effective potential, and so this replacement does not introduce distinct perturbed wavefunctions. The number of distinct perturbation series is always given by Q, the number of effective potentials or sublattices. This will be illustrated when we carry out the perturbation theory explicitly in Section 3.2.

Overall, we will obtain a ladder of states for each effective potential trough in a unit cell, and will group together states that correspond to the same energy to form a subband. An exact solution would show an exponentially small energy splitting between equivalent rungs due to the tunnelling effects that we neglect. Ignoring these is a good approximation in most cases where a finite temperature or the interaction strength would easily overcome the exponentially small splitting (and render it unresolvable).

Since we can only resolve subbands, these are the useful structures in the energy spectrum and should be considered as a whole. We find numerically that the total bandwidth and Berry curvature (defined as the trace of the Berry matrix) of the subband again decay exponentially with M/N, and that the total Chern number of the subband is given by Q. We justify the Chern number and Berry curvature in Appendix 3.D, and expect the band flatness can be verified analytically using a generalisation of the WKB approach discussed in Sec. 2.3.

Finally, we note that for a given total system size the number of **k**-states in a subband is given by the same expression, no matter what size the unit cell is and no matter how many mini-bands the subband consists of. If the unit cell is extended so that there are more mini-bands, the Brillouin zone is correspondingly reduced in the k_x-direction (and vice versa). These effects cancel out so that the number of **k**-states in each subband is always QL_xL_yM/N where L_xL_y is the area of the system. We should think of this as a mapping to Q copies of a Landau level with magnetic field $B = 2\pi M/N$, which are then each individually perturbed by the lattice.

3.2 Perturbative Approach for $\phi = P/Q \pm M/N$

3.2.1 Preliminary Algebra and Definitions

We begin this section by carrying out some preliminary algebra on the Harper equation, before returning to our perturbative approach in subsection 3.2.2. We will find that the perturbed wavefunctions may still be expressed in terms of LLs, but that the amplitudes and precise perturbation series now oscillate from site to site with period Q, as originally suggested in Ref. [102].

We recall that there are Q possible offsets to the cosine potential $V(x)$ in Harper's equation (3.2), and so the equation itself can take Q different forms. The form it takes depends on three variables: the lattice index modulo Q (which affects the offset term $2\pi Px/Q$ in the cosine potential); the value of k_y (which translates the effective cosine potentials); and the trough that we are expanding about, which we will choose by shifting x by a multiple of $N/(MQ)$.

To keep track of these contributions, we first note that for a given $0 \leq k_y < 2\pi$, the troughs will be located at

$$x = \frac{k_y N}{2\pi M} + \frac{sN}{QM}, \tag{3.3}$$

where s is an integer that is constrained so that x lies within the unit cell $0 \leq x < q$. (Recall that the unit cell size is determined by q which depends on the cancellation between N, M, P and Q.) To expand about a given trough, we choose a k_y and s and let

$$x = \frac{k_y N}{2\pi M} + \frac{sN}{QM} + x',$$

so that x' is small.

With this substitution we may rewrite the cosine potential in Eq. (3.2) as

$$V(x) \;=\; -2\cos\left[\frac{2\pi}{Q}\left(Px+s\right) + \frac{2\pi M x'}{N}\right].$$

We have not substituted for the first x, since in this instance we are interested in its value modulo Q. Defining $\lambda = x \mod Q$, the cosine potential for the λth sublattice (all sites with indices satisfying $x \mod Q = \lambda$) is then

$$V(x) \;=\; -2\cos\left[\frac{2\pi}{Q}\left(P\lambda+s\right) + \frac{2\pi M x'}{N}\right].$$

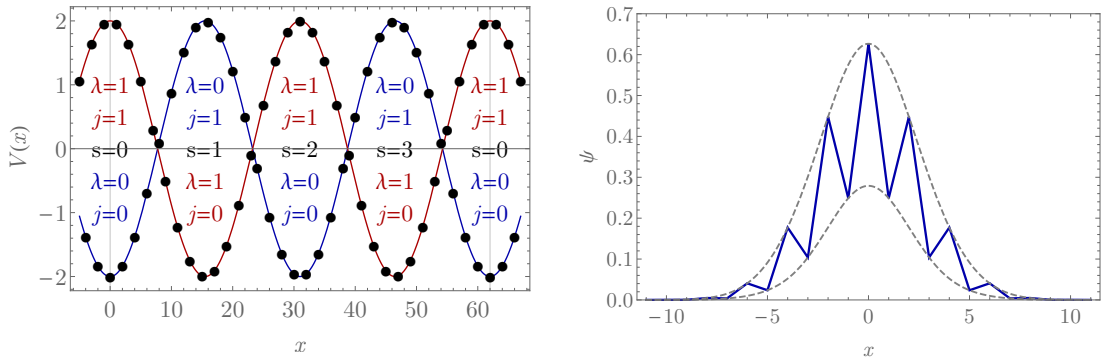

(a) (b)

Figure 3.3: (a) Effective potentials for $\phi = 1/2 + 1/31 = 33/62$, illustrating the values of s, j and λ for each sublattice in each trough. (b) First order perturbative wavefunction plotted near to the origin for $\phi = 33/62$. The grey dashed lines indicate the continuum functions $A_j\psi^j(x)$.

We see that the form the potential takes depends only on the integer $j(\lambda, s) = (P\lambda + s) \mod Q$, so that no matter what size the unit cell is, there are always Q different forms that the potential in Harper's equation may take. We illustrate the values that s, λ and j may take for the case $\phi = 1/2 + 1/31 = 33/62$ in Fig. 3.3a.

To proceed, we choose a trough and obtain a discrete equation that links together sites on a single sublattice only. We achieve this by writing out Harper equations for several neighbouring lattice sites, and algebraically eliminating amplitudes $\psi_{x'}$ on all but one of the sublattices. For example, let us consider $\phi = 1/2 + 1/N$ and choose the trough at $s = 0$. On the even sublattice ($\lambda = 0$), the Harper equation for x' is

$$-\psi^1_{x'-1} - \psi^1_{x'+1} - 2\cos\left(\frac{2\pi x'}{N}\right)\psi^0_{x'} = E\psi^0_{x'}, \tag{3.4}$$

where the superscripts give the value of $j(\lambda, s)$ on each site.[1] Correspondingly, the Harper equation for $(x' + 1)$ is

$$-\psi^0_{x'} - \psi^0_{x'+2} + 2\cos\left(\frac{2\pi(x'+1)}{N}\right)\psi^1_{x'+1} = E\psi^1_{x'+1},$$

where we note that the sign has changed in front of the cosine term because $(x' + 1)$ lies on the opposite sublattice to x'. If we also write down the Harper equation for $(x' - 1)$ then we can eliminate $\psi^1_{x'-1}$ and $\psi^1_{x'+1}$ to obtain

$$\frac{\psi^0_{x'-2} + \psi^0_{x'}}{E - 2\cos\left(\frac{2\pi(x'-1)}{N}\right)} + \frac{\psi^0_{x'+2} + \psi^0_{x'}}{E - 2\cos\left(\frac{2\pi(x'+1)}{N}\right)} = \left[E + 2\cos\left(\frac{2\pi x'}{N}\right)\right]\psi^0_{x'},$$

[1] In this case, the value of $j(\lambda, s) = j(\lambda, 0)$ just gives the sublattice parity (which could be read off from the value of x), but we introduce the superscript here for comparison with later cases when $s \neq 0$.

which is written entirely in terms of the even sublattice, corresponding to $j(\lambda, s) = 0$. We can obtain a similar equation for the odd sublattice by setting $\lambda = 1$ in the Harper equation for x'. Note that if we move to the trough located at $s = 1$, the equations for the even and odd lattices interchange because the corresponding values of $j(\lambda, s)$ interchange.

For general P/Q we obtain a discrete difference equation for each of the Q different sublattices. The equations near to other troughs and for different values of k_y can be found by choosing an appropriate s and k_y and then changing the offset of x' according to Eq. (3.3). However, there will only ever be Q distinct equations corresponding to the Q possible values of j. We might worry that the variable x' is not necessarily an integer, but this is allowed within our approximation: the lattice discreteness means that there is a different wavefunction on each sublattice, but within each sublattice the true wavefunctions differ from their continuum forms by only exponentially small factors.

If we had chosen $\phi = P/Q - 1/N$ (with a negative sign) instead, then the troughs would move to the left as we increase k_y rather than to the right. However, we can obtain the same discrete difference equations as before if we instead define

$$x = -\left(\frac{k_y N}{2\pi M} + \frac{sN}{QM} + x'\right).$$

The definition of x should therefore take the same $\pm$ sign as the magnetic field $P/Q \pm 1/N$. Discrete difference equations near to some simple $\phi = P/Q$ are given in Appendix 3.B.

3.2.2 Perturbation Theory

Once we have obtained a discrete difference equation for a single sublattice, we again make the continuum substitution $\psi^j_{x'} \to \psi^j(x')$, where x' is now a continuous variable. As before, we rewrite the discrete differences using the operators $\hat{T}_m = e^{m\partial_{x'}}$, where $\hat{T}_m$ is a discrete translation of m lattice sites in the x-direction. We expand the cosine terms (and generically also sine terms) in powers of $1/N$ and collect everything together order by order. This step is more complicated than for the case of small flux, and for $Q > 2$ there will be terms present at half-integer powers of $1/N$.

At first order in $1/N$, we always recover a harmonic oscillator equation for $\psi^j(x')$ with characteristic frequency $\omega = 2\pi M/N \equiv 1/l_B^2$. This is what we found in Section 2.4, and we have checked that it is also the case for all values of P/Q with $Q \leq 5$—we expect it to hold in general. This permits the use of the ladder operators defined in Eq. (1.7) and allows us to write the perturbed wavefunctions in terms of Landau levels. We again define unitary operators

which generate the perturbation series from the unperturbed oscillator state, $\left|\tilde{n};j\right\rangle = U_j^\dagger \left|n\right\rangle$ with

$$\tilde{\psi}_n^j\left(x'\right) = \left\langle x'\middle|\tilde{n};j\right\rangle \equiv \tilde{\psi}_n^j\left(x - \frac{k_y N}{2\pi M} - \frac{sN}{QM}\right).$$

These quantities now have the additional label $j(\lambda, s)$ that tells us which discrete difference equation we have expanded.

For a given trough, defined by s and k_y, the complete x-wavefunction has amplitudes on every lattice site and we must write it as a sum over sublattice wavefunctions,

$$\tilde{\psi}^s_{n,k_y}\left(x'\right) \;=\; \sum_{\lambda=0}^{Q-1} A_{j(\lambda,s)} \tilde{\psi}_n^{j(\lambda,s)}\left(x'\right) \delta^{(Q)}_{x,\lambda}. \tag{3.5}$$

Here, $A_{j(\lambda,s)}$ is the coefficient for the wavefunction on the λth sublattice, and the δ function $\delta^{(Q)}_{x,\lambda}$ is equal to one only when $x \mod Q = \lambda$. It therefore picks out the wavefunction only on the correct sublattice. To find the coefficients A_j, we return to the original Harper equation (3.4) which connects amplitudes from different sublattices. By substituting the full wavefunction in from (3.5), we obtain a set of simultaneous equations for the A_j that can be solved using standard methods (up to normalisation).[2] We give perturbed wavefunctions $\tilde{\psi}^s_{n,k_y}$ and coefficients A_j for some simple flux fractions in Appendix 3.C.

Eq. (3.5) gives the general x-wavefunction near a specified trough with momentum k_y. If we want to consider a different trough we simply change s accordingly. This will cause the correspondence between the sublattices and the functions $\psi^j(x')$ to permute through a change in the function $j(\lambda, s) \equiv (P\lambda + s) \mod Q$, but the set of underlying functions will remain the same.

In Figure 3.3b, we plot the perturbative wavefunction $\tilde{\psi}^0_{0,0}(x)$ near to the origin for $\phi = 1/2 + 1/31 = 33/62$ (i.e. $n = s = k_y = 0$). The discrete wavefunction oscillates between the continuous functions $A_j\psi^j(x)$, which are also shown as a guide to the eye. We have normalised the wavefunction by integrating over each sublattice component as if it were a continuum function. Exponentially small corrections to this normalisation can be found from the Euler-Maclaurin formula [156]. We note that the magnetic length of the wavefunction for any P/Q is always $l_B^2 = N/(2\pi M)$, if we consider each sublattice individually.

[2] In fact, at lowest order these coefficients coincide with the amplitudes ψ_x we would find for the Q lattice sites in the simple $\phi = P/Q$ case.

Including the y-dependence, the perturbative wavefunctions are written

$$\tilde{\psi}^s_{n,k_y}\left(x',y\right) = e^{ik_y y}\tilde{\psi}^s_{n,k_y}\left(x'\right) \equiv e^{ik_y y}\sum_{\lambda=0}^{Q-1} A_{j(\lambda,s)}\tilde{\psi}^{j(\lambda,s)}_n\left(x'\right)\delta^{(Q)}_{x,\lambda} \tag{3.6}$$

which we will find in Section 3.6 are related to the Wannier orbitals of Qi et al. [136]. Finally, we form Bloch wavefunctions by introducing k_x,

$$\Psi^s_{n,\mathbf{k}}(\mathbf{r}) \;\sim\; \sum_m e^{ik_x mq}e^{ik_y y}\tilde{\psi}^s_{n,k_y}\left(x - \frac{k_y N}{2\pi M} - \frac{sN}{QM} - mq\right). \tag{3.7}$$

On the right hand side we have used the general unit cell length q in the formation of the Bloch solution. Once the cell size is fixed, there are always n_s possible choices of s for each value of k_y.

We will obtain a final Bloch wavefunction of this form no matter what flux fraction $\phi = P/Q + M/N$ we choose (for suitably small $M/N \ll 1$ and with P and Q coprime). The only effect of different choices of M and N will be in the cancellation of the field fraction ϕ and, in turn, the unit cell size. We will always find that there is a Q-fold structure described by the labels $j(\lambda, s)$.

There are also perturbative solutions at very high energies, and near to the extrema of intermediate bands in the $\phi = P/Q$ band structure—we outline how these can be found in Appendix 3.A. In Appendix 3.C we give the perturbed energies and wavefunctions that are obtained by expanding near to some simple fractions $\phi \approx P/Q$, and show how to calculate the Chern number of these perturbative wavefunctions in Appendix 3.D.

Finally, we note that for large Q it becomes increasingly difficult to rearrange Harper's equation into a discrete difference equation for a single sublattice. In these cases the perturbation theory can also be carried out by choosing an ansatz wavefunction for each sublattice that is a sum of Landau level wavefunctions. An ansatz wavefunction for the perturbed lowest subband would be

$$\tilde{\psi}^j_0(x') = \sum_{l,p} C^j_{l,p}\left(\frac{1}{N}\right)^p \psi_l(x'),$$

where the sum over l is over all Landau levels and the sum over p is up to as high an order in $1/N$ as required. The $\psi_l(x')$ on the right hand side is an unperturbed Landau level wavefunction and $C^j_{l,p}$ is the perturbation series coefficient for the lth Landau level at pth order in $1/N$. These ansatz wavefunctions may be substituted into Harper's equation directly, and the coefficients equated at each order in $1/N$. However, if this approach is used, in order to

fix the coefficients consistently at order $(1/N)^p$ we must expand Harper's equation to order $(1/N)^{p+1}$—otherwise the solution is unconstrained. We believe that this leads to an error in the perturbative wavefunction given in Ref. [101].

3.3 Two-body Interactions

3.3.1 Landau Gauge

We now follow Sec. 2.5 and consider the two-body matrix elements for the δ-function interaction, which, for the lowest subband, may be written

$$V^{s_1 s_2 s_3 s_4}_{\mathbf{k}_1\mathbf{k}_2\mathbf{k}_3\mathbf{k}_4} = \left\langle \Psi^{s_1}_{0,\mathbf{k}_1}(\mathbf{r}_1)\Psi^{s_2}_{0,\mathbf{k}_2}(\mathbf{r}_2)\right| \delta\left(\mathbf{r}_1-\mathbf{r}_2\right) \left|\Psi^{s_3}_{0,\mathbf{k}_3}(\mathbf{r}_1)\Psi^{s_4}_{0,\mathbf{k}_4}(\mathbf{r}_2)\right\rangle .$$

These are now labelled by s indices in addition to $\mathbf{k}$ labels (for the previously considered case of $\phi = 1/N$, the only allowed value of s was zero).

Two x-wavefunctions, $\psi^{s_1}_{n,k_{1y}}(x')$ and $\psi^{s_2}_{n,k_{2y}}(x')$, will obviously have nonzero overlap if $s_2 = s_1$ and $k_{2y} \approx k_{1y}$. However, they will also have nonzero overlap if $s_2 = s_1 + r$ and $k_2 \approx k_1 - 2\pi r/Q$ (with integer r), as can be seen by noting that each wavefunction centre is located at $k_y N/(2\pi M) + sN/(QM)$. Provided that these overlaps are not prohibited by momentum constraints, we should expect them to feature in the calculation of $V^{s_1 s_2 s_3 s_4}_{\mathbf{k}_1\mathbf{k}_2\mathbf{k}_3\mathbf{k}_4}$.

We let $k_{1y} = K + k_1'$ where $|k_1'| \ll \pi/Q$ and write the other wavevectors in terms of this,

$$\begin{aligned} k_{2y} &= K - \tfrac{2\pi r_2}{Q} + k_2'; \qquad s_2 = s_1 + r_2 \\ k_{3y} &= K - \tfrac{2\pi r_3}{Q} + k_3'; \qquad s_3 = s_1 + r_3 \\ k_{4y} &= K - \tfrac{2\pi r_4}{Q} + k_4'; \qquad s_4 = s_1 + r_4, \end{aligned}$$

where again the r_i are integers and the $|k_i'| \ll \pi/Q$. In this way, K is the large momentum that centres the wavefunctions, and k_i' are small changes that translate the wavefunctions away from this centre. For nonzero overlap the r_i are fixed once we have chosen the s_i, and so the only leftover freedom is with the primed momenta.

The overlap integrals will require us to multiply wavefunction components from the same sublattice together, carry out the integration, and then sum over the contributions from each sublattice. This sum over different sublattices means that the absolute values of s will be unimportant: what matters is only the relative values of the s_i compared to s_1. For example, we expect $V^{0101}_{\mathbf{k}_1\mathbf{k}_2\mathbf{k}_3\mathbf{k}_4}$ to be the same as $V^{1212}_{\mathbf{k}_1\mathbf{k}_2\mathbf{k}_3\mathbf{k}_4}$ (up to a shift of K).

After carrying out the integration we find

$$V^{s_1 s_2 s_3 s_4}_{\mathbf{k}_1\mathbf{k}_2\mathbf{k}_3\mathbf{k}_4} = \frac{1}{(2\pi)^2}\delta\left(\Sigma k_x\right)\delta\left(\Sigma k_y\right) T^{s_1 s_2 s_3 s_4}_{\kappa_1\kappa_2\kappa_3\kappa_4},$$

where the summation notation is as defined in Sec. 2.5 and where the matrix elements $T^{s_1 s_2 s_3 s_4}_{\kappa_1\kappa_2\kappa_3\kappa_4}$ will be defined below. As usual, the integration over space enforces conservation of Bloch momentum, but we are now able to separate the large and small contributions to k_y. The y-momentum conserving delta function $\delta\left(\Sigma k_y\right)$ may be written out as

$$\delta\left(k'_{1y} + k'_{2y} - k'_{3y} - k'_{4y} - \frac{2\pi}{Q}(r_2 - r_3 - r_4)\right).$$

Since the primed momenta are much smaller than the r-dependent terms, and since the r_i can only take integer values, the large and small contributions in the delta function must be set to zero independently. We can also replace the r_i with the equivalent s_i, since these just differ by an offset that will cancel, and so

$$\delta\left(\Sigma k_y\right) = \delta\left(\Sigma k'_y\right)\delta\left(\frac{2\pi}{Q}(s_1 + s_2 - s_3 - s_4)\right).$$

Finally, we note that the argument of the final delta function need only be satisfied modulo 2π, and so $\delta\left(\Sigma k_y\right) = \delta\left(\Sigma k'_y\right)\delta^{(Q)}_{\Sigma s}$. The second delta function is now written as a Kronecker delta, and by adding the superscript (Q) we mean that $s_1 + s_2 - s_3 - s_4 = 0$ modulo Q. In contrast to the case of small flux, this allows for the possibility of umkapp (and non s-conserving) processes.

The T functions are defined as in Sec. 2.5 but with additional s labels,

$$T^{s_1 s_2 s_3 s_4}_{\kappa_1\kappa_2\kappa_3\kappa_4} = \int \mathrm{d}x \left[\tilde{\psi}^{s_1}_0\left(x - \kappa_1\right)\right]^* \left[\tilde{\psi}^{s_2}_0\left(x - \kappa_2\right)\right]^* \tilde{\psi}^{s_3}_0\left(x - \kappa_3\right)\tilde{\psi}^{s_4}_0\left(x - \kappa_4\right)$$

and where now $\kappa_i = k'_{iy}N/(2\pi)$. We can expand this further by writing the integral over x in terms of a sum over sublattices and an integral over coordinates belonging to each sublattice (x_λ), so that $\int \mathrm{d}x \to \sum_\lambda \int \mathrm{d}x_\lambda$. Then,

$$T^{\{s_i\}}_{\{\kappa_i\}} = \sum_{\lambda=0}^{Q-1} A^*_{j_1} A^*_{j_2} A_{j_3} A_{j_4} \int \mathrm{d}x_\lambda \left[\tilde{\psi}^{j_1}_0(x_\lambda - \kappa_1)\right]^* \left[\tilde{\psi}^{j_2}_0(x_\lambda - \kappa_2)\right]^* \tilde{\psi}^{j_3}_0(x_\lambda - \kappa_3)\tilde{\psi}^{j_4}_0(x_\lambda - \kappa_4),$$

where we let $j_i \equiv j(\lambda, s_i) = (Ps_i + \lambda) \mod Q$. Since we have split the space up into Q sublattices, integration over each x_λ yields only $1/Q$ of the continuum value of the integral. As before, the explicit form of the T is a product of Gaussian and polynomial factors in the κ_i.

In principle, these quantities allow us to calculate the low-lying many-body states. We would

first project to the lowest single-particle subband and form noninteracting many-body states. Then, using these states as a basis, we could calculate the $V^{s_1 s_2 s_3 s_4}_{\mathbf{k}_1 \mathbf{k}_2 \mathbf{k}_3 \mathbf{k}_4}$ and diagonalise. However, for the reasons discussed previously we will switch to the symmetric gauge and calculate the Haldane pseudopotentials instead.

3.3.2 Symmetric Gauge

3.3.2.1 Gauge Transformation

To calculate the Haldane pseudopotentials, we must first find the perturbed wavefunctions in the symmetric gauge. For the small flux case we interpreted the operator $U^\dagger$ in the symmetric gauge, but for general P/Q it is not immediately clear how to carry out the transformation: there is a Q-periodic oscillation in the x-direction.

One approach would be to write down a Harper-like discrete difference equation for the symmetric gauge and find the perturbative wavefunctions directly from this by expanding order by order in $1/N$. We have carried out this approach elsewhere but find that we can equivalently (and more simply) obtain the symmetric gauge wavefunctions by transforming from the Landau gauge wavefunctions.

On the lattice, we have shown that the Bloch wavefunctions are not true continuum LL wavefunctions but rather are periodic, oscillate in amplitude and have corrections from higher Landau levels. However, we can obtain semi-localised Wannier functions that are analogous to the Landau gauge states of the continuum by simply taking the repeating part of the Bloch wavefunction. These are the perturbed Hofstadter wavefunctions from Eq. (3.6), which we now centre at the origin to find

$$\tilde{\psi}^s_{0,k-2\pi isy/Q}(\mathbf{r}) = e^{-2\pi isy/Q} \sum_{\lambda=0}^{Q-1} A_j \tilde{\psi}^{j,\mathrm{LG}}_{0,k}(x,y) \delta^{(Q)}_{x,\lambda}. \tag{3.8}$$

In this expression, $\tilde{\psi}^{j,\mathrm{LG}}_{0,k}(x,y)$ is a Landau gauge wavefunction that has been perturbed using the unitary operator $U^\dagger_j$, and we have replaced $k_y \to k$. The initial phase factor of $e^{-2\pi isy/Q}$ is necessary for the centred wavefunctions to agree with the standard definitions of $\psi^{\mathrm{LG}}_{n,k}(x,y)$ given in Eq. (1.5)—it arises when we translate a wavefunction with $s \neq 0$ to the origin.

In terms of operators, Eq. (3.8) may be written $|\tilde{n},k,s\rangle = e^{-2\pi isy/Q} U^\dagger_s |n,k\rangle$, where we have left the sum over sublattices implicit. We can transform this to the symmetric gauge by taking a linear combination of k-states as outlined in Sec. 1.4.3. The linear combination of k-states required was described by the function $B_m(k)$ in Eq. 1.13: we now represent this as an operator

$\hat{B}$ (which commutes with $U^\dagger$) so that $|\tilde{n}, m, s\rangle = e^{-2\pi isy/Q}\hat{B}U_s^\dagger |n, k\rangle$. This is equivalent to multiplying Eq. (3.8) by the function $B_m(k)$ and integrating over k. We find

$$\tilde{\psi}^s_{0,k-2\pi isy/Q}(\mathbf{r}) \to \tilde{\psi}^s_{0,m}(\mathbf{r}) = e^{-2\pi isy/Q}\sum_{\lambda=0}^{Q-1} A_j \tilde{\psi}^{j,\mathrm{SG}}_{0,m}(x,y)\delta^{(Q)}_{x,\lambda} \tag{3.9}$$

In this way, we have transferred the sublattice structure described by λ to the symmetric gauge.

By introducing this transformation, we are free to use whichever gauge we choose. The Landau gauge basis ($|\tilde{n}, k\rangle$) is useful for calculating the Chern number (see Appendix 3.D), for justifying the no-tunnelling approximation, and for many-body calculations on a torus. The symmetric gauge basis ($|\tilde{n}, m\rangle$) is useful for many-body calculations in the disk geometry and for calculating pseudopotentials. For small m, the symmetric gauge states are localised, and so these are the states that will be of interest for short-range interactions.

3.3.2.2 Haldane Pseudopotentials

We can use the symmetric gauge wavefunctions to directly calculate the Haldane pseudopotentials. We first form two-particle states of relative angular momentum L,

$$\tilde{\psi}_0^{L,s_1s_2}(\mathbf{r}_1\mathbf{r}_2) \;=\; \sum_{\{m_1,m_2\}}^{m_1+m_2=L} D^L_{m_1m_2}\tilde{\psi}^{s_1}_{0,m_1}(\mathbf{r}_1)\tilde{\psi}^{s_2}_{0,m_2}(\mathbf{r}_2),$$

where $D^L_{m_1m_2} = \Big[\langle m_1| \otimes \langle m_2|\Big]|L\rangle$ are the appropriate Clebsch-Gordan coefficients (given explicitly in Appendix 3.F). We have set the centre-of-mass (COM) angular momentum $M = 0$ without loss of generality, as this remains conserved even in the presence of the lattice. Next, we calculate the overlap integrals with our chosen interaction. From the form of the wavefunctions in Eq. (3.9), we see that the overlap integral will involve a sum of terms corresponding to each λ, and that the combination of initial phase factors will ensure that Σs is conserved modulo Q. In practice we can ignore the implicit transformation that is occurring between Landau and symmetric gauges and instead just read off our perturbation series in the symmetric gauge (remembering to separately enforce $\Sigma s = 0 \mod Q$).

The pseudopotentials again have matrix indices that indicate L and L', but now also possess a species degree of freedom given by s,

$$V^{LL'}_{s_1s_2s_3s_4} \;=\; \delta^{(Q)}_{\Sigma s}\,\langle L|\,U_{is_1}U_{js_2}V\left(z_i - z_j\right)U^\dagger_{is_3}U^\dagger_{js_4}\,\big|L'\big\rangle\,.$$

The $U_s^\dagger$ are the single particle unitary operators defined earlier which apply the perturbation

due to the lattice to particles (i, j), and the labels s_i take at least Q different values depending on the size of the unit cell.

For the purposes of calculation we use COM and relative coordinates rather than particle coordinates—full definitions of these are given in Appendix 3.E. Since the unitary operators $U^\dagger$ mix in components from higher LLs, the general two-body state that we must consider is $|L, M; Y, Z\rangle$, where L and M respectively indicate the relative and COM angular momentum and Y and Z indicate the relative and COM LL index. Terms in a pseudopotential calculation then involve the general overlap integral

$$\langle L, M; Y, Z| \, \delta\left(z_i - z_j\right) \left|L', M'; Y', Z'\right\rangle \;=\; \frac{(-1)^{L+L'}}{4\pi l_B^2} \delta_{YL}\delta_{Y'L'}\delta_{ZZ'}\delta_{MM'}, \tag{3.10}$$

where a proof of the right hand side can be found in Appendix 3.E. An explicit pseudopotential calculation is given in Appendix 3.F.

In the previous chapter, we found that the $\phi \to 0$ limit connected precisely to the case of LLs, and at zeroth order we recovered the pseudopotential coefficients of the continuum (only V^{00} was nonzero for the contact interaction). As we switched on the lattice (i.e. as we considered nonzero $\phi = M/N$), other elements in the pseudopotential matrix became nonzero, with each element given by a perturbation series in powers of M/N. For general P/Q there is no exact continuum limit, but we can use what we know about pseudopotentials to predict which many-body states will be energetically favoured. In the next section we give the pseudopotential matrices for $\phi = 1/2 \pm M/N$ and $\phi = 1/3 \pm M/N$.

3.4 Pseudopotential Matrices

The pseudopotential matrix for a delta function interaction with $\phi = 1/N$ was given in Section 2.5, and extends to a general small $\phi = M/N$ under the substitution $\delta = 1/N \to M/N$. Below we give pseudopotential matrices near to other simple flux fractions and interactions, and assume that $\delta = M/N \ll 1$ throughout.

3.4.1 $\phi = 1/2 \pm \delta$

Near $\phi = 1/2$, there are four types of two-particle state, described by $s_1, s_2 \in \{00, 01, 10, 11\}$. However, as mentioned previously, only interactions which conserve s modulo two are nonzero. Below, we give the three distinct pseudopotential matrices—all others can be derived from these. Equivalent matrices are defined under the substitutions $s_i \to s_i + r$ for integer r (where

the transformed s_i are defined modulo n_s). The matrix $V_{0110}^{LL'}$ differs from $V_{0101}^{LL'}$ only in the V^{11} element, which picks up a minus sign due to the symmetry of the two-particle basis states [Eq. (1.28)].

We give the even columns and rows corresponding to $L, L' \in \{0, 2, 4, 6, 8\}$, but also give the $L = 1$ and $L' = 1$ elements (bordered by lines) since the $(1, 1)$ entry can now be nonzero. Although we cannot usually form bosonic continuum states with $L = 1$, we now have two distinct particle species, and so a two-particle state formed from both species is not prohibited by particle statistics.

$$V_{0000}^{LL'} = \frac{V}{8\pi l_B^2} \left(\begin{array}{c|c|cccc} 3 - \frac{11}{32}(\pi\delta)^2 & 0 & -\frac{\sqrt{2}}{4}(\pi\delta) - \frac{7\sqrt{2}}{16}(\pi\delta)^2 & \frac{\sqrt{6}}{8}(\pi\delta) + \frac{5\sqrt{6}}{16}(\pi\delta)^2 & -\frac{\sqrt{5}}{16}(\pi\delta)^2 & \frac{\sqrt{70}}{64}(\pi\delta)^2 \\ \hline 0 & 0 & 0 & 0 & 0 & 0 \\ \hline -\frac{\sqrt{2}}{4}(\pi\delta) - \frac{7\sqrt{2}}{16}(\pi\delta)^2 & 0 & \frac{5}{16}(\pi\delta)^2 & -\frac{\sqrt{3}}{48}(\pi\delta)^2 & 0 & 0 \\ \frac{\sqrt{6}}{8}(\pi\delta) + \frac{5\sqrt{6}}{16}(\pi\delta)^2 & 0 & -\frac{\sqrt{3}}{48}(\pi\delta)^2 & \frac{1}{32}(\pi\delta)^2 & 0 & 0 \\ -\frac{\sqrt{5}}{16}(\pi\delta)^2 & 0 & 0 & 0 & 0 & 0 \\ \frac{\sqrt{70}}{64}(\pi\delta)^2 & 0 & 0 & 0 & 0 & 0 \end{array}\right)$$

$$V_{0101}^{LL'} = \frac{V}{8\pi l_B^2} \left(\begin{array}{c|c|cccc} 1 - \frac{67}{96}(\pi\delta)^2 & 0 & \frac{\sqrt{2}}{4}(\pi\delta) + \frac{7\sqrt{2}}{16}(\pi\delta)^2 & \frac{\sqrt{6}}{24}(\pi\delta) + \frac{\sqrt{6}}{16}(\pi\delta)^2 & \frac{\sqrt{5}}{16}(\pi\delta)^2 & \frac{\sqrt{70}}{192}(\pi\delta)^2 \\ \hline 0 & \frac{1}{2}(\pi\delta)^2 & 0 & 0 & 0 & 0 \\ \hline \frac{\sqrt{2}}{4}(\pi\delta) + \frac{7\sqrt{2}}{16}(\pi\delta)^2 & 0 & \frac{3}{16}(\pi\delta)^2 & \frac{\sqrt{3}}{48}(\pi\delta)^2 & 0 & 0 \\ \frac{\sqrt{6}}{24}(\pi\delta) + \frac{\sqrt{6}}{16}(\pi\delta)^2 & 0 & \frac{\sqrt{3}}{48}(\pi\delta)^2 & \frac{1}{96}(\pi\delta)^2 & 0 & 0 \\ \frac{\sqrt{5}}{16}(\pi\delta)^2 & 0 & 0 & 0 & 0 & 0 \\ \frac{\sqrt{70}}{192}(\pi\delta)^2 & 0 & 0 & 0 & 0 & 0 \end{array}\right)$$

$$V_{1100}^{LL'} = \frac{V}{8\pi l_B^2} \left(\begin{array}{c|c|cccc} 1 - \frac{91}{96}(\pi\delta)^2 & 0 & \frac{\sqrt{2}}{4}(\pi\delta) + \frac{7\sqrt{2}}{16}(\pi\delta)^2 & \frac{\sqrt{6}}{24}(\pi\delta) + \frac{3\sqrt{6}}{16}(\pi\delta)^2 & \frac{\sqrt{5}}{16}(\pi\delta)^2 & \frac{\sqrt{70}}{192}(\pi\delta)^2 \\ \hline 0 & 0 & 0 & 0 & 0 & 0 \\ \hline \frac{\sqrt{2}}{4}(\pi\delta) + \frac{7\sqrt{2}}{16}(\pi\delta)^2 & 0 & -\frac{1}{16}(\pi\delta)^2 & \frac{\sqrt{3}}{48}(\pi\delta)^2 & 0 & 0 \\ \frac{\sqrt{6}}{24}(\pi\delta) + \frac{3\sqrt{6}}{16}(\pi\delta)^2 & 0 & \frac{\sqrt{3}}{48}(\pi\delta)^2 & \frac{1}{96}(\pi\delta)^2 & 0 & 0 \\ \frac{\sqrt{5}}{16}(\pi\delta)^2 & 0 & 0 & 0 & 0 & 0 \\ \frac{\sqrt{70}}{192}(\pi\delta)^2 & 0 & 0 & 0 & 0 & 0 \end{array}\right).$$

Motivated by Ref. [102], we note that pseudopotential matrices are simplified if we define the new basis states $\psi_{0,m}^{\pm} = \frac{1}{\sqrt{2}}\left(\psi_{0,m}^{0} \pm i\psi_{0,m}^{1}\right)$. The pseudopotential matrices in this basis are given below using the same notation as before. Equivalent matrices may now be obtained under the exchange $+ \leftrightarrow -$ and by noting that $V_{+-+-}^{11} = -V_{+--+}^{11}$ from the symmetry of the basis states:

$$V^{LL'}_{++++} = \frac{V}{4\pi l_B^2}\left(\begin{array}{c|c|cccc} 1-\frac{19}{96}(\pi\delta)^2 & 0 & 0 & \frac{\sqrt{6}}{24}(\pi\delta)+\frac{\sqrt{6}}{16}(\pi\delta)^2 & 0 & \frac{\sqrt{70}}{192}(\pi\delta)^2 \\ \hline 0 & 0 & 0 & 0 & 0 & 0 \\ \hline 0 & 0 & \frac{3}{16}(\pi\delta)^2 & 0 & 0 & 0 \\ \frac{\sqrt{6}}{24}(\pi\delta)+\frac{\sqrt{6}}{16}(\pi\delta)^2 & 0 & 0 & \frac{1}{96}(\pi\delta)^2 & 0 & 0 \\ 0 & 0 & 0 & 0 & 0 & 0 \\ \frac{\sqrt{70}}{192}(\pi\delta)^2 & 0 & 0 & 0 & 0 & 0 \end{array}\right),$$

$$V^{LL'}_{+-+-} = \frac{V}{4\pi l_B^2}\left(\begin{array}{c|c|cccc} 1-\frac{31}{96}(\pi\delta)^2 & 0 & 0 & \frac{\sqrt{6}}{24}(\pi\delta)+\frac{\sqrt{6}}{16}(\pi\delta)^2 & 0 & \frac{\sqrt{70}}{192}(\pi\delta)^2 \\ \hline 0 & \frac{1}{4}(\pi\delta)^2 & 0 & 0 & 0 & 0 \\ \hline 0 & 0 & \frac{1}{16}(\pi\delta)^2 & 0 & 0 & 0 \\ \frac{\sqrt{6}}{24}(\pi\delta)+\frac{\sqrt{6}}{16}(\pi\delta)^2 & 0 & 0 & \frac{1}{96}(\pi\delta)^2 & 0 & 0 \\ 0 & 0 & 0 & 0 & 0 & 0 \\ \frac{\sqrt{70}}{192}(\pi\delta)^2 & 0 & 0 & 0 & 0 & 0 \end{array}\right),$$

$$V^{LL'}_{++--} = \frac{V}{4\pi l_B^2}\left(\begin{array}{c|c|cccc} \frac{1}{2}(\pi\delta)^2 & 0 & -\frac{\sqrt{2}}{4}(\pi\delta)-\frac{7\sqrt{2}}{16}(\pi\delta)^2 & 0 & -\frac{\sqrt{5}}{16}(\pi\delta)^2 & 0 \\ \hline 0 & 0 & 0 & 0 & 0 & 0 \\ \hline -\frac{\sqrt{2}}{4}(\pi\delta)-\frac{7\sqrt{2}}{16}(\pi\delta)^2 & 0 & 0 & -\frac{\sqrt{3}}{48}(\pi\delta)^2 & 0 & 0 \\ 0 & 0 & -\frac{\sqrt{3}}{48}(\pi\delta)^2 & 0 & 0 & 0 \\ -\frac{\sqrt{5}}{16}(\pi\delta)^2 & 0 & 0 & 0 & 0 & 0 \\ 0 & 0 & 0 & 0 & 0 & 0 \end{array}\right).$$

At zeroth order we see that only the species-conserving terms V^{00}_{++++}, V^{00}_{+-+-} and V^{00}_{+--+} are nonzero, and are equal. In general, angular momentum is conserved modulo 4 for species-conserving interactions, but is only conserved modulo 2 for an umklapp interaction. We discuss possible ground states for these pseudopotentials in Section 3.6.

3.4.2 $\phi = 1/3 + 1/N$

Below, we give the three distinct pseudopotential matrices for $\phi = 1/3 + 1/N$ to first order in $1/N$. Other pseudopotential matrices equivalent to the ones given below may be obtained under the substitutions $s_i \to s_i + r$, where r is an integer, and by noting that $V^{LL'}_{1200} = \left(V^{LL'}_{0012}\right)^T$. Only even columns (corresponding to $L, L' \in \{0, 2, 4\}$) are shown:

$$V^{LL'}_{0000} = \left(\begin{array}{ccc} \frac{6+\sqrt{3}}{4} & -\frac{3\sqrt{2}+\sqrt{6}}{16}(\pi\delta) & \frac{9(\sqrt{2}+2\sqrt{6})}{128}(\pi\delta) \\ -\frac{3\sqrt{2}+\sqrt{6}}{16}(\pi\delta) & 0 & 0 \\ \frac{9(\sqrt{2}+2\sqrt{6})}{128}(\pi\delta) & 0 & 0 \end{array}\right),$$

$$V^{LL'}_{0101} = \left(\begin{array}{ccc} \frac{6-\sqrt{3}}{8} & \frac{3\sqrt{2}+\sqrt{6}}{32}(\pi\delta) & \frac{9(2\sqrt{6}-\sqrt{2})}{256}(\pi\delta) \\ \frac{3\sqrt{2}+\sqrt{6}}{32}(\pi\delta) & 0 & 0 \\ \frac{9(2\sqrt{6}-\sqrt{2})}{256}(\pi\delta) & 0 & 0 \end{array}\right),$$

$$V_{0012}^{LL'} = \begin{pmatrix} \frac{\sqrt{3}}{4} & \frac{\sqrt{6}}{8}(\pi\delta) & \frac{9\sqrt{2}}{128}(\pi\delta) \\ \frac{3\sqrt{2}-\sqrt{6}}{16}(\pi\delta) & 0 & 0 \\ \frac{9\sqrt{2}}{128}(\pi\delta) & 0 & 0 \end{pmatrix}.$$

We have not been able to find a single-particle rotation that simplifies the pseudopotential matrices near to $\phi = 1/3$. Nevertheless, we make some suggestions for the supported many-body ground state in Section 3.6.

3.4.3 $\phi = 1/3 - 1/N$

We again give the three distinct pseudopotential matrices to first order in $1/N$, but corrections now appear at half order in $1/N$. Columns and rows corresponding to $L, L' \in \{0, 1, 2, 4\}$ are shown, with the $L = 1$ and $L' = 1$ elements bordered by lines. Equivalent pseudopotential matrices may be obtained under the substitutions $s_i \to s_i + r$ where r is an integer. We again note that $V_{1200}^{LL'} = \left(V_{0012}^{LL'}\right)^T$, but now due to the symmetry of the basis states, the $L = 1$ row picks up a minus sign under the interchange of the first two s indices, and the column $L' = 1$ picks up a minus sign under the interchange of the last two s indices:

$$V_{0000}^{LL'} = \left(\begin{array}{c|c|cc} \frac{6+\sqrt{3}}{4} & 0 & -\frac{5(7\sqrt{2}-3\sqrt{6})}{16}(\pi\delta) & \frac{9(\sqrt{2}+2\sqrt{6})}{128}(\pi\delta) \\ \hline 0 & 0 & 0 & 0 \\ \hline -\frac{5(7\sqrt{2}-3\sqrt{6})}{16}(\pi\delta) & 0 & 0 & 0 \\ \frac{9(\sqrt{2}+2\sqrt{6})}{128}(\pi\delta) & 0 & 0 & 0 \end{array}\right),$$

$$V_{0101}^{LL'} = \left(\begin{array}{c|c|cc} \frac{6-\sqrt{3}}{8} - \frac{(9-5\sqrt{3})}{2}(\pi\delta) & -\frac{(3\sqrt{2}-\sqrt{6})}{8}\sqrt{\pi\delta} & \frac{5(7\sqrt{2}-3\sqrt{6})}{32}(\pi\delta) & \frac{9(2\sqrt{6}-\sqrt{2})}{256}(\pi\delta) \\ \hline -\frac{(3\sqrt{2}-\sqrt{6})}{8}\sqrt{\pi\delta} & \frac{9-5\sqrt{3}}{2}(\pi\delta) & 0 & 0 \\ \hline \frac{5(7\sqrt{2}-3\sqrt{6})}{32}(\pi\delta) & 0 & 0 & 0 \\ \frac{9(2\sqrt{6}-\sqrt{2})}{256}(\pi\delta) & 0 & 0 & 0 \end{array}\right),$$

$$V_{0012}^{LL'} = \left(\begin{array}{c|c|cc} \frac{\sqrt{3}}{4} + \frac{(21-13\sqrt{3})}{4}(\pi\delta) & \frac{(2\sqrt{6}-3\sqrt{2})}{4}\sqrt{\pi\delta} & \frac{(2\sqrt{2}+\sqrt{6})}{8}(\pi\delta) & \frac{9\sqrt{2}}{128}(\pi\delta) \\ \hline 0 & 0 & 0 & 0 \\ \hline \frac{(31\sqrt{2}-17\sqrt{6})}{16}(\pi\delta) & 0 & 0 & 0 \\ \frac{9\sqrt{2}}{128}(\pi\delta) & 0 & 0 & 0 \end{array}\right).$$

3.5 Extensions

3.5.1 General Lattices

A Harper-like discrete Schrödinger equation can be derived for many closely related models, and the perturbative approach outlined above follows accordingly. In Appendix 3.G we consider the anisotropic square lattice, the square lattice with next-nearest-neighbour hopping and the

triangular lattice, giving the discrete Schrödinger equation in each case, along with the energy bands and wavefunction corrections for vanishing flux. In each case we find that the wavefunctions include the higher LL corrections that allow them to adopt the symmetry of the lattice ($|n \pm 2\rangle$ for the anisotropic square lattice and $|n \pm 6\rangle$ for the triangular lattice).

3.5.2 Higher Hofstadter Bands

For higher Hofstadter bands, the pseudopotential overlap integrals are

$$V^{LL'}_{P\text{th LL}} = \langle N_L, 0; 0, 0| \frac{\left(a_j\right)^P}{\sqrt{P!}} \frac{\left(a_i\right)^P}{\sqrt{P!}} U_i U_j \delta\left(z_1 - z_2\right) U_i^\dagger U_j^\dagger \frac{\left(a_i^\dagger\right)^P}{\sqrt{P!}} \frac{\left(a_j^\dagger\right)^P}{\sqrt{P!}} |N'_L, 0; 0, 0\rangle .$$

We may rewrite the ladder operators in our relative and centre of mass coordinate basis, but the procedure in general remains the same as for the lowest band. We find that the wavefunction corrections have larger coefficients for higher bands, but that there are more stringent conditions on N for the flat band limit to be valid.

3.5.3 General Interactions

In order to consider fermions and more realistic systems, we need to go beyond the simple delta function interaction. Since we are on a lattice, it is natural to generalise the on-site interaction to a site-site interaction, $V(z_1, z_2) = U\delta\left(z_1 - z_2 - (u + iv)\right)$, with $u + iv$ the relative lattice vector of the interaction. On its own, this extends the approach to systems with, for example, near-neighbour exchange interactions. For long-range (e.g., Coulombic) interactions, matrix elements can be calculated by summing over weighted site-site interactions using

$$V(z_1, z_2) = \sum_{u,v} U(u, v)\delta\left(z_1 - z_2 - (u + iv)\right),$$

where $U(u, v)$ is the amplitude of the interaction between sites separated by a displacement $u+iv$. Pseudopotential matrix elements for a general interaction can then be calculated through

$$V^{LL'}_{s_1 s_2 s_3 s_4} = \sum_{u,v} U(u, v) \left\langle L; s_1, s_2\right| \delta\left(z_1 - z_2 - (u + iv)\right) \left|L'; s_3, s_4\right\rangle ,$$

where the expectation value under the summation is a pseudopotential for a site-site interaction, $V^{LL',u+iv}_{s_1 s_2 s_3 s_4}$. We outline the procedure to calculate these quantities below and give a full derivation of the final expression in Appendix 3.H.

A shift in the delta function has three effects on the interaction matrix elements. First, the

continuum-like wavefunctions are shifted relative to one another. We take this into account by acting on the wavefunctions with a translation operator $\hat{T}_{u+iv}$ that shifts the relative coordinate $z_R \to z_R+u+iv$, and by then setting z_R to zero. This operator involves the complex derivatives,

$$\vec{\partial}_{z_R} = \left(\hat{L} - \hat{Y}^\dagger\right)/4l_B, \quad \vec{\partial}_{\bar{z}_R} = \left(\hat{Y} - \hat{L}^\dagger\right)/4l_B,$$

which mix relative angular momentum states (see Appendix 3.E for operator definitions). As long as $|u + iv| \ll l_B \sim \sqrt{N}$, this gives a valid perturbation series for the initial and final wavefunctions. This operator should act in addition to the perturbation from the lattice and is written explicitly as

$$\hat{T}_{u+iv} = e^{(u+iv)\left(L-Y^\dagger\right)/(4l_B)+(u-iv)\left(Y-L^\dagger\right)/(4l_B)}. \tag{3.11}$$

The second effect of the delta function (for $Q \geq 2$) is to mix the different sublattice components of the wavefunction: amplitudes on different lattice sites are derived from different perturbation series. This effect is not captured by the (continuum) Taylor series approximation using $\hat{T}$, so we must enforce δ_{x_i,x_j+u} when expanding the wavefunction components instead of the usual δ_{x_i,x_j}.

Finally, there is a phase factor which comes from shifting y in each wavefunction. This is given by $e^{\pi iv(s_3-s_4+s_2-s_1)}$ as shown in Appendix 3.H. Overall, the pseudopotential matrix for a site-site interaction is given by the perturbative expression

$$V^{LL',u+iv}_{s_1s_2s_3s_4} = e^{\pi iv(s_3-s_4+s_2-s_1)}\left[\hat{T}_{u+iv}U^\dagger_{s_1s_2}\left|L',0;0,0\right\rangle\right]^\dagger \delta_{x_i,x_j+u}\delta(z_R)\delta(\bar{z}_R)\left[\hat{T}_{u+iv}U^\dagger_{s_3s_4}\left|L,0;0,0\right\rangle\right].$$

We give the pseudopotential matrix elements for a nearest-neighbour interaction with $\phi = M/N$ in Appendix 3.H.

3.6 Discussion

In this section we discuss some possible uses for our perturbative method—although we leave a full investigation of these applications to elsewhere.

3.6.1 Many-body Energies and Wavefunctions

One natural use is in the calculation of energy spectra and wavefunctions. The single-particle energy levels we calculated previously (given in full in Appendix 3.C) describe the Landau

level-like features of the (noninteracting) Hofstadter Butterfly very well. To find the many-body energy levels, we must diagonalise a suitable many-body Hamiltonian. This will be the subject of Chapter 4.

We can, however, make some qualitative statements about the many-body ground state just by looking at our pseudopotential matrices. For $\phi = M/N \ll 1$, the only nonzero pseudopotential at zeroth order was the element V_{00} (Eq. (2.30)), which, according to the discussion in Sec. 1.6.2, has the Laughlin $\nu = 1/2$ state as its exact many-body ground state. Switching on the lattice then has two effects: the underlying single-particle wavefunctions are perturbed according to the unitary operators $U^\dagger$, and the occupation of the many-body states are perturbed according to the pseudopotential matrix, $V_{LL'}$. The single particle perturbations mix in contributions from higher LLs and cause the symmetric gauge wavefunctions to develop a C_4 symmetry. The pseudopotential corrections at first order occur in the elements V_{04} and V_{40}, and will mix in contributions from many-body states with four units of angular momentum higher and lower than the Laughlin $\nu = 1/2$ ground state. However, due to the small coefficients in the pseudopotential matrix, the deviations from the Laughlin state are likely to be very small. We discuss these, and higher order corrections, in Chapter 4.

For $\phi \approx P/Q$ the situation is more complicated. For $\phi \approx 1/2$, as shown in subection 3.4.1, a convenient basis change completely removes the umklapp terms to zeroth order, leaving only V^{0000}_{++++}, V^{0000}_{+-+-}, and their symmetric partners nonzero. In this way, the complete system behaves like the Halperin-221 state [54],

$$\psi_{221}\left(\{z_i^\pm\}\right) \;\sim\; \prod_{i<j}\left(z_i^+ - z_j^+\right)^2\left(z_i^- - z_j^-\right)^2\prod_{i,j}\left(z_i^+ - z_j^-\right)$$

where $z_i^\pm$ is the (complex) position of the ith particle with rotated species index $\pm$. In fact, to zeroth order, any unitary rotation of the species produces an equally valid Halperin-221, as this ground state is a singlet. Turning on the lattice breaks this degeneracy and also breaks rotational symmetry, meaning the 221 state is no longer an exact eigenstate. However, it is unlikely that the many-body state changes significantly for small δ due to the small coefficients in the pseudopotential matrix.

For $\phi \approx 1/3$ there does not appear to be a single-particle species rotation that completely removes the zeroth-order Umklapp terms. Nonetheless, any Halperin-222111 state formed from three orthogonal species is an allowed zero-energy ground state at lowest order. We recall that in this case there are also corrections to the wavefunction at half-integer powers of $1/N$ (although

for the lowest band these only occur at $\phi \lesssim 1/3$).

The discussion above considers states in the disk geometry, but this may be adapted to the torus by instead considering perturbed linear momentum states $|k_i\rangle$ and interaction matrix elements $V^{s_1 s_2 s_3 s_3}_{\mathbf{k}_1 \mathbf{k}_2 \mathbf{k}_3 \mathbf{k}_4}$. In this case, there will be a subtle dependence on the size of the system, since species may map into one another across the boundary—the many body states will in general be analogous to the *colour-entangled* Halperin states of Ref. [38], with our species labels corresponding to colour.

Ref. [186] considers the specific colour-entangled states formed when layers of the Hofstadter model (each individually corresponding to small flux densities) are stacked together in different conformations. The resulting many-body states have a nontrivial ground state degeneracy that depends on the stacking arrangement and system size. These features also determine whether the states may be interpreted as a single-layer system or a multilayer system. This is similar to our findings for flux values $\phi \approx P/Q$, where the noninteracting states act like Q copies of a Landau level. The precise form of the fraction $\phi = p/q$ determines how the effective Landau levels are connected (in a similar way to the stacking of single Hofstadter layers in Ref. [186]). This feature, in conjunction with the length of the system modulo Q, will determine the degeneracy (and colour entanglement properties) of the many-body eigenstates on a torus.

A useful diagnostic tool in the study of Chern insulators is the two-particle energy spectrum, which exhibits energy levels that are analogous to the Haldane pseudopotentials [129], as outlined in Sec. 1.7.4. This analogy can be seen directly through our pseudopotential matrices. For example, diagonalising the zeroth order pseudopotential matrix for $\phi \approx 1/2$ yields three bosonic excited states with relative angular momentum $L = 0$. These may be written in the rotated basis as $\{|{+}{+}\rangle, |{-}{-}\rangle, (|{+}{-}\rangle + |{-}{+}\rangle)/\sqrt{2}\}$ and have respective energies $V/(4\pi l_B^2) \times \{1, 1, 2\}$. In the two-particle spectrum on a torus, these excited states would correspond to bands in $\mathbf{k}$-space with an energy ratio of $1:2$ and degeneracy ratio of $2:1$. As N is made finite, these bands would gain structure from the lattice corrections, but may still be interpreted as arising from the V^{00} pseudopotential element. Similarly, for vanishing flux, the two-particle spectrum should show a single energy level, and for $\phi \approx 1/3$ the spectrum should show two sets of bands with energy ratio $1:3$ and degeneracy ratio $3:3$.

3.6.2 Relation to Wannier Orbitals and Lattice Dislocations

Recent work by Qi and others [136, 137, 187] represents FCI states in terms of semilocalised Wannier functions, which were introduced in Sec. 1.7.4. These are related to our perturbative single-particle wavefunctions, as we show below.

If we form Wannier functions from our Bloch wavefunctions using the expression in Eq. (1.48), the transformation will simply undo the Fourier transform we have put in by hand, and will return the local, perturbative wavefunctions that we derived in Section 3.2,

$$\langle x, y | W_n(k_y, R) \rangle \;=\; e^{ik_y y} \tilde{\psi}^s_{n,k_y} \left(x - \frac{k_y N}{2\pi M} - \frac{sN}{QM} - R \right).$$

Here, $\tilde{\psi}^s_{n,k_y}$ is the x-dependent wavefunction from Eq. (3.5) and $R \equiv mq$ is the location of the mth magnetic unit cell. In our approximation, we have ignored the tunnelling processes that are responsible for nonuniformity in the Berry curvature, and so the centre of mass of these wavefunctions translates linearly with $K_y = 2\pi x + Ck_y$ as in the pure LL case. This is in contrast to ordinary FCI Wannier states, whose centre of mass translates in a characteristic staircase manner (Sec. 1.7.4). In this way, the true Wannier states of the Hofstadter model tend towards our perturbative wavefunctions in the limit $N \to \infty$, assuming that some finite temperature or interaction energy overcomes the exponentially small splitting within the subband.

We also note that, due to their simple phase, the perturbative Wannier states constructed above do not suffer from the finite-size orthogonalisation problems exhibited by the true Wannier states (see the discussion in Ref. [137]). Instead, perturbative Wannier functions corresponding to different (k_y, R) are orthogonal up to exponentially small corrections (in N) due to the Gaussian tails permeating into neighbouring cells. The trade-off is that our perturbative states neglect to capture the interesting behaviour that accompanies Berry curvature fluctuations, and the exact form of the wavefunctions is only accurate in the large N limit.

For $Q \geq 2$ there will be several Wannier orbitals per unit cell, each labelled by a species index s (this is in addition to the higher energy Wannier orbitals labelled by the Landau level index n). As noted previously, these states will take different smooth forms on each x-sublattice (defined by λ).

Barkeshli, Wen and Qi [188, 189] have considered multilayer systems analogous to our multicomponent wavefunctions in the presence of lattice dislocations. Since the wavefunction amplitude depends sensitively on the site index in the x-direction, translating a Wannier state around a dislocation in the x-direction will permute the sublattices, and so permute one species into

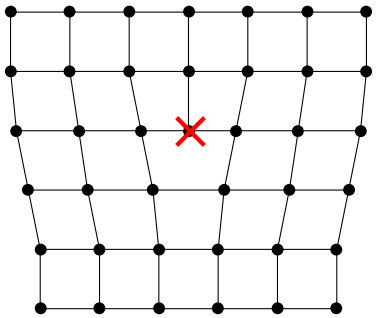

Figure 3.4: Dislocation corresponding to a Burgers vector of $\mathbf{b} = -\hat{x}$.

another (see Figure 3.4). This property of the system changes its effective topology: if we have two such defects in a bilayer system, then the layers become connected through a 'wormhole' and the system gains a topological degeneracy [188].

In contrast to Ref. [188], we do not need to translate the wavefunction around an entire $(N \times 1)$ unit cell: we only need to translate it around the dislocation, which is on the order of the lattice spacing. Translation around a lattice dislocation with Burgers vector $\mathbf{b} = b_x\hat{x}$ will move the wavefunction weight formerly associated with sublattice λ onto sublattice $\lambda' = \lambda + b_x$. If we consider the action of magnetic translation operators, we see that this is equivalent to changing $s \to s - Pb_x$ and $k_y \to k_y + 2\pi b_x/Q$. Defining a translation around a dislocation with Burgers vector $\mathbf{b}$ by the operator $\hat{O}(\mathbf{b})$, we find that $\hat{O}(b_x\hat{x})\big|\tilde{n}, k_y, s\big\rangle = e^{i\theta_{\mathrm{AB}}}\big|\tilde{n}, k_y + 2\pi b_x/Q, s - Pb_x\big\rangle$, where $\big|\tilde{n}, k_y, s\big\rangle$ are the perturbative wavefunctions from Eq. (3.8) and θ_{AB} is an Aharonov-Bohm phase that depends on the flux enclosed during the translation. Similarly, translation around a dislocation in the y-direction leads to $\hat{O}(b_y\hat{y})\big|\tilde{n}, k_y, s\big\rangle = e^{ik_y b_y}e^{i\theta_{\mathrm{AB}}}\big|\tilde{n}, k_y, \big\rangle$. Translations around dislocations with a general Burgers vector will have an additional phase that depends on b_x, b_y, and the path taken.

If we wish to physically move the wavefunction around the defect, it makes more sense to consider the localised (for small enough m) symmetric gauge states discussed earlier in Section 3.3.2, rather than the Wannier states which are only semi-localised. In the symmetric gauge, translation around an x-dislocation leads to $\hat{O}(b_x\hat{x})\big|\tilde{n}, m, s\big\rangle = e^{i\theta_{\mathrm{AB}}}\big|\tilde{n}, m, s - Pb_x\big\rangle$, and again permutes wavefunctions with different s-indices into one another.

Appendices for Chapter 3

3.A Expanding Harper's Equation Near Other Band Extremeties

In the main text we found the lowest energy states by expanding near the Brillouin zone points $(k_x, k_y) = (0, 2r\pi/Q)$. These are the correct points to expand about because they correspond to troughs in the lowest energy band of the pure $\phi = P/Q$ Hofstadter model from which the expansion is derived. From the symmetry of the energy bands, other troughs in the lowest energy band are located at $(k_x, k_y) = (2m\pi/Q, 2r\pi/Q)$, while the peaks are located at $(k_x, k_y) = ((2m+1)\pi/Q, (2r+1)\pi/Q)$—although in the Landau gauge only the Q repeating units in the y-direction are distinct.

The Q bands alternate the orientation of their curvature as they increase in energy, so the **k**-points of the peaks of the highest band are located at even multiples of π/Q if Q is even and at odd multiples of π/Q if Q is odd. Peak and trough locations in intermediate bands can be worked out accordingly.

We find numerically that there are harmonic oscillator-like wavefunctions and energy levels near the peaks and troughs of *all* of the Q original bands (see Fig. 3.A.1). We considered only the lowest bands in the main text, but our approach is applicable near to all $2Q$ band extremities. We simply need to set (k_x, k_y) to appropriate values and choose the zeroth order solution for E that corresponds to the desired original band energy.

For even multiples of π/Q we can set $k_x = 0$ and expand about the Q different values $k_y = 2r\pi/Q$ as described in the main text. For odd multiples of π/Q we should be at $k_x = \pi/Q$ in the original system and cycle through values $k_y = (2r+1)\pi/Q$. To set $k_x = \pi/Q$ we change $\psi_x \to e^{i\pi x/Q}\psi_x$ in Harper's equation as if the ψ_x were Bloch solutions. The true Bloch wavenumber of the perturbed system is fixed by the magnetic unit cell size to lie between $0 \leq k_x \lesssim 2\pi/N$: the larger contribution of π/Q ensures we are perturbing about the correct point in the original P/Q system. Figure 3.A.1 illustrates this for $\phi = 1/3$, which provides six sets of extrema about which we may expand.

3.B Discrete Difference Equations for Some $\phi = P/Q \pm M/N$

Below we give the discrete difference equations near to some simple flux filling fractions. As always, we will assume that M/N is small.

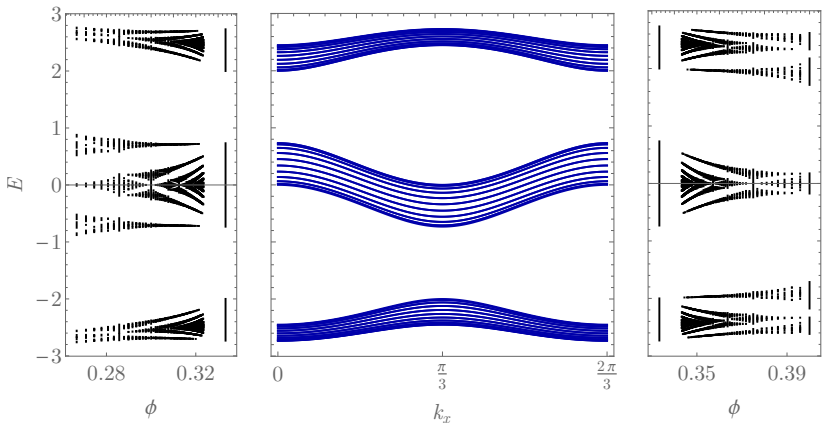

Figure 3.A.1: *Centre*: Band structure for $\phi = 1/3$ (lines correspond to equally spaced k_y values). The bands alternate in orientation from top to bottom and the troughs and peaks are located at $(k_x, k_y) = (0, 0)$ and $(k_x, k_y) = (\pi/3, \pi/3)$. We may expand about any of these extreme points, located at energies $E = \pm(1 + \sqrt{3}), \pm(1 - \sqrt{3}), \pm 2$. *Left and Right*: Butterfly spectrum for $\phi \approx 1/3$, showing LL-like lines emanating from each band extremum (two sets per band).

3.B.1 $\phi = M/N$

For close to vanishing flux, there is only one sublattice, and we can use perturbation theory on Harper's equation directly,

$$-\psi_{x-1} - \psi_{x+1} - 2\cos\left(\frac{2\pi M x}{N} - k_y\right)\psi_x = E\psi_x.$$

3.B.2 $\phi = 1/2 \pm M/N$

Close to $\phi = 1/2$, the wavefunction depends on whether the site index is even or odd and which of the two distinct effective potential troughs we are expanding about. Writing

$$x = \pm\left(\frac{k_y N}{2\pi M} + \frac{sN}{QM} + x'\right),$$

where the sign is the same as in the definition of ϕ, Harper's equation simplifies to

$$-\psi^{j(\lambda-1)}_{x'-1} - \psi^{j(\lambda+1)}_{x'+1} - 2(-1)^{j(\lambda)}\cos\left(\frac{2\pi M x'}{N}\right)\psi^{j(\lambda)}_{x'} \quad = \quad E\psi^{j(\lambda)}_{x'}.$$

(where $j(\lambda) \equiv j(\lambda, s) = (P\lambda + s) \mod Q$). We can eliminate sites of each parity in turn to find

$$\frac{\psi^0_{x'-2} + \psi^0_{x'}}{E - 2\cos\left(\frac{2\pi M(x'-1)}{N}\right)} + \frac{\psi^0_{x'+2} + \psi^0_{x'}}{E - 2\cos\left(\frac{2\pi M(x'+1)}{N}\right)} = \left[E + 2\cos\left(\frac{2\pi M x'}{N}\right)\right]\psi^0_{x'}$$

for j even and

$$\frac{\psi^1_{x'-2}+\psi^1_{x'}}{E+2\cos\left(\frac{2\pi M(x'-1)}{N}\right)}+\frac{\psi^1_{x'+2}+\psi^1_{x'}}{E+2\cos\left(\frac{2\pi M(x'+1)}{N}\right)}=\left[E-2\cos\left(\frac{2\pi Mx'}{N}\right)\right]\psi^1_{x'}$$

for j odd. We can use these equations to find both the lowest and highest energy states by choosing (respectively) $E=-2\sqrt{2}$ or $E=+2\sqrt{2}$ to zeroth order. Additionally, we can use the method outlined in Appendix 3.A to find the system behaviour in the middle of the spectrum where the two bands meet. This will require us to expand about $(k_x,k_y)=(\pi/2,\pi/2)$ and choose the $E\approx 0$ solutions, resulting in a graphene-like Landau level spectrum.

3.B.3 $\phi = 1/3 \pm M/N$

Close to $\phi=1/3$, there are three types of site index and Harper's equation for the lowest energy states takes the form

$$-\psi^{j(\lambda-1)}_{x'-1}-\psi^{j(\lambda+1)}_{x'+1}-2\cos\left(\frac{2\pi j(\lambda)}{3}+\frac{2\pi Mx'}{N}\right)\psi^{j(\lambda)}_{x'} \;=\; E\psi^{j(\lambda)}_{x}.$$

Defining the functions

$$\begin{aligned}
A(x') &= 2\cos\left(\tfrac{2\pi Mx'}{N}\right)\\
B(x') &= 2\cos\left(\tfrac{2\pi}{3}+\tfrac{2\pi Mx'}{N}\right) = -\cos\left(\tfrac{2\pi Mx'}{N}\right)-\sqrt{3}\sin\left(\tfrac{2\pi Mx'}{N}\right)\\
C(x') &= 2\cos\left(\tfrac{4\pi}{3}+\tfrac{2\pi Mx'}{N}\right) = -\cos\left(\tfrac{2\pi Mx'}{N}\right)+\sqrt{3}\sin\left(\tfrac{2\pi Mx'}{N}\right),
\end{aligned}$$

the three effective Harper equations for $\phi=1/3+M/N$ may be written as

$$\begin{aligned}
[E+A(x)]\,\psi^0_x &= \frac{\psi^0_{x-3}-[E+B(x-2)]\,\psi^0_x}{1-[E+B(x-2)]\,[E+C(x-1)]}+\frac{\psi^0_{x+3}-[E+C(x+2)]\,\psi^0_x}{1-[E+C(x+2)]\,[E+B(x+1)]}\\
[E+B(x)]\,\psi^1_x &= \frac{\psi^1_{x-3}-[E+C(x-2)]\,\psi^1_x}{1-[E+C(x-2)]\,[E+A(x-1)]}+\frac{\psi^1_{x+3}-[E+A(x+2)]\,\psi^1_x}{1-[E+A(x+2)]\,[E+C(x+1)]}\\
[E+C(x)]\,\psi^2_x &= \frac{\psi^2_{x-3}-[E+A(x-2)]\,\psi^2_x}{1-[E+A(x-2)]\,[E+B(x-1)]}+\frac{\psi^2_{x+3}-[E+B(x+2)]\,\psi^2_x}{1-[E+B(x+2)]\,[E+A(x+1)]}.
\end{aligned}$$

For $\phi=1/3-M/N$ we should make the usual substitution for x,

$$x=-\left(\frac{k_yN}{2\pi M}+\frac{sN}{QM}+x'\right).$$

However, since increasing x' by one *decreases* x by one, we cycle through the sublattices in the opposite sense. This requires us to interchange $B\leftrightarrow C$ in the equations above, which

we find leads to different corrections to the energies and wavefunctions (see Appendix 3.C). The corresponding equations for $\phi = 2/3 \pm M/N$ can be easily derived by setting $P = 2$ in $j = (P\lambda + s) \mod Q$.

The highest energy states are located at odd multiples of $\pi/3$ in the original $\phi = 1/3$ Brillouin zone. To find these states we substitute $\psi_x \to e^{i\pi x/3}\psi_x$ and

$$x = \pm\left(\frac{k_y N}{2\pi M} + \frac{(s+1/2)N}{QM} + x'\right)$$

to arrive at the discrete difference equation

$$-e^{-i\pi/3}\psi_{x-1}^{j(\lambda-1)} - e^{i\pi/3}\psi_{x+1}^{j(\lambda+1)} - 2\cos\left(\frac{2\pi}{3}\left(j(\lambda)+\frac{1}{2}\right) + \frac{2\pi M x'}{N}\right)\psi_x^{j(\lambda)} \;=\; E\psi_x^{j(\lambda)}.$$

This time we define the functions

$$\begin{aligned}
A(x') &= 2\cos\left(\tfrac{\pi}{3} + \tfrac{2\pi M x'}{N}\right) &&= \cos\left(\tfrac{2\pi M x'}{N}\right) - \sqrt{3}\sin\left(\tfrac{2\pi M x'}{N}\right)\\
B(x') &= 2\cos\left(\pi + \tfrac{2\pi M x'}{N}\right) &&= -2\cos\left(\tfrac{2\pi M x'}{N}\right)\\
C(x') &= 2\cos\left(\tfrac{5\pi}{3} + \tfrac{2\pi M x'}{N}\right) &&= \cos\left(\tfrac{2\pi M x'}{N}\right) + \sqrt{3}\sin\left(\tfrac{2\pi M x'}{N}\right),
\end{aligned}$$

which differ from before. The discrete difference equations for the three sublattices are written in terms of these new functions A, B, C and have some additional sign changes due to the $\pi/3$ phases,

$$\begin{aligned}
[E + A(x)]\,\psi_x^0 &= \frac{-\psi_{x-3}^0 - [E + B(x-2)]\,\psi_x^0}{1 - [E + B(x-2)]\,[E + C(x-1)]} + \frac{-\psi_{x+3}^0 - [E + C(x+2)]\,\psi_x^0}{1 - [E + C(x+2)]\,[E + B(x+1)]}\\
[E + B(x)]\,\psi_x^1 &= \frac{-\psi_{x-3}^1 - [E + C(x-2)]\,\psi_x^1}{1 - [E + C(x-2)]\,[E + A(x-1)]} + \frac{-\psi_{x+3}^1 - [E + A(x+2)]\,\psi_x^1}{1 - [E + A(x+2)]\,[E + C(x+1)]}\\
[E + C(x)]\,\psi_x^2 &= \frac{-\psi_{x-3}^2 - [E + A(x-2)]\,\psi_x^2}{1 - [E + A(x-2)]\,[E + B(x-1)]} + \frac{-\psi_{x+3}^2 - [E + B(x+2)]\,\psi_x^2}{1 - [E + B(x+2)]\,[E + A(x+1)]}.
\end{aligned}$$

As before, we must interchange $B \leftrightarrow C$ if we wish to consider the high energy states of $\phi = 1/3 - M/N$. Expansions near to intermediate band extrema may be obtained by choosing the correct set of equations from above and selecting the desired intermediate solution for E at zeroth order, as described in Appendix 3.A.

3.C Perturbed Wavefunctions and Energies for some $\phi = P/Q \pm M/N$

3.C.1 $\phi = M/N$

To second order the energy levels of the lowest subbands are (setting $\delta = M/N$)

$$E_n = -4 + 4(\pi\delta)\left(n + \frac{1}{2}\right) - \frac{1}{2}(\pi\delta)^2\left(2n^2 + 2n + 1\right)$$

and the unitary operator that generates the second-order wavefunctions from the unperturbed states is given by

$$U^\dagger = \exp\left[\left(\frac{1}{96}(\pi\delta) + \frac{1}{128}(\pi\delta)^2\right)\left(\left(a^\dagger\right)^4 - (a)^4\right) + \frac{1}{320}(\pi\delta)^2\left(\left(a^\dagger\right)^5 a - a^\dagger(a)^5\right)\right]$$

such that $|\tilde{n}\rangle = U^\dagger|n\rangle$. The highest energy wavefunctions are identical, and the corresponding energies are given by setting $E_n \to -E_n$.

3.C.2 $\phi = 1/2 \pm M/N$

The lowest energy levels and wavefunctions are symmetric about $\phi = 1/2$, with

$$E_n = -2\sqrt{2} + 2\sqrt{2}(\pi\delta)\left(n + \frac{1}{2}\right) - \sqrt{2}(\pi\delta)^2\left(n^2 + n + \frac{3}{4}\right)$$

(and where we have again set $\delta = M/N$). The unitary operators are cumbersome to write out, so here we just give the perturbations to the LLL, $|\tilde{n}; j(\lambda, s)\rangle$.

$$\begin{aligned}|\tilde{0}; 0\rangle = {} & |0\rangle + (\pi\delta)\left[\left(\frac{\sqrt{2}+2}{4}\right)|2\rangle + \frac{\sqrt{24}}{24}|4\rangle\right] + (\pi\delta)^2\left[\frac{3\sqrt{2}+6}{8}|2\rangle + \frac{3\sqrt{6}}{16}|4\rangle\right. \\ & \left. + \frac{\sqrt{5}+\sqrt{10}}{8}|6\rangle + \frac{\sqrt{70}}{48}|8\rangle - \frac{5+3\sqrt{2}}{24}|0\rangle\right]\end{aligned}$$

$$\begin{aligned}|\tilde{0}; 1\rangle = {} & |0\rangle + (\pi\delta)\left[-\left(\frac{2-\sqrt{2}}{4}\right)|2\rangle + \frac{\sqrt{24}}{24}|4\rangle\right] + (\pi\delta)^2\left[-\left(\frac{6-3\sqrt{2}}{8}\right)|2\rangle + \frac{3\sqrt{6}}{16}|4\rangle\right. \\ & \left. - \left(\frac{\sqrt{10}-\sqrt{5}}{8}\right)|6\rangle + \frac{\sqrt{70}}{48}|8\rangle - \left(\frac{5-3\sqrt{2}}{24}\right)|0\rangle\right]\end{aligned}$$

In the Landau gauge, a ground state wavefunction is labelled by s and involves contributions from all sublattices. We can write this in ket notation as

$$\left|\tilde{0};s\right\rangle \;=\; \sum_{\lambda\in\{0,1\}} A_{j(\lambda,s)}\delta^{(2)}_{x,\lambda}\left|\tilde{0};j(\lambda,s)\right\rangle$$

with $j(\lambda,s)=(\lambda+s) \mod 2$ and where the normalised amplitudes are found to be

$$A_0=\sqrt{\frac{2-\sqrt{2}}{2}},\qquad A_1=(1+\sqrt{2})A_0.$$

The real space wavefunction is given by $\tilde{\psi}^s_{0,k_y}(x')=\left\langle x'\middle|\tilde{0};s\right\rangle$ with x' an offset coordinate defined in the main text. We can form Bloch and Wannier states from these x-wavefunctions as outlined in Section 3.2.2.

The highest energy states $(+)$ are related to these low energy states $(-)$ by the transformations

$$E^+_l=-E^-_l,\qquad \left|\tilde{0};j\right\rangle^+=\left|\tilde{0};j\right\rangle^-,\qquad A^+_0=-A^-_1,\qquad A^+_1=A^-_0.$$

3.C.3 $\phi=1/3\pm M/N$

The energy levels and wavefunctions are asymmetric about one third and now have additional wavefunction corrections at order $\sqrt{M/N}$. The lowest energy states at $\phi=1/3+M/N$ have energy corrections

$$\begin{aligned}E \;=\; &-\left(1+\sqrt{3}\right)+(\pi\delta)\left[3\left(\sqrt{3}-1\right)n+\frac{(1+\sqrt{3})}{2}\right]-(\pi\delta)^2\left[\frac{(1+5\sqrt{3})}{8}+\frac{3(\sqrt{3}-1)n}{4}\right.\\ &\left.+\frac{9(-11+7\sqrt{3})n^2}{4}\right]\end{aligned}$$

and corrections to the ground-state wavefunction:

$$\begin{aligned}\left|\tilde{0};0\right\rangle &= |0\rangle+(\pi\delta)\left[-\tfrac{(\sqrt{6}-\sqrt{2})}{4}|2\rangle+\tfrac{3\sqrt{6}}{16}|4\rangle\right]\\ \left|\tilde{0};1\right\rangle &= |0\rangle+(\pi\delta)\left[\tfrac{(\sqrt{6}+\sqrt{2})}{4}|2\rangle+\tfrac{3\sqrt{6}}{16}|4\rangle\right]\\ \left|\tilde{0};2\right\rangle &= |0\rangle+(\pi\delta)\left[\tfrac{(\sqrt{6}+\sqrt{2})}{4}|2\rangle+\tfrac{3\sqrt{6}}{16}|4\rangle\right]\end{aligned}$$

(the half-order corrections to state $|n\rangle$ are proportional to $|n-1\rangle$ and so do not affect the lowest subband).

The lowest energy states at $\phi = 1/3 - M/N$ have energy corrections

$$E_l = -\left(1+\sqrt{3}\right) + (\pi\delta)\left[3\left(\sqrt{3}-1\right)n + \frac{(-7+5\sqrt{3})}{2}\right] - (\pi\delta)^2\left[\frac{(-191+125\sqrt{3})}{8} + \frac{3(41\sqrt{3}-65)n}{4} + \frac{9(-11+7\sqrt{3})n^2}{4}\right]$$

and corrections to the ground state:

$$\begin{aligned}
\left|\tilde{0};0\right\rangle &= |0\rangle + (\pi\delta)\left[\frac{(15\sqrt{2}-11\sqrt{6})}{12}|2\rangle + \frac{3\sqrt{6}}{16}|4\rangle\right] \\
\left|\tilde{0};1\right\rangle &= |0\rangle + (\pi\delta)^{\frac{1}{2}}(\sqrt{3}-1)|1\rangle + (\pi\delta)\left[\frac{3\sqrt{6}}{16}|4\rangle + \frac{(7\sqrt{6}+3\sqrt{2})}{12}|2\rangle + (-2+\sqrt{3})|0\rangle\right] \\
\left|\tilde{0};2\right\rangle &= |0\rangle - (\pi\delta)^{\frac{1}{2}}(\sqrt{3}-1)|1\rangle + (\pi\delta)\left[\frac{3\sqrt{6}}{16}|4\rangle + \frac{(7\sqrt{6}+3\sqrt{2})}{12}|2\rangle + (-2+\sqrt{3})|0\rangle\right].
\end{aligned}$$

These states *do* have corrections at half order in δ. In the Landau gauge, assuming the Harmonic oscillator states are normalised, the full wavefunction then takes the form

$$\left|\tilde{0};s\right\rangle = \sum_{\lambda\in\{0,1,2\}} A_{j(\lambda,s)}\delta^{(3)}_{x,\lambda}\left|\tilde{0};j(\lambda,s)\right\rangle$$

with

$$A_0 = \sqrt{\frac{3+\sqrt{3}}{2}}, \qquad A_1 = A_2 = \frac{\sqrt{3}-1}{2}A_0.$$

The real space wavefunction is again given by $\tilde{\psi}^s_{0,k_y}(x') = \left\langle x'\middle|\tilde{0};s\right\rangle$.

The highest energy states may be found by expanding about a different point in the Brillouin zone, as described in Appendix 3.A. The high energy states (+) are related to the low energy states given above (−) through the substitutions

$$\begin{aligned}
E_l^- &= -E_l^+, \qquad \left|\tilde{0};j\right\rangle^+ = \left|\tilde{0};j+1\right\rangle^-, \\
A_1^- &= \sqrt{\tfrac{3+\sqrt{3}}{2}}, \qquad A_0^- = -e^{i\pi/3}\tfrac{\sqrt{3}-1}{2}A_1^-, \qquad A_2^- = -e^{-i\pi/3}\tfrac{\sqrt{3}-1}{2}A_1^-.
\end{aligned}$$

3.D Chern Number and Berry Curvature of the Subbands

The Chern number of a mini-band can be extracted from the TKNN diophantine equation (2.3). If we increase the denominator of the magnetic field fraction by increasing N, then the Chern numbers of the mini-bands generically also increase. However, the total Chern number of a subband stays fixed and equal to $\pm Q$, as described in Sec. 3.1.

In our perturbative approximation, we ignore the tunnelling that endows the mini-bands

with such large Chern numbers. We therefore expect the Chern numbers of our perturbative wavefunctions to be different from the true values, although the total Chern number of a subband should be the same.

One way to show this is to consider pumping k_y (e.g. through an adiabatic flux threading) and to observe how the weight of the wavefunction moves in the x-direction. This approach was originally followed by TKNN [52], and we outline it heuristically in Appendix G of Ref. [1]. In this thesis, however, we will use a complementary Berry matrix approach.

We start by obtaining the periodic part of the perturbative Bloch solutions from Eq. (3.7), finding

$$u^s_{n,\mathbf{k}}(\mathbf{r}) \sim \sum_m e^{ik_x(mq-x)} \tilde{\psi}^s_{n,k_y}\left(x \mp \frac{k_y N}{2\pi M} \mp \frac{sN}{QM} \mp mq\right). \tag{3.12}$$

In our perturbative approach, the n_s states from each unit cell are degenerate and together form a subband: these are the states from which we will form the $n_s \times n_s$ Berry matrix. For large N, the n_s different $u^s_{n,\mathbf{k}}$ states have vanishing overlap with each other because the x-dependent parts of the wavefunctions are exponentially localised around different centres. The nonabelian Berry connection, $\mathbf{A}^{\alpha\beta} = i\langle u^\alpha_{\mathbf{k}} | \nabla_{\mathbf{k}} | u^\beta_{\mathbf{k}} \rangle$, is therefore only nonzero on the diagonal. Correspondingly, the Berry matrix also reduces to diagonal form with elements $F^{ss}(\mathbf{k})$ giving the (abelian) Berry curvature for each value of s. We therefore only need to calculate $\mathbf{A}^{ss}(\mathbf{k})$ and $F^{ss}(\mathbf{k})$.

The y-component of the Berry connection, $A^{ss}_y(\mathbf{k})$, vanishes for our gauge choice, which we find by considering

$$\begin{aligned}
\langle u^s_{n\mathbf{k}} | \, \partial_{k_y} \, | u^s_{n\mathbf{k}} \rangle &= i\left\langle \tilde{\psi}^s_{n,k_y}\left(x \mp \frac{k_y N}{2\pi M} \mp \frac{sN}{QM} \mp mq\right) \partial_{k_y} \tilde{\psi}^s_{n,k_y}\left(x \mp \frac{k_y N}{2\pi M} \mp \frac{sN}{QM} \mp mq\right)\right\rangle \\
&= i\left\langle \tilde{\psi}^s_{n,k_y}\left(x \mp \frac{k_y N}{2\pi M} \mp \frac{sN}{QM} \mp mq\right) \left(\frac{-N\partial_x}{2\pi M}\right) \tilde{\psi}^s_{n,k_y}\left(x \mp \frac{k_y N}{2\pi M} \mp \frac{sN}{QM} \mp mq\right)\right\rangle \\
&\sim \langle a^\dagger - a \rangle = 0.
\end{aligned}$$

The last expression vanishes because the perturbed states have terms whose LL indices differ only by multiples of four. The x-component is nonzero and is found to be

$$\begin{aligned}
A^{ss}_x(\mathbf{k}) &= i\left\langle \tilde{\psi}^s_{n,k_y}\left(x \mp \frac{k_y N}{2\pi M} \mp \frac{sN}{QM} \mp mq\right) [i(mq-x)] \, \tilde{\psi}^s_{n,k_y}\left(x \mp \frac{k_y N}{2\pi M} \mp \frac{sN}{QM} \mp mq\right)\right\rangle \\
&= i\left\langle \tilde{\psi}^s_{n,k_y}(x') \left[-i\left(x' \pm \frac{k_y N}{2\pi M} \pm \frac{sN}{QM}\right)\right] \tilde{\psi}^s_{n,k_y}(x')\right\rangle \\
&= \pm\frac{k_y N}{2\pi M} \pm \frac{sN}{QM}.
\end{aligned}$$

Finally, we obtain

$$F^{ss}(\mathbf{k}) = -\nabla_{\mathbf{k}} \times \mathbf{A}^{ss}(\mathbf{k}) = \pm\frac{N}{2\pi M}. \tag{3.13}$$

The Chern number this corresponds to depends on the Brillouin zone size, which in turn depends on the cancellation in the fraction ϕ. For the three cancellation possibilities considered in Eq. (3.1) with Q prime and $M = 1$, we find that in case (a) the unit cell is QN lattice sites long and the Brillouin zone is $2\pi/(QN) \times 2\pi$ in size. The Chern number of each s-state is therefore

$$C^{ss} = \frac{1}{2\pi} \int_{BZ} \mathrm{d}^2\mathbf{k}\, F^{ss}(\mathbf{k}) = \pm\frac{1}{Q}.$$

There are Q^2 mini-bands (spatial centres) in a subband, and so the total Chern number of the subband is $\mathrm{Tr}_s C^{ss} = \pm Q$.

In case (b) the unit cell size is N, the Brillouin zone has dimensions $2\pi/(N) \times 2\pi$ and we find Q mini-bands each with Chern number ± 1. Finally, in the maximally cancelling case (c), the unit cell size is N/Q, the Brillouin zone has dimensions $2\pi Q/N \times 2\pi$ and we have a single mini-band with Chern number $\pm Q$. In all three cases, the total Chern number of the subband ($\pm Q$) is shared equally between the component mini-bands—this is also true for general $\phi = P/Q \pm M/N$ when Q is not necessarily prime and $M \neq 1$. Of course, the fractional Chern numbers of the mini-bands given above are unphysical: only the total Chern number of the degenerate mini-bands is well defined in our approximation.

Finally, we mention that a system with Chern number $C \geq 2$ can in general have wavefunctions which are subtly different in character: when we go around the Brillouin zone by changing k_y, each species can stay the same, or the species can be interchanged. This is studied in Ref. [38], where it is shown that this effect depends sensitively on the system size. In our case, in the large N limit, the unit cell size is much larger than both the magnetic length and the interaction distances, so these small effects should not be important.

3.E Symmetric Gauge Two-particle Wavefunctions

In the symmetric gauge we define the centre of mass and relative coordinates by

$$z_C = \tfrac{z_1+z_2}{2}, \qquad z_R = z_1 - z_2, \qquad \partial_{z_C} = \partial_{z_1} + \partial_{z_2}, \qquad \partial_{z_R} = \tfrac{\partial_{z_1}-\partial_{z_2}}{2},$$

with magnetic lengths $l_R = \sqrt{2} l_B$ and $l_C = \frac{l_B}{\sqrt{2}}$. The conjugate variables are defined similarly. In terms of these new coordinates, we define Landau level and angular momentum ladder

operators,

$$\hat{Z}^\dagger = \sqrt{2}\left(\frac{1}{4l_C}\bar{z}_C - l_C\partial_{z_C}\right), \qquad \hat{Y}^\dagger = \sqrt{2}\left(\frac{1}{4l_R}\bar{z}_R - l_R\partial_{z_R}\right),$$
$$\hat{M}^\dagger = \sqrt{2}\left(\frac{1}{4l_C}z_C - l_C\partial_{\bar{z}_C}\right), \qquad \hat{L}^\dagger = \sqrt{2}\left(\frac{1}{4l_R}z_R - l_R\partial_{\bar{z}_R}\right).$$

which are analogous to the ladder operators defined in Eq. 1.9. These are related to the single particle operators through

$$a_1^\dagger = \tfrac{1}{\sqrt{2}}\left(\hat{Z}^\dagger + \hat{Y}^\dagger\right), \qquad a_2^\dagger = \tfrac{1}{\sqrt{2}}\left(\hat{Z}^\dagger - \hat{Y}^\dagger\right) \qquad b_1^\dagger = \tfrac{1}{\sqrt{2}}\left(\hat{M}^\dagger + \hat{L}^\dagger\right), \qquad b_2^\dagger = \tfrac{1}{\sqrt{2}}\left(\hat{M}^\dagger - \hat{L}^\dagger\right),$$

etc. In terms of these, a general two-particle state then takes the form

$$|N_L, N_M; N_Z, N_Y\rangle = \frac{\left(\hat{Z}^\dagger\right)^{N_Z}}{\sqrt{N_Z!}}\frac{\left(\hat{Y}^\dagger\right)^{N_Y}}{\sqrt{N_Y!}}\frac{\left(\hat{L}^\dagger\right)^{N_L}}{\sqrt{N_L!}}\frac{\left(\hat{M}^\dagger\right)^{N_M}}{\sqrt{N_M!}}\frac{1}{2\pi l_R l_C}\exp\left[-\frac{1}{4l_C^2}|z_C|^2 - \frac{1}{4l_R^2}|z_R|^2\right],$$

which can be written in terms of Laguerre polynomials through

$$\begin{aligned}\langle z_R, \bar{z}_R; z_C, \bar{z}_C\,|N_L, N_M; N_Z, N_Y\rangle \;=\; & (-1)^{N_Y}\sqrt{\frac{N_Y!}{2\pi l_R^2 N_L!}}\left(\frac{z_R}{\sqrt{2}l_R}\right)^{N_L-N_Y} L_{N_Y}^{N_L-N_Y}\left[\frac{\bar{z}_R z_R}{2l_R^2}\right] e^{-\frac{|z_R|^2}{4l_R^2}} \times \\ & (-1)^{N_Z}\sqrt{\frac{N_Z!}{2\pi l_C^2 N_M!}}\left(\frac{z_C}{\sqrt{2}l_C}\right)^{N_M-N_Z} L_{N_Z}^{N_M-N_Z}\left[\frac{\bar{z}_C z_C}{2l_C^2}\right] e^{-\frac{|z_C|^2}{4l_C^2}}.\end{aligned}$$

In the text we are interested in the overlap integral $O = \langle N_L', N_M'; N_Y', N_Z'|\,\delta(z_R)\,|N_L, N_M; N_Y, N_Z\rangle$, where the δ function only affects the z_R-dependent terms. Integration over $z_C, \bar{z}_C$ just leads to the usual orthonormality condition,

$$\begin{aligned}O \;=\; & \delta_{N_Z,N_Z'}\delta_{N_M,N_M'}\int \mathrm{d}z_R\mathrm{d}\bar{z}_R\,(-1)^{N_Y}\sqrt{\frac{N_Y!}{2\pi l_R^2 N_L!}}\left(\frac{z_R}{\sqrt{2}l_R}\right)^{N_L-N_Y} L_{N_Y}^{N_L-N_Y}\left[\frac{\bar{z}_R z_R}{2l_R^2}\right] e^{-\frac{\bar{z}_R z_R}{4l_R^2}} \times \\ & (-1)^{N_Y'}\sqrt{\frac{N_Y'!}{2\pi l_R^2 N_L'!}}\left(\frac{\bar{z}_R}{\sqrt{2}l_R}\right)^{N_L'-N_Y'} \text{Ł}_{N_Y'}^{N_L'-N_Y'}\left[\frac{\bar{z}_R z_R}{2l_R^2}\right] e^{-\frac{\bar{z}_R z_R}{4l_R^2}}\,\delta(x_R)\delta(y_R).\end{aligned}$$

For the remaining terms to be nonzero we must have $N_L = N_Y$ and $N_L' = N_Y'$—otherwise the factors in round brackets will vanish when the delta function is enacted. Then,

$$O \;=\; \delta_{N_Z,N_Z'}\delta_{N_M,N_M'}\delta_{N_Y,N_L}\delta_{N_Y',N_L'}\frac{(-1)^{N_Y+N_Y'}}{4\pi l_B^2},$$

where we have used the property of Laguerre polynomials that $L_n^\alpha(0) = (n+\alpha)!/(n!\alpha!)$.

Finally, we remark that in general we calculate overlap integrals between particular sublattice components of the single particle wavefunctions. If a single particle wavefunction is split into Q components, integration over one component only samples $1/Q$ of space and (with lattice

spacing fixed at one) the integration should only return $1/Q$ of its continuum value.

3.F Further Details on the Symmetric Gauge Pseudopotentials

We showed in Section 3.3.2 that we could transform between Landau gauge and symmetric gauge states using the functions $B_m(k)$. We can equivalently transform the interaction matrix elements themselves through

$$V^{m_1m_2m_3m_4}_{s_1s_2s_3s_4} = \int \mathrm{d}k'_{y1}\mathrm{d}k'_{y2}\mathrm{d}k'_{y3}\mathrm{d}k'_{y4} B_{m_1}(k'_{y1})B_{m_2}(k'_{y2})B_{m_3}(k'_{y3})B_{m_4}(k'_{y4}) V^{\mathbf{k}_1\mathbf{k}_2\mathbf{k}_3\mathbf{k}_4}_{s_1s_2s_3s_4}.$$

To find the pseudopotentials $V^{LL'}$ from these, we can use the appropriate Clebsch-Gordan coefficients,

$$D^{LM}_{m_1m_2} = \langle L, M | m_1, m_2\rangle = \delta_{m_1+m_2,L+M}\sqrt{\frac{m_1!m_2!}{2^{L+M}L!M!}}\sum_{\alpha=0}^{L}(-1)^\alpha \begin{pmatrix} L \\ \alpha \end{pmatrix}\begin{pmatrix} M \\ m_1-\alpha \end{pmatrix}.$$

In practice it is easiest to interpret the wavefunction perturbation series in the symmetric gauge and compute the overlap integral in Eq. (3.10), making sure that Σs is conserved modulo Q.

As an example, we calculate the zeroth and first order pseudopotential matrix elements for $\phi = 1/2 + 1/N$ with $s_1 = s_2 = 1$ and $s_3 = s_4 = 0$, i.e. $V^{LL'}_{1100}$. We see from Appendix 3.C that the two possible perturbation series are given by the unitary operators

$$U_0^\dagger = 1 + \left(\frac{\pi}{N}\right)\left(\left(\frac{1+\sqrt{2}}{4}\right)\left(a^\dagger\right)^2 + \frac{1}{24}\left(a^\dagger\right)^4\right), \qquad U_1^\dagger = 1 + \left(\frac{\pi}{N}\right)\left(\left(\frac{1-\sqrt{2}}{4}\right)\left(a^\dagger\right)^2 + \frac{1}{24}\left(a^\dagger\right)^4\right).$$

The two possible LLL one-particle wavefunctions are then

$$\left|\tilde{0};0\right\rangle = \sqrt{\tfrac{2-\sqrt{2}}{2}}\left[\delta^{(2)}_{x,0}U_0^\dagger + (1+\sqrt{2})\delta^{(2)}_{x,1}U_1^\dagger\right]|0\rangle, \quad \left|\tilde{0};1\right\rangle = \sqrt{\tfrac{2-\sqrt{2}}{2}}\left[(1+\sqrt{2})\delta^{(2)}_{x,0}U_1^\dagger + \delta^{(2)}_{x,1}U_0^\dagger\right]|0\rangle,$$

where the kets on the left have perturbed Landau level index $\tilde{n}$ and species index s labelled through $|\tilde{n};s\rangle$, and the kets on the right are labelled only by unperturbed Landau level index n (we have suppressed the angular momentum quantum numbers).

For $V^{LL'}_{1100}$, the initial two particle state is formed from two single-particle states with $s_1 = s_2 = 0$,

$$\left|\tilde{0};0\right\rangle \otimes \left|\tilde{0};0\right\rangle = \left(\frac{2-\sqrt{2}}{2}\right)\left\{\left[\delta^{(2)}_{x_1,0}U_0^\dagger + (1+\sqrt{2})\delta^{(2)}_{x_1,1}U_1^\dagger\right]\otimes\left[\delta^{(2)}_{x_2,0}U_0^\dagger + (1+\sqrt{2})\delta^{(2)}_{x_2,1}U_1^\dagger\right]\right\}|0\rangle\otimes|0\rangle.$$

Here the left factors of the tensor products refer to particle 1 and the right factors to particle 2. As we will eventually be enacting a delta function which sets $x_1 = x_2$, the cross terms in the

above expression will vanish. Therefore, keeping only diagonal terms to first order, we have

$$\begin{aligned}|\tilde{0},0\rangle\otimes|\tilde{0};0\rangle &= \left(\frac{2-\sqrt{2}}{2}\right)\left[\left\{1+\left(\frac{\pi}{N}\right)\left(\frac{1+\sqrt{2}}{4}\right)\left(\left(a_1^\dagger\right)^2+\left(a_2^\dagger\right)^2\right)+\frac{1}{24}\left(\left(a_1^\dagger\right)^4+\left(a_2^\dagger\right)^4\right)\right\}\delta^{(2)}_{x_1,0}\delta^{(2)}_{x_2,0}\right.\\ &\quad\left.+(3+2\sqrt{2})\left\{1+\left(\frac{\pi}{N}\right)\left(\frac{1-\sqrt{2}}{4}\right)\left(\left(a_1^\dagger\right)^2+\left(a_2^\dagger\right)^2\right)+\frac{1}{24}\left(\left(a_1^\dagger\right)^4+\left(a_2^\dagger\right)^4\right)\right\}\delta^{(2)}_{x_1,1}\delta^{(2)}_{x_2,1}\right]\\ &\quad|0\rangle\otimes|0\rangle\,.\end{aligned}$$

The operator subscripts indicate which particle (1 or 2) is being raised in Landau level. Next we convert to the relative and centre of mass Landau level raising operators $\{a_1^\dagger,a_2^\dagger\}\to\{Y^\dagger,Z^\dagger\}$, and write the states in this basis through $|\tilde{n}_1;s_1\rangle\otimes|\tilde{n}_2;s_2\rangle\to\left|N_L,N_M;\tilde{N}_Y,\tilde{N}_Z;s_1;s_2\right\rangle$. We have also now included relative and centre of mass angular momentum labels, N_L and N_M. The perturbation series is valid for any angular momentum state, so we leave N_L and N_M unspecified.

$$\begin{aligned}\left|N_L,N_M;\tilde{0},\tilde{0};0,0\right\rangle &= \left(\frac{2-\sqrt{2}}{2}\right)\left[\left\{1+\left(\frac{\pi}{N}\right)\left(\frac{1+\sqrt{2}}{4}\right)\left(\left(\hat{Z}^\dagger\right)^2+\left(\hat{Y}^\dagger\right)^2\right)\right.\right.\\ &\quad\left.+\frac{1}{48}\left(\left(\hat{Z}^\dagger\right)^4+6\left(\hat{Z}^\dagger\right)^2\left(\hat{Y}^\dagger\right)^2+\left(\hat{Y}^\dagger\right)^4\right)\right\}\delta^{(2)}_{x_1,0}\delta^{(2)}_{x_2,0}\\ &\quad+(3+2\sqrt{2})\left\{1+\left(\frac{\pi}{N}\right)\left(\frac{1-\sqrt{2}}{4}\right)\left(\left(\hat{Z}^\dagger\right)^2+\left(\hat{Y}^\dagger\right)^2\right)\right.\\ &\quad\left.\left.+\frac{1}{48}\left(\left(\hat{Z}^\dagger\right)^4+6\left(\hat{Z}^\dagger\right)^2\left(\hat{Y}^\dagger\right)^2+\left(\hat{Y}^\dagger\right)^4\right)\right\}\delta^{(2)}_{x_1,1}\delta^{(2)}_{x_2,1}\right]|N_L,N_M;0,0\rangle\,.\end{aligned}$$

Enacting the operators leaves us with

$$\begin{aligned}\left|N_L,N_M;\tilde{0},\tilde{0};0,0\right\rangle &= \left(\frac{2-\sqrt{2}}{2}\right)\left[\left\{|N_L,N_M;0,0\rangle+\left(\frac{\pi}{N}\right)\left(\frac{\sqrt{2}+2}{4}\right)\Big(|N_L,N_M;0,2\rangle+|N_L,N_M;2,0\rangle\Big)\right.\right.\\ &\quad\left.+\frac{1}{48}\Big(\sqrt{24}\,|N_L,N_M;0,4\rangle+12\,|N_L,N_M;2,2\rangle+\sqrt{24}\,|N_L,N_M;4,0\rangle\Big)\right\}\delta^{(2)}_{x_1,0}\delta^{(2)}_{x_2,0}\\ &\quad+(3+2\sqrt{2})\left\{|N_L,N_M;0,0\rangle+\left(\frac{\pi}{N}\right)\left(\frac{\sqrt{2}-2}{4}\right)\Big(|N_L,N_M;0,2\rangle+|N_L,N_M;2,0\rangle\Big)\right.\\ &\quad\left.\left.+\frac{1}{48}\Big(\sqrt{24}\,|N_L,N_M;0,4\rangle+12\,|N_L,N_M;2,2\rangle+\sqrt{24}\,|N_L,N_M;4,0\rangle\Big)\right\}\delta^{(2)}_{x_1,1}\delta^{(2)}_{x_2,1}\right].\end{aligned}$$

Similarly, the final two-particle state is given by

$$\begin{aligned}\left\langle N_L,N_M;\tilde{0},\tilde{0};1,1\right| &= \left(\frac{2-\sqrt{2}}{2}\right)\Big[(3+2\sqrt{2})\left\{\langle N_L,N_M;0,0|+\left(\frac{\pi}{N}\right)\left(\frac{\sqrt{2}-2}{4}\right)\Big(\langle N_L,N_M;0,2|+\langle N_L,N_M;2,0|\Big)\right.\right.\\ &\quad\left.+\frac{1}{48}\Big(\sqrt{24}\,\langle N_L,N_M;0,4|+12\,\langle N_L,N_M;2,2|+\sqrt{24}\,\langle N_L,N_M;4,0|\Big)\right\}\delta^{(2)}_{x_1,0}\delta^{(2)}_{x_2,0}\\ &\quad+\left\{\langle N_L,N_M;0,0|+\left(\frac{\pi}{N}\right)\left(\frac{\sqrt{2}+2}{4}\right)\Big(\langle N_L,N_M;0,2|+\langle N_L,N_M;2,0|\Big)\right.\\ &\quad\left.\left.+\frac{1}{48}\Big(\sqrt{24}\,\langle N_L,N_M;0,4|+12\,\langle N_L,N_M;2,2|+\sqrt{24}\,\langle N_L,N_M;4,0|\Big)\right\}\delta^{(2)}_{x_1,1}\delta^{(2)}_{x_2,1}\right].\end{aligned}$$

Finally, we calculate the delta function overlap integral between these two states using Equation 3.10, (including the factor of 1/2 since each integral is over only half of space). We now also enact the modulo-2 Kronecker deltas which would remove the cross-terms we have chosen to

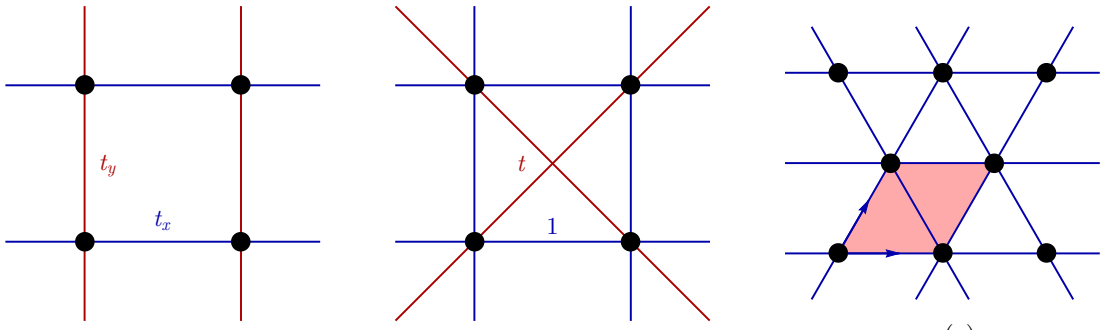

(a) (b) (c)

Figure 3.G.1: (a) Anisotropic square lattice. (b) Square lattice with diagonal hopping. (c) Triangular lattice with unit cell shaded in red.

ignore. We set $N_M = N'_M = 0$ without loss of generality and keep terms only to first order:

$$\begin{aligned}\left\langle N_L, 0; \tilde{0}, \tilde{0}; 1, 1\right| \delta\left(z_R\right) \left|N'_L, 0; \tilde{0}, \tilde{0}; 0, 0\right\rangle &= \frac{1}{8\pi l_B^2}\left[\delta_{N_L 0}\delta_{N'_L 0} + \left(\frac{\pi}{N}\right)\left(\frac{\sqrt{2}}{4}\delta_{N'_L 0}\delta_{N_L 2} + \frac{\sqrt{2}}{4}\delta_{N'_L 2}\delta_{N_L 0}\right.\right. \\ &\left.\left. + \frac{\sqrt{6}}{24}\delta_{N'_L 0}\delta_{N_L 4} + \frac{\sqrt{6}}{24}\delta_{N'_L 4}\delta_{N_L 0}\right)\right] + O\left(\frac{\pi}{N}\right)^2.\end{aligned}$$

This pseudopotential matrix can then be read off to find

$$V_{1100}^{LL'} = \frac{1}{8\pi l_B^2}\begin{pmatrix} 1 & \frac{\sqrt{2}}{4}(\pi\delta) & \frac{\sqrt{6}}{24}(\pi\delta) \\ \frac{\sqrt{2}}{4}(\pi\delta) & 0 & 0 \\ \frac{\sqrt{6}}{24}(\pi\delta) & 0 & 0 \end{pmatrix},$$

where we have only included even rows and columns and where $\delta = 1/N$.

3.G Summary of Energy and Wavefunction Corrections for Other Lattice Types

3.G.1 Anisotropic square lattice

On the anisotropic square lattice with hopping parameters t_x and t_y (see Fig. 3.G.1a), the discrete Schrödinger equation for the symmetric gauge may be written as

$$E\psi(x,y) = -t_x e^{i\pi\phi y}\psi(x+1,y) - t_x e^{-i\pi\phi y}\psi(x-1,y) - t_y e^{-i\pi\phi x}\psi(x,y+1) - t_y e^{i\pi\phi x}\psi(x,y-1).$$

If we expand this in the $\phi = 1/N$ limit, we may again use the symmetric gauge ladder operators (from Eq. (1.9)) with $l_B = \sqrt{N/2\pi}$, but now $z = \sqrt[4]{\frac{t_y}{t_x}}x + i\sqrt[4]{\frac{t_x}{t_y}}y$. This leads to the energy

corrections

$$E_n = -2(t_x+t_y) + \frac{4\pi\sqrt{t_x t_y}}{N}\left(n+\frac{1}{2}\right) - \frac{t_x+t_y}{4}\left(\frac{\pi}{N}\right)^2\left(1+2n+2n^2\right)$$

and the wavefunction corrections

$$\begin{aligned}|\tilde{n}\rangle = |n\rangle &- \frac{1}{192}\left(\frac{\pi}{N}\right)\frac{t_x+t_y}{\sqrt{t_x t_y}}\left[\sqrt{n(n-1)(n-2)(n-3)}\,|n-4\rangle - \sqrt{(n+1)(n+2)(n+3)(n+4)}\,|n+4\rangle\right] \\ &-\frac{1}{16}\left(\frac{\pi}{N}\right)\frac{t_x-t_y}{\sqrt{t_x t_y}}\left[\sqrt{n(n-1)}\,|n-2\rangle - \sqrt{(n+1)(n+2)}\,|n+2\rangle\right] \\ &-\frac{1}{24}\left(\frac{\pi}{N}\right)\frac{t_x-t_y}{\sqrt{t_x t_y}}\left[(n-2)\sqrt{n(n-1)}\,|n-2\rangle - n\sqrt{(n+1)(n+2)}\,|n+2\rangle\right].\end{aligned}$$

With anisotropic hopping, the wavefunction takes on the new symmetry of the system, which reduces from C_4 to C_2. The isotropic case can be recovered if we set $t_x = t_y$. We note that if we take the hopping amplitude in one direction to be much larger than the amplitude in the other direction (by a factor $O(N)$), then our perturbation theory becomes invalid.

3.G.2 Square lattice with next-nearest-neighbour hopping

We also consider next-nearest-neighbour hopping on the square lattice, defining the horizontal and vertical hopping amplitude to be one and the diagonal hopping amplitude to be t (as in Fig. 3.G.1b). The discrete difference equation in the Landau gauge (with $\mathbf{k} = 0$) is given by

$$\begin{aligned}E\psi(x) = &-\psi(x-1) - \psi(x+1) - 2\cos(2\pi x\phi)\,\psi(x) \\ &-2t\cos(2\pi x\phi + \pi\phi)\,\psi(x+1) - 2t\cos(2\pi x\phi - \pi\phi)\,\psi(x-1).\end{aligned}$$

Expanding as usual, we find that the energy bands are

$$E_n = -4(1+t) + 4(1+2t)\left(\frac{\pi}{N}\right)\left(n+\frac{1}{2}\right) - \left(\frac{\pi}{N}\right)^2(1+4t)\left(\frac{1}{2}+n+n^2\right)$$

and the wavefunction corrections are given by

$$|\tilde{n}\rangle = |n\rangle - \frac{1}{96}\left(\frac{\pi}{N}\right)\frac{1-4t}{1+2t}\left[\sqrt{n(n-1)(n-2)(n-3)}\,|n-4\rangle + \sqrt{(n+1)(n+2)(n+3)(n+4)}\,|n+4\rangle\right].$$

We note that increasing t from zero only decreases the relative wavefunction correction, so we expect the pseudopotential corrections to be even smaller than they are for the ordinary square lattice—the results may be interesting when t is negative, however. We recover the original square lattice case if we set $t = 0$.

3.G.3 Triangular lattice

For the triangular lattice we define $\phi = 1/N$ to be the magnetic flux per unit cell rather than per plaquette, as shown in Figure 3.G.1c. The discrete difference equation is

$$\begin{aligned} E\psi(x) &= -\psi(x-1) - \psi(x+1) - 2\cos\left(\pi\phi\left(x+\frac{1}{2}\right) + \frac{\sqrt{3}k_y}{2}\right)\psi(x+1/2) \\ &\quad -2\cos\left(\pi\phi\left(x-\frac{1}{2}\right) + \frac{\sqrt{3}k_y}{2}\right)\psi(x-1/2). \end{aligned}$$

If we substitute $\phi = p/q$, we notice that this is cyclic under the substitution $n \to n+q$ if p is even, and it is cyclic under the substitution $n \to n+2q$ if p is odd. Bloch periodicity therefore requires that $|n+q\rangle = e^{ik_x q/2}|n\rangle$ if p is even and $|n+2q\rangle = e^{ik_x q}|n\rangle$ if p is odd. Setting $\phi = 1/N$ and expanding as usual, we find that the characteristic frequency is now $\omega = 2\pi/(\sqrt{3}N)$ and the energy levels are given by

$$E_n = -6 + 4\sqrt{3}\left(\frac{\pi}{N}\right)\left(n+\frac{1}{2}\right) - \left(\frac{\pi}{N}\right)^2\left(2n^2+2n+1\right).$$

There is no correction to the wavefunction at first order, but at second order we find

$$|\tilde{n}\rangle = |n\rangle - \frac{1}{3240}\left(\frac{\pi}{N}\right)^2\left[\left(a^\dagger\right)^6 - (a)^6\right]|n\rangle$$

The addition of $|n \pm 6\rangle$ allows the wavefunction to adopt the six-fold symmetry of the lattice—but we notice that these corrections come with a factor of $1/N^2$ and so will be highly suppressed. In this sense, the triangular lattice is a better approximation to the continuum than the square lattice. The hexagonal lattice gives the same results as the triangular lattice but with $\omega = 4\pi/(3\sqrt{3}N)$ and with two copies of each wavefunction per unit cell.

3.H Derivation of Formula for Site-Site Interactions

We begin with the expression for a pseudopotential element in terms of Landau gauge wavefunctions

$$\begin{aligned} V_{s_1s_2s_3s_4}^{LL',u+iv} &= \sum_{m_1m_2m_3m_4} D_{m_1m_2}^{L*} D_{m_3m_4}^{L'} \int \mathrm{d}x_1\mathrm{d}x_2\mathrm{d}y_1\mathrm{d}y_2\, \delta(x_1-x_2-u)\,\delta(y_1-y_2-v) \times \\ &\quad e^{-2\pi i s_1 y_1/Q} e^{-2\pi i s_2 y_2/Q} e^{2\pi i s_3 y_1/Q} e^{2\pi i s_4 y_2/Q} \int \{\mathrm{d}k\} B_{m_1}(k_1') B_{m_2}(k_2') B_{m_3}(k_3') B_{m_4}(k_4') \times \\ &\quad e^{ik_1' y_1} e^{ik_2' y_2} e^{-ik_3' y_2} e^{-ik_4' y_1} \left[\tilde{\psi}_{0,k_1'}^{s_1}(x_1)\right]^* \left[\tilde{\psi}_{0,k_2'}^{s_2}(x_2)\right]^* \tilde{\psi}_{0,k_3'}^{s_3}(x_1) \tilde{\psi}_{0,k_4'}^{s_4}(x_2) \end{aligned}$$

where the definitions follow from Section 3.3.2 and the initial sum is over the appropriate Clebsch-Gordan coefficients $D^{L0}_{m_1 m_2}$ defined in Appendix 3.F . The final integral transforms to the symmetric gauge, giving

$$\begin{aligned} V^{LL',u+iv}_{s_1 s_2 s_3 s_4} &= \sum_{m_1 m_2 m_3 m_4} D^{L*}_{m_1 m_2} D^{L'}_{m_3 m_4} \int \mathrm{d}x_1 \mathrm{d}x_2 \mathrm{d}y_1 \mathrm{d}y_2 \delta\left(x_1 - x_2 - u\right) \delta\left(y_1 - y_2 - v\right) \times \\ & e^{2\pi i y_1 (s_3 - s_1)/Q} e^{2\pi i y_2 (s_4 - s_2)/Q} \left[\tilde{\psi}^{s_1}_{0,m_1}(z_1)\right]^* \left[\tilde{\psi}^{s_2}_{0,m_2}(z_2)\right]^* \tilde{\psi}^{s_3}_{0,m_3}(z_1) \tilde{\psi}^{s_4}_{0,m_4}(z_2). \end{aligned}$$

We convert to relative coordinates and fix $s_1 + s_2 = (s_3 + s_4) \mod Q$ to give

$$V^{LL',u+iv}_{s_1 s_2 s_3 s_4} = e^{-\pi i v (s_3 - s_4 - s_1 + s_2)/Q} \int \mathrm{d}x_C \mathrm{d}y_C \left[\tilde{\psi}^{s_1 s_2}_{L}(u + iv, z_C)\right]^* \delta_{\lambda_1, \lambda_2 + u} \tilde{\psi}^{s_3 s_4}_{L'}(u + iv, z_C).$$

Finally, we introduce the translation operators to give the final expression

$$V^{LL',u+iv}_{s_1 s_2 s_3 s_4} = e^{\pi i v (s_3 - s_4 + s_2 - s_1)} \left[\hat{T}_{u+iv} U^{\dagger}_{s_1 s_2} \left|L', 0; 0, 0\right\rangle\right]^{\dagger} \delta_{\lambda_1, \lambda_2 + u} \delta(z_R) \delta(\bar{z}_R) \left[\hat{T}_{u+iv} U^{\dagger}_{s_3 s_4} \left|L, 0; 0, 0\right\rangle\right],$$

where the explicit form of the $\hat{T}$ operators is given in Eq. (3.11). In this way, we transfer the spatial offset from the delta function to the wavefunctions themselves.

As an example we consider the nearest neighbour interaction,

$$\hat{V} = V\left[\delta_{z_2, z_1 + 1} + \delta_{z_2, z_1 - 1} + \delta_{z_2, z_1 + i} + \delta_{z_2, z_1 - i}\right],$$

for small flux $\phi = M/N \ll 1$ on the square lattice. The pseudopotential matrix in this case is

$$\begin{pmatrix} 4 - 2(\pi\delta) + \frac{185}{384}(\pi\delta)^2 & 0 & 0 & 0 & \frac{\sqrt{6}}{24}(\pi\delta) + \frac{\sqrt{6}}{96}(\pi\delta)^2 & 0 & 0 & 0 & \frac{\sqrt{70}}{768}(\pi\delta)^2 \\ 0 & 2(\pi\delta) - (\pi\delta)^2 & 0 & 0 & 0 & \frac{\sqrt{30}}{48}(\pi\delta)^2 & 0 & 0 & 0 \\ 0 & 0 & \frac{33}{64}(\pi\delta)^2 & 0 & 0 & 0 & 0 & 0 & 0 \\ 0 & 0 & 0 & 0 & 0 & 0 & 0 & 0 & 0 \\ \frac{\sqrt{6}}{24}(\pi\delta) + \frac{\sqrt{6}}{96}(\pi\delta)^2 & 0 & 0 & 0 & \frac{1}{384}(\pi\delta)^2 & 0 & 0 & 0 & 0 \\ 0 & \frac{\sqrt{30}}{48}(\pi\delta)^2 & 0 & 0 & 0 & 0 & 0 & 0 & 0 \\ 0 & 0 & 0 & 0 & 0 & 0 & 0 & 0 & 0 \\ 0 & 0 & 0 & 0 & 0 & 0 & 0 & 0 & 0 \\ \frac{\sqrt{70}}{768}(\pi\delta)^2 & 0 & 0 & 0 & 0 & 0 & 0 & 0 & 0 \end{pmatrix},$$

where the entire matrix is multiplied by $\frac{V}{4\pi l_B^2}$ and all rows and columns for $L \in \{0, 1, 2, 3, 4, 5, 6, 7, 8\}$ are shown. Unlike the pure delta function interaction, the nearest neighbour interaction could be experienced by both fermions and bosons.

4. The Hofstadter Model in an External Trap

We now put our perturbative approach to the Hofstadter model into practice, and use the machinery outlined in the previous chapters to calculate the energy spectra and wavefunctions that might arise in an experiment. The specific experimental set-up we consider is a system of ultracold bosonic atoms, trapped in a harmonic potential, and hopping on a lattice according to the Hofstadter Hamiltonian (2.1). This arrangement has been realised by a number of groups [153, 152], although the interaction strengths and low temperatures required to enter the fractional regime are yet to be achieved [190]. We note also that few-body FQH droplets, similar to our numerical systems, have been realised separately in rotating lattices [191]. An important complicating factor in the experimental case is the external harmonic trapping potential used to confine the atoms—we begin by discussing some of the subtle features of this trap.

4.1 Harmonic Trapping Potential

We can describe the external potential by adding a harmonic term to the noninteracting Hamiltonian, obtaining, for the continuum system,

$$\hat{H} = \sum_{i}^{N_P} \frac{1}{2m} \left(\mathbf{p}_i + e\mathbf{A}_i\right)^2 + \sum_{i}^{N_P} \frac{1}{2} m\omega_0^2 |\mathbf{r}_i|^2. \tag{4.1}$$

In this expression, $\mathbf{p}_i = -i\hbar\nabla_i$, $\mathbf{A}_i = \mathbf{A}(\mathbf{r}_i)$, N_P is the number of particles, and ω_0 describes the strength of the trap.

4.1.1 Fock-Darwin States

Hamiltonian (4.1) has been studied in great detail in the continuous regime, where it is known as the Fock-Darwin Hamiltonian [192, 193]. When the external potential is weak, the system differs very little from the Landau level description. However, as ω_0 is increased, energies and wavefunctions become closer in structure to those of a two-dimensional quantum harmonic oscillator.

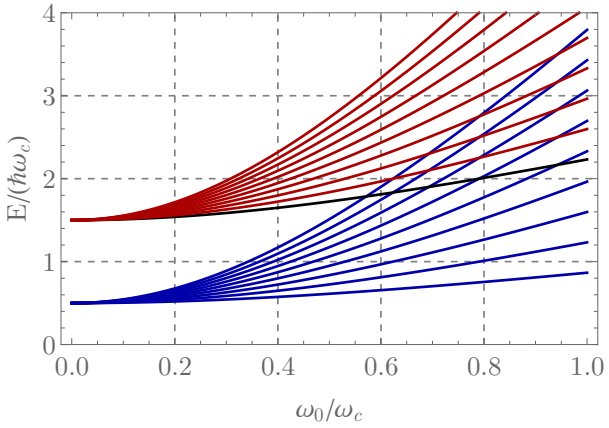

Figure 4.1: Fock-Darwin energy spectrum as the relative strength of the external trapping potential is increased from the Landau Level limit ($\omega_0 = 0$). Energy levels shown correspond to $n = 0, l \geq 0$ (blue), $n = 1, l \geq 0$ (red) and $n = 0, l = -1$ (black).

A full solution to Eq. (4.1) yields the single-particle Fock-Darwin states and energies,

$$\psi_{n,l}(r,\theta) = \frac{1}{l_N}\sqrt{\frac{n!}{\pi(n+|l|)!}}e^{-r^2/(2l_N^2)}\left(\frac{r}{l_N}\right)^{|l|}L_n^{|l|}\left[\left(\frac{r}{l_N}\right)^2\right]e^{il\theta} \tag{4.2}$$

$$E_{n,l} = (2n+1+|l|)\,\hbar\omega - \frac{1}{2}l\hbar\omega_c \tag{4.3}$$

where $L_n^{|l|}$ is an associated Laguerre polynomial, l is any integer, and n is an integer greater than or equal to zero. These states have a characteristic length and frequency defined through $l_N^2 = 1/\omega = \left(\omega_c^2/4 + \omega_0^2\right)^{-1/2}$, where we have set $\hbar = e = m = 1$ as usual. It is easily verified that the $(n = 0, l \geq 0)$ Fock-Darwin states map onto the $(n = 0, m \geq 0)$ LLL angular momentum eigenstates in the limit $\omega_0 \to 0$ (which also sets $l_N \to \sqrt{2}l_B$). In Fig. 4.1, we plot the Fock-Darwin energy spectrum as the strength of the external trap is increased.

Much of the operator algebra that we outlined in Sec. 1.4 carries over directly to Fock-Darwin case. We can again define the ladder operators

$$\tilde{a}^\dagger = \left(\frac{1}{2l_N}\bar{z} - l_N\partial_z\right), \qquad \tilde{b}^\dagger = \left(\frac{1}{2l_N}z - l_N\partial_{\bar{z}}\right), \tag{4.4}$$

which generate all of the Fock-Darwin states and are analogous to the $a^\dagger, b^\dagger$ ladder operators that arise when discussing LLs in the symmetric gauge. In terms of these operators, Hamiltonian (4.1) may be rewritten

$$\hat{H} = \left(\tilde{a}^\dagger\tilde{a} + \frac{1}{2}\right)\left(\omega + \frac{\omega_c}{2}\right) + \left(\tilde{b}^\dagger\tilde{b} + \frac{1}{2}\right)\left(\omega - \frac{\omega_c}{2}\right). \tag{4.5}$$

Once again, we note that the operators in Eq. 4.4 and the Hamiltonian above reduce to the equivalent LL expressions in the limit $\omega_0 \to 0$.

4.1.2 Kohn's Theorem

The harmonic trapping potential breaks translational symmetry and lifts the perfect degeneracy of the LLs. Rotational symmetry, however, remains preserved, and is evident in the form of the wavefunctions in Eq. (4.2). This symmetry enforces the conservation of angular momentum, but it is not immediately clear that pairwise *relative* angular momentum between particles remains conserved: if true, this would permit a description in terms of Haldane pseudopotentials. This question is resolved by Kohn's Theorem [194], which, in its original form, states:

Theorem (Kohn, 1961)**.** *The behaviour of a system of interacting charged particles with masses m_i and charges e_i in a uniform magnetic field can be decomposed into a centre of mass coordinate part and a relative coordinate part, as long as the ratio e_i/m_i is the same for all particles, i.*

Kohn's Theorem can be extended to include any external quadratic potential and any interaction that depends only on the relative displacement between pairs of particles. The simplest way to show this is directly from the interacting system Hamiltonian,

$$\hat{H} = \sum_i^{N_P} \frac{1}{2m} \left(\mathbf{p}_i + e\mathbf{A}(\mathbf{r}_i)\right)^2 + \sum_i^{N_P} \frac{1}{2} m\omega_0^2 |\mathbf{r}_i|^2 + \sum_{i<j}^{N_P} V_{\text{int}}\left(|\mathbf{r}_i - \mathbf{r}_j|\right). \tag{4.6}$$

Making use of the identity,

$$\sum_{i=1}^{N_P} \mathbf{r}_i^2 = \frac{1}{N_P}\left(\sum_{i=1}^{N_P} \mathbf{r}_i\right)^2 + \frac{1}{N_P}\sum_{i<j}^{N_P} \left(\mathbf{r}_i - \mathbf{r}_j\right)^2, \tag{4.7}$$

and defining the centre of mass quantities, $M = N_P m$, $\rho = N_P e$, $\mathbf{R} = (1/N_P)\sum_i \mathbf{r}_i$ and $\mathbf{P} = \sum_i \mathbf{p}_i$, Eq. (4.6) may be rewritten as

$$\begin{aligned} \hat{H} = {} & \frac{1}{2M}\left(\mathbf{P} + \rho\mathbf{A}(\mathbf{R})\right)^2 + \frac{1}{2} M\omega_0 |\mathbf{R}|^2 \\ & + \frac{1}{N_P}\sum_{i<j}\left[\frac{1}{2m}\left(\mathbf{p}_{ij} + e\mathbf{A}\left(\mathbf{r}_{ij}\right)\right)^2 + \frac{1}{2} m\omega_0^2 \left|\mathbf{r}_{ij}\right|^2\right] + \sum_{i<j} V_{\text{int}}\left(|\mathbf{r}_{ij}|\right). \end{aligned} \tag{4.8}$$

In this expression we have used the shorthand $\mathbf{r}_{ij} = \mathbf{r}_i - \mathbf{r}_j$, $\mathbf{p}_{ij} = \mathbf{p}_i - \mathbf{p}_j$ and the symmetric gauge $\mathbf{A}(\mathbf{r}) = -(1/2)\mathbf{r} \times \mathbf{B}$. In this form, there are no terms which mix relative and centre of mass coordinates, and so we can consider the behaviour of each independently.

Unfortunately, the presence of a lattice introduces further complications. As we have shown previously, perturbative corrections to the Hofstadter model yield quartic (and higher) powers of the position vector and its derivatives (see, for example, Eq. (2.21)). For power sums such as these, which have higher than quadratic degree, there is no simple identity akin to Eq. (4.7) that separates the COM and relative degrees of freedom. On a lattice, Kohn's theorem no longer holds, and the COM and relative motion are correlated.

In the previous chapters, we were able to circumvent this issue. Since the system was assumed to be translationally invariant, the perturbative corrections could be written entirely in terms of the LL ladder operators, $(a, a^\dagger)$, and had no dependence on the momentum ladder operators, $(b, b^\dagger)$. The only mixing of COM and relative coordinates arose in the LL index, which we ignored by always projecting to the lowest band. If we add a lattice to the Fock-Darwin system, the perturbations now involve both $(\tilde{a}, \tilde{a}^\dagger)$ and $(\tilde{b}, \tilde{b}^\dagger)$ operators, which mixes COM and relative degrees of freedom even after projection to the lowest band.

4.2 Perturbed Fock-Darwin States

We now proceed to calculate the perturbative wavefunctions of the full Hofstadter-Fock-Darwin (HFD) system, comprising a background magnetic field, square lattice, external harmonic trap, and two-body interactions. We assume that the trap is weak enough for the Landau level structure to remain intact, and that the lowest energy wavefunctions are the $n = 0, l \geq 0$ Fock-Darwin states given in (4.2).[1] We will also focus exclusively on the weak-field regime, with $\phi = 1/N$.

As in previous chapters, we consider the leading perturbative corrections to Eq. 4.5 due to discrete lattice effects. These may be written

$$\hat{H}_2 + \hat{H}_3 = -\frac{1}{24}\left(\frac{\pi}{N}\right)^2\left[\left(a - a^\dagger\right)^4 + \left(a + a^\dagger\right)^4\right] - \frac{1}{720}\left(\frac{\pi}{N}\right)^3\left[\left(a - a^\dagger\right)^6 - \left(a + a^\dagger\right)^6\right], \tag{4.9}$$

with $a, a^\dagger$ the *old* LL ladder operators (these corrections were derived in Eq. (2.21)). To proceed, we express a and $a^\dagger$ in terms of the Fock-Darwin operators through

$$a = \frac{1}{2}\left[s^{-1}\left(\tilde{a} + \tilde{b}^\dagger\right) - s\left(\tilde{b}^\dagger - \tilde{a}\right)\right], \qquad a^\dagger = \frac{1}{2}\left[s^{-1}\left(\tilde{a}^\dagger + \tilde{b}\right) - s\left(\tilde{b} - \tilde{a}^\dagger\right)\right], \tag{4.10}$$

[1] These are simply the LLL angular momentum eigenstates with the new characteristic length scale $l_B \to l_N/\sqrt{2}$.

where we have introduced the quantity

$$s = \frac{\sqrt{2}l_B}{l_N} = \left(1 + \frac{4\omega_0^2}{\omega_c^2}\right)^{\frac{1}{4}}. \tag{4.11}$$

Note that $s \to 1^+$ as $\omega_0 \to 0$. With this replacement, much of the perturbation theory carries over directly from the previous chapters. For this reason, our discussion here will be comparatively brief, and we refer the reader to Sec. 2.4 for additional details.

Recalling our previously calculated unitary perturbation operator (Eq. (2.25)),

$$U^\dagger = \exp\left\{ \left[\frac{1}{96}(\pi\delta) + \frac{1}{128}(\pi\delta)^2\right]\left[\left(a^\dagger\right)^4 - (a)^4\right] + \frac{1}{320}(\pi\delta)^2\left[\left(a^\dagger\right)^5 a - a^\dagger (a)^5\right]\right\}, \tag{4.12}$$

we simply need to replace $(a, a^\dagger) \to (\tilde{a}, \tilde{a}^\dagger, \tilde{b}, \tilde{b}^\dagger)$ according to Eq. (4.10) in order to obtain the HFD version. This will act on unperturbed FD states to give perturbed wavefunctions and energies in the same way as before, with the new feature that the expressions depend on the angular momentum quantum number.

To investigate the many-body properties of the HFD system, we return to the toolkit of Haldane pseudopotentials. We calculate perturbed two-body basis states as before, but we must now be careful to keep track of both the relative angular momentum and the COM angular momentum. We again define perturbed two-body states through

$$\left|\tilde{N}_L, \tilde{N}_M; \tilde{N}_Y, \tilde{N}_Z\right\rangle = U_1^\dagger U_2^\dagger \left|N_L, N_M; N_Y, N_Z\right\rangle,$$

where N_L and N_M are relative and COM angular momentum indices, N_Y and N_Z are relative and COM LL indices, and $U_i^\dagger$ is the single-particle unitary operator for particle i given in Eq. (4.12). Full details of the two-particle basis states are given in Appendix 3.E.

Next, we calculate the matrix elements between these basis states and our chosen interaction to find the new Haldane pseudopotentials,

$$V^{L'L;M'M} = \left\langle \tilde{L}', \tilde{M}'; \tilde{0}, \tilde{0}\right| V_{\text{int}}(z_i - z_j) \left|\tilde{L}, \tilde{M}; \tilde{0}, \tilde{0}\right\rangle, \tag{4.13}$$

where we have considered only states from the lowest HFD band. Due to the breakdown of Kohn's Theorem, these quantities now have four indices and go beyond the pseudopotential matrix formalism that we developed previously. Although this does not appear to be much of a simplification—since a projected interaction in the single-body basis would also generically

have four indices—we will find that the M-dependence takes a simple form in the HFD system, and in many cases can be ignored altogether.

For the bosonic delta function interaction, we find that the first order pseudopotentials are, written in full,

$$\begin{aligned} V^{L'L;M'M} &= \frac{1}{2\pi l_N^2}\left(\frac{\pi}{N}\right)\left[\frac{s^4}{16\sqrt{6}}\delta_{M,M'}\Big(\delta_{L',0}\delta_{L,4}+\delta_{L',4}\delta_{L,0}\Big)\right. \\ &\left.+\frac{\left(s^2-1\right)^2}{64\sqrt{2}}\Big(\delta_{L,2}\delta_{L',0}\delta_{M',M-2}\sqrt{M(M-1)}+\delta_{L,0}\delta_{L',2}\delta_{M',M+2}\sqrt{M'(M'-1)}\Big)\right]. \end{aligned} \tag{4.14}$$

For completeness, we also give the new second order pseudopotentials in Appendix 4.A.

These expressions are significantly more complicated than those in Eq. (2.30), but we note that they still conserve total angular momentum $(L+M)$ modulo four, and are symmetric if the initial and final quantum numbers are interchanged. We also note that in the weak trap limit $(\omega_0 \to 0)$, Eq. (4.14) reduces to the pseudopotentials of the pure Hofstadter model (Eq. (2.30)).

We are interested in an experimental regime that realises the Hofstadter model as closely as possible. For this reason, the external trap should only provide a small perturbation to the system, an effect that we can quantify by expanding

$$s = \left(1+\frac{4\omega_0^2}{\omega_c^2}\right)^{\frac{1}{4}} \approx 1+\alpha, \tag{4.15}$$

with $\alpha = \omega_0^2/\omega_c^2$. The first order pseudopotentials (in π/N) then have the following α-dependence, expanded up to $O(\alpha^2)$,

$$\begin{aligned} V^{L'L;M'M} &= \frac{1}{2\pi l_N^2}\left(\frac{\pi}{N}\right)\left[\frac{1+4\alpha+6\alpha^2}{16\sqrt{6}}\delta_{M,M'}\Big(\delta_{L',0}\delta_{L,4}+\delta_{L',4}\delta_{L,0}\Big)\right. \\ &\left.+\frac{\alpha^2}{16\sqrt{2}}\Big(\delta_{L,2}\delta_{L',0}\delta_{M',M-2}\sqrt{M(M-1)}+\delta_{L,0}\delta_{L',2}\delta_{M',M+2}\sqrt{M'(M'-1)}\Big)\right]. \end{aligned} \tag{4.16}$$

We see from this expression that the leading COM momentum-nonconserving terms arise at $O(\omega_0^4/\omega_c^4)$ and will be negligible if $\alpha \ll 1$—we will assume that this is the case in the numerical approaches outlined in Sec. 4.3.

4.3 Numerical Approaches

In this section we describe the numerical procedures used to calculate the energy spectra and wavefunctions, which we then compare with the exact Laughlin state. We use both exact diagonalisation on a lattice (lattice ED) and exact diagonalisation with our perturbed continuum wavefunctions (pseudopotential ED).

4.3.1 Lattice Exact Diagonalisation

Our first approach will be to solve the exact HFD lattice model in the presence of an external trap,

$$\hat{H}_{\mathrm{HFD}} = -t \sum_{\langle \mathbf{r}\mathbf{r}' \rangle} \left[c^{\dagger}_{\mathbf{r}'} c_{\mathbf{r}} \exp \left[i \int_{\mathbf{r}}^{\mathbf{r}'} \mathbf{A} \cdot \mathrm{d}\mathbf{l} \right] \right] + \frac{1}{2}\omega_0^2 \sum_{\mathbf{r}} |\mathbf{r}|^2 \hat{n}_{\mathbf{r}} + V_{\mathrm{int}} \sum_{\mathbf{r}} c^{\dagger}_{\mathbf{r}} c^{\dagger}_{\mathbf{r}} c_{\mathbf{r}} c_{\mathbf{r}}. \tag{4.17}$$

Using the symmetric gauge, we will initially solve the noninteracting Hamiltonian directly by diagonalising the discrete difference equation,

$$\begin{aligned} \hat{H}\,|x,y\rangle \;\; = \;\; & -te^{-\pi i \phi y}\,|x+1,y\rangle - te^{\pi i \phi y}\,|x-1,y\rangle - te^{\pi i \phi x}\,|x,y+1\rangle - te^{-\pi i \phi x}\,|x,y-1\rangle \\ & +\omega_0^2(x^2+y^2)\,|x,y\rangle\,. \end{aligned} \tag{4.18}$$

We note that, expanded to first order in π/N, this Hamiltonian is equivalent to the FD Hamiltonian Eq. (4.6) (up to an overall factor of two). In order to minimise the effects of a finite lattice, we choose the lattice length to be $30l_N$, which is much larger than the characteristic length scale of the FD wavefunctions, l_N. We have also verified separately that increasing this length further has only negligible effects on the single-particle energies and wavefunctions.

At this stage, we must make some approximations so that the many-body problem remains numerically tractable. First, we will keep only eigenstates that correspond to the lowest band. This amounts to a band projection, and will be a good approximation as long as the interaction strength is much less than the energy gap to the first excited band.

Secondly, within this lowest band, we will impose a cut-off, keeping only the m_c states with the lowest energy. For a weak harmonic trap, the low-energy lattice states resemble angular momentum eigenstates, and so our approximation here just imposes an angular momentum cutoff ($m < m_{\mathrm{c}}$). This cutoff is necessary because of the harmonic trap, which causes some states from the lowest band (but with large angular momentum) to mix with states in the first excited band (c.f. Fig. 4.1). The justification for this is that the Laughlin ground state (and its low-energy excitations) are made up only of single-particle states with low values of angular momentum, provided the number of particles is small (see Sec. 1.6.1).[2] Perturbative corrections can in principle introduce components with very high angular momentum, but these will be suppressed by energy denominators and the perturbation parameter $1/N$. We have also checked numerically that the energies and wavefunctions calculated in this way do not depend

[2] In general, we would need to increase m_c if we increase the number of particles, according to $m_c \propto \nu N_P$.

noticeably on the value of m_c, provided it is large enough.

We now populate this restricted single-particle basis with bosons in order to form the many-body Hilbert space. If our single-particle basis has m_c elements, and our many-body system has N_P particles, the dimension of the many-body Hilbert space can be shown to be

$$D = \begin{pmatrix} m_c - 1 + N_P \\ N_P \end{pmatrix}, \tag{4.19}$$

the number of ways of putting N_P identical objects into m_c bins.

For the results below, we will choose $m_c = 20$ and $N_P = 6$, yielding a Hilbert space dimension $D = O(10^5)$. We will reduce this dimension by a further factor of four by considering each angular momentum sector (modulo four) separately. Finally, we calculate the interaction matrix elements between these many-body basis states for the chosen lattice interaction, and diagonalise the resulting matrix numerically.

4.3.2 Pseudopotential Exact Diagonalisation

Our second numerical technique will use the perturbed wavefunctions directly. For the single-particle basis states, we take the perturbed HFD wavefunctions that correspond to the lowest Hofstadter band, which again amounts to a band projection. We apply the same angular momentum cutoff as before, setting $m < m_c$, and also choose all parameter values to agree with those used for lattice ED. With these restrictions, there should be a one-to-one correspondence between our perturbed continuum wavefunctions and the numerical single-particle wavefunctions found from lattice ED.

Next, we populate these single-particle states to form the many-body basis, which has the same dimension as in Eq. (4.19). To form the interaction matrix, we take a many-body basis state and consider each pair of particles in turn. We consider the hopping processes that can be induced by the interaction term, and calculate the matrix elements using our perturbed pseudopotential matrix. Showing only the perturbed angular momentum quantum numbers, the matrix elements are explicitly given by

$$V^{m_1 m_2 m_3 m_4} = \langle \tilde{m}_1, \tilde{m}_2 | \, \hat{V}_{\text{int}} \, | \tilde{m}_3, \tilde{m}_4 \rangle = \sum_{LL'} \sum_{M} D^{LM}_{m_1 m_2} V^{LL'} D^{L'M}_{m_3 m_4},$$

where $V^{LL'}$ is the pseudopotential matrix and $D^{LM}_{m_1 m_2}$ is the Clebsch-Gordan coefficient between single-particle and two-particle angular momentum bases, $D^{LM}_{m_1 m_2} = \langle m_1, m_2 | L, M \rangle$ (see Ap-

ϕ	1/50	1/40	1/30	1/20	1/15	1/10	1/5
W	2.19×10^{-25}	2.85×10^{-20}	3.85×10^{-15}	5.53×10^{-10}	2.20×10^{-7}	9.36×10^{-5}	4.74×10^{-2}
E_G	0.251	0.314	0.419	0.628	0.838	1.26	2.51

Table 4.1: Bandwidth and band gap for a range of ϕ.

pendix 3.F for the explicit expression). At this stage we can again diagonalise the resulting matrix numerically.

4.4 Energy Scale Considerations

There are four main energy scales in the system we are considering. These are the bandwidth, W, the gap between the two lowest HFD bands, E_G, the harmonic potential strength $\langle \hat{H}_{\text{trap}} \rangle$, and the on-site interaction strength $\langle \hat{V}_{\text{int}} \rangle$. The first two of these change intrinsically with the magnetic flux fraction, $\phi = 1/N$, while the last two can be set independently. We recall that the bandwidth is exponentially small in N, and that the energy gap is algebraically small in N. We give some specific values for these two energy scales in Table 4.1 (calculated from Eq. (2.16)).

Given that the bandwidth and band gap are set by the external magnetic field, we would ideally like to choose the harmonic trap strength and interaction strength so that they satisfy the inequality

$$W \ll \left\langle \hat{H}_{\text{trap}} \right\rangle \ll \left\langle \hat{V}_{\text{int}} \right\rangle \ll E_G, \tag{4.20}$$

where the angle brackets indicate that we are interested in the effective strength of each term on a single particle. We would like this to hold as we sweep the magnetic field strength, allowing us to explore a wide region of the butterfly spectrum. The trap strength should be larger than the bandwidth so that the droplet of particles is confined, and so that states with different angular momentum values are separated in energy. The interaction strength should be much larger than the bandwidth and trap strength so that it is the dominant energy scale and is able to stabilise an FCI state. In order for our band projection to be a good approximation, the band gap should be much larger than all other energy scales. In practice, however, FCI states often persist even when the interaction strength far exceeds the bandgap (see the discussion in Sec. 1.7.2).

We first consider the harmonic trap strength. From Eq. (4.17), we see that

$$\left\langle \hat{H}_{\text{trap}} \right\rangle \sim \omega_0^2 l_B^2 \sim \omega_0^2 N, \tag{4.21}$$

since at weaker fields the magnetic length is larger and the trap has a proportionally stronger effect. We should therefore adjust the parameter ω_0 as the magnetic field strength is changed so that the trap remains a small perturbation and we remain in the Hofstadter regime (the trap strength may be easily tuned in a cold atom experiment). If we expand the Fock-Darwin energy levels (Eq. (4.3)) in powers of ω_0, we find

$$E_{0,l\geq 0} \approx \omega_c + 2(1+l)\,\omega_c\left(\frac{\omega_0^2}{\omega_c^2}\right) = \left(\frac{2\pi}{N}\right) + 2(1+l)\left(\frac{N}{2\pi}\right)\omega_0^2, \tag{4.22}$$

We will therefore scale $\omega_0 \sim 1/\sqrt{N}$, so that the single particle HFD energy levels are the same for all magnetic flux fractions, to leading order.

However, we also found in Sec. 4.2 that the harmonic trap introduced terms in the interaction energies that broke conservation of COM angular momentum. These corrections depend on the parameter α, which in turn depends on the trap strength, ω_0. Writing the scaled trap strength as $\omega_0 = \tilde{\omega}_0/\sqrt{N}$, we see that

$$\alpha = \frac{\omega_0^2}{\omega_c^2} = \frac{N\tilde{\omega}_0^2}{4\pi^2}. \tag{4.23}$$

In this way, with the scaling chosen above, the COM momentum conservation-breaking terms become *more* significant at weak fields. Since we wish to ignore these corrections altogether, we will choose the prefactor $\tilde{\omega}_0$ small enough that α remains negligible throughout our chosen range of magnetic field strengths. Specifically, we will choose $\tilde{\omega}_0 = 2\pi \times 10^{-2}$ so that $\alpha = 10^{-4}N$.

Next we consider the interaction energy, which we recall enters the Hamiltonian through the term

$$\hat{V}_{\text{int}} = V_{\text{int}} \sum_{\mathbf{r}} c_{\mathbf{r}}^\dagger c_{\mathbf{r}}^\dagger c_{\mathbf{r}} c_{\mathbf{r}}. \tag{4.24}$$

The specific quantity of interest to us is the expectation value $\langle \hat{V}_{\text{int}} \rangle$, which should satisfy the inequality in (4.20). We recall from Eq. (4.2) that the single-particle wavefunctions have support over a circular region whose area scales as N, and correspondingly are normalised by a factor which scales as $1/\sqrt{N}$. A general interaction element between two two-body states therefore scales *at worst* as

$$\left\langle \hat{V}_{\text{int}} \right\rangle \sim V_{\text{int}} \sum_{\mathbf{r}} \psi_1^*(\mathbf{r})\psi_2^*(\mathbf{r})\psi_3(\mathbf{r})\psi_4(\mathbf{r}) \sim V_{\text{int}} \left(\frac{1}{\sqrt{N}}\right)^4 \times N = \frac{V_{\text{int}}}{N}. \tag{4.25}$$

It is this final quantity, V_{int}/N, that should satisfy inequality (4.20).[3] In an electronic system,

[3]The single-particle effect of this quantity should not depend significantly on the total number of particles, since the interaction is local and the density is expected to remain constant as the particle number is changed.

the strength of the Coulomb interaction is fixed by the material properties, but in a cold atom experiment, interactions may be tuned using Feschbach resonances [195]. For the purpose of this thesis, we will tune the interaction strength so that the quantity V_{int}/N remains fixed: this will allow us to ignore the overall scaling of the pseudopotentials in Eq. (4.14), and to instead study the effect of the off-diagonal elements, whose relative size is adjusted as the magnetic field is changed. Specifically, we will choose $V_{\text{int}}/N = 0.3$. From Table 4.1 we see that this is of the order of the band gap at weak fields, and so does not satisfy the inequality in (4.20). However, we have motivated previously that in practice this inequality does not usually matter, and we choose this value of V_{int}/N since it provides a good numerical resolution. If desired, one can use a much weaker interaction strength than this and find qualitatively similar results.[4]

4.5 Numerical Energy Spectra

In this section, we look at the changes that occur in the energy spectrum as the magnetic field strength is increased and lattice effects become more important.

First, we consider the pure many-body energy spectrum obtained directly from exact diagonalisation. In Fig. 4.2a we plot the lowest energy level in each angular momentum sector for thirteen values of the magnetic flux fraction (with $1/50 \leq \phi \leq 1/3$), using a system with six particles. We show results from both pseudopotential ED (blue) and lattice ED (red), and offset the energy levels by the magnetic flux fraction, ϕ, so that the trend can be seen more clearly. The dominant shift in energy as a function of magnetic field is due to the change in single-particle energies: higher energy levels in the spectrum, which are not plotted, would be indistinguishable from the ground state at this resolution.

The grey dashed lines show the expected single-particle energy contributions from perturbation theory, and we see that for the most part our many-body levels follow this trend closely. At magnetic field strengths beyond $\phi \approx 1/5$, however, the lattice ED energy levels start to diverge from both the pseudopotential ED values and the perturbative single-particle contribution. This divergence is due to bandwidth effects becoming important, and presages the breakdown of the Laughlin many-body state.

In Fig. 4.2b, we plot shifted energy spectra for the pseudopotential ED, obtained by subtracting off the ground state energy for each magnetic flux value. This allows us to focus on the many-body energy splitting, and indeed we observe that the ground state occurs at the mo-

[4] We note that our band projection approximation means that band-mixing effects will be ignored altogether in the numerics presented here.

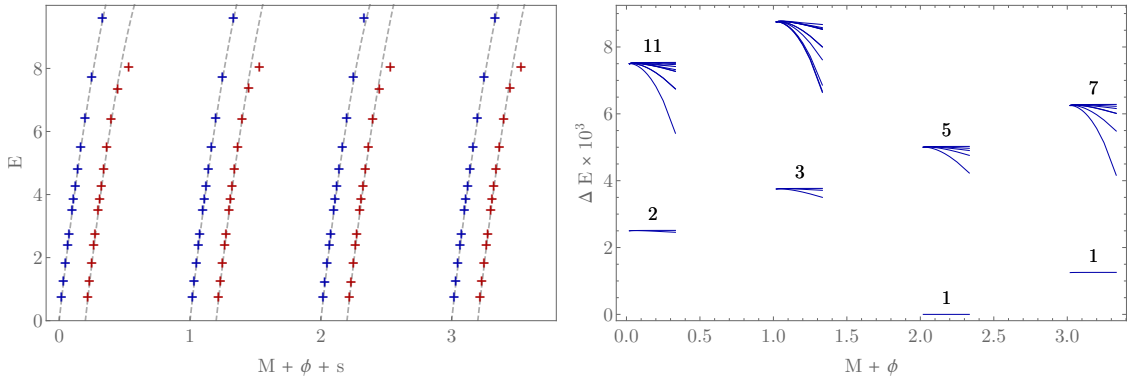

(a) (b)

Figure 4.2: (a) Lowest energy level in each angular momentum sector for thirteen magnetic flux values between $1/50 \leq \phi \leq 1/3$, considering a trapped Hofstadter system with six particles and parameters as in Sec. 4.4. Values shown are for both pseudopotential ED (blue) and lattice ED (red). Energies are offset from the angular momentum value by the magnetic flux fraction, ϕ, and the lattice ED results are shifted by a further offset, $s = 0.2$. Grey dashed lines show the single-particle contribution expected from perturbation theory. (b) Energy spectrum shifted relative to ground state energy for pseudopotential ED (blue) with six particles. Energies are offset from the angular momentum value by their magnetic flux, ϕ, with the degeneracy of each multiplet indicated above.

mentum value expected for the $\nu = 1/2$ Laughlin state, $M_{\nu=1/2} = N_P(N_P - 1)$ (modulo four), and the excited states above this have the expected edge state counting degeneracies (given in Table 1.1). We also verify in Sec. 4.6 that the components of these wavefunctions in the Fock state basis agree with the amplitudes expected for the Laughlin wavefunction, confirming that we have produced a Laughlin-like state.

The edge state spectrum in Fig. 4.2(b) shows a splitting which varies as $1/N^2$ as the magnetic field strength is increased, which is expected from our perturbation theory: the pseudopotential matrix mixes states with different angular momentum at first order in $1/N$, but only has diagonal corrections at quadratic order. These two contributions combine to give a leading energy dependence that varies as $1/N^2$. In principle, these quadratic corrections could be calculated explicitly using elementary perturbation theory, but the precise coefficients obtained would depend on the number of particles in the system.

The many-body edge spectra obtained from lattice ED are significantly more complicated, as shown in Fig. 4.3. Although the energy levels follow the pseudopotential values closely at weak magnetic fields, beyond $\phi \approx 1/7$, the values start to diverge substantially. In particular, Fig. 4.3a appears to show an avoided level crossing near $\phi = 1/5$, where the multiplet with four more units of angular momentum than the ground state ($\Delta M = 4$) would intersect the Laughlin ground state.

In Fig. 4.3b, we show a close-up of the splitting of this $\Delta M = 4$ multiplet at small magnetic

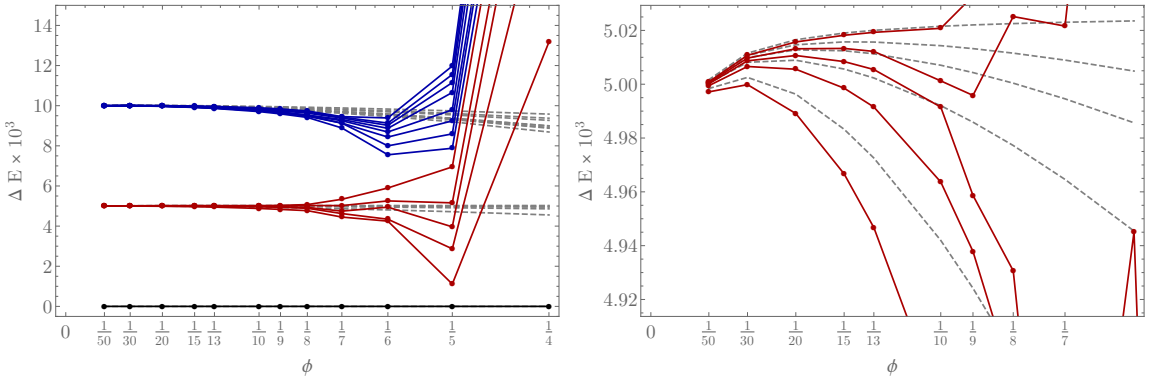

(a) (b)

Figure 4.3: (a) Energy levels in the $M = 2$ sector from lattice ED, plotted against the magnetic flux fraction, ϕ. Black, red and blue lines indicate states which originate from the $M = 6$, $M = 10$, and $M = 14$ multiplets (corresponding to the Laughlin ground state and $\Delta M = 4$ and $\Delta M = 8$ edge excitations). Grey dashed lines indicate the energy levels obtained from pseudopotential ED. (b) Close-up of energy levels in the $\Delta M = 4$ multiplet at small magnetic flux fractions. Red solid lines indicate results from lattice ED; grey dashed lines indicate results from pseudopotential ED.

flux fractions. The grey dashed lines show the quadratic energy shift from pseudopotential ED, while the red solid lines show the numerical energy shifts from lattice ED. Both sets of data agree at $O(N^{-2})$, but the lattice ED, which is exact after the band projection, takes into account higher order corrections and varies from the pseudopotential results by contributions at $O(N^{-3})$.[5] We also observe in this figure that the energy levels turn over and start decreasing for very small fields. This is a consequence of our choice of trapping potential strength, ω_0^2: by choosing this to scale as $\omega_0 \sim 1/\sqrt{N}$, higher order corrections in Eq. (4.22) eventually dominate the low-order terms that we have assumed are the leading contributions. However, it should be emphasised that all of these energy scales provide only small corrections to the zeroth order energy gap, and are eventually eclipsed by the bandwidth corrections, as evident in Fig. 4.3a.

Although an analytic expression for the edge state splitting is not easily calculated, the splittings within each multiplet exhibit certain structural features that may be predicted from the HFD Hamiltonian. We noted in Sec. 1.6.3 that Laughlin edge state excitations are related to the ground state by an additional symmetric polynomial factor. The presence of the lattice and the harmonic trap complicate this discussion substantially. However, the first elementary symmetric polynomial, $p_1 = \sum_i z_i$, continues to generate an exact eigenstate, owing to it being proportional to the centre of mass coordinate, $\mathbf{R}$.

Returning to Eq. (4.4), we see that the first elementary symmetric polynomial may be

[5]The $O(N^{-2})$ agreement between the two sets of data is not obvious from Fig. 4.3b because the quadratic dependence, which has a very small coefficient, is dwarfed by the cubic dependence in the lattice ED data. We have verified numerically that the difference between the two sets of data varies as $O(N^{-3})$, and may be improved by including higher order terms in the pseudopotential matrices.

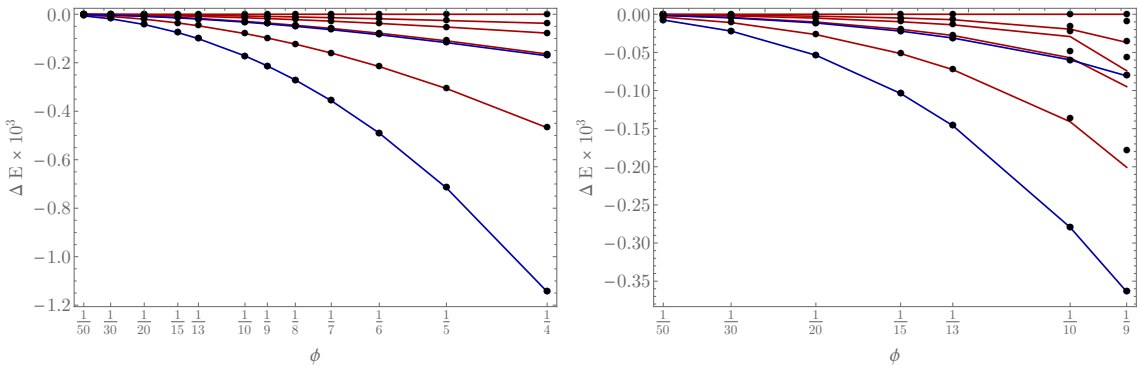

(a) (b)

Figure 4.4: Edge state spectrum in the $\Delta M = 5$ multiplet for (a) pseudopotential ED and (b) lattice ED (weak-field regime only). Energy levels are shown relative to the highest energy state (which we associate with the polynomial $(p_1)^5$) and are shown as black points. Red solid lines show the shifted energy levels from the $\Delta M = 4$ multiplet, while blue solid lines show the energy levels that appear for the first time in the $\Delta M = 5$ multiplet.

expressed as

$$p_1 = \sum_i l_N \left(\tilde{b}_i^\dagger + \tilde{a}_i \right). \tag{4.26}$$

Following the discussion in Sec. 1.6.3, we would expect to form the first edge excitation of the perturbed Laughlin ground state through

$$\begin{aligned} |\Psi_{\Delta M=1}\rangle &= \frac{1}{\mathcal{N}} \left(\prod_j U_j^\dagger \right) \left(\sum_i l_N \left(\tilde{b}_i^\dagger + \tilde{a}_i \right) \right) |\Psi_{\nu=1/2}\rangle \\ &= \frac{1}{\mathcal{N}} \left(\sum_i l_N b_i^\dagger \right) \left(\prod_j U_j^\dagger \right) |\Psi_{\nu=1/2}\rangle \equiv \frac{1}{\mathcal{N}'} B^\dagger \left| \tilde{\Psi}_{\nu=1/2} \right\rangle, \end{aligned}$$

where in the final line we have defined $B^\dagger$, a centre of mass angular momentum operator. It is clear that this operator only couples to the COM degree of freedom of the HFD model, and, in the case of a weak trapping potential, it is easily verified (from Eqs. (4.17), (4.8) and (4.5)) that

$$\left[\hat{H}_{\mathrm{HFD}}, B^\dagger \right] = 2 \left(\omega - \frac{\omega_c}{2} \right) B^\dagger \approx 4\pi \left(10^{-4} \right) B^\dagger, \tag{4.27}$$

where in the final expression we have substituted in our parameter values (and we have also noted the extra factor of two that arises in the HFD Hamiltonian compared to the FD Hamiltonian). Crucially, we find that the edge excitation obtained by multiplying the Laughlin ground state by p_1 and perturbing with the set of $U^\dagger$ operators is an exact eigenstate of the HFD model. For our choice of parameter values, the resulting state has an energy which is offset from the ground state energy by an amount $4\pi \left(10^{-4} \right)$.

	1	2	3	4	5	6	M
4.5a	$\|101000040\rangle$	$\|020000040\rangle$	$\|100200003\rangle$	$\|100101102\rangle$	$\|101000121\rangle$	$\|020000121\rangle$	30
4.5b	$\|1010012100\rangle$	$\|1010030001\rangle$	$\|0201010020\rangle$	$\|1010102010\rangle$	$\|1010110110\rangle$	$\|2001010002\rangle$	26

Table 4.2: The Fock states with largest amplitudes shown in Fig. 4.5a and Fig. 4.5b. The first row gives the six largest Fock states present in the exact Laughlin state; the second row gives the six largest perturbative corrections that are not present in the exact Laughlin state. States are labelled in the occupation number basis, $|n_{m=0}, n_{m=1}, \ldots\rangle$ etc. as outlined in Sec. 1.6.

This procedure does not work for other wavefunctions in the edge state series: in general, we must use higher order symmetric polynomials, which couple to both COM and relative coordinates. This requires us to take the full interaction potential into account, and in general we would need to diagonalise within the higher order polynomial basis. We note, however, that the elementary symmetric polynomials commute with each other. This fact, coupled with Eq. (4.27), tells us that if we have found one edge state, we can always obtain another edge state with one more unit of angular momentum by multiplying by p_1. In other words, the edge state energy spectrum at angular momentum M looks like the edge state energy spectrum at angular momentum $M-1$, shifted by an energy $4\pi\left(10^{-4}\right)$, plus some additional energy levels that do not contain the polynomial p_1. We illustrate this in Fig. 4.4 where we plot the $\Delta M = 5$ edge spectrum superimposed on the previous energy levels. We note, however, this additive structure breaks down at strong field strengths when bandwidth effects become significant, and also if the harmonic trap is strong enough that the corrections discussed in Eq. (4.16) become relevant.

4.6 Numerical Wavefunctions

We also study the form of the wavefunctions obtained from numerics. As expected, in the limit $\phi \to 0$, the ground state wavefunction tends towards the exact Laughlin $\nu = 1/2$ wavefunction. We study this by looking at the coefficients of the wavefunctions in the angular momentum occupation number (Fock state) basis, which was introduced in Sec. 1.6.

In Fig. 4.5a and Fig. 4.5c we plot the amplitudes of the dominant components of the ground state and see that they connect smoothly onto the expected continuum values as the magnetic flux is reduced. Only the six largest Fock state amplitudes are shown, and the explicit Fock states that these amplitudes correspond to are given in Table 4.2. For finite values of the magnetic flux, the amplitudes of these components show a weak quadratic decay, as expected from second order perturbation theory.

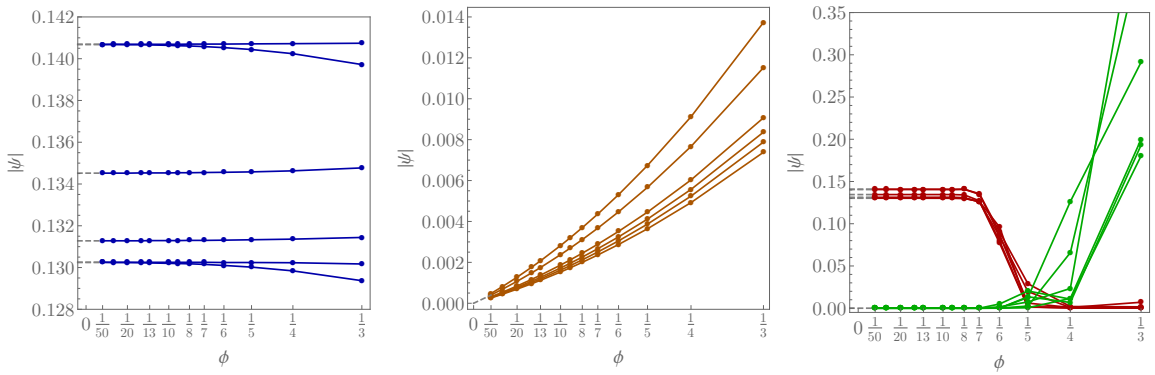

(a) (b) (c)

Figure 4.5: Ground state wavefunction amplitudes for simulations of six particles and parameter values as described in Sec. 4.4. (a) Blue solid lines show the six largest Fock state amplitudes in the ground state wavefunction obtained from pseudopotential ED (explicit Fock states given in Table 4.2). These components have total angular momentum $M = 30$ and map smoothly onto their continuum values (shown as grey dashed lines) as the field strength is reduced. (b) Six largest Fock state amplitudes from pseudopotential ED that break angular momentum conservation (by each having total $M = 26$). The explicit Fock states are given in Table 4.2. (c) Single-particle amplitudes obtained from lattice ED. Red lines show the six largest amplitudes at $\phi = 1/50$, while green lines show the six largest amplitudes at $\phi = 1/3$. Grey dashed lines show the expected amplitudes in the limit $\phi \to 0$. The Fock states corresponding to the red lines are given in Row 1 of Table 4.2; the explicit Fock states corresponding to the green lines are not given, since in this region our numerical approach breaks down.

The leading new single-particle components have four fewer units of angular momentum (occurring at $M = 26$, while the Laughlin ground state occurs at $M = 30$). The six largest of these are plotted in Fig. 4.5b, with the explicit Fock states given in Table 4.2. These amplitudes show a linear increase with the magnetic flux, as expected from the form of our perturbed pseudopotential matrix (4.16), where first order corrections are off-diagonal and mix states which have an angular momentum difference of four units. Since the exact Laughlin ground state does not contain any pairs of particles with relative angular momentum $L = 0$, the first order pseudopotential matrix can only mix in new states with four *fewer* units of angular momentum.

In a similar manner to the energy spectra considered previously, beyond $\phi \approx 1/7$, our perturbation theory breaks down. Fig. 4.5c shows both the six largest wavefunction amplitudes at $\phi = 1/50$ and the six largest wavefunction amplitudes at $\phi = 1/3$ from lattice ED. The erratic behaviour observed at large magnetic flux signals the breakdown of the Laughlin ground state.

Finally in this section, we consider the overlap of our numerical wavefunctions with the true Laughlin wavefunction as a function of magnetic flux. We define the overlap of two states ψ_A

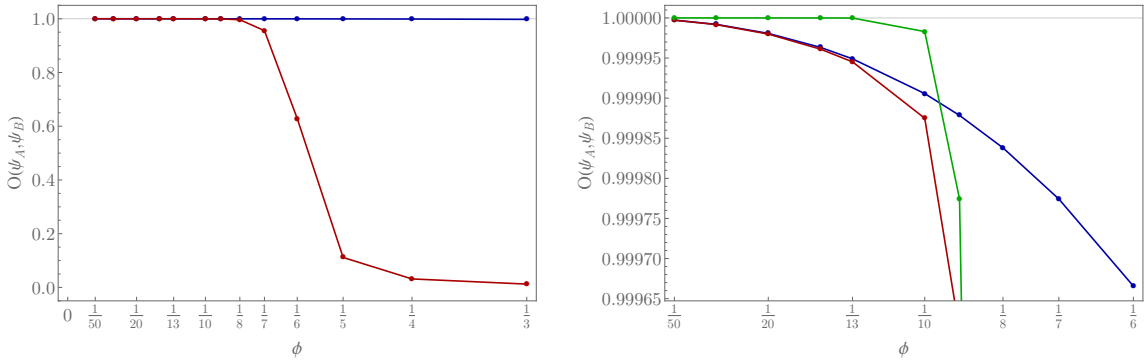

(a) (b)

Figure 4.6: Overlap of numerical wavefunctions with the exact Laughlin state ((a) full ϕ-range; (b) weak field only). Blue line shows overlap with state obtained from pseudopotential ED, red line shows overlap with state obtained from lattice ED, and green line (in (b) only) shows overlap between the two numerical wavefunctions.

and ψ_B through

$$O(\psi_A, \psi_B) = \frac{\left|\langle\psi_A|\psi_B\rangle\right|}{\sqrt{\langle\psi_A|\psi_A\rangle\langle\psi_B|\psi_B\rangle}}, \tag{4.28}$$

and in Fig. 4.6 we plot this quantity for our numerical ground states and the exact Laughlin wavefunction. This remains very close to unity until $\phi \approx 1/7$, beyond which the overlap with the state obtained from lattice ED rapidly decays to zero due to bandwidth effects.[6] Pseudopotential ED yields a ground state that is much closer to the Laughlin state, but this only accurately captures the quadratic decay of the overlap that occurs at weak fields. In Fig. 4.6 we also show the overlap between the ground states obtained from our two numerical techniques. This remains extremely close to unity until $\phi \approx 1/9$, indicating that our perturbative approach describes the exact wavefunction very accurately in the weak field regime.

4.7 Relation to Experiments

In this section we briefly discuss how our numerical results compare to the recent experimental realisations of the Hofstadter model. We will focus particularly on the optical lattice experiment in Ref. [196], in which researchers generated the Hofstadter Hamiltonian with $\phi = 1/4$ using rubidium atoms.

There are two crucial differences between this realisation and our own numerical results presented above. First, optical lattice experiments usually start from a Bose-Einstein Condensate (BEC), typically involving $O(10^5)$ atoms [152]. Although it may be possible to extend our

[6] We note that calculation of the overlap between the exact Laughlin state and the numerical lattice wavefunction have been carried out previously in Ref. [63], where the authors observed a similar decay at strong magnetic fields.

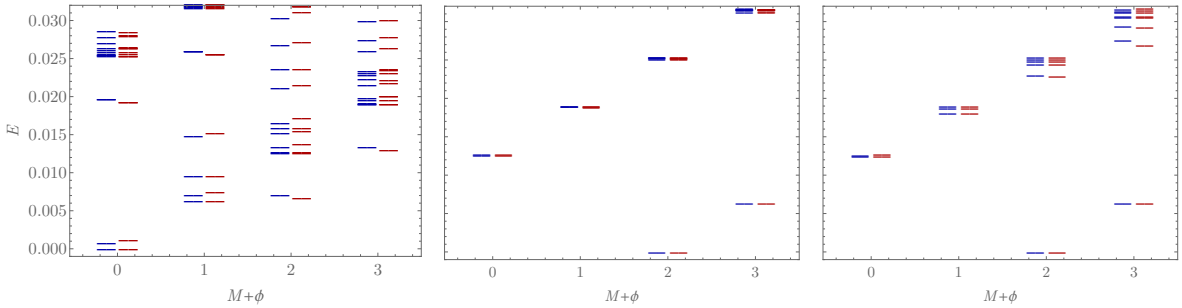

(a) $U/t = 5 \times 10^{-2}$ (b) $U/t = 5 \times 10^{-1}$ (c) $U/t = 5 \times 10^{0}$

Figure 4.7: Edge state spectrum for six particles in a Hofstadter experiment with parameters $\omega_0^2/2 = 10^{-3}t$ and $\phi = 1/10$, for three different interaction strengths. Results from pseudopotential ED (blue) and lattice ED (red) are shown, and spectra have been shifted so that the lowest energy state occures at $E = 0$. Small discrepancies between ED and pseudopotential data are due to higher order terms being neglected in the pseudopotential approximation.

approach to the thermodynamic limit, our perturbation theory as presented is most suited to systems with a small number of particles. Secondly, the interactions between particles in the cited experiments are weak enough that they may be ignored altogether at leading order [196]. We are most interested in stabilising FCI states, however, which require strong interparticle interactions.

It is likely that future experiments will circumvent these difficulties. In particular, it is already possible to tune interaction strengths in cold atom experiments using Feshbach resonances [195], and this approach might be applicable to realisations of the Hofstadter model. In addition, Ref. [191] has demonstrated the formation of few-body ($N_P = 4$) FQHE droplets in rotating optical lattices where the effective interaction strength is large—although these realisations are of the continuum FQHE, rather than the Hofstadter lattice model.

With this in mind, we will apply our perturbation theory to a set of parameter values that is experimentally realistic. From Ref. [196], we take the hopping parameter strength $t = h \times 75\text{Hz}$ and the confining potential $\omega_0^2/2 = 10^{-3}t$ (mass and lattice scales are absorbed into these definitions). Rather than using the experimental flux value $\phi = 1/4$, we choose $\phi = 1/10$, which should still be achievable in experiment but which, from above, is within the reach of our perturbative approach. Our major approximation will be to consider a system of only six particles, which is substantially different from the experimental set-up. We will allow the interaction strength to vary, so that we may identify the strength required to stabilise an FCI state.

In Fig. 4.7, we plot edge spectra for the parameter set given above and three different interaction strengths, using both pseudopotential and lattice ED. We note that there are three

distinct regimes: for very weak interactions, as in Fig. 4.7a, the energy levels are dominated by properties of the bandwidth and harmonic trap, and there is no FCI state stabilised. For moderately weak interaction strengths, as in Fig. 4.7b, an FCI state is stabilised, and we observe the edge state spectrum and degeneracies expected from the continuum Laughlin state. Finally, for interaction strengths on the order of the bandgap (although recall that the effective interaction strength $\langle V_{\text{int}} \rangle$ is reduced by a factor of N as in (4.25)), effects due to the lattice cause significant splitting in the edge state multiplets, which depend polynomially on $1/N$ and which may in principle be calculated from perturbation theory.

We therefore conclude that the relative strength of the harmonic trap and hopping parameters used in experiments so far appear to be suitable for stabilising an FCI state in the Hofstadter model. In order to detect effects specifically due to the lattice, the interaction strength should be made comparable to the hopping parameter—it remains to be seen whether this is achievable in experiments. We note, however, that the very large number of particles usually involved in a cold atom experiment may alter the results above substantially.

4.8 Discussion

We close this chapter by summarising our findings and discussing some of the advantages of our pseudopotential formalism.

In the previous sections, we have considered some of the additional features that must be taken into account if the Hofstadter model is placed in a trapping potential, as would be the case in a cold atom experiment. We found that the full system mixes COM and relative degrees of freedom, and in general we must include additional contributions in the interaction matrix elements. For a strong trapping potential, these corrections render the Haldane pseudopotential formalism somewhat unwieldy, and we may be better off using exact numerical methods. However, for a weak trapping potential, the corrections induced by the trap are essentially negligible, and our perturbative approach functions well.

We used our pseudopotential matrix to generate perturbative energy spectra and wavefunctions using exact diagonalisation, and compared the results to conventional, lattice exact diagonalisation. For weaker field strengths, with $\phi \lesssim 1/7$, both sets of numerical data agree well, and in this regime our approach has significant advantages over lattice ED. First, the pseudopotential matrix allows us to observe and quantify the connection between many-body Hofstadter states and the corresponding FQHE states. For weak fields, we find a perturbative

connection to the Laughlin $\nu = 1/2$ state when a contact interaction is used: this connection should extend to more complex FQHE states under different interactions, and to generalised Halperin states near to other regions of the butterfly spectrum. In all cases, the zeroth order state is rotationally symmetric and may be predicted from the values of the Haldane pseudopotentials.

In principle, the perturbative corrections to the energy and wavefunctions could be calculated analytically using elementary perturbation theory, although the calculations rapidly become cumbersome for large numbers of particles. Even without explicit calculation, the form of the perturbative corrections, and corresponding dependence on the small parameter $1/N$, may be read off directly from the pseudopotential matrix, enabling a phenomenological study of the many-body states.

Furthermore, pseudopotential ED does not require the storage of any single-particle wavefunctions, significantly increasing the numerical efficiency at weak fields. At the single-particle level, lattice ED requires the storage of L^2 lattice site amplitudes per state, which are then used to calculate many-body matrix elements; in pseudopotential ED the many-body matrix may be generated much more quickly from the matrix $V^{LL'}$. Of course, both methods ultimately require the diagonalisation of a large many-body matrix, whose dimension is the same in each case. In the pseudopotential case, however, this matrix is significantly sparser, which improves the efficiency of the ED algorithm significantly.

At weak fields, our pseudopotential approach gives an excellent description of the true, numerical state (see the overlap integral in Fig. 4.6b). For larger magnetic field values, however, the approximations required for our perturbative approach break down, and pseudopotential ED no longer gives an accurate description of the system. In this regime, bandwidth effects become dominant and the Laughlin-like description becomes invalid.

It is likely that our pseudopotential formalism would be most useful at other magnetic flux fractions and in more general lattice systems. For example, we found in Appendix 3.G that further neighbour hopping could lead to large perturbative corrections to the single-particle wavefunctions. This, in turn, would lead to larger pseudopotential corrections and more substantial changes to the energy spectra and wavefunctions. Furthermore, expansion about other flux fractions, as in Chapter 3, or the use of different interactions may lead to the formation of states that differ substantially from the Laughlin wavefunction, even at zeroth order in $1/N$. We leave a discussion of these extensions to elsewhere.

Appendices for Chapter 4

4.A Second Order Pseudopotential Corrections

In this appendix, we give the second order corrections to the pseudopotential matrix that arise in the HFD model.

$$
\begin{aligned}
& V^{L'L;M'M}, \text{ 2nd order} \\
= \; & \frac{1}{2\pi l_N^2}\left(\frac{\pi}{N}\right)^2\Bigg[-\frac{1}{49152s^4}\Big(3M^2\left(s^4+1\right)\left(s^2-1\right)^4 \\
& +3M\left(3s^8+2s^6+22s^4+2s^2+3\right)\left(s^2-1\right)^2+2\left(5s^{12}+57s^8+47s^4+3\right)\Big)\delta_{L,0}\delta_{L',0}\delta_{M,M'} \\
& +\frac{\left(1-s^2\right)^2}{1024\sqrt{2}s^2}\Big[\sqrt{M(M-1)}\left(1+4s^2+7s^4+M(1-s^2)^2\right)\delta_{L,2}\delta_{L',0}\delta_{M',M-2} \\
& +\sqrt{M'(M'-1)}\left(1+4s^2+7s^4+M'(1-s^2)^2\right)\delta_{L,0}\delta_{L',2}\delta_{M,M'-2}\Big] \\
& +\frac{(1-s^2)^3}{12288\sqrt{2}s^2}\Big[\sqrt{M(M-1)}\left(1+M+2s^2-Ms^2+3s^4\right)\delta_{L,0}\delta_{L',2}\delta_{M',M-2} \\
& +\sqrt{M'(M'-1)}\left(1+M'+2s^2-M's^2+3s^4\right)\delta_{L,2}\delta_{L',0}\delta_{M,M'-2}\Big] \\
& +\frac{\sqrt{3}(1-s^2)^4}{8192\sqrt{2}}\Big[\sqrt{M(M^3-6M^2+11M-6)}\delta_{L,4}\delta_{L',0}\delta_{M',M-4} \\
& +\sqrt{M'((M')^3-6(M')^2+11M'-6)}\delta_{L,0}\delta_{L',4}\delta_{M,M'-4}\Big] \\
& +\frac{\sqrt{3}s^2}{256\sqrt{2}}\Big[\left(1+3s^4+M(1-s^2)^2\right)\delta_{L,4}\delta_{L',0}\delta_{M,M'}+\left(1+3s^4+M'(1-s^2)^2\right)\delta_{L,0}\delta_{L',4}\delta_{M,M'}\Big] \\
& +\frac{\sqrt{5}s^4(1-s^2)^2}{2048}\Big[\sqrt{M(M-1)}\delta_{L,6}\delta_{L',0}\delta_{M',M-2}+\sqrt{M'(M'-1)}\delta_{L,0}\delta_{L',6}\delta_{M,M'-2}\Big] \\
& +\frac{\sqrt{35}s^8}{1536\sqrt{2}}\Big[\delta_{L,8}\delta_{L',0}\delta_{M',M}+\delta_{L,0}\delta_{L',8}\delta_{M',M}\Big]+\frac{\left(1+s^2\right)^4}{4096}\Big[\delta_{L,2}\delta_{L',2}\delta_{M',M}\Big] \\
& +\frac{\left(1+s^2\right)^4}{4096}\Big[\delta_{L,2}\delta_{L',2}\delta_{M',M}\Big]+\frac{(1-s^2)^2}{8192}\Big[M(3+10s^2+3s^4+M(1-s^2)^2\Big]\delta_{L,2}\delta_{L',2}\delta_{M',M} \\
& +\frac{s^4(1-s^2)^2}{2048\sqrt{3}}\Big[\sqrt{(M^2+3M+2)}\delta_{L,4}\delta_{L',2}\delta_{M',M+2}+\sqrt{((M')^2+3M'+2)}\delta_{L,2}\delta_{L',4}\delta_{M,M'+2}\Big] \\
& +\frac{s^8}{1536}\delta_{L,4}\delta_{L',4}\delta_{M,M'}\Big]
\end{aligned}
$$

5. Fractional Chern Insulators in Bands with Zero Berry Curvature

In this chapter, we move away from the Hofstadter model and describe a general method for creating *interaction-stabilised* FCI states. In Sec. 5.1 we provide some background to the approach and introduce the Haldane honeycomb model, which we will use as a representative FCI system throughout this chapter. In Sec. 5.2 we describe the approach in detail and extend it to time-reversal symmetric systems in Sec. 5.3. In Sec. 5.4 we provide numerical evidence to support our argument, observing many of the FCI numerical signatures that were discussed in Sec. 1.7.3. Finally, in Sec. 5.5 we give some general remarks and discuss the experimental feasibility of the approach.

5.1 Background

The usual method for generating an FCI state, as outlined in Sec. 1.7, is to fractionally fill a single-particle Chern band and switch on interactions. If the interaction is chosen correctly, the resulting state will have a fractionally quantised Hall conductivity. While this has proved to be a reasonable and successful approach to the problem, we believe it overemphasises the structure of the noninteracting band, which may be irrelevant if the particles interact strongly.

To make this point clear, we will construct an example that starts with a noninteracting system having zero Berry curvature everywhere in the Brillouin zone. Then, by adding an appropriately chosen interaction that breaks time reversal symmetry (either explicitly or spontaneously), we will find that the ground state is an FCI. We will then show how similar interactions may be used to generate a time reversal-symmetric, fractional quantum spin Hall insulator [197], which is an example of a fractional topological insulator (FTI). We support our findings with numerical evidence from exact diagonalisation studies. While our analytic arguments rely on the use of long-range interactions, we find in our numerical work that even fairly short-range interactions can form FCIs in bands with zero Berry curvature.

5.1.1 The Haldane Model

In this subsection, we briefly outline the Haldane model [104], which we will use as an example of a 'typical' Chern insulator later in this chapter. The system is defined on a honeycomb, as

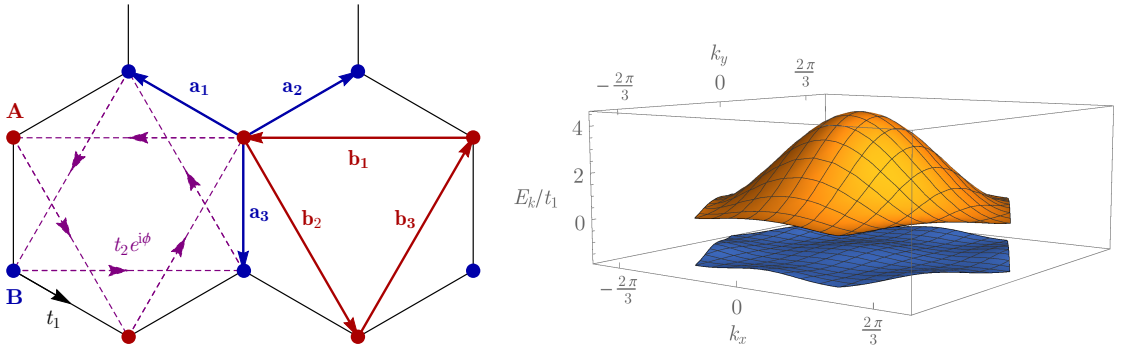

(a) (b)

Figure 5.1: (a) Haldane honeycomb model, with A-sublattice shown in red and B-sublattice shown in blue. Blue vectors labelled $\mathbf{a}_i$ show nearest neighbour displacements, red vectors labelled $\mathbf{b}_i$ show next-nearest neighbour vectors (or equivalently, lattice vectors). Purple dashed lines indicate hopping directions with positive phase. (b) Band structure of the Haldane model using parameter values $\cos\phi = 3\sqrt{3/43} = t_1/(4t_2)$ to achieve a flatness ratio of $F \approx 7$ [111]. Nearest neighbour distance is taken to be one.

shown in Fig. 5.1a, where we label the two sublattices by the letters A and B. In real space, the tight-binding Hamiltonian may be written

$$\hat{H} = t_1 \sum_{\langle \mathbf{r}\mathbf{r}' \rangle} \left[c^\dagger_{\mathbf{r}'} c_{\mathbf{r}} + h.c. \right] + t_2 \sum_{\langle\langle \mathbf{r}\mathbf{r}' \rangle\rangle} \left[c^\dagger_{\mathbf{r}'} c_{\mathbf{r}} e^{i\phi_{\mathbf{r}\mathbf{r}'}} + h.c. \right] + \sum_{\mathbf{r}} M_{\mathbf{r}} c^\dagger_{\mathbf{r}} c_{\mathbf{r}}, \tag{5.1}$$

where $\langle \cdot \rangle$ indicates nearest neighbours (NN) and $\langle\langle \cdot \rangle\rangle$ indicates next-nearest neighbours (NNN). The phase $\phi_{\mathbf{r}\mathbf{r}'} = \pm\phi$ is positive for anticlockwise hops around a hexagonal plaquette (shown as arrows in Fig. 5.1b) and negative for clockwise hops, and the offset $M_{\mathbf{r}} = \pm M$ is positive for sites on the A-sublattice and negative for sites on the B-sublattice.

Since we have two distinct sites within a unit cell (corresponding to each sublattice), taking the Fourier transform yields a 2×2 matrix, which we write in terms of the Pauli matrices $\boldsymbol{\sigma}_i$ as

$$\begin{aligned} \hat{H}(\mathbf{k}) &= 2t_2 \cos\phi \left[\sum_i \cos(\mathbf{k}\cdot\mathbf{b}_i) \right] \mathbf{I} + t_1 \left[\sum_i \left[\cos(\mathbf{k}\cdot\mathbf{a}_i)\boldsymbol{\sigma}_1 + \sin(\mathbf{k}\cdot\mathbf{a}_i)\boldsymbol{\sigma}_2 \right] \right] \\ &\quad + \left[M - 2t_2 \sin\phi \left[\sum_i \sin(\mathbf{k}\cdot\mathbf{b}_i) \right] \right] \boldsymbol{\sigma}_3 \\ &\equiv H_0(\mathbf{k})\mathbf{I} + H_x(\mathbf{k})\boldsymbol{\sigma}_1 + H_y(\mathbf{k})\boldsymbol{\sigma}_2 + H_z(\mathbf{k})\boldsymbol{\sigma}_3. \end{aligned} \tag{5.2}$$

In this expression, $\mathbf{a}_i$ are NN lattice vectors and $\mathbf{b}_i$ are NNN lattice vectors, as shown in Fig. 5.1a. We can diagonalise this to find the band solutions

$$E_\pm(\mathbf{k}) = H_0(\mathbf{k}) \pm |\mathbf{H}(\mathbf{k})|\,, \tag{5.3}$$

with $|\mathbf{H}(\mathbf{k})| = \sqrt{H_x(\mathbf{k})^2 + H_y(\mathbf{k})^2 + H_z(\mathbf{k})^2}$. These are plotted for a set of parameter values in

Fig. 5.1b.

We can calculate the Berry curvature from the wavefunctions as outlined in Sec. 1.7.1, and find a nonzero Chern number when $|M/t_2| < 3\sqrt{3}\,|\sin\phi|$: $C = +1$ when $0 \leq \phi \leq \pi$ and $C = -1$ when $-\pi \leq \phi \leq 0$. By adjusting the strengths of t_1 and t_2, it is possible to obtain a flatness ratio of $F \approx 7$ for the lowest band [111]. If one adds next-next-nearest neighbour hopping it is possible to obtain a flatness ratio of $F \approx 50$ [126], making the lowest band very suitable for supporting an FCI state. Indeed, bosonic FCI states at $\nu = 1/2$ and $\nu = 1/4$ [126], and fermionic FCI states at $\nu = 1/3$ [127] have been numerically observed in flattened Haldane models. These have been shown to be adiabatically connected to the FQHE Laughlin states at the same filling fraction [19, 20].

5.2 Interaction-Stabilised FCI States

5.2.1 FCI in a Band with Nonzero Chern Number

Following the general discussion in Sec. 1.7, we first outline some notation for the realisation of a conventional FCI state. In Sec. 5.2.1 we will then attempt to reproduce this state, starting from a band with zero Berry curvature.

Although our construction is very general, let us restrict our attention to the case of spinless particles on a honeycomb. We consider a kinetic energy,

$$\tilde{K} \;=\; \sum_{\mathbf{r},\mathbf{r}'} \tilde{t}_{\mathbf{r}\mathbf{r}'}\, c^\dagger_{\mathbf{r}} c_{\mathbf{r}'}, \tag{5.4}$$

where $\mathbf{r}$ and $\mathbf{r}'$ are summed over the sites of the lattice and $\tilde{t}_{\mathbf{r}\mathbf{r}'}$ describes the hopping amplitudes. In order to produce a Chern band, the hoppings (which are short-range) couple the sublattices, and phases are introduced which break time reversal symmetry. For example, $\tilde{t}_{\mathbf{r}\mathbf{r}'}$ may be chosen to describe the flattened Haldane honeycomb model (Sec. 5.1.1).

We now introduce a suitable short-range interaction (such as a nearest-neighbour repulsion), which we write as

$$\tilde{V} = \sum_{\mathbf{r}\mathbf{r}'} v_{\mathbf{r}\mathbf{r}'} \hat{n}_{\mathbf{r}} \hat{n}_{\mathbf{r}'}, \tag{5.5}$$

with $\hat{n}_{\mathbf{r}} = c^\dagger_{\mathbf{r}} c_{\mathbf{r}}$ the particle number on site $\mathbf{r}$. If chosen correctly, the total Hamiltonian $\tilde{H} = \tilde{K} + \tilde{V}$ will produce an FCI ground state at the appropriate particle filling fraction. For example, the interaction might stabilise a Laughlin-like FCI state at $\nu = 1/p$ (see discussion in Sec. 5.1.1).

5.2.2 FCI in a Band with Zero Berry Curvature

We now consider a different band structure, described by a kinetic energy K, which has zero Berry curvature throughout the Brillouin zone. We claim that we can switch on an interaction, V, such that the ground state of this new model is also an FCI and is adiabatically connected to the FCI described in Sec. 5.2.1. Our plan is to choose the interaction V such that $H = K + V$ mimics the Hamiltonian $\tilde{H}$, which is known to give an FCI.

To be specific, let us write the noninteracting kinetic energy as

$$K = \sum_{\mathbf{r},\mathbf{r}'} t_{\mathbf{r}\mathbf{r}'}\, c^\dagger_{\mathbf{r}} c_{\mathbf{r}'} \tag{5.6}$$

where $t_{\mathbf{r}\mathbf{r}'}$ describes new hopping parameters. For simplicity we will consider a hopping model which is diagonal in the sublattices, i.e.

$$t_{\mathbf{r}\mathbf{r}'} = \begin{cases} t^A_{\mathbf{r}\mathbf{r}'} & \text{if } \mathbf{r}, \mathbf{r}' \in A \\ t^B_{\mathbf{r}\mathbf{r}'} & \text{if } \mathbf{r}, \mathbf{r}' \in B \\ 0 & \text{otherwise} \end{cases} .$$

We also break the symmetry between sublattices by giving each one a different on-site energy, $t_{\mathbf{r}\mathbf{r}}$. In this way, we can arrange such that the two bands do not overlap in energy, the eigenstates are of the simple plane wave form $e^{i\mathbf{k}\cdot\mathbf{R}}$, and each band involves only one sublattice. Since the bands are completely decoupled, for any translationally invariant hopping $t_{\mathbf{r}\mathbf{r}'}$, the eigenfunctions have trivial structure and all bands have zero Berry curvature (F) throughout the Brillouin zone (see Sec. 1.7 for the definition of this quantity).

Now, certain interactions, which are short-range with a decay length ξ on the order of several lattice spacings, can be treated accurately within mean field theory as long as ξ is much larger than the interparticle spacing. Consider an operator

$$\hat{N}_{\mathbf{r}} = \frac{1}{\bar{n}} \sum_{\mathbf{r}'} f(\mathbf{r}' - \mathbf{r}) \hat{n}_{\mathbf{r}'} \tag{5.7}$$

where $\bar{n}$ is the average density of electrons in the system. In this expression, f is some function (like a Gaussian) that is smooth and slowly decaying with length scale ξ, and has normalisation $\sum_{\mathbf{r}'} f(\mathbf{r}' - \mathbf{r}) = 1$. By short-range with decay length ξ, we mean that the function $f(\mathbf{r}' - \mathbf{r})$ satisfies

$$\left| f(\mathbf{r}' - \mathbf{r}) \right| < C e^{-|\mathbf{r}' - \mathbf{r}|/\xi} \tag{5.8}$$

for all sufficiently large $|\mathbf{r}' - \mathbf{r}|$ and with finite constants C and ξ.

In this way, the operator $\hat{N}_{\mathbf{r}}$ measures the density of particles in a region of length scale ξ and compares it to the average density, $\bar{n}$. If the state being operated on has approximately uniform density, and if we take ξ to be large enough, it must be the case that $\hat{N}_{\mathbf{r}}$ is extremely close to unity (since we are comparing the average density in a very large region to the real average density). We can then accurately approximate $\hat{N}_{\mathbf{r}}$ by unity and do not need to treat it as an operator. As we take ξ larger and larger, this approximation becomes more and more accurate (assuming there is no phase separation). The fluctuations of $\hat{N}_{\mathbf{r}}$ around this average may be treated perturbatively (see Appendix 5.A).

We may now consider the interaction term

$$U = \frac{1}{2}\sum_{\mathbf{r}\mathbf{r}'} T_{\mathbf{r}\mathbf{r}'} : \left[\hat{N}_{\mathbf{r}} c^\dagger_{\mathbf{r}} c_{\mathbf{r}'} + c^\dagger_{\mathbf{r}} c_{\mathbf{r}'} \hat{N}_{\mathbf{r}'}\right] :, \tag{5.9}$$

where $T_{\mathbf{r}\mathbf{r}'}$ is an interaction strength (to be described below) and the entire expression is normal ordered. This operator is Hermitian and includes four particle operators, although it is not generally a density-density interaction. The interaction is short-range in that it involves particles that are separated by a maximum distance on the order of ξ. In the mean field limit, $\hat{N}_{\mathbf{r}}$ becomes unity and we obtain $U \to \sum_{\mathbf{r}\mathbf{r}'} T_{\mathbf{r}\mathbf{r}'}\, c^\dagger_{\mathbf{r}} c_{\mathbf{r}'}$, which is simply a hopping term. Thus, let us choose

$$T_{\mathbf{r}\mathbf{r}'} = \tilde{t}_{\mathbf{r}\mathbf{r}'} - t_{\mathbf{r}\mathbf{r}'}, \tag{5.10}$$

where $t_{\mathbf{r}\mathbf{r}'}$ and $\tilde{t}_{\mathbf{r}\mathbf{r}'}$ were defined in Eqs. (5.2.2) and (5.4) respectively, so that $K + U \to \tilde{K}$ at the mean field level. In this way, our scheme uses an interaction to modify the 'effective' band structure of the underlying (topologically trivial) model. Note that since $\tilde{t}_{\mathbf{r}\mathbf{r}'}$ breaks time reversal, so too does $T_{\mathbf{r}\mathbf{r}'}$.[1]

One might worry that this density-dependent interaction is unstable to phase separation—and indeed, it is fairly simple to write down an expression for $T_{\mathbf{r}\mathbf{r}'}$ for which this occurs. To make sure that this is always disfavoured, we can add a diagonal term to the interaction strength, writing

$$T_{\mathbf{r}\mathbf{r}'} \to T_{\mathbf{r}\mathbf{r}'} + D\delta_{\mathbf{r}\mathbf{r}'}, \tag{5.11}$$

where the second term may be absorbed into the amplitude $T_{\mathbf{r}\mathbf{r}'}$. When added to Eq. (5.9), this diagonal term generates a density-density interaction between a particle at $\mathbf{r}$ and its surrounding

[1] The normal ordering is important if U is to be a pure interaction: if they are not normal ordered, terms of the form $c^\dagger_{\mathbf{r}'} c_{\mathbf{r}} c^\dagger_{\mathbf{r}} c_{\mathbf{r}}$ will contain pieces that may be written as pure hopping terms using anti-commutation relations.

neighbourhood, suppressing density fluctuations on the scale of ξ. By adjusting the strength of D, we can ensure that complete phase separation is never favoured, but that the small density fluctuations required for an FCI state are allowed.

As mentioned previously, our mean field picture is exact in the large ξ limit. Another concern is whether this mean field state remains stable in the presence of fluctuations about this limit. In Appendix 5.A we discuss the perturbative corrections due to the interaction term U, and justify the stability of the FCI state. We also provide numerical evidence in support of the FCI state in Sec. 5.4.

The interaction U changes the effective band structure of the model, and so if we now use the total interaction $V = \tilde{V} + U$, then the Hamiltonian $H = K + V$ completely mimics the $\tilde{H}$ from Sec. 5.2.1 and will have an FCI ground state. As required, the noninteracting band structure of K has zero Berry curvature and the topological properties are induced purely by the interaction term, V.

The idea underpinning this approach is that hopping terms are essentially a subset of all possible interaction terms. By introducing an auxiliary operator—in this case a local density operator—that acts as a number on the ground state, an interaction can be written down that modifies the effective single-particle band structure. The trade-off for this is that the interactions are no longer density-density, and have a range that is finite but may cover several unit cell lengths.

In the expression above we have broken time-reversal symmetry by hand with our choice of interaction U. If preferred, it is possible to generate an FCI state spontaneously with a time reversal-invariant interaction, as discussed in the next section. This requires us to introduce a spin-1/2 degree of freedom, but will also allow quantum spin Hall insulator (or FTI) states to be realised.

5.3 Time Reversal Invariant Interactions

5.3.1 Spinful Band Models

One objection to the approach outlined above is that it breaks time reversal (TR) symmetry explicitly through the interaction U. In order to use a TR-symmetric interaction, we now promote the spinless particles to spin-1/2 fermions. These obey the usual interrelations under TR, which can be written as

$$\Theta c_{\mathbf{r}\sigma}\Theta^{-1} = i\tau^{y}_{\sigma\sigma'}c_{\mathbf{r}\sigma'}, \tag{5.12}$$

where τ^y is the Pauli y-matrix, σ and σ' are spin labels, and Θ is the TR operator (discussed in Sec. 1.7.1). We have also included a spin index on the field operators, $c_{\mathbf{r}\sigma}$.

The underlying topologically trivial bands must now have a spin dependence. For simplicity, we will treat spin as a good quantum number and write the kinetic energy term as

$$K' = \sum_{\mathbf{r}\mathbf{r}'\sigma} t'_{\mathbf{r}\mathbf{r}'\sigma}\, c^\dagger_{\mathbf{r}\sigma} c_{\mathbf{r}'\sigma},$$

although in general we could include spin-flipping terms. As before, we will assume that the different sublattices have different on-site energies. Then, following the arguments of Sec. 5.2.2, each of the four bands will have exactly zero Berry curvature.

For the hopping parameters of our target Chern band model, we take $\tilde{t}_{\mathbf{r}\mathbf{r}'}$ from Eq. (5.4) for one spin species but, crucially, invert the Chern number for the other spin species by taking the conjugate hopping. In other words, we take

$$\tilde{t}'_{\mathbf{r}\mathbf{r}'\uparrow\uparrow} = \tilde{t}_{\mathbf{r}\mathbf{r}'}, \qquad \tilde{t}'_{\mathbf{r}\mathbf{r}'\downarrow\downarrow} = \left[\tilde{t}_{\mathbf{r}\mathbf{r}'}\right]^*$$

and set any spin-flipping terms to zero. This defines a new topologically nontrivial kinetic energy, $\tilde{K}'$, which one can easily show is symmetric under TR symmetry. This kinetic energy therefore generates a low-energy band for each spin species, and these have equal and opposite (nonzero) Chern number when filled.

The framework outlined above leads to a Hamiltonian that conserves spin. For example, $\tilde{K}'$ could describe the kinetic energy of the Kane-Mele model *without* the Rashba spin-orbit term [197]. In principle, our approach could be generalised to TR-invariant models that do not conserve spin, such as the full Kane-Mele model. However, in that case, the interactions we describe below would involve complicated terms that mix both physical spin species—we will restrict our discussion to the simpler, spin-conserving case.

To generate a fractional state, we would partially fill the lowest band for each spin species and turn on a short-range interaction,

$$\tilde{V}' = \sum_{\mathbf{r}\mathbf{r}'\sigma} v'_{\mathbf{r}\mathbf{r}'\sigma} \hat{n}_{\mathbf{r}\sigma} \hat{n}_{\mathbf{r}'\sigma}.$$

This is diagonal in the spin index and so at this stage there is no interaction between spins. The total Hamiltonian, $\tilde{H}' = \tilde{K}' + \tilde{V}'$, would generate a fractional topological state, but the overall Chern number would depend on the filling fraction of each of the two lowest spin bands.

If both bands are filled equally, say at $\nu = 1/3$ each, then the system will retain its time reversal symmetry and will form a fractional topological insulator (FTI) state. If one band remains empty but the other is (fractionally) filled, then the system could spontaneously break time reversal symmetry and form an FCI state, depending on the interaction V. The relative stability of these two possibilities will be discussed in Sec. 5.3.3.

5.3.2 Topological Phases in Bands with Zero Berry Curvature

We now follow a similar approach to Sec. 5.2.2 to write down an interaction which changes the effective band structure from K' to $\tilde{K}'$. We use the local density operator $\hat{N}_{\mathbf{r}}$ as defined in Eq. (5.7), but the lattice site density operator now sums over both spin species, $\hat{n}_{\mathbf{r}} = \sum_\sigma \hat{n}_{\mathbf{r}\sigma}$. We write

$$U' = \sum_{\mathbf{r}\mathbf{r}'\sigma\sigma'} T'_{\mathbf{r}\mathbf{r}'\sigma\sigma'} : \left[\hat{N}_{\mathbf{r}} c^\dagger_{\mathbf{r}\sigma} c_{\mathbf{r}'\sigma'} + c^\dagger_{\mathbf{r}\sigma} c_{\mathbf{r}'\sigma'} \hat{N}_{\mathbf{r}'}\right] :, \tag{5.13}$$

where any diagonal interaction-hopping terms necessary to prevent phase separation have been absorbed into $T'_{\mathbf{r}\mathbf{r}'}$. Choosing

$$T'_{\mathbf{r}\mathbf{r}'} = \tilde{t}'_{\mathbf{r}\mathbf{r}'} - t'_{\mathbf{r}\mathbf{r}'}, \tag{5.14}$$

and following our previous reasoning, in the mean field limit we find $K' + U' \to \tilde{K}'$, which generates a topological band for each spin species. Finally, using the complete interaction $U' + \tilde{V}'$, it is possible to generate a fractional topological state from the noninteracting, zero Berry curvature system.

5.3.3 Tuning Ferromagnetism

We noted previously that Hamiltonian $\tilde{H}'$ could generate either an FCI or an FTI state, depending on whether or not TR symmetry was spontaneously broken. For example, if the lowest two bands were filled with density $(\nu_\uparrow, \nu_\downarrow) = (1/3, 1/3)$ then a state with zero Chern number but nonzero spin Chern number would be produced, where we define the spin Chern number through $C_{\text{spin}} = C_\uparrow - C_\downarrow$, with C_σ the Chern number of particles with spin σ. On the other hand, if the fillings were $(\nu_\uparrow, \nu_\downarrow) = (1/3, 0)$ then an FCI state with nonzero Chern number would be produced.[2]

These states occur at different overall fillings, but also depend on whether the system is

[2]One might prefer to compare the stability of $(\nu_\uparrow, \nu_\downarrow) = (1/3, 1/3)$ to the state $(\nu_\uparrow, \nu_\downarrow) = (2/3, 0)$, which has the same overall filling fraction. However, it was suggested in Ref. [129] that particle-hole conjugate FCI states are not easily stabilised in band systems due to the lack of particle-hole symmetry. There could, however, be direct competition between bosonic (Laughlin-like) fractional phases, such as between $(\nu_\uparrow, \nu_\downarrow) = (1/4, 1/4)$ and $(\nu_\uparrow, \nu_\downarrow) = (1/2, 0)$ phases.

susceptible to spontaneous ferromagnetism. In order to tune this susceptibility, we introduce the spin-spin interaction

$$V_{\text{spin}} = \alpha \sum_{\mathbf{r}} \left(\hat{N}_{\mathbf{r}\uparrow} - \hat{N}_{\mathbf{r}\downarrow} \right)^2 \tag{5.15}$$

where the operators

$$\hat{N}_{\mathbf{r}\sigma} = \frac{1}{\bar{n}} \sum_{\mathbf{r}'} f(\mathbf{r} - \mathbf{r}') \hat{n}_{\mathbf{r}\sigma} \tag{5.16}$$

calculate the local *spin* density in a region of linear size ξ. For $\alpha > 0$, differences in spin density will lead to an energy penalty, encouraging the fermions to be split equally between both spin species. For $\alpha < 0$, spontaneous ferromagnetism will be energetically favoured, and fermion spins will tend to align. By tuning α, it is therefore possible to produce both FTI and FCI states from a topologically trivial system by adding a TR-invariant interaction.

The philosophy of this section is essentially the same as the spinless fermion case: by choosing a suitable interaction, the effective band structure of the single particle problem can be altered. Using spin-1/2 fermions allows us to do this without breaking symmetry explicitly, and we can thus generate both FCI and FTI phases.

5.4 Numerical Results

To support the arguments in the previous sections, we now give some finite-size numerical results which show an FCI state that has been generated using interactions of the form described above. Although our previous arguments are rigorous in the limit of very long-range interactions, we will find that even for a short-range interaction, we can stabilise an FCI state in a band with zero Berry curvature.

We will consider a model of bosons hopping on a honeycomb, forming bands with zero Berry curvature (as in Sec. 5.2.1). We will consider a case where the interaction strength (which determines the scale of $\tilde{K}$) is much greater than the hopping bandwidth of K. For simplicity we can set $t_{\mathbf{r}\mathbf{r}'} = K = 0$, which is appropriate in this limit. For the kinetic energy $\tilde{K}$ that we wish to simulate, we consider the flattened Haldane model, which, following the discussion in Sec. 5.1.1, we write as

$$\tilde{K}_{\text{HH}} = -\tilde{t}_1 \sum_{\langle \mathbf{r}\mathbf{r}' \rangle} \left[c^\dagger_{\mathbf{r}'} c_{\mathbf{r}} + h.c. \right] - \tilde{t}_2 \sum_{\langle\langle \mathbf{r}\mathbf{r}' \rangle\rangle} \left[c^\dagger_{\mathbf{r}'} c_{\mathbf{r}} e^{i\phi_{\mathbf{r}\mathbf{r}'}} + h.c. \right] - \tilde{t}_3 \sum_{\langle\langle\langle \mathbf{r}\mathbf{r}' \rangle\rangle\rangle} \left[c^\dagger_{\mathbf{r}'} c_{\mathbf{r}} + h.c. \right] + D \sum_{\mathbf{r}} c^\dagger_{\mathbf{r}} c_{\mathbf{r}}, \tag{5.17}$$

where $\tilde{t}_1 = 1, \tilde{t}_2 = 0.6, \tilde{t}_3 = -0.58$, $\phi = 0.4\pi$, and 'HH' stands for Haldane honeycomb. This has a flatness ratio of about 50, and exhibits a $\nu = 1/2$ FCI state that remains stable even in the presence of first and second neighbour density-density interactions [126]. In order to

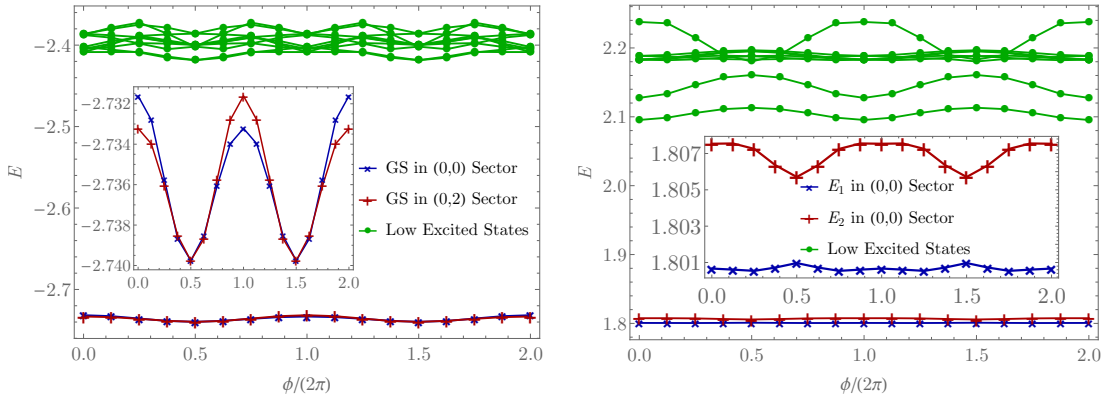

(a) (b)

Figure 5.2: Low-energy spectra as flux ϕ is inserted through one handle of the torus for the half-filled honeycomb with (a) 24 sites and (b) 32 sites. Insets show a close-up of the ground state energy splitting. See main text for details of the model.

prevent phase separation, we have also added a diagonal term with strength D, which in the noninteracting model appears as a chemical potential.

For simplicity, we assume we have hardcore bosons and we take the function $f(\mathbf{r})$ to be a simple top hat,

$$f(\mathbf{r}' - \mathbf{r}) = \begin{cases} \frac{1}{n(l)} & \text{if } |\mathbf{r}' - \mathbf{r}| \leq l \\ 0 & \text{otherwise} \end{cases} .$$

In this expression, l is a length scale that covers a small number of nearest neighbours and $n(l)$ is the number of sites that lie within the top hat, so that the function is normalised. Using Eq. (5.7), we can now write the flattened Haldane model as the interaction

$$U_{\text{HH}} = \frac{1}{2} \sum_{\mathbf{r}\mathbf{r}'} T^{\text{HH}}_{\mathbf{r}\mathbf{r}'} : \left[\hat{N}_{\mathbf{r}} c^{\dagger}_{\mathbf{r}} c_{\mathbf{r}'} + c^{\dagger}_{\mathbf{r}} c_{\mathbf{r}'} \hat{N}_{\mathbf{r}'} \right] :,$$

where $T^{\text{HH}}_{\mathbf{r}\mathbf{r}'}$ contains all the hopping parameters from Eq. (5.17). Since we are considering hardcore bosons, we do not need to add any additional interactions in order to stabilise the FCI state at half filling.

We carry out exact diagonalisation of U_{HH} on a 24-site lattice (3×4 unit cells) with 6 particles and on a 32-site lattice (4×4 unit cells) with 8 particles. In both cases we choose the size of the top hat, defined by l, to extend up to third-nearest neighbours—note that this is no further than the hopping distance. For the 24-site case we set $D = 2$ and for the 32-site case we set $D = 3$, chosen to give the largest many-body gap to ground-state splitting ratio. In both cases, we find strong numerical evidence to suggest that the ground state is a $\nu = 1/2$ FCI.

In Fig. 5.2 we plot the low-lying energy levels for each lattice size as magnetic flux ϕ is threaded through one handle of the torus. In each case we find a twofold degenerate ground

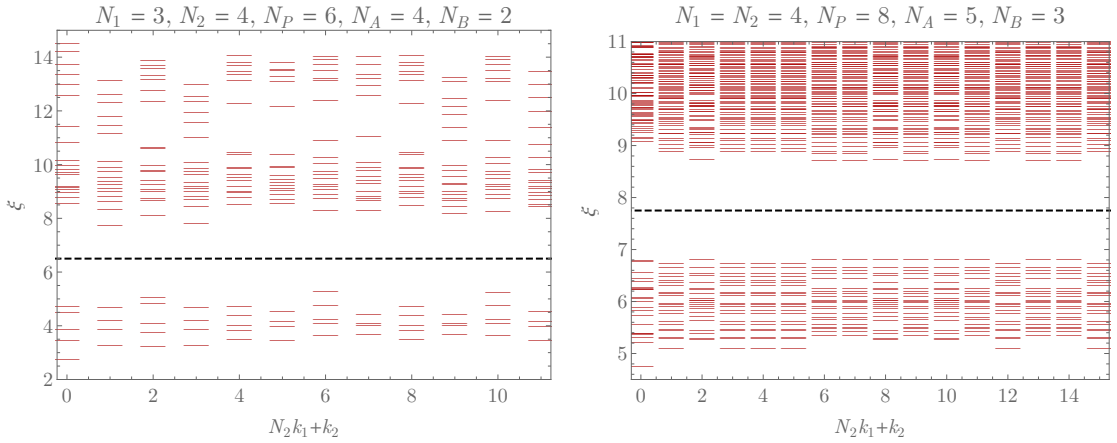

(a) (b)

Figure 5.3: Particle entanglement spectra for (a) $N = 6$ hardcore bosons on a 24-site honeycomb, with $N_B = 2$ particles traced out and (b) $N = 8$ hardcore bosons on a 32-site honeycomb, with $N_B = 3$ particles traced out. N_1 and N_2 are the number of unit cells in each direction, with k_1 and k_2 the corresponding momentum integers in the Brillouin zone. The number of states below the dashed line matches the expected quasihole counting rules in each case: (a) 4 or 5 states in each sector depending on whether k_2 is odd or even, giving a total of 54 states and (b) 22 states in each sector, giving a total of 352 states. See main text for details of the model.

state that is separated from excited states by a large many-body gap, and which occurs at the momentum values predicted for a $\nu = 1/2$ FCI by the generalised Pauli principle [73]. As flux is threaded through the handles of the torus, the two ground states for the 24-site case evolve into each other with a level crossing. For the 32-site case, the two ground states are in the same momentum sector, and display an avoided crossing under a flux insertion.

We have also calculated the particle entanglement spectrum (PES) for various partitions for each lattice size [134, 39]. In Fig 5.3 we show the PES for the 24-site lattice, tracing out two of the particles, and for the 32-site lattice, tracing out three of the eight particles (in the latter case we form the density matrix from an incoherent superposition of the two degenerate ground states, $\hat{\rho} = \frac{1}{2}\sum |\psi_i\rangle \langle\psi_i|$, as motivated in Ref. [39]). The entanglement spectrum shows a clear entanglement gap, and the number of states below this gap obeys the expected $(1, 2)$-admissible quasihole counting rules for each momentum sector [73]. This strongly suggests that our interaction-stabilised state is in the same universality class as other $\nu = 1/2$ FQH and FCI states.

5.5 Discussion

In this chapter we have proposed a type of interaction that may be used to generate fractional topological phases from a topologically trivial band structure. The underlying idea throughout is that hopping, i.e. kinetic energy terms, are effectively a subset of the possible interaction

terms. As such, it is possible to change the single particle spectrum using an interaction rather than a kinetic energy term. We have outlined how this may be achieved by interacting with a local density in a region of size ξ: it is possible that other approaches exist which use the same philosophy.

We note, however, that to change the Chern number of a band using an interaction, the interaction must be strong enough to mix the single-particle bands—i.e. it must be on the order of the gap between the bands before the interaction is added. It is often the case that FCIs are studied for flat bands in the very weak interaction limit. For this case our strategy will not work, since a very weak interaction would not be able to change the effective Chern number of the band. However, one could also consider a more complicated strategy where the lattice translational symmetry is broken down further, enlarging the unit cell such that a band with zero Chern number is broken into two bands with opposing nonzero Chern numbers. This could be achieved with an arbitrarily weak perturbation.

Although the interactions we consider are not of the density-density type, density-dependent hopping interactions are known to arise in systems of cold atoms. These may arise as higher-order terms in certain tight-binding approximations [198], but may also be induced directly using time-dependent magnetic fields [199, 200]. More recently, it has been shown that density-dependent synthetic gauge fields can be generated in spin-dependent optical lattices [201]. We also note that similar *vacancy*-assisted hoppings have recently been discussed in the context of kinetically constrained models, where they may also lead to topologically ordered phases [202].

We note that our construction provides a nice counterexample to the claims of Ref. [203], which proposed a formula for the Hall conductivity of an FCI as an integral over the Brillouin zone of the single-particle Berry curvature multiplied by some many-body occupancies. It is clear that this cannot be correct, since in our construction the Berry curvature of the noninteracting bands is strictly zero (so that Ref. [203] would always predict zero Hall conductivity) whereas, due to the (TR-breaking) interaction, the system is an FCI with quantised, nonzero, Hall conductivity. This counterexample complements separate work in Ref. [204], in which we disproved the claim in another manner.

Appendices for Chapter 5

5.A Stability Beyond Mean Field Theory

In Sec. 5.2.2 we introduced an interaction that reproduces the kinetic energy of a target Chern band model exactly in the mean field limit. In this appendix we will consider perturbative corrections to this mean field picture, and justify the stability of the FCI ground state.

When the correlation length ξ tends to infinity (or reaches the system size in the finite size case), the 'local' density operator $\hat{N}_{\mathbf{r}}$ can be replaced with unity. In general, the operator U can be written as $U = U_{\mathrm{MF}} + \delta U$, with

$$U_{\mathrm{MF}} = \sum_{\mathbf{r}\mathbf{r}'} T_{\mathbf{r}\mathbf{r}'} c^\dagger_{\mathbf{r}} c_{\mathbf{r}'}, \qquad \delta U = \frac{1}{2} \sum_{\mathbf{r}\mathbf{r}'} T_{\mathbf{r}\mathbf{r}'} : \left[\delta\hat{N}_{\mathbf{r}} c^\dagger_{\mathbf{r}} c_{\mathbf{r}'} + c^\dagger_{\mathbf{r}} c_{\mathbf{r}'} \delta\hat{N}_{\mathbf{r}'} \right] :$$

and

$$\delta\hat{N}_{\mathbf{r}} = \hat{N}_{\mathbf{r}} - 1 = \frac{1}{\bar{n}} \sum_{\mathbf{r}'} f(\mathbf{r}' - \mathbf{r}) \left[\hat{n}_{\mathbf{r}} - \bar{n} \right].$$

In this way, the perturbation δU depends on the density fluctuations in a region of linear dimension ξ, scaled by the average particle density, $\bar{n}$.

In order to estimate the size of the corrections due to δU, we first recall that for a general, uncorrelated Poisson process, density fluctuations in an area of linear size ξ scale as $\delta\hat{N}_{\mathbf{r}} \sim 1/\xi$. Quantum Hall states are more correlated than this, and so we expect their density fluctuations to scale as $\delta\hat{N}_{\mathbf{r}} \sim 1/\xi$ *at most*. Assuming that this property transfers to systems on a lattice, we expect $\delta N_{\mathbf{r}}$ acting on an FCI ground state to have an effect that is no larger than $O(1/\xi)$.

The action of the hopping component of δU is bounded by the maximum bandwidth, W, multiplied by the number of neighbouring sites and orbitals involved in the sum, h. At pth order in perturbation theory, the action of δU on the FCI ground state is then bounded by $\delta U^{(p)} < \left(A \frac{hW}{\xi} \right)^p$, with A a constant that depends on energy denominators and scale factors of order unity. By choosing ξ large enough, we can ensure that perturbative corrections of this form are negligible and convergent.

However, our assumption that $\delta\hat{N}_{\mathbf{r}} \sim 1/\xi$ is only valid at low orders in perturbation theory when the state being acted upon is close to a (homogeneous) FCI ground state. After applying δU many times, perturbative hopping processes may generate virtual phase-separated states, which have $\delta\hat{N}_{\mathbf{r}} \sim 1$. Assuming that the hopping described by $T_{\mathbf{r}\mathbf{r}'}$ can transfer particles by

up to L sites, virtual states that move particles by linear dimension ξ will first start to appear at order ξ/L in perturbation theory. A finite density of particles, over a region of area ξ^2 may then be moved, hence significantly changing the value of $\hat{N}$, at order $(\xi/L)^{C\xi^2}$ in perturbation theory where C is some constant. We can push these contributions to arbitrarily high order in perturbation theory by making ξ larger. Additionally, we can suppress these perturbative corrections with a large energy denominator by choosing D, the diagonal interaction term in Eq. (5.11), to be large and by adding additional density-density interactions between nearby neighbours. Finally we note that our numerical work confirms that even for small ξ, FCI states may be stabilised.

6. Summary and Outlook

We close this thesis by recalling some of the topics we have discussed and noting a few open questions.

Throughout this document, we have been concerned with lattice effects in topological phases of matter: specifically, we have been interested in the additional features and complications that arise in FCIs, as compared to the QHEs of the continuum. In Chapter 2, we began our study of this crossover in the context of the Hofstadter model, whose single-particle wavefunction solutions connect smoothly to LLs in the weak-field limit. We used a mixture of analytic and numerical methods to quantify the deviation from the LL limit as the magnetic flux per plaquette was tuned, which acted as a proxy for altering the strength of the lattice effects.

We found that the deviations from LL physics fall into two distinct categories. On the one hand, the energy bands and Berry curvature are no longer precisely flat, and deviate from their mean values by an amount that is exponentially small in the magnetic flux denominator. We obtained nonperturbative expressions for these deviations in Sec. 2.3, and found them to compare favourably with numerical results. On the other hand, the energy levels and wavefunctions of the Hofstadter model also gain corrections that are perturbative in the magnetic flux, which allow the wavefunctions to adopt the broken rotational symmetry of the lattice. In the weak-field limit, it is these algebraic corrections that are most important: the dominant effect of the lattice is to break rotational symmetry and the corresponding conservation of angular momentum. We extended this perturbative approach to many-body systems by defining and calculating the Haldane pseudopotential matrix, a set of two-body interaction matrix elements expressed in terms of relative angular momentum.

In Chapter 3 we generalised this analysis to other regions of the Hofstadter butterfly spectrum. In contrast to the weak-field limit, the band structure very close to simple magnetic flux fractions $\phi = P/Q$ behaves like Q copies of a Landau level. Although these regions do not connect to the conventional continuum limit, the wavefunctions and energy levels can nonetheless be interpreted as perturbed continuum functions, albeit with a multicomponent, sublattice structure. The multicomponent nature of the system near to these magnetic field values makes it an area ripe for further investigation. In this thesis, we considered some of the multicomponent FCI states that may be stabilised in these regions—notably, we found that the contact interaction supported generalised Halperin states. It is likely that more complicated interac-

tions would stabilise more complicated FCI states, with umklapp scattering processes playing a leading role.

Our perturbative method has natural applications to the recent experimental realisations of the Hofstadter model using optical lattices [152, 153]. To this end, in Chapter 4 we presented some numerical studies of the many-body energy spectra and wavefunctions for the Hofstadter model in an external trap, which would be present in the experimental set-up. Although the trapping potential adds significant complications, we found that provided the trap is weak, these additional features are negligible compared to the effects of the lattice. We observed the formation of a perturbed, bosonic Laughlin-like wavefunction in the presence of a contact interaction, which agreed well with the numerical state obtained from exact diagonalisation of the lattice model. We suggest that this state could be produced in a cold atom laboratory if experimenters are able to reach the strongly interacting regime.

There are many more parameter sets and generalisations to the approach outlined in this thesis that are worthy of further analytical and numerical study. We presented a number of such extensions in Sec. 3.5, including further lattice models and interactions. It is likely that in many of these cases, a study of the pseudopotentials, coupled with numerical simulations, may lead to predictions for novel topological states that could be realised experimentally. The ability to fine-tune model parameters in optical lattice experiments makes this an exciting prospect.

For general flux densities, we also found that a lattice dislocation may stabilise a topological genon defect, in the same way as might be observed in a multilayer fractional quantum Hall system [188]. The resulting orbifold states are predicted to harbour phases with nonabelian statistics, and a detailed study of their stability and experimental feasibility would be worth pursuing. In addition, the central $E = 0$ region of the Hofstadter spectrum exhibits Dirac cones and, if the magnetic field is perturbed slightly away from one of these points, a graphene-like Landau level spectrum is observed. The large energy gap above the lowest energy level of these systems, coupled with the discrete sublattice structure of the Hofstadter model, makes this regime a rich area for investigation.

In Chapter 5 we used the presence of a lattice to generate FCI states in a completely new way. Using strong interactions, we described a method that can be used to change the effective band structure of a tight-binding model and generate a fractional topological state, even if the original model is topologically trivial. We demonstrated the validity of this approach using numerical results for the Haldane model, and illustrated how it may be extended to FTI states.

Further numerical work is required to confirm the validity of our approach in the thermody-

namic limit, and it remains to be seen whether the interaction-hopping terms we describe may be realised experimentally. However, this approach also opens the door to other methods for generating interaction-stabilised FCI states using the same philosophy. In particular, it may be possible to split a single band with zero Berry curvature into two (or more) bands with equal and opposite Chern numbers through a spontaneous breaking of the lattice symmetry. We leave a study of this to elsewhere.

Throughout this thesis we have been able to make analytical progress in the study of FCIs, a field which has largely been the subject of numerical work. We achieved this using links to the QHE in Chapters 2–4 and using mean field theory in Chapter 5—we hope that this will provide encouragement for further analytical studies of FCIs. Ultimately, however, the validity of our methods and results relies on numerical and experimental evidence. We have presented some of our own simulations in this thesis, and outlined the applicability of our work to the optical lattice experiments that are at the cutting edge of modern experimental physics. We look to the future for further developments in this direction.

Bibliography

[1] F. Harper, S. H. Simon, and R. Roy, Phys. Rev. B **90**, 075104 (2014).
[2] S. H. Simon, F. Harper, and N. Read, arXiv:1506.08197 (2015).
[3] K. V. Klitzing, G. Dorda, and M. Pepper, Phys. Rev. Lett. **45**, 494 (1980).
[4] D. C. Tsui, H. L. Stormer, and A. C. Gossard, Phys. Rev. Lett. **48**, 1559 (1982).
[5] R. E. Prange and S. M. Girvin, *The Quantum Hall effect*, *Graduate texts in contemporary physics* (Springer-Verlag, New York, 1987).
[6] L. Balents, Nature **464**, 199 (2010).
[7] X. G. Wen, *Quantum Field Theory of Many-Body Systems*, *Oxford Graduate Texts* (Oxford University Press, Oxford, 2004).
[8] E. J. Bergholtz and Z. Liu, Int. J. Mod. Phys. B **27**, 1330017 (2013).
[9] S. A. Parameswaran, R. Roy, and S. L. Sondhi, C. R. Phys. **14**, 816 (2013).
[10] A. Y. Kitaev, Ann. Phys. (New York) **303**, 2 (2003).
[11] X. Chen, Z.-C. Gu, and X.-G. Wen, Phys. Rev. B **82**, 155138 (2010).
[12] C. Nayak *et al.*, Rev. Mod. Phys. **80**, 1083 (2008).
[13] A. Kitaev and J. Preskill, Phys. Rev. Lett. **96**, 110404 (2006).
[14] E. Fradkin, *Field Theories of Condensed Matter Physics*, *Field Theories of Condensed Matter Physics* (Cambridge University Press, Cambridge, 2013).
[15] Y.-M. Lu and A. Vishwanath, Phys. Rev. B **86**, 125119 (2012).
[16] M. Hasan and C. Kane, Rev. Mod. Phys. **82**, 3045 (2010).
[17] X. Chen, Z.-C. Gu, Z.-X. Liu, and X.-G. Wen, Phys. Rev. B **87**, 155114 (2013).
[18] X.-L. Qi and S.-C. Zhang, Rev. Mod. Phys. **83**, 1057 (2011).
[19] T. Scaffidi and G. Möller, Phys. Rev. Lett. **109**, 246805 (2012).
[20] Y.-H. Wu, J. K. Jain, and K. Sun, Phys. Rev. B **86**, 165129 (2012).
[21] D. R. Hofstadter, Phys. Rev. B **14**, 2239 (1976).
[22] P. G. Harper, P. R. Soc. A **68**, 879 (1955).
[23] E. H. Hall, Am. J. Math. **2**, 287 (1879).
[24] N. W. Ashcroft and N. D. Mermin, *Solid state physics*, *Science: Physics* (Saunders College, Philadelphia, 1976).
[25] P. A. Lee and T. V. Ramakrishnan, Rev. Mod. Phys. **57**, 287 (1985).
[26] T. Ando, A. B. Fowler, and F. Stern, Rev. Mod. Phys. **54**, 437 (1982).
[27] K. S. Novoselov *et al.*, Nature **438**, 197 (2005).
[28] V. P. Gusynin and S. G. Sharapov, Phys. Rev. Lett. **95**, 146801 (2005).
[29] Y. Zhang, Y.-W. Tan, H. L. Stormer, and P. Kim, Nature **438**, 201 (2005).
[30] J. S. Blakemore, J. Appl. Phys. **53**, R123 (1982).
[31] L. D. Landau and E. M. Lifshitz, *Quantum Mechanics: Non-relativistic Theory*, *Butterworth Heinemann* (Butterworth-Heinemann, Oxford, 1977).
[32] J. K. Jain, *Composite Fermions* (Cambridge University Press, Cambridge, 2007).
[33] D. J. Thouless, J. Phys. C: Solid State **17**, L325 (1984).
[34] X. G. Wen and A. Zee, Phys. Rev. Lett. **69**, 953 (1992).
[35] F. Haldane and E. H. Rezayi, Phys. Rev. B **31**, 2529 (1985).
[36] F. Haldane and E. H. Rezayi, Phys. Rev. Lett. **54**, 237 (1985).
[37] Z. Liu and E. J. Bergholtz, Phys. Rev. B **87**, 035306 (2013).
[38] Y.-L. Wu, N. Regnault, and B. A. Bernevig, Phys. Rev. Lett. **110**, 106802 (2013).
[39] A. Sterdyniak, N. Regnault, and G. Möller, Phys. Rev. B **86**, 165314 (2012).
[40] A. Tsukazaki *et al.*, Science **315**, 1388 (2007).
[41] S. Contreras, W. Knap, and C. Skierbiszewski, Mat. Sci. Eng. B **46**, 92 (1997).
[42] Y. Xu *et al.*, Nat. Phys. **10**, 956 (2014).
[43] R. Willett *et al.*, Phys. Rev. Lett. **59**, 1776 (1987).
[44] B. Huckestein, Rev. Mod. Phys. **67**, 357 (1995).

[45] D. J. Thouless, J. Phys. C: Solid State **14**, 3475 (1981).
[46] B. I. Halperin, Phys. Rev. B **25**, 2185 (1982).
[47] R. Landauer, Philos. Mag. **21**, 863 (1969).
[48] M. Buttiker, Phys. Rev. B **38**, 9375 (1988).
[49] J. K. Jain and S. A. Kivelson, Phys. Rev. B **37**, 4276 (1988).
[50] P. Streda, J. Kucera, and A. H. MacDonald, Phys. Rev. Lett. **59**, 1973 (1987).
[51] R. B. Laughlin, Phys. Rev. B **23**, 5632 (1981).
[52] D. J. Thouless, M. Kohmoto, M. P. Nightingale, and M. Den Nijs, Phys. Rev. Lett. **49**, 405 (1982).
[53] P. Streda, J. Phys. C: Solid State **15**, 1299 (1982).
[54] B. I. Halperin, Helv. Phys. Acta **56**, 75 (1983).
[55] D. Yoshioka, J. Phys. Soc. Jap. **53**, 3740 (1984).
[56] I. Sodemann and A. H. MacDonald, Phys. Rev. B **87**, 245425 (2013).
[57] M. R. Peterson and C. Nayak, Phys. Rev. B **87**, 245129 (2013).
[58] S. H. Simon and E. H. Rezayi, Phys. Rev. B **87**, 155426 (2013).
[59] S. M. Girvin and T. Jach, Phys. Rev. B **29**, 5617 (1984).
[60] R. B. Laughlin, Phys. Rev. Lett. **50**, 1395 (1983).
[61] N. K. Wilkin and J. M. F. Gunn, Phys. Rev. Lett. **84**, 6 (2000).
[62] N. Regnault and T. Jolicoeur, Phys. Rev. Lett. **91**, 030402 (2003).
[63] M. Hafezi, A. Sørensen, E. Demler, and M. Lukin, Phys. Rev. A **76**, 023613 (2007).
[64] D. Arovas, J. R. Schrieffer, and F. Wilczek, Phys. Rev. Lett. **53**, 722 (1984).
[65] J. M. Leinaas and J. Myrheim, Nuovo Cim. **B37**, 1 (1977).
[66] S. A. Trugman and S. Kivelson, Phys. Rev. B **31**, 5280 (1985).
[67] F. D. M. Haldane, Phys. Rev. Lett. **51**, 605 (1983).
[68] G. Fano, F. Ortolani, and E. Colombo, Phys. Rev. B **34**, 2670 (1986).
[69] D. J. Thouless, Surf. Sci. **142**, 147 (1984).
[70] R. Tao and D. J. Thouless, Phys. Rev. B **28**, 1142 (1983).
[71] E. H. Rezayi and F. Haldane, Phys. Rev. B **50**, 17199 (1994).
[72] E. J. Bergholtz and A. Karlhede, J. Stat. Mech. P04015 (2009).
[73] B. A. Bernevig and N. Regnault, Phys. Rev. B **85**, 075128 (2012).
[74] B. A. Bernevig and F. Haldane, Phys. Rev. Lett. **100**, 246802 (2008).
[75] T. Mazaheri, G. Ortiz, Z. Nussinov, and A. Seidel, Phys. Rev. B **91**, 085115 (2015).
[76] S. Simon, E. Rezayi, and N. R. Cooper, Phys. Rev. B **75**, 195306 (2007).
[77] S. M. Girvin, A. H. MacDonald, and P. M. Platzman, Phys. Rev. Lett. **54**, 581 (1985).
[78] S. M. Girvin, A. H. MacDonald, and P. M. Platzman, Phys. Rev. B **33**, 2481 (1986).
[79] J. H. Oaknin, L. Martin-Moreno, J. J. Palacios, and C. Tejedor, Phys. Rev. Lett. **74**, 5120 (1995).
[80] M. Stone, Phys. Rev. B **42**, 8399 (1990).
[81] X.-G. Wen, Int. J. Mod. Phys. B **6**, 1711 (1992).
[82] S. Tomonaga, Prog . Theor. Phys. (Kyoto) **5**, 544 (1950).
[83] J. M. Luttinger, J. Math. Phys. **4**, 1154 (1963).
[84] A. M. Chang, Rev. Mod. Phys. **75**, 1449 (2003).
[85] R. B. Laughlin, Surf. Sci. **142**, 163 (1984).
[86] S. M. Girvin, Phys. Rev. B **29**, 6012 (1984).
[87] B. I. Halperin, Phys. Rev. Lett. **52**, 1583 (1984).
[88] J. K. Jain, Phys. Rev. Lett. **63**, 199 (1989).
[89] Y. J. Chen, Phys. Lett. A **148**, 475 (1990).
[90] N. Read, Phys. Rev. Lett. **65**, 1502 (1990).
[91] B. Blok and X. G. Wen, Phys. Rev. B **43**, 8337 (1991).
[92] R. L. Willett, Rep. Prog. Phys. **76**, 076501 (2013).
[93] G. Moore and N. Read, Nucl. Phys. B **360**, 362 (1991).
[94] N. Read and E. Rezayi, Phys. Rev. B **59**, 8084 (1999).

[95] J. S. Xia *et al.*, Phys. Rev. Lett. **93**, 176809 (2004).
[96] A. Sørensen, E. Demler, and M. Lukin, Phys. Rev. Lett. **94**, 086803 (2005).
[97] G. Möller and N. R. Cooper, Phys. Rev. Lett. **103**, 105303 (2009).
[98] A. Kol and N. Read, Phys. Rev. B **48**, 8890 (1993).
[99] M. Kohmoto, Phys. Rev. B **39**, 11943 (1989).
[100] F. F. Assaad and S. Biskamp, Phys. Rev. B **51**, 1605 (1995).
[101] L. Hormozi, G. Möller, and S. H. Simon, Phys. Rev. Lett. **108**, 256809 (2012).
[102] R. Palmer and D. Jaksch, Phys. Rev. Lett. **96**, 180407 (2006).
[103] J. A. Kjäll and J. E. Moore, Phys. Rev. B **85**, 235137 (2012).
[104] F. Haldane, Phys. Rev. Lett. **61**, 2015 (1988).
[105] B. A. Bernevig and T. L. Hughes, *Topological Insulators and Topological Superconductors* (Princeton University Press, Princeton, 2013).
[106] M. V. Berry, P. R. Soc. A **392**, 45 (1984).
[107] M. Kohmoto, Ann. Phys. (New York) **160**, 343 (1985).
[108] D. Xiao, M.-C. Chang, and Q. Niu, Rev. Mod. Phys. **82**, 1959 (2010).
[109] R. Karplus and J. M. Luttinger, Phys. Rev. **95**, 1154 (1954).
[110] E. Kapit and E. Mueller, Phys. Rev. Lett. **105**, 215303 (2010).
[111] T. Neupert, L. Santos, C. Chamon, and C. Mudry, Phys. Rev. Lett. **106**, 236804 (2011).
[112] K. Sun, Z. Gu, H. Katsura, and S. Das Sarma, Phys. Rev. Lett. **106**, 236803 (2011).
[113] D. N. Sheng, Z.-C. Gu, K. Sun, and L. Sheng, Nat. Commun. **2**, 389 (2011).
[114] Q. Niu, D. J. Thouless, and Y.-S. Wu, Phys. Rev. B **31**, 3372 (1985).
[115] S. Kourtis, T. Neupert, C. Chamon, and C. Mudry, Phys. Rev. Lett. **112**, 126806 (2014).
[116] L. Chen, T. Mazaheri, A. Seidel, and X. Tang, J. Phys. A: Math. Theor. **47**, 152001 (2014).
[117] T. Scaffidi and S. H. Simon, Phys. Rev. B **90**, 115132 (2014).
[118] R. Roy, Phys. Rev. B **90**, 165139 (2014).
[119] S. A. Parameswaran, R. Roy, and S. L. Sondhi, Phys. Rev. B **85**, 241308 (2012).
[120] T. S. Jackson, G. Möller, and R. Roy, arXiv:1408.0843 (2014).
[121] X.-L. Qi, T. L. Hughes, and S.-C. Zhang, Phys. Rev. B **78**, 195424 (2008).
[122] E. Tang, J.-W. Mei, and X.-G. Wen, Phys. Rev. Lett. **106**, 236802 (2011).
[123] F. Wang and Y. Ran, Phys. Rev. B **84**, 241103 (2011).
[124] X. Hu, M. Kargarian, and G. A. Fiete, Phys. Rev. B **84**, 155116 (2011).
[125] M. Trescher and E. J. Bergholtz, Phys. Rev. B **86**, 241111 (2012).
[126] Y.-F. Wang, Z.-C. Gu, C.-D. Gong, and D. N. Sheng, Phys. Rev. Lett. **107**, 146803 (2011).
[127] Y.-L. Wu, B. A. Bernevig, and N. Regnault, Phys. Rev. B **85**, 075116 (2012).
[128] T. Liu, C. Repellin, B. A. Bernevig, and N. Regnault, Phys. Rev. B **87**, 205136 (2013).
[129] A. M. Läuchli, Z. Liu, E. J. Bergholtz, and R. Moessner, Phys. Rev. Lett. **111**, 126802 (2013).
[130] Y.-F. Wang *et al.*, Phys. Rev. Lett. **108**, 126805 (2012).
[131] N. R. Cooper and J. Dalibard, Phys. Rev. Lett. **110**, 185301 (2013).
[132] Z. Liu, D. L. Kovrizhin, and E. J. Bergholtz, Phys. Rev. B **88**, 081106 (2013).
[133] N. Regnault and B. A. Bernevig, Phys. Rev. X **1**, 021014 (2011).
[134] H. Li and F. Haldane, Phys. Rev. Lett. **101**, 010504 (2008).
[135] A. Chandran, M. Hermanns, N. Regnault, and B. A. Bernevig, Phys. Rev. B **84**, 205136 (2011).
[136] X.-L. Qi, Phys. Rev. Lett. **107**, 126803 (2011).
[137] Y.-L. Wu, N. Regnault, and B. A. Bernevig, Phys. Rev. B **86**, 085129 (2012).
[138] D. Xiao *et al.*, Nat. Commun. **2**, 596 (2011).
[139] X. Hu, A. Rüegg, and G. A. Fiete, Phys. Rev. B **86**, 235141 (2012).
[140] C.-Z. Chang *et al.*, Science **340**, 167 (2013).
[141] J. G. Checkelsky *et al.*, Nat. Phys. **10**, 731 (2014).

[142] L. A. Ponomarenko *et al.*, Nature **497**, 594 (2013).
[143] C. R. Dean *et al.*, Nature **497**, 598 (2013).
[144] B. Hunt *et al.*, Science **340**, 1427 (2013).
[145] A. Celi *et al.*, Phys. Rev. Lett. **112**, 043001 (2014).
[146] M. Aidelsburger *et al.*, Phys. Rev. Lett. **107**, 255301 (2011).
[147] S. K. Baur and N. R. Cooper, Phys. Rev. A **88**, 033603 (2013).
[148] D. Jaksch and P. Zoller, New J. Phys. **5**, 56 (2003).
[149] L. Wang and M. Troyer, Phys. Rev. A **89**, 011603 (2014).
[150] J. Dalibard, F. Gerbier, G. Juzeliūnas, and P. Öhberg, Rev. Mod. Phys. **83**, 1523 (2011).
[151] N. R. Cooper, Adv. Phys. **57**, 539 (2008).
[152] H. Miyake *et al.*, Phys. Rev. Lett. **111**, 185302 (2013).
[153] M. Aidelsburger *et al.*, Phys. Rev. Lett. **111**, 185301 (2013).
[154] G. Jotzu *et al.*, Nature **515**, 237 (2015).
[155] N. Y. Yao *et al.*, Phys. Rev. Lett. **110**, 185302 (2013).
[156] M. Abramowitz and I. A. Stegun, *Handbook of Mathematical Functions: With Formulas, Graphs, and Mathematical Tables*, *Applied mathematics series* (Dover Publ., New York, 1965).
[157] R. A. Kennedy and P. Sadeghi, *Hilbert Space Methods in Signal Processing* (Cambridge University Press, Cambridge, 2013).
[158] G. I. Watson, J. Phys. A: Math. Gen. **24**, 4999 (1991).
[159] R. Peierls, Z. Phys. **80**, 763 (1933).
[160] M. Y. Azbel, Sov. Phys. JETP **19**, 634 (1964).
[161] A. Rauh, G. H. Wannier, and G. Obermair, Phys. Status Solidi B **63**, 215 (1974).
[162] J. Zak, Phys. Rev. **134**, A1602 (1964).
[163] J. Zak, Phys. Rev. **134**, A1607 (1964).
[164] G. M. Obermair and G. H. Wannier, Phys. Status Solidi B **76**, 217 (1976).
[165] G. H. Wannier, Phys. Status Solidi B **88**, 757 (1978).
[166] G. H. Wannier, G. M. Obermair, and R. Ray, Phys. Status Solidi B **93**, 337 (1979).
[167] S. Aubry and G. André, Ann. Isr. Phy. **3**, 133 (1980).
[168] B. Simon, Phys. Rev. Lett. **51**, 2167 (1983).
[169] J. E. Avron, R. Seiler, and B. Simon, Phys. Rev. Lett. **51**, 51 (1983).
[170] Y. Hatsugai, Phys. Rev. Lett. **71**, 3697 (1993).
[171] I. Dana, Y. Avron, and J. Zak, J. Phys. C: Solid State **18**, L679 (1985).
[172] J. E. Avron, O. Kenneth, and G. Yehoshua, J. Phys. A: Math. Theor. **47**, 185202 (2014).
[173] H. J. Fischbeck, Phys. Status Solidi **38**, 11 (1970).
[174] M. Wilkinson, J. Phys. A: Math. Gen. **17**, 3459 (1984).
[175] M. Wilkinson, P. R. Soc. A **391**, 305 (1984).
[176] R. Rammal and J. Bellissard, J. Phys. France **51**, 1803 (1990).
[177] J. Bellissard, in *The Harald Bohr Centenary*, edited by C. Berg and B. Fuglede (The Royal Danish Academy of Sciences and Letters, Copenhagen, 1989), pp. 35–76.
[178] Y. Last, in *XIth International Congress of Mathematical Physics*, edited by D. Iagolnitzer (World Scientific, Paris, 1994), pp. 366–372.
[179] Y. Last, in *Sturm-Liouville Theory*, edited by W. O. Amrein, A. M. Hinz, and D. P. Pearson (Birkhäuser, Basel, 2005), pp. 99–120.
[180] A. Avila and S. Jitomirskaya, Ann. Math. **170**, 303 (2009).
[181] J. H. Han, D. J. Thouless, H. Hiramoto, and M. Kohmoto, Phys. Rev. B **50**, 11365 (1994).
[182] R. Barnett, G. R. Boyd, and V. Galitski, Phys. Rev. Lett. **109**, 235308 (2012).
[183] P. Wilmott, IMA Journal of Applied Mathematics **34**, 295 (1985).
[184] G. Khanna, S. Mukhopadhyay, R. Simon, and N. Mukunda, Ann. Phys. (New York) **253**, 55 (1997).
[185] W. Pfeifer, *The Lie Algebras Su(n): An Introduction* (Birkhäuser, Basel, 2003).
[186] Y.-H. Wu, J. K. Jain, and K. Sun, Phys. Rev. B **91**, 041119 (2015).

[187] Z. Huang and D. P. Arovas, Phys. Rev. B **86**, 245109 (2012).
[188] M. Barkeshli and X.-G. Wen, Phys. Rev. B **84**, 115121 (2011).
[189] M. Barkeshli and X.-L. Qi, Phys. Rev. X **2**, 031013 (2012).
[190] C. Chin and E. Mueller, Physics **6**, 118 (2013).
[191] N. Gemelke, E. Sarajlic, and S. Chu, arXiv:1007.2677 (2010).
[192] C. G. Darwin, Mathematical Proceedings of the Cambridge Philosophical Society **27**, 86 (1931).
[193] V. Fock, Z. Phys. **47**, 446 (1928).
[194] W. Kohn, Phys. Rev. **123**, 1242 (1961).
[195] T. Köhler, K. Góral, and P. S. Julienne, Rev. Mod. Phys. **78**, 1311 (2006).
[196] M. Aidelsburger *et al.*, Nat. Phys. **11**, 162 (2014).
[197] C. L. Kane and E. J. Mele, Phys. Rev. Lett. **95**, 226801 (2005).
[198] J. E. Hirsch, Physica C: Superconductivity **158**, 326 (1989).
[199] Á. Rapp, X. Deng, and L. Santos, Phys. Rev. Lett. **109**, 203005 (2012).
[200] M. D. Liberto, C. E. Creffield, G. I. Japaridze, and C. M. Smith, Phys. Rev. A **89**, 013624 (2014).
[201] S. Greschner, G. Sun, D. Poletti, and L. Santos, Phys. Rev. Lett. **113**, 215303 (2014).
[202] S. Kourtis and C. Castelnovo, Phys. Rev. B **91**, 155134 (2015).
[203] T. Neupert, L. Santos, C. Chamon, and C. Mudry, Phys. Rev. B **86**, 165133 (2012).
[204] S. H. Simon, F. Harper, and N. Read, Phys. Rev. B **89**, 127101 (2014).